



A University of Sussex PhD thesis

Available online via Sussex Research Online:

<http://sro.sussex.ac.uk/>

This thesis is protected by copyright which belongs to the author.

This thesis cannot be reproduced or quoted extensively from without first obtaining permission in writing from the Author

The content must not be changed in any way or sold commercially in any format or medium without the formal permission of the Author

When referring to this work, full bibliographic details including the author, title, awarding institution and date of the thesis must be given

Please visit Sussex Research Online for more information and further details



University of Sussex

Numerical Analysis and Simulations of a Tractable Model for Tumour Growth

by

Joe Eyles

supervised by Vanessa Styles

Submitted for the degree of Doctor of Philosophy
Department of Mathematics, University of Sussex
2019

Declaration

I hereby declare that this thesis has not been and will not be submitted in whole or in part to another University for the award of any other degree. This thesis is my own work, produced under the supervision of Vanessa Styles. Where applicable, the papers that inspired and informed this work are referenced.

Signature:

Joe Eyles

Abstract

This thesis begins with the description of a tractable model for tumour growth. The unique feature of this model is that we pass through the thin rim limit. We derive the sharp interface weak form and finite element scheme. We discuss the mesh smoothing techniques used in the implementation of the sharp interface finite element scheme. We then introduce an unfitted finite element scheme, and a sharp interface finite element scheme in \mathbb{R}^3 . We also write the model in the diffuse interface paradigm, along with the associated weak form. We prove the existence and uniqueness of the solution to the diffuse interface version of the model, and prove convergence of the diffuse interface finite element method. We conclude this thesis with a number of simulations in \mathbb{R}^2 and \mathbb{R}^3 . Here, we present rates of convergence, and also investigate the effect of parameter spaces on the morphology of the tumour. A biologically motivated investigation is made, and a brief comparison with *in vivo* tumours is presented.

Acknowledgements

- The Engineering and Physical Sciences Research Council (EPSRC), for their generous funding.
- The University of Sussex library.
- John King, for deriving and advising on the model.
- Vanessa Styles, for supervision.

Dedication

I dedicate this thesis to the people who helped me over the years:

- Dr Eyles, Dr Eyles, and Dr Eyles, for unwavering support, love, and (sometimes surprising) insight.
- Amy Boo, for always believing that I would solve it, even when I didn't believe. Also for putting up with my complaining.
- Destinies Children, best of friends allow for the best of escapes. You kept me sane - although not by example.
- Perry Yan Chloe, laughter may not be the best of medicines, but it is not far off.
- My bike, you carried me to the university daily. Without you I would have been broken by the bus.
- The unsung heroes: Judo, Dom, computer games, music, and the South Downs.

Thank you all. I could have done it without you, but it would have been twice as hard and half as fun.

Contents

1	Introduction	20
1.1	The model	21
1.1.1	Derivation of the model	22
1.1.2	Comparison with existing models	27
1.2	Approaches	29
1.2.1	Sharp interface approach	29
1.2.2	Diffuse interface approach	31
1.2.3	Other approaches	32
1.2.4	Comparison of approaches	32
1.3	Thesis overview	34
2	Sharp interface approaches	35
2.1	Derivation of a weak formulation of (\mathbb{M}) in \mathbb{R}^2	36
2.2	Finite element scheme	40
2.3	Fitted mesh smoothing	42
2.3.1	Harmonic extension method	43
2.3.2	DeTurck method	44
2.3.3	Re-meshing via GMSH	50
2.4	Unfitted finite element approximation of (\mathbb{M}) in \mathbb{R}^2	51
2.5	Fitted sharp interface finite element scheme in \mathbb{R}^3	56
3	Applied and numerical analysis of a diffuse interface model	59
3.1	Diffuse interface formulation	61
3.2	Existence of a solution to \mathbb{P}_{DI} for $D \subset \mathbb{R}^2$	64
3.3	Uniqueness of a solution to \mathbb{P}_{DI} for $D \subset \mathbb{R}^2$	82

3.4	Finite element scheme	90
3.5	Numerical analysis	92
3.5.1	Existence and uniqueness of the finite element scheme	93
3.5.2	Convergence of the finite element scheme	93
4	Numerical simulations	110
4.1	Alternate formulation of the model	111
4.2	Diffuse interface without regularisation	113
4.2.1	Weak form	113
4.2.2	Finite element scheme	114
4.2.3	Diffuse interface approximation to $(\tilde{\mathbb{M}})$	115
4.3	Summary of the implementations	116
4.3.1	Sharp interface	116
4.3.2	Unfitted sharp interface scheme	117
4.3.3	Diffuse interface	118
4.4	Radially symmetric simulations	118
4.4.1	Sharp interface experimental order of convergence	122
4.4.2	Comparison of the radius in \mathbb{R}^3	134
4.4.3	Effect of the regularisation parameter γ in $(\tilde{\mathbb{M}})$	137
4.4.4	Diverging from radial symmetry: reducing invasion	137
4.5	Simulations in \mathbb{R}^2	142
4.5.1	The parameter space $\alpha < \beta$	143
4.5.2	The parameter space $\alpha > \beta$	143
4.5.3	The parameter space $\alpha, \beta \ll 1.0$	147
4.5.4	Example of tumours <i>in vivo</i>	152
4.6	Simulations in \mathbb{R}^3	154
4.6.1	The parameter space $\alpha > \beta$	155
4.6.2	The parameter space $\alpha, \beta \ll 1.0$	159
4.6.3	Example of tumours <i>in vivo</i>	161
5	Conclusion	163
5.1	Summary	164

5.2 Future directions 165

Bibliography **166**

List of Figures

1.1	Closed surface or curve $\Gamma(t)$, with interior $\Omega(t)$, both in \mathbb{R}^d . We denote by \mathbf{n} the outward unit normal to $\Gamma(t)$. Here $\Omega(t)$ represents the tumour interior, and $\Gamma(t)$ represents the tumour boundary.	22
2.1	Two illustrations of the fitted meshes with \mathcal{T}_Ω^h in blue and \mathcal{T}_Γ^h in red. . . .	41
2.2	Evolution via mean curvature at $t = 0.8$, with the initial condition on the left. Middle left: $\omega = 0.1$. Middle right: $\omega = 0.01$. Right: $\omega = 0.001$	42
2.3	Evolution via an outward normal velocity, with mesh smoothing via the harmonic extension method detailed in Section 2.3.1. Left: $t = 0$. Right: $t = 10$	44
2.4	Schematic of the reparametrization of the time-dependent embedding $\mathbf{s}(t)$ by the solution $\psi(t)$ of the harmonic map heat flow.	45
2.5	Snapshots of a single quadrant of \mathcal{T}_Ω^h , showing the difference in mesh quality between the harmonic extension method, and the DeTurck method. The left image is the initial condition. The center image is taken at $t = 100$, and shows the mesh under the harmonic extension method (Section 2.3.1). The right image is also taken at $t = 100$, and shows the mesh under the DeTurck method (Section 2.3.2). The evolution of the circle is given by the outward normal velocity (2.3.2). The DeTurck method appears significantly more effective.	49

2.6	Graph showing the difference in mesh quality between the harmonic extension method (Section 2.3.1), and the DeTurck method (Section 2.3.2), measured by (2.3.3). A quality of $q = 1.0$ is ideal (this corresponds to a mesh consisting of equilateral triangles), and higher values imply a worse mesh. The evolution of the circle is given by the outward normal velocity (2.3.2). The simulation was run from $t = 0$ until $t = 100$, and at $t = 0$ we had $h := \max_{\mu \in \mathcal{T}_\Omega^h} H(\mu) \approx 0.05$ and $\Delta t = 10^{-2}$. We can see that the DeTurck method maintains the quality of the initial mesh, while the harmonic extension method degrades as time goes by. The quality oscillates with the velocity (2.3.2) (and thus with the radius of the circle).	50
2.7	Comparison of a coarse mesh created by ALBERTA (left) and a coarse mesh created by GMSH (right).	51
2.8	This figure displays an illustration of the unfitted finite element mesh \mathcal{T}_D^h . Γ_h^n is the bold black line, with $(\Omega_h^n)^+$ to its left, the <i>interior</i> triangles are in blue, the <i>exterior</i> triangles are in green, and the <i>cut</i> triangles are in red.	52
2.9	The left hand image is an example of an element, π , that is intersected by Γ_h^n but is not classified as <i>cut</i> . The centre and right hand images display different possibilities for Γ_h^n (in green) intersecting $\pi \in \mathcal{T}_D^h$ (in black), and the choice of $[\mathbf{r}_1, \mathbf{r}_2]$ (in red).	52
2.10	This image displays an illustration of Γ_h^n (in green) overlaid by $\tilde{\Gamma}_h^n$ (in red), and $(\tilde{\Omega}_h^n)^+$ (blue region).	53
3.1	The diffuse interfacial region $\Gamma_\varepsilon(t)$ in D , with outward unit normal $\boldsymbol{\nu}$. Here $\Gamma(t)$ is approximated by the zero level set of φ	60
3.2	The polyhedral domain D . Here $\boldsymbol{\nu}$ is the outward unit normal to ∂D , the boundary of D	90
4.1	Comparison of the analytic solution $u(r)$ (blue line) and the diffuse interface approximation $u_h(r)$ (red line). The x -axis is the radius, r . The edges of the diffuse interfacial region are denoted by two black lines. The diffuse interfacial region is of approximate width 0.3, centred at $r = 2.0$	116

- 4.2 Top plot: comparison of the radius, in \mathbb{R}^2 , computed using the sharp interface scheme \mathbb{P}_{SI}^h (blue line), diffuse interface scheme $\tilde{\mathbb{P}}_{DI}^h$ (red line) and the unfitted sharp interface scheme \mathbb{P}_{SIU}^h (green line), with the analytical radius from (4.4.2) (dashed yellow line, computed numerically). Bottom plot: comparison of u_h from the sharp interface scheme (blue line), from the diffuse interface scheme (red line), and from the unfitted sharp interface scheme, with the extended analytic solution u from (4.4.1) (dashed yellow line), taken at $t = 0.5$. In both plots the blue line is behind the dashed yellow and solid green lines. The diffuse interface solution was obtained with $\varepsilon = 0.09$, $\Delta t = 5 \times 10^{-7}$, $h = 0.0048$ and $dofs \approx 1.7 \times 10^5$, the fitted sharp interface scheme with $\Delta t = 5 \times 10^{-4}$, $h = 0.0046$ and $dofs \approx 5.3 \times 10^5$ and the unfitted sharp interface scheme with $\Delta t = 10^{-4}$, $h = 0.00057$ and $dofs = 1.3 \times 10^5$ 120
- 4.3 Top plot: comparison of the radius, in \mathbb{R}^2 , computed using the diffuse interface scheme $\tilde{\mathbb{P}}_{DI}^h$ and the analytical radius from (4.4.2) (dashed yellow line, computed numerically). Bottom plot: comparison of u_h from the diffuse interface scheme with the extended analytic solution u from (4.4.1) (dashed yellow line), taken at $t = 0.1$. Here we take $\varepsilon = 0.39, 0.27, 0.19, 0.09$, and 0.049 , $h \approx 0.028, 0.020, 0.014, 0.0098$, and 0.0049 , $\Delta t = 9 \times 10^{-5}, 6 \times 10^{-5}, 2 \times 10^{-5}, 10^{-5}$, and 10^{-6} , and $dofs \approx 9.2 \times 10^3, 1.5 \times 10^4, 2.9 \times 10^4, 4.6 \times 10^4$, and 1.7×10^5 121
- 4.4 Top plot: comparison of the radius, in \mathbb{R}^3 , computed using the sharp interface scheme $\mathbb{P}_{SI\mathbb{R}^3}^h$ (blue line) and diffuse interface scheme $\tilde{\mathbb{P}}_{DI}^h$ (red line), with the analytical radius from (4.4.2) (dashed yellow line, computed numerically). Bottom plot: comparison of u_h from the sharp interface scheme (blue line), from the diffuse interface scheme (red line), and with the extended analytic solution u from (4.4.1) (dashed yellow line), taken at $t = 0.3$. For the diffuse interface scheme we choose $\varepsilon = 0.1$, $h = 0.014$, $\Delta t = 5 \times 10^{-6}$, $dofs = 8.2 \times 10^5$, and for the sharp interface scheme we choose $\Delta t = 1.0 \times 10^{-5}$, $h = 0.06$, $dofs = 1.5 \times 10^4$ 122
- 4.5 Uniform mesh, with Γ_h^0 given by (4.4.3). 123

4.6	Non-uniform mesh, with Γ_h^0 given by (4.4.4).	129
4.7	Left: the DeTurck method with $\omega = 1$. Center left: the DeTurck method with $\omega = 10^{-3}$. Center right: the harmonic extension method with $\omega = 1$. Right: the harmonic extension method with $\omega = 10^{-3}$. All at $t = 20$	131
4.8	DeTurck method with $\omega = 1$, $\bar{\omega} = 0.1$ (recall that $\bar{\omega}$ is the timescale parameter for the DeTurck method). Taken at $t = 0.1$	131
4.9	Top plot: comparison of the radius, in \mathbb{R}^3 , computed using the sharp interface scheme $\mathbb{P}_{SI\mathbb{R}^3}^h$, with varying values of h , and the analytical radius (dashed red line). Center plot: the error $ R - R_h $ for different values of h . Bottom plot: Comparison of u_h from the sharp interface scheme, with the extended analytical solution u (dashed red), taken at $t = 0.3$. We take $h \approx 0.45, 0.35$, and 0.21 , we take $\Delta t = 5 \times 10^{-3}, 2.5 \times 10^{-3}$, and 1.25×10^{-3} , and the number of degrees of freedom $dofs$ are $dofs \approx 3.9 \times 10^3, 1.5 \times 10^4$, and 6.3×10^4	135
4.10	Top plot: comparison of the radius, in \mathbb{R}^3 , computed using the diffuse interface scheme $\tilde{\mathbb{P}}_{DI}^h$, with varying values of h , and the analytical radius (dashed red line). Center plot: the error $ R - R_h $ for different values of h . Bottom plot: comparison of u_h from the diffuse interface scheme, with the extended analytical solution u (dashed red line), taken at $t = 0.3$. We take $\varepsilon = 0.151, 0.125$, and 0.1 for the values $h \approx 0.027, 0.024$, and 0.014 , $\Delta t = 5 \times 10^{-5}, 10^{-5}$, and 5×10^{-6} , and the number of degrees of freedom $dofs$, at $t = 0$, are $dofs \approx 1.1 \times 10^5, 2.6 \times 10^5$, and 8.2×10^5	136
4.11	Two examples of slices of spheroids <i>in vivo</i> (outlined in red). The images are taken from the database used in [22, 29]. There is more information on the database in Section 4.5.4. The tumour type (both meningiomas), file number, and patient ID are written above the images.	138

- 4.12 This figure shows a rounded star shape converging to a spheroid steady state. Here we solve the sharp interface scheme \mathbb{P}_{SI}^h , with $Q = 1.0$, $\beta = 0.3$, $\alpha = 1.0$, $h \approx 0.075$ and $\Delta t = 10^{-2}$. From left to right we have $t = 0, 0.1, 1$, and 10. The geometry does not change significantly for $t > 10$. The initial geometry is formed by distorting a circle of initial radius $R_0 = 1.0$ in the normal direction by $0.2 \sin(6\theta)$, where θ is the polar angle. 138
- 4.13 Solving the finite element scheme \mathbb{P}_{SI}^h with $\alpha = 10^{-2}$, $\beta = 0.5$, $Q = 1.5$, and initial radius $R_0 = 2.62$. Taken at $t = 0, 11, 16$, and 21. We choose $\Delta t = 10^{-3}$ and $h \approx 0.076$. We can see that at $t = 11$ the radial symmetry begins to break. 139
- 4.14 Solution u_h from the sharp interface scheme \mathbb{P}_{SI}^h (top row) with $h \approx 0.03$ and $\Delta t = 10^{-3}$ (top row), from the unfitted sharp interface scheme \mathbb{P}_{SIU}^h with $h \approx 0.05$ and $\Delta t = 5 \times 10^{-3}$ (second row), and from the diffuse interface scheme $\tilde{\mathbb{P}}_{DI}^h$, with $\varepsilon = 0.075$, $h \approx 0.07$ and $\Delta t = 10^{-4}$ (third row). On the fourth row: a comparison between \mathbf{X}_h from the sharp interface scheme (in white), \mathbf{X}_h from the unfitted sharp interface scheme (in black), and φ_h from the diffuse interface scheme (in red and blue). The black line is covered by the white line. With $\alpha = 1.0$, $\beta = 0.1$, and $Q = 1.0$. Taken at $t = 0, 15, 30$, and 45. 144
- 4.15 φ_h from the diffuse interface scheme $\tilde{\mathbb{P}}_{DI}^h$ (red and blue, top row). Diffuse interface solution u_h (bottom row). Taken at $t = 0, 25, 50$, and 75, with $\alpha = 1.0$, $\beta = 0.1$, $Q = 1.0$, $\varepsilon = 0.075$, $h \approx 0.07$, and $\Delta t = 10^{-4}$. This extends Figure 4.14 in time. 145
- 4.16 Two simulations (top row and bottom row) using the sharp interface scheme \mathbb{P}_{SI}^h with different initial geometries. The initial geometries are created by distorting an ellipse of width 0.5 and height 1.0 in the $\frac{\mathbf{X}_h}{|\mathbf{X}_h|}$ direction, by a distance of either $0.2 \sin(5\theta)$ on the top row, or $0.2 \sin(6\theta)$ on the bottom row. We choose $\alpha = 1.0$, $\beta = 0.1$, $Q = 1.0$, $\Delta t = 10^{-3}$, and $h \approx 0.017$. The snapshots are at $t = 0, 14, 29$, and 46. 146

- 4.17 Diffuse interface scheme $\tilde{\mathbb{P}}_{DI}^h$, with $\alpha = 1.0$, $\beta = 0.1$, $Q = 1.0$, $\varepsilon = 0.07$, $\Delta t = 5 \times 10^{-4}$, and $h \approx 0.03$, taken at $t = 0, 1, 6, 20, 30$, and 40 . Rows one and two represent φ_h at these times, while rows three and four represent u_h at these times. 147
- 4.18 Solution u_h from the sharp interface scheme \mathbb{P}_{SI}^h with $h \approx 0.03$, $\Delta t = 10^{-3}$, (top row), from the unfitted sharp interface scheme \mathbb{P}_{SIU}^h with $h \approx 0.02$, $\Delta t = 10^{-3}$ (second row), and from the diffuse interface scheme $\tilde{\mathbb{P}}_{DI}^h$ with $\varepsilon = 0.01$, $h \approx 0.02$, $\Delta t = 10^{-4}$ (third row) at $t = 0, 3$, and 7 . On the fourth row: a comparison between \mathbf{X}_h from the sharp interface scheme (in white), \mathbf{X}_h from the unfitted sharp interface scheme (in black), and φ_h from the diffuse interface scheme (in red and blue, fourth row). The black line is covered by the white line. With $\alpha = 0.1$, $\beta = 0.1$, and $Q = 1.0$ 148
- 4.19 φ_h from the diffuse interface scheme $\tilde{\mathbb{P}}_{DI}^h$ (in red and blue) (top row). Diffuse interface solution u_h (bottom row). All taken at $t = 0, 10, 20$, and 24 , with $\alpha = 0.1$, $\beta = 0.1$, $Q = 1.0$, $\varepsilon = 0.01$, $\Delta t = 10^{-4}$, and $h \approx 0.02$. This extends Figure 4.18 in time. 149
- 4.20 Two simulations (top row and bottom row) using the sharp interface scheme \mathbb{P}_{SI}^h , with different initial geometries. The initial geometries are created as described in Section 4.5.2, with the top row generated by $0.2 \sin(5\theta)$ and the bottom row generated by $0.2 \sin(6\theta)$. We choose $\alpha = 0.1$, $\beta = 0.1$, $Q = 1.0$, $\Delta t = 10^{-3}$, and $h \approx 0.017$. The snapshots are taken at $t = 0, 1, 5$, and 7 . . . 150
- 4.21 u_h from the sharp interface schemes \mathbb{P}_{SI}^h (first row) and $\tilde{\mathbb{P}}_{SI}^h$ (second row). Comparison of \mathbf{X}_h from each scheme (third row). Here \mathbb{P}_{SI}^h is in red and $\tilde{\mathbb{P}}_{SI}^h$ is in blue. The red line is almost entirely behind the blue line. We choose $\alpha = 0.01$, $\beta = 0.1$, $Q = 1.0$, $h \approx 0.026$, and $\Delta t = 10^{-3}$. The initial geometry is an ellipse of width 0.5 and height 1.0. The snapshots are taken at $t = 0$ and 5 151
- 4.22 We solve the sharp interface scheme $\tilde{\mathbb{P}}_{SI}^h$ with $\alpha = 0$, $\beta = 0.1$, $Q = 1.0$, $\Delta t = 10^{-3}$, and $h \approx 0.03$, with an ellipse of width 0.5 and height 1.0 for the initial geometry. The snapshots are taken at $t = 0, 2, 3, 4$, and 5 152

4.23	Slices of <i>in vivo</i> tumours from [22, 29]. The slice is shown in grey scale, while the tumour is outlined in red. Above each image is the tumour type (in this case they are all gliomas), the file number, and the patient ID. Each image is taken from a different patient.	153
4.24	Slices of <i>in vivo</i> tumours from [22, 29]. The slice is shown in grey scale, while the tumour is outlined in red. Above each image is the tumour type (in this case they are all pituitary tumours), the file number, and the patient ID. Each image is taken from a different patient.	154
4.25	\mathbf{X}_h for the sharp interface scheme $\mathbb{P}_{SI\mathbb{R}^3}^h$, looking down the x -axis (first line), looking down the y -axis (second line), cross section in the plane $z = 0$ (third line), and u_h in the plane $z = 0$ (fourth line). Taken at $t = 0, 5, 10$, and 15. The initial geometry is an oblate spheroid with the equation $\frac{x^2}{1.0^2} + \frac{y^2}{0.5^2} + \frac{z^2}{1.0^2} = 1$. We take $\alpha = 1.0$, $\beta = 0.1$, $Q = 1.25$, $h \approx 0.014$, and $\Delta t = 5 \times 10^{-3}$	156
4.26	The level set $\varphi_h = 0$ for the diffuse interface scheme $\tilde{\mathbb{P}}_{DI}^h$, looking down the x -axis (first line), looking down the y -axis (second line), cross section in the plane $z = 0$ (third line), and u_h in the plane $z = 0$ (fourth line). Taken at $t = 0, 5, 10$, and 15. The initial geometry is an oblate spheroid with the equation $\frac{x^2}{1.0^2} + \frac{y^2}{0.5^2} + \frac{z^2}{1.0^2} = 1$. We take $\alpha = 1.0$, $\beta = 0.1$, $Q = 1.25$, $\varepsilon = 0.1$, $h \approx 0.04$, and $\Delta t = 10^{-3}$	157
4.27	\mathbf{X}_h for the sharp interface scheme $\mathbb{P}_{SI\mathbb{R}^3}^h$ looking down the y -axis (first line), looking down the z -axis (second line), cross section in the plane $x = 0$ (third line), and u_h in the plane $x = 0$ (fourth line). Taken at $t = 0, 10$, and 18. The initial geometry is an oblate and prolate spheroid with the equation $\frac{x^2}{1.0^2} + \frac{y^2}{0.5^2} + \frac{z^2}{1.5^2} = 1$. We take $\alpha = 1.0$, $\beta = 0.1$, $Q = 1.25$, $h \approx 0.014$, and $\Delta t = 5 \times 10^{-3}$	158
4.28	The level set $\varphi_h = 0$ for the diffuse interface scheme $\tilde{\mathbb{P}}_{DI}^h$, displayed as a cross section in the plane $z = 0$. Taken at $t = 0, 15, 19$, and 24. The parameters match Figure 4.26 (but with h increased to $h \approx 0.09$).	159

- 4.29 \mathbf{X}_h for the sharp interface scheme $\mathbb{P}_{SIR^3}^h$, looking down the x -axis (first line), looking down the y -axis (second line), cross section in the plane $y = 0$ (third line), and u_h in the plane $x = 0$ (fourth line). Taken at $t = 0, 1.4, 2.9$, and 4.1. The initial geometry is an oblate spheroid with the equation $\frac{x^2}{1.0^2} + \frac{y^2}{0.5^2} + \frac{z^2}{1.0^2} = 1$. With $\alpha = 0.1$, $\beta = 0.1$, $Q = 1.25$, $h \approx 0.019$, and $\Delta t = 5 \times 10^{-3}$. . 160
- 4.30 \mathbf{X}_h for the sharp interface scheme $\mathbb{P}_{SIR^3}^h$, looking down the y -axis (first line), looking down the z -axis (second line), cross section in the plane $x = 0$ (third line), and u_h in the plane $y = 0$ (fourth line). Taken at $t = 0, 1.4, 2.9$, and 4.3. The initial geometry is an oblate and prolate spheroid with the equation $\frac{x^2}{1.0^2} + \frac{y^2}{0.5^2} + \frac{z^2}{1.5^2} = 1$. With $\alpha = 0.1$, $\beta = 0.1$, $Q = 1.25$, $h \approx 0.019$, and $\Delta t = 5 \times 10^{-3}$ 161
- 4.31 Two hepatic tumours taken from the IRCAD database. The first tumour is on the top row, and the second tumour is on the bottom row. We see each tumour looking down the x -axis, down the y -axis, and down the z -axis. . . 162

List of Tables

- 4.1 Errors for the given norms, solving the sharp interface scheme \mathbb{P}_{SI}^h with $\omega = 1$, and the DeTurck method. With Γ_h^0 given by (4.4.3). Here $L^2(v, U)$ for function v and set U denotes the norm $\Delta t \sum_{n=0}^N \|v_h^n - v(t_n)\|_{L^2(U)}^2$, and $H^1(v, U)$ for function v and set U denotes the norm $\Delta t \sum_{n=0}^N |v_h^n - v(t_n)|_{H^1(U)}^2$ 125
- 4.2 Experimental order of convergence for the given norms, solving the sharp interface scheme \mathbb{P}_{SI}^h with $\omega = 1$, and the DeTurck method. With Γ_h^0 given by (4.4.3). Here $L^2(v, U)$ for function v and set U denotes the experimental orders of convergence for the norm $\Delta t \sum_{n=0}^N \|v_h^n - v(t_n)\|_{L^2(U)}^2$, and $H^1(v, U)$ for function v and set U denotes the experimental orders of convergence for the norm $\Delta t \sum_{n=0}^N |v_h^n - v(t_n)|_{H^1(U)}^2$ 125
- 4.3 Errors for the given norms, solving the sharp interface scheme \mathbb{P}_{SI}^h with $\omega = 10^{-3}$, and the DeTurck method. With Γ_h^0 given by (4.4.3). Here $L^2(v, U)$ for function v and set U denotes the norm $\Delta t \sum_{n=0}^N \|v_h^n - v(t_n)\|_{L^2(U)}^2$, and $H^1(v, U)$ for function v and set U denotes the norm $\Delta t \sum_{n=0}^N |v_h^n - v(t_n)|_{H^1(U)}^2$ 126
- 4.4 Experimental order of convergence for the given norms, solving the sharp interface scheme \mathbb{P}_{SI}^h with $\omega = 10^{-3}$, and the DeTurck method. With Γ_h^0 given by (4.4.3). Here $L^2(v, U)$ for function v and set U denotes the experimental orders of convergence for the norm $\Delta t \sum_{n=0}^N \|v_h^n - v(t_n)\|_{L^2(U)}^2$, and $H^1(v, U)$ for function v and set U denotes the experimental orders of convergence for the norm $\Delta t \sum_{n=0}^N |v_h^n - v(t_n)|_{H^1(U)}^2$ 126

- 4.5 Errors for the given norms, solving the sharp interface scheme \mathbb{P}_{SI}^h with $\omega = 1$, and the harmonic extension method. With Γ_h^0 given by (4.4.3). Here $L^2(v, U)$ for function v and set U denotes the norm $\Delta t \sum_{n=0}^N \|v_h^n - v(t_n)\|_{L^2(U)}^2$, and $H^1(v, U)$ for function v and set U denotes the norm $\Delta t \sum_{n=0}^N \|v_h^n - v(t_n)\|_{H^1(U)}^2$ 126
- 4.6 Experimental order of convergence for the given norms, solving the sharp interface scheme \mathbb{P}_{SI}^h with $\omega = 1$, and the harmonic extension method. With Γ_h^0 given by (4.4.3). Here $L^2(v, U)$ for function v and set U denotes the experimental orders of convergence for the norm $\Delta t \sum_{n=0}^N \|v_h^n - v(t_n)\|_{L^2(U)}^2$, and $H^1(v, U)$ for function v and set U denotes the experimental orders of convergence for the norm $\Delta t \sum_{n=0}^N \|v_h^n - v(t_n)\|_{H^1(U)}^2$ 127
- 4.7 Errors for the given norms, solving the sharp interface scheme \mathbb{P}_{SI}^h with $\omega = 10^{-3}$, and the harmonic extension method. With Γ_h^0 given by (4.4.3). Here $L^2(v, U)$ for function v and set U denotes the norm $\Delta t \sum_{n=0}^N \|v_h^n - v(t_n)\|_{L^2(U)}^2$, and $H^1(v, U)$ for function v and set U denotes the norm $\Delta t \sum_{n=0}^N \|v_h^n - v(t_n)\|_{H^1(U)}^2$ 127
- 4.8 Experimental order of convergence for the given norms, solving the sharp interface scheme \mathbb{P}_{SI}^h with $\omega = 10^{-3}$, and the harmonic extension method. With Γ_h^0 given by (4.4.3). Here $L^2(v, U)$ for function v and set U denotes the experimental orders of convergence for the norm $\Delta t \sum_{n=0}^N \|v_h^n - v(t_n)\|_{L^2(U)}^2$, and $H^1(v, U)$ for function v and set U denotes the experimental orders of convergence for the norm $\Delta t \sum_{n=0}^N \|v_h^n - v(t_n)\|_{H^1(U)}^2$ 127
- 4.9 Errors for the given norms, solving the unfitted sharp interface scheme \mathbb{P}_{SIU}^h with $\omega = 1$. With Γ_h^0 given by (4.4.3). Here $L^2(v, U)$ for function v and set U denotes the norm $\sup_{n=0, \dots, N} \|v_h^n - v(t_n)\|_{L^2(U)}^2$, and $H^1(v, U)$ for function v and set U denotes the norm $\sup_{n=0, \dots, N} \|v_h^n - v(t_n)\|_{H^1(U)}^2$ 128

- 4.10 Experimental order of convergence for the given norms, solving the unfitted sharp interface scheme \mathbb{P}_{SIU}^h with $\omega = 1$. With Γ_h^0 given by (4.4.3). Here $L^2(v, U)$ for function v and set U denotes the experimental orders of convergence for the norm $\sup_{n=0, \dots, N} \|v_h^n - v(t_n)\|_{L^2(U)}^2$, and $H^1(v, U)$ for function v and set U denotes the experimental orders of convergence for the norm $\sup_{n=0, \dots, N} |v_h^n - v(t_n)|_{H^1(U)}^2$ 128
- 4.11 Errors for the given norms, solving the sharp interface scheme \mathbb{P}_{SI}^h with $\omega = 1$, and the DeTurck method. With Γ_h^0 given by (4.4.4). Here $L^2(v, U)$ for function v and set U denotes the norm $\Delta t \sum_{n=0}^N \|v_h^n - v(t_n)\|_{L^2(U)}^2$, and $H^1(v, U)$ for function v and set U denotes the norm $\Delta t \sum_{n=0}^N |v_h^n - v(t_n)|_{H^1(U)}^2$ 131
- 4.12 Experimental order of convergence for the given norms, solving the sharp interface scheme \mathbb{P}_{SI}^h with $\omega = 1$, and the DeTurck method. With Γ_h^0 given by (4.4.4). Here $L^2(v, U)$ for function v and set U denotes the experimental orders of convergence for the norm $\Delta t \sum_{n=0}^N \|v_h^n - v(t_n)\|_{L^2(U)}^2$, and $H^1(v, U)$ for function v and set U denotes the experimental orders of convergence for the norm $\Delta t \sum_{n=0}^N |v_h^n - v(t_n)|_{H^1(U)}^2$ 132
- 4.13 Errors for the given norms, solving the sharp interface scheme \mathbb{P}_{SI}^h with $\omega = 10^{-3}$, and the DeTurck method. With Γ_h^0 given by (4.4.4). Here $L^2(v, U)$ for function v and set U denotes the norm $\Delta t \sum_{n=0}^N \|v_h^n - v(t_n)\|_{L^2(U)}^2$, and $H^1(v, U)$ for function v and set U denotes the norm $\Delta t \sum_{n=0}^N |v_h^n - v(t_n)|_{H^1(U)}^2$ 132
- 4.14 Experimental order of convergence for the given norms, solving the sharp interface scheme \mathbb{P}_{SI}^h with $\omega = 10^{-3}$, and the DeTurck method. With Γ_h^0 given by (4.4.4). Here $L^2(v, U)$ for function v and set U denotes the experimental orders of convergence for the norm $\Delta t \sum_{n=0}^N \|v_h^n - v(t_n)\|_{L^2(U)}^2$, and $H^1(v, U)$ for function v and set U denotes the experimental orders of convergence for the norm $\Delta t \sum_{n=0}^N |v_h^n - v(t_n)|_{H^1(U)}^2$ 132

- 4.15 Errors for the given norms, solving the sharp interface scheme \mathbb{P}_{SI}^h with $\omega = 1$, and the harmonic extension method. With Γ_h^0 given by (4.4.4). Here $L^2(v, U)$ for function v and set U denotes the norm $\Delta t \sum_{n=0}^N \|v_h^n - v(t_n)\|_{L^2(U)}^2$, and $H^1(v, U)$ for function v and set U denotes the norm $\Delta t \sum_{n=0}^N \|v_h^n - v(t_n)\|_{H^1(U)}^2$ 133
- 4.16 Experimental order of convergence for the given norms, solving the sharp interface scheme \mathbb{P}_{SI}^h with $\omega = 1$, and the harmonic extension method. With Γ_h^0 given by (4.4.4). Here $L^2(v, U)$ for function v and set U denotes the experimental orders of convergence for the norm $\Delta t \sum_{n=0}^N \|v_h^n - v(t_n)\|_{L^2(U)}^2$, and $H^1(v, U)$ for function v and set U denotes the experimental orders of convergence for the norm $\Delta t \sum_{n=0}^N \|v_h^n - v(t_n)\|_{H^1(U)}^2$ 133
- 4.17 Errors for the given norms, solving the sharp interface scheme \mathbb{P}_{SI}^h with $\omega = 10^{-3}$, and the harmonic extension method. With Γ_h^0 given by (4.4.4). Here $L^2(v, U)$ for function v and set U denotes the norm $\Delta t \sum_{n=0}^N \|v_h^n - v(t_n)\|_{L^2(U)}^2$, and $H^1(v, U)$ for function v and set U denotes the norm $\Delta t \sum_{n=0}^N \|v_h^n - v(t_n)\|_{H^1(U)}^2$ 133
- 4.18 Experimental order of convergence for the given norms, solving the sharp interface scheme \mathbb{P}_{SI}^h with $\omega = 10^{-3}$, and the harmonic extension method. With Γ_h^0 given by (4.4.4). Here $L^2(v, U)$ for function v and set U denotes the experimental orders of convergence for the norm $\Delta t \sum_{n=0}^N \|v_h^n - v(t_n)\|_{L^2(U)}^2$, and $H^1(v, U)$ for function v and set U denotes the experimental orders of convergence for the norm $\Delta t \sum_{n=0}^N \|v_h^n - v(t_n)\|_{H^1(U)}^2$ 134
- 4.19 Comparison of errors for different values of γ when solving $\tilde{\mathbb{P}}_{SI}^h$ with $h \approx 0.03$ and $\Delta t = 10^{-4}$. Here $\|f\|_{L^2(L^2(U))} := \Delta t \sum_{n=0}^N \|f^n\|_{L^2(U)}^2$, and $\|f\|_{L^2(H^1(U))} := \Delta t \sum_{n=0}^N \|f^n\|_{H^1(U)}^2$ for a set U and function f 137
- 4.20 Time at which the $L^2(\mathbb{I})$ error in \mathbf{X}_h for the finite element scheme \mathbb{P}_{SI}^h is first greater than 0.1. Here $\alpha = 10^{-2}$, $\Delta t = 10^{-3}$, and the values of h can be found in Table 4.23. The initial shape is a circle, with initial radius given in Table 4.24. For entries of > 100 the error did not diverge for $t \in [0, 100]$. We did not use GMSH. The blank entries have no steady state. 140

4.21	Time at which the $L^2(\mathbb{I})$ error in \mathbf{X}_h for the finite element scheme \mathbb{P}_{SI}^h is first greater than 0.1. Here $Q = 1.4$, $\Delta t = 10^{-3}$, and the values of h can be found in Table 4.23. The initial shape is a circle, with initial radius given in Table 4.24. Recall that R_0 (and thus h) depends only on β and Q . For entries of > 100 the error did not diverge for $t \in [0, 100]$. We did not use GMSH.	141
4.22	Time at which the $L^2(\mathbb{I})$ error in \mathbf{X}_h for the finite element scheme \mathbb{P}_{SI}^h is first greater than 0.1. Here $\beta = 0.6$, $\Delta t = 10^{-3}$, and the values of h can be found in Table 4.23. The initial shape is a circle, with initial radius given in Table 4.24. Recall that R_0 (and thus h) depends only on β and Q . For entries of > 100 the error did not diverge for $t \in [0, 100]$. We did not use GMSH.	141
4.23	This table shows the values of h (to 3 decimal places) for the initial meshes used in the simulations of Section 4.4.4. The values of h are different for each initial radius, as we generate the mesh by refining a triangulation of a circle a fixed number of times. These initial radii can be found in Table 4.24. The blank entries have no steady state.	142
4.24	Here we show the radius of the radially symmetric stable steady state for the given Q and β . These are shown to 2 decimal places. The blank entries have no steady state.	142

Chapter 1

Introduction

The two most notable reasons for mathematically modelling cancer are to predict the behaviour, and to gain insights into the mechanisms at play; thus the field has great potential for research. The study of tissue growth, in particular the growth of a tumour, is a complex problem, and has attracted the interest of mathematicians, for example [13, 34]. They have been able to apply a range of techniques to the problem, from game theory [71] to Bayesian calibration [57].

Predicting a particular tumour's behaviour has obvious medical uses, and if more advanced models are analysed then the field has the potential to be highly useful to oncologists. An accurate model could be used not only to predict the growth, and thus the potential malignancy, of a given tumour, but also to test treatments. For example, the model could predict the minimum drug treatment that would see a reduction in size. Further research could also allow the surgeon to debulk (or remove part of the tumour) *in silico*. The model would then give an indication of the tumour's response. Predicting various growth behaviours, such as the formation of blood vessels (angiogenesis) and invasion or spreading (metastases), would also be an important tool in treating a tumour. Although this work is a far cry from these applications, it represents, along with many others, a step towards these goals.

The mathematical modelling of tumours can help us to understand the mechanisms that underpin their behaviour, and to gain insights into the complex systems that govern them. Given a model of sufficient fidelity, a mathematician is able to investigate a wide range of parameter dependent behaviours. As an example, mathematical modelling has

helped to quantify the effects of nutrient availability on the stability of tumour morphology, see page 235 of [34] and some of the references contained within. In this work, they show that what might seem an intuitive approach to treating a tumour, namely starving it of nutrients, can actually lead to increased instability and invasiveness.

In this thesis we physically model the tumour, deriving a model for tumour growth based on mechanical laws (as opposed to biological or chemical processes - although some of these have mechanical effects that are included, for example cell-cell adhesion). This thesis considers the tumour as a continuum, rather than a collection of discrete cells undergoing stochastic or deterministic behaviour. The literature has a number of examples of continuum tumour growth models, with some of the earliest tumour growth models stretching back as far as the 1970s, see [54, 55]. These are sharp interface approaches, in which the boundary between the interior and exterior of the tumour is given by a hypersurface. There are also a number of diffuse interface approaches, see for instance [32, 50]. The model studied in this thesis considers a region of necrotic (dead) cells, surrounded by a thin rim of viable live cells on the tumour's boundary. This is a sharp interface model. The next section gives an overview of the derivation of the model.

1.1 The model

The model investigated is one of the simplest mathematical descriptions of tumour growth (or, more generally, multicellular tissue, or a bacterial population). The goal is not biological realism, but rather to clarify and fully investigate the properties of this model. Additional complexity could then (in future work) be added as required.

In Figure 1.1 we see the set up, in which $\Gamma(t)$ is a closed surface or curve, with interior $\Omega(t)$, both in \mathbb{R}^d . We denote by \mathbf{n} the outward unit normal to $\Gamma(t)$. Here $\Omega(t)$ represents the tumour interior, and $\Gamma(t)$ represents the tumour boundary.

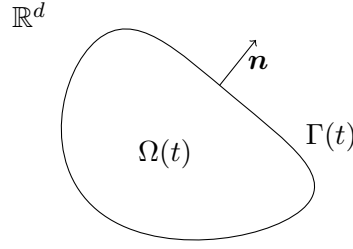


Figure 1.1: Closed surface or curve $\Gamma(t)$, with interior $\Omega(t)$, both in \mathbb{R}^d . We denote by \mathbf{n} the outward unit normal to $\Gamma(t)$. Here $\Omega(t)$ represents the tumour interior, and $\Gamma(t)$ represents the tumour boundary.

The model is given by

$$\Delta u = 1, \quad \text{in } \Omega(t), \quad (\text{Ma})$$

$$\nabla u \cdot \mathbf{n} + \frac{u}{\alpha} = Q, \quad \text{on } \Gamma(t), \quad (\text{Mb})$$

$$V = \frac{u}{\alpha} + \beta\kappa, \quad \text{on } \Gamma(t), \quad (\text{Mc})$$

with $\alpha, \beta, Q \in \mathbb{R}$, where $\alpha, \beta, Q > 0$. Here V denotes the normal velocity of the boundary $\Gamma(t)$, κ denotes the mean curvature, taken negative for a sphere, and u corresponds to the tissue pressure.

1.1.1 Derivation of the model

In this section we derive the model (M) that is considered in this thesis. The derivation is taken directly from Section 2 of [47]. The model corresponds to a distinguished limit of the following dimensionless formulation (here we elaborate, with some minor differences, on analysis briefly outlined in [48]). We have

$$\left. \begin{aligned} \frac{\partial n}{\partial t} + \nabla \cdot (\mathbf{v}n) &= (k_b(c) - k_d(c))n, & \frac{\partial m}{\partial t} + \nabla \cdot (\mathbf{v}m) &= k_d(c)n - \varepsilon\lambda m, \\ n + m &= 1, \\ \varepsilon^2 \nabla \cdot (D(n)\nabla c) &= K(c)n, & \mathbf{v} &= -\nabla p/\mu(n; \varepsilon), \end{aligned} \right\} \quad (1.1.2)$$

wherein n and m are the volume fractions of live and dead cells, c is the nutrient concentration, k_b and k_d are the cellular birth and death rates (the former being an increasing function of c and the latter a decreasing one), $\varepsilon\lambda$ specifies the (slow) degradation rate of the necrotic material, $K(c)/\varepsilon^2$ expresses the nutrient consumption rate, which will be

taken to be large, $D(n)$ is the nutrient diffusivity (nutrient transport can be treated as quasi-steady), \mathbf{v} is the velocity field (the two phases being treated as a single continuum), p is the pressure (i.e. Darcy's law is adopted as the constitutive assumption, in keeping with many existing models) and $\mu(n; \varepsilon)$ is proportional to the tissue viscosity; ε is a small parameter.

The system (1.1.2) is taken to hold in a finite domain $\Omega(t)$, with boundary $\Gamma(t)$ and dimensionless boundary conditions (recall the sign convention being such that $\kappa < 0$ for a sphere)

$$c = 1, \quad p = -\varepsilon^2 \gamma(n) \kappa, \quad q_n = \mathbf{v} \cdot \mathbf{n}, \quad \text{on } \Gamma(t), \quad (1.1.3)$$

where $\varepsilon^2 \gamma(n)$ expresses cell-cell adhesion, κ is the mean curvature of $\Gamma(t)$, \mathbf{n} is its unit outward normal, and q_n its normal velocity. Since we shall be concerned with what is in effect the large time behaviour, initial conditions are not important, though

$$n(x, 0) = 1, \quad \text{in } \Omega(0),$$

would represent a plausible assumption.

In addition to the powers of ε already introduced in (1.1.2) - (1.1.3), the final condition that leads to the distinguished limit in question involves

$$\mu(n; \varepsilon) \sim \mu_0(n), \quad \text{for } n = O(1), \quad n > 0, \quad \mu(0; \varepsilon) \sim \varepsilon \mu_1, \quad \text{as } \varepsilon \rightarrow 0, \quad (1.1.4)$$

for constant μ_1 , associated with the physically reasonable assumption that the necrotic material is much less viscous than living tissue.

We now derive the asymptotic structure of the problem in the limit $\varepsilon \rightarrow 0$, which comprises two regions, namely a boundary layer around the tissue edge in which the living cells are concentrated and a necrotic core. The former is governed by a one dimensional travelling wave balance, described next; the latter generates, on matching to the former, the moving boundary problem that is the subject of the rest of this thesis.

The boundary layer scalings are as follows

$$\nu = \varepsilon \zeta, \quad \mathbf{v} \cdot \mathbf{n} = \varepsilon V_n, \quad q_n = \varepsilon Q_n, \quad p = \varepsilon^2 P, \quad \text{and} \quad t = \varepsilon^{-1} T,$$

with ν denoting the outward normal distance from $\Gamma(T)$; the tangential velocity components are of $O(\varepsilon^2)$ but are not needed in the sequel. Thus to leading order

$$\begin{aligned} \frac{d}{d\zeta}(W_n n) &= (k_b(c) - k_d(c))n, & \frac{d}{d\zeta}(W_n m) &= k_d(c)n, \\ n + m &= 1, \\ \frac{d}{d\zeta} \left(D(n) \frac{dc}{d\zeta} \right) &= K(c)n, & V_n &= -\frac{1}{\mu_0(n)} \frac{dP}{d\zeta}, \end{aligned} \tag{1.1.5}$$

in $\zeta < 0$ with

$$c = 1, \quad P = -\gamma(n)\kappa, \quad W_n = 0, \quad \text{on } \zeta = 0, \tag{1.1.6}$$

where $W_n = V_n - Q_n$; we note that the leading order solution depends only on ζ , so that ordinary derivative notation is indeed appropriate, and P decouples, the remaining system being independent of the constitutive assumption and depending on V_n and Q_n only through W_n . It follows from (1.1.6) that (1.1.5) implies

$$\frac{dW_n}{d\zeta} = k_b(1) - k_d(1), \quad m \frac{dW_n}{d\zeta} = k_d(1), \quad \text{at } \zeta = 0,$$

so that

$$n = 1 - \frac{k_d(1)}{k_b(1)}, \quad m = \frac{k_d(1)}{k_b(1)}, \quad \text{at } \zeta = 0,$$

and (1.1.6) in consequence involves the constant

$$\gamma_0 = \gamma \left(1 - \frac{k_d(1)}{k_b(1)} \right),$$

which serves as a surface tension parameter in what follows.

As $\zeta \rightarrow -\infty$ we have

$$n \rightarrow 0, \quad m \rightarrow 1, \quad c \rightarrow c_\infty, \quad \text{and} \quad W_n \rightarrow -Q, \tag{1.1.7}$$

where the positive constants c_∞ and Q are to be determined as part of the solution to (1.1.5) - (1.1.7); Q plays a crucial role in what follows, providing a surface source of material that contrasts with the volumetric sink λ . To complete the matching we must turn to the pressure P ; the assumption (1.1.4) implies a non-uniformity here, but it is a

consequence of P decoupling that

$$V_n \sim -\frac{1}{\mu(n; \varepsilon)} \frac{dP}{d\zeta},$$

holds uniformly in the boundary layer regions (it will be clear that there is an *ad hoc* flavour to this statement, but it can readily be fully justified in the sense of formal asymptotics).

In consequence

$$P \sim \varepsilon \mu_1 (Q - Q_n) \zeta + Q_n \int_{\zeta}^0 (\mu(n(\zeta'); \varepsilon) - \varepsilon \mu_1) d\zeta' + \int_{\zeta}^0 (\mu(n(\zeta'); \varepsilon) W_n(\zeta') + \varepsilon \mu_1 Q) d\zeta' - \gamma_0 \kappa$$

applies, with (1.1.5) implying that $W_n(\zeta)$ satisfies

$$\frac{dW_n}{d\zeta} = k_b(c)n.$$

Hence as $\zeta \rightarrow -\infty$, $\varepsilon \rightarrow 0$ with $\zeta = O(1/\varepsilon)$,

$$P \sim \varepsilon \mu_1 (Q - Q_n) \zeta + a Q_n - b - \gamma_0 \kappa, \quad (1.1.8)$$

for positive constants

$$a \equiv \int_{-\infty}^0 \mu_0(n(\zeta)) d\zeta, \quad b \equiv - \int_{-\infty}^0 \mu_0(n(\zeta)) W_n(\zeta) d\zeta.$$

We can now turn to the necrotic core region, wherein n is exponentially small in ε , so (1.1.2) reduces in $\Omega(t)$ at leading order to, on setting $\mathbf{v} = \varepsilon \mathbf{V}$,

$$\nabla \cdot \mathbf{V} = -\lambda, \quad \mathbf{V} = -\nabla P / \mu_1, \quad (1.1.9)$$

with $m = 1$ and

$$\Delta c = 0. \quad (1.1.10)$$

The boundary conditions on (1.1.9) - (1.1.10) result from matching to (1.1.7) - (1.1.8) (i.e. by the usual matching arguments from singular perturbation theory, (1.1.2) does not

apply to the core). Thus (1.1.9) is subject on $\Gamma(t)$ to

$$V_n = Q_n - Q, \quad P = aQ_n - b - \gamma_0\kappa, \quad (1.1.11)$$

while (1.1.7) - (1.1.10) simply give $c = c_\infty$; note that the first term on the right hand side of (1.1.8) gives the matching condition

$$\mathbf{n} \cdot \nabla P = \mu_1 V_n,$$

which is automatically satisfied given (1.1.9), (1.1.11). Finally we obtain, on translating P by b , the moving boundary problem

$$\begin{aligned} \Delta P &= \lambda\mu_1, & \text{in } \Omega(t), & (1.1.12) \\ Q_n &= Q - \frac{1}{\mu_1} \nabla P \cdot \mathbf{n}, & P &= aQ_n - \gamma_0\kappa, & \text{on } \Gamma(t). \end{aligned}$$

For $a = \gamma_0 = Q = 0$ this is the classical Hele-Shaw reverse (negative) squeeze film problem (see, for example, [59]), which is ill posed. The a term corresponds to kinetic undercooling regularisation, and γ_0 to a surface energy regularising (compare with [58], for example, for a discussion of such regularisations in the Hele-Shaw context); both are stabilising, but for small enough values (1.1.12) will be susceptible to fingering instabilities. The surface source term Q is novel, making (1.1.12) distinct from previous Hele-Shaw formulations; since the instabilities are associated with shrinking fluid domains (due to $\lambda\mu_1 > 0$), it might be expected to play a stabilising role, though the linear stability analysis in Section 3 of [47] quantifies the extent to which this intuition is misleading.

Setting the cell-cell adhesion coefficient $\gamma_0 = 0$, $P = u$, $a = \alpha$, $Q_n = V$ and scaling such that $\mu_1 = \lambda = 1$ yields

$$\Delta u = 1, \quad \text{in } \Omega(t), \quad (1.1.13a)$$

$$\nabla u \cdot \mathbf{n} + \frac{u}{\alpha} = Q, \quad \text{on } \Gamma(t), \quad (1.1.13b)$$

$$V = \frac{u}{\alpha}, \quad \text{on } \Gamma(t), \quad (1.1.13c)$$

with t being reinstated as the time variable, in place of (and equivalent to) T above. For

numerical purposes we add an artificial curvature regularisation term to the velocity law (1.1.13c), yielding the model (M).

1.1.2 Comparison with existing models

There are a number of models of vascular tumour growth in the literature, for example [2, 11, 17, 25, 34]. In these examples the tumour has an internal vasculature, or blood vessel network, in order to supply nutrients. The model considered in this thesis, however, assumes an avascular tumour. This means that the tumour has not developed a blood vessel network.

In avascular tumour models cell movement (as opposed to the movement of the tumour via growth) is often incorporated by modelling a combination of chemotaxis [66], diffusion [26], and convection [19, 36, 61, 62]. In the derivation of our model, we consider convection.

The model that we consider is more tractable than many found in the literature, for example [19, 26, 33, 51, 54, 55, 61]. Two-component mixture models of tumour cells and healthy cells are considered in [33, 51]; these models take the form of Cahn-Hilliard type diffuse interface models in which the interfacial region between the tumour and the healthy cells has a non-zero thickness. In [33] both Darcy and Stokes constitutive laws are considered, allowing the tumour to be modelled as a highly viscous fluid moving through a porous medium; nutrient density is modelled using a diffusion equation, giving rise to chemotaxis (the movement of cells along chemical gradients). In [51] a Cahn-Hilliard-Darcy model is considered that models chemotaxis and active transport. A formally matched asymptotic expansion is performed, yielding a sharp interface model.

The constitutive law in [21] combines the stress-strain relation of linear-elasticity with a growth term. This differs from our constitutive law, in which we use Darcy flow to simulate the tumour as a liquid in a porous medium. In [21] the authors choose this constitutive law in order to investigate the effects of mechanical stress on the growth of the tumour. They, as in other models (for example [61]), assume the nutrients are diffusing into the tumour. In doing this, they are able to describe the stresses and strains in terms of the nutrient density. We do not model nutrient diffusion due to the thin rim limit (there is also no need to model the diffusion of any trace nutrients in the necrotic core).

In [54] the author considers a radially symmetric tumour, and focuses on the diffusion of

nutrients and waste products in order to model tumour growth patterns. The geometrically constrained model in [54] is extended in [55] to a model in which, among other things, the geometric constraints are dropped; here surface tension is taken to be proportional to the mean curvature, and Darcy's law is adopted. In this model, the authors simulate nutrient diffusion within the tumour. This allows them to consider both live and necrotic cells, the birth and death of which lead to internal pressure differentials. Although there are similarities, this is significantly different from our model, in which we consider only necrotic cells inside the tumour, and do not model nutrient diffusion.

In [19] the authors consider a single nutrient sharp interface model with two growth inhibitors; one external to the tumour, for example an anti-cancer drug or immune response, and one internal to the tumour, for example a by product of the degradation of necrotic cells. The diffusion of the nutrient is considered, and the nutrient density on the boundary is taken proportional to the curvature. Although we do not consider anti-cancer drugs or immune responses, a simplified proxy to these could be modelled by reducing the size of our nutrient term.

As previously mentioned, [26] models the movement of the cells through diffusion. In this paper a continuum model is developed in which live, quiescent, and necrotic cells are modelled. Similar to our model, there is a generic nutrient/growth factor term. The model in [26] differs from our model in that it is orientated towards an *in vivo* setting, in which the external medium is modelled allowing for a nutrient supply from the underlying tissue. We do not model the external medium.

The model derivation in [61] has a number of similarities to our derivation. Both models assume a continuum of living and dead cells (albeit with our living cells confined to the thin rim). Both models have a generic nutrient term. In [61] the authors model the nutrient diffusion into the tumour interior via Fick's laws, whereas our model passes through the thin rim limit, meaning that the nutrients do not diffuse into the tumour interior. This also means that the authors of [61] require a velocity field in the interior of the tumour in order to model the mixing of the two cell types. Since we only have necrotic cells in the interior of the tumour, we only need a velocity field on the boundary of the tumour. The biggest difference is that the model in [61] is restricted to a radially symmetric geometry; a restriction that we do not have.

1.2 Approaches

1.2.1 Sharp interface approach

We consider two sharp interface approaches (also called parametric approaches), one in which the mesh on the interior of the tumour is fitted to the nodes on the boundary mesh, and one in which the two meshes are independent. This second approach is called the unfitted approach. In Chapter 4 numerical simulations are presented for both approaches. We take $\Gamma(t)$ as either a closed curve in \mathbb{R}^2 or a closed surface in \mathbb{R}^3 , and in both cases the free boundary, $\Gamma(t)$, is parametrised by a function $\mathbf{x} : M \times [0, T] \rightarrow \mathbb{R}^d$, where M is a suitable manifold. We can then describe geometric quantities in terms of \mathbf{x} . In \mathbb{R}^2 , using the short hand $\mathbf{x} := \mathbf{x}(\rho)$, the unit normal is given by

$$\mathbf{n} := \frac{\mathbf{x}_\rho^\perp}{|\mathbf{x}_\rho|},$$

(note that this depends upon the orientation of \mathbf{x}) and the mean curvature is given by (recalling that κ is taken negative for a sphere)

$$\kappa \mathbf{n} := \frac{1}{|\mathbf{x}_\rho|} \left(\frac{\mathbf{x}_\rho}{|\mathbf{x}_\rho|} \right)_\rho. \quad (1.2.1)$$

Here \mathbf{x}_ρ is the derivative with respect to ρ , and \mathbf{x}_ρ^\perp denotes a counter-clockwise rotation by $\frac{\pi}{2}$. A number of techniques for simulating forced mean curvature flow have been introduced, for example in [40]. Another approach was presented in [9], which includes mesh smoothing via a tangential velocity. This was then extended in [43], allowing a convergence result to be proved.

In order to construct a finite element scheme we approximate $\Gamma(t_n)$ by a collection of linear simplexes, denoted by \mathcal{T}_Γ^h . The union of the closure of these simplexes (denoted by Γ_h^n) will be the approximation to $\Gamma(t_n)$. These will be line segments in \mathbb{R}^2 and triangles in \mathbb{R}^3 . Here we have partitioned the time interval $[0, T]$ into $N + 1$ equidistant steps: $0 = t_0 < t_1 < \dots < t_{N-1} < t_N = T$, with $\Delta t := t_i - t_{i-1}$ denoting the uniform time step size.

When constructing a finite element scheme, we triangulate the interior of Γ_h^n with a conformal collection of simplexes of one dimension higher than those of Γ_h^n (so triangles

in \mathbb{R}^2 , and tetrahedrons in \mathbb{R}^3). We denote this collection of simplexes by \mathcal{T}_Ω^h , the union of the closure of the simplexes is denoted by Ω_h^n , and the triangulation is chosen such that the vertices and elements of Γ_h^n coincide with the vertices and faces of the elements that make up the boundary of Ω_h^n . This ensures that, if Γ_h^n approximates $\Gamma(t_n)$, then Ω_h^n approximates $\Omega(t_n)$. Although at each time step the mesh for Ω_h^n depends only on Γ_h^n (not on Ω_h^{n-1}), we will use a number of techniques that allow us to derive the mesh for Ω_h^n from the mesh for Ω_h^{n-1} as much as possible. We must ensure that as Γ_h^n evolves, the fitted mesh for Ω_h^n evolves with it, maintaining good mesh properties throughout.

Unfitted sharp interface approach in \mathbb{R}^2

Similar to the fitted sharp interface approach discussed in Section 1.2.1, the unfitted sharp interface approach, in \mathbb{R}^2 , approximates $\Gamma(t_n)$ by a collection of straight line segments, denoted by \mathcal{T}_Γ^h . This piecewise linear approximation to $\Gamma(t_n)$ is denoted Γ_h^n . Unlike the fitted approach, we embed $\Omega(t)$ in a larger domain D . This domain is independent of Γ_h^n , however it is chosen large enough to contain Γ_h^n for $n = 0, \dots, N$. We triangulate D by a conforming triangular mesh, denoted by \mathcal{T}_D^h . Importantly \mathcal{T}_D^h is independent of \mathcal{T}_Γ^h , so as Γ_h^n evolves \mathcal{T}_D^h retains its original mesh properties, and thus no mesh smoothing is required on \mathcal{T}_D^h .

In order to construct the finite element method for the elliptic PDE on the bulk that is present in our model, we split the triangles of \mathcal{T}_D^h into the classes *interior*, *exterior*, and *cut*, using algorithms found in [68]. Here, in most cases, the *interior* triangles are those fully within Γ_h^n , the *exterior* triangles are those fully outside Γ_h^n , and the *cut* triangles are those for which the intersection with Γ_h^n is non-empty. This is followed by the definition of an approximation to Γ_h^n on D , denoted by $\tilde{\Gamma}_h^n$; the interior of $\tilde{\Gamma}_h^n$ is our approximation to $\Omega(t)$. We then carefully define the integrals of the finite element method, paying particular attention to the interaction between Γ_h^n and D . This definition is inspired by [8].

Although the meshes \mathcal{T}_Γ^h and \mathcal{T}_D^h are independent, in practice we adapt the mesh for D by refining in the interior of Γ_h^n , and coarsening in the exterior. Due to the complexity of the programming task, we have restricted our implementation to \mathbb{R}^2 , however the unfitted sharp interface approach can be generalised to \mathbb{R}^3 (see, for example, [8]).

1.2.2 Diffuse interface approach

In the diffuse interface approach (also called the phase field approach) we approximate $\Gamma(t)$ by a diffuse interface $\Gamma_\varepsilon(t)$ of width $\mathcal{C}\varepsilon$, where \mathcal{C} is a positive constant. $\Gamma(t)$ is approximated by the zero level set of a phase field function $\varphi : D \times [0, T] \rightarrow \mathbb{R}$, where $D \subset \mathbb{R}^d$ is a bounded domain that contains $\Gamma_\varepsilon(t)$, $\forall t \in [0, T]$. In general, the phase field function takes values of approximately 1 inside $\Gamma_\varepsilon(t)$, and approximately -1 outside $\Gamma_\varepsilon(t)$. These values correspond to the minima of a homogeneous energy function; traditionally the energy functions are either the double well or the double obstacle energy [15, 27, 37]. We will consider only the double obstacle energy, since this enforces that $\varphi \in [-1, 1]$, with $\varphi = 1$ inside $\Gamma_\varepsilon(t)$ and $\varphi = -1$ outside $\Gamma_\varepsilon(t)$. Additionally we have that the diffuse interface is defined by

$$\Gamma_\varepsilon(t) := \{ \mathbf{x} \in D \mid |\varphi(\mathbf{x}, t)| < 1 \}.$$

When constructing the finite element scheme we ensure that D contains the set

$$\left\{ \mathbf{x} \in \mathbb{R}^d \mid \varphi_h^n(\mathbf{x}) > -1 \text{ for some } n = 0, \dots, N \right\},$$

where φ_h^n is a piecewise linear approximation of $\varphi(t_n)$. We triangulate D by a conforming collection of simplexes (as before, triangles in \mathbb{R}^2 , tetrahedrons in \mathbb{R}^3). We must ensure that the mesh is sufficiently refined across the diffuse interface in order to fully resolve it. Since we also solve an elliptic PDE when $\varphi_h^n > -1$, we must also ensure that the mesh is sufficiently refined in this region. Resolving the entirety of D to this degree is computationally wasteful; we instead adaptively refine the mesh to achieve this level of resolution when $\varphi_h^n > -1$, and coarsen the mesh as much as possible when $\varphi_h^n = -1$. This greatly improves the simulation's run time.

We solve an elliptic PDE with Robin boundary conditions by using the results in [1, 64] to write a diffuse interface approximation of the PDE and boundary conditions in D . This is achieved by using two weight functions, $\delta(\varphi), \zeta(\varphi) : \mathbb{R} \rightarrow \mathbb{R}$. The weight function $\delta(\varphi)$ approximates the boundary conditions, and is defined such that it is large and positive in the interfacial region, but zero elsewhere. The weight function $\zeta(\varphi)$ imposes the geometry of $\Omega(t)$, it is defined such that $\zeta(\varphi) = 1$ if $\varphi = 1$ (inside $\Gamma_\varepsilon(t)$), and $\zeta(\varphi) = 0$ if $\varphi = -1$ (outside $\Gamma_\varepsilon(t)$). Both $\zeta(\varphi)$ and $\delta(\varphi)$ are zero outside the interfacial region, meaning that

the weighted PDE is degenerate. We closely follow the results in [39] in order to treat the degeneracy when proving a convergence result.

1.2.3 Other approaches

There are many other approaches that we do not consider in this thesis. We mention a few, namely graph and level set.

In the graph approach, $\Gamma(t) \subset \mathbb{R}^{n+1}$ is written as a graph over some base domain $\mathbb{D} \subset \mathbb{R}^n$ such that

$$\Gamma(t) = \{ (\mathbf{x}, \phi(\mathbf{x}, t)) \mid \mathbf{x} \in \mathbb{D} \}$$

where $\phi : \mathbb{D} \times [0, T) \rightarrow \mathbb{R}$ is the height function. Here \mathbb{D} is to be found, along with ϕ . This approach is not used as it is somewhat restrictive; there are many situations when $\Gamma(t)$ is not a graph, even after smoothly evolving from an initial state that is a graph.

The level set approach is similar to the diffuse interface approach, in that $\Gamma(t)$ is tracked by the zero level set of a function. Let $\rho : D \times [0, \infty) \rightarrow \mathbb{R}$ be an auxiliary function, and set

$$\Gamma(t) = \{ \mathbf{x} \in D \mid \rho(\mathbf{x}, t) = 0 \}.$$

Intrinsic to this approach is the notion of an interior and exterior to $\Gamma(t)$, denoted by the positive and negative regions of ρ .

1.2.4 Comparison of approaches

The approaches described above can be grouped into either implicit or explicit approaches. Implicit approaches (sometimes called front capturing), carry the information needed to reconstruct $\Gamma(t)$, as opposed to $\Gamma(t)$ itself. Often $\Gamma(t)$ is reconstructed (or approximated) by computing the zero level set of a function. The level set approach and diffuse interface approach are examples of implicit approaches.

A major advantage of implicit approaches is their natural handling of changes in topology, for example pinching off and merging. Merging occurs when $\Gamma(t)$ intersects with itself, and joins at the point of intersection to change the topology of $\Omega(t)$ (for example two previously independent circles merging, see Figure 4.17); pinching off is the opposite of this. Being able to model topology change is important to us, as many parameter values cause

a topology change in a relatively short amount of time. Additionally, the concept of the interior and exterior of $\Gamma(t)$ is intrinsic to implicit approaches, which is advantageous in our setting. A disadvantage of these approaches, however, is that the problem gains another dimension in space (from d to $d + 1$), so the efficiency is greatly decreased. The diffuse interface approach introduces an additional parameter, ε , which is proportional to the interfacial region's width. This can be both an advantage and disadvantage; in some models ε might arise quite naturally, and relate to a physical quantity. For example in tissue growth it might relate to a region of mixing between two competing cell types. In our case we want ε small, as we are approximating a model that naturally has a sharp interface. When using the diffuse interface approach, and coupling a quantity on the bulk to the evolution of $\Gamma_\varepsilon(t)$, we have a major limitation: we cannot resolve the gradient of the quantity on $\Gamma_\varepsilon(t)$. This can be quite restrictive, and we have to be careful to avoid this when formulating our diffuse interface model; we discuss this in more detail in Section 4.2.3.

The sharp interface and graph approaches are examples of explicit approaches. Explicit approaches (sometimes called front tracking) are characterised by directly following $\Gamma(t)$ as it evolves; no reconstruction is required.

A disadvantage of explicit approaches is that there is no intrinsic handling of topological changes. However recent advances, see [18], allow the robust detection of collisions, as well as performing topological change. Although the sharp interface approach is less efficient than the graph approach, it is significantly more efficient than the diffuse interface approach; we solve a system of parabolic equations in d space dimensions, as opposed to the $d + 1$ space dimensions of the diffuse interface approach. The sharp interface approach has a unique problem when simulating a free boundary: the meshes for Γ_h^n and Ω_h^n . As the free boundary evolves, the mesh will quickly become degraded. There have been many recent advances that tackle this problem, for example [42, 43] introduce powerful algorithms to help maintain the quality of the mesh. Additionally, the mesh generation software GMSH (see [52]) allows us to recreate the mesh if needed. The unfitted sharp interface approach only suffers from this problem on the mesh for Γ_h^n , not on the mesh for D .

1.3 Thesis overview

In Chapter 2 we consider the sharp interface approach. We first consider the case where $\Gamma(t)$ is an evolving closed curve in \mathbb{R}^2 ; we introduce a weak formulation of the problem which we then use to derive a finite element approximation. Next, the implementation of mesh smoothing techniques is discussed, and then an unfitted finite element approximation is considered. Lastly, we introduce a finite element approximation for the case where $\Gamma(t)$ is an evolving closed hypersurface in \mathbb{R}^3 .

In Chapter 3 we restrict ourselves to \mathbb{R}^2 . We first transform the model into the diffuse interface paradigm, regularise it, and present the associated weak form. We then perform some analysis in order to prove the existence and uniqueness of the solution. This is followed by the presentation of a finite element scheme, on which we then perform some numerical analysis. This first consists of an existence and uniqueness result for the finite element scheme, followed by a convergence result.

In Chapter 4, the numerical simulations are presented (in both \mathbb{R}^2 and \mathbb{R}^3). Before presenting these, we first introduce an alternate formulation of the model. We then present a diffuse interface weak form and finite element scheme without the regularisation introduced in Chapter 3. This is followed by a summary of the techniques used in the implementations. The simulations are first run with the restriction of a radially symmetric geometry. These show the accuracy of the finite element schemes, and present the experimental order of convergence in the sharp interface case. Numerical convergence of the radius in \mathbb{R}^3 is presented, as the mesh size and time step are reduced. Next we investigate the morphological stability of the radially symmetric geometry in the sharp interface case. We follow this by presenting some numerical simulations that investigate the parameters of the model; in particular we fix Q and vary α against β . This is done in \mathbb{R}^2 and \mathbb{R}^3 . This investigation shows a strong agreement between all of the finite element schemes presented in this thesis. There are also a number of images of *in vivo* tumours included (in both \mathbb{R}^2 and \mathbb{R}^3).

Chapter 5 concludes this thesis with an overview of the analytical results and numerical simulations presented in this thesis, and a discussion of possible future directions.

Chapter 2

Sharp interface approaches

In this chapter we study the model (M) using a sharp interface approach (also called a parametric approach). In this approach we explicitly represent $\Gamma(t)$ by parametrising it by a function \boldsymbol{x} over $\mathbb{I} := \mathbb{R}/(2\pi\mathbb{Z})$.

We introduce both fitted and unfitted approaches. In the fitted case we are able to explicitly define the set $\Omega(t)$ using \boldsymbol{x} , so we can solve (Ma) coupled with (Mb) over $\Omega(t)$ using standard techniques. The unfitted case requires careful consideration with regard to the interaction between the mesh for $\Gamma(t)$ and the mesh for D , where $\Omega(t) \subset D$.

In the fitted approach the difficulty arises with maintaining the quality of the finite element meshes. Since $\Gamma(t)$ (and thus $\Omega(t)$) is evolving over time, the mesh generated for $\Gamma(0)$ may not be appropriate for future times. Although we can naively update the mesh for $\Gamma(t)$ by using the computed velocity, this is likely lead to an uneven distribution of mesh points. For this reason we introduce a weak form and finite element method for (Mc) that includes mesh smoothing.

The evolution of the mesh for $\Omega(t)$ is more complex. Since our model does not define a velocity on $\Omega(t)$, we do not have the opportunity to attempt a naive mesh updating procedure. For this reason, when implementing the finite element scheme, we consider a number of mesh smoothing techniques.

The issue with mesh smoothing is a unique disadvantage of the sharp interface approach when compared to the diffuse interface approach. A second disadvantage is that the sharp interface approach also does not have a natural handling of topology change (although recently advances, for example [18], allow the implementation of topology change).

This is the converse of the diffuse interface approach, in which topology change is handled smoothly and naturally. The biggest advantage of the sharp interface approach is the speed of execution. This is followed by stability for a large range of the parameters α, β , and Q .

The chapter is organised as follows: we focus first, in Sections 2.1 - 2.4, on the case where $\Gamma(t)$ is an evolving closed curve in \mathbb{R}^2 . In Section 2.1 we introduce a weak formulation of (M) which we then use in Section 2.2 to derive a finite element approximation of (M). The implementation of mesh smoothing techniques is discussed in Section 2.3 and in Section 2.4 an unfitted finite element approximation of (M) is considered. We conclude with Section 2.5, in which we introduce a finite element approximation of (M) for the case where $\Gamma(t)$ is an evolving closed hypersurface in \mathbb{R}^3 .

2.1 Derivation of a weak formulation of (M) in \mathbb{R}^2

We first present a weak formulation of (Ma) and (Mb). Multiplying (Ma) by a test function $\phi \in H^1(\Omega(t))$ and integrating over $\Omega(t)$ yields

$$-\int_{\Omega(t)} \nabla u \cdot \nabla \phi \, dv + \int_{\Gamma(t)} \nabla u \cdot \mathbf{n} \phi \, ds = \int_{\Omega(t)} \phi \, dv$$

noting (Mb) then gives

$$\int_{\Omega(t)} \nabla u \cdot \nabla \phi \, dv + \frac{1}{\alpha} \int_{\Gamma(t)} u \phi \, ds + \int_{\Omega(t)} \phi \, dv = \int_{\Gamma(t)} Q \phi \, ds, \quad \forall \phi \in H^1(\Omega(t)). \quad (2.1.1)$$

We now present a weak formulation of (Mc) for the case where $\Gamma(t)$ is an evolving closed curve in \mathbb{R}^2 . There are a number of weak formulations for curve shortening flow, for example those introduced in [9, 40, 43]. The formulation in [40] results in the motion of $\Gamma(t)$ being purely in the normal direction which may lead to the accumulation of mesh points in numerical simulations, while the formulation in [9] include an artificial tangential motion that equidistributes the mesh points of the associated finite element approximations. We chose to adopt the weak formulation derived in [43], it also includes an artificial tangential motion and is presented together with a proof of convergence of the associated finite

element approximation. The main idea for the formulation of curve shortening flow (and its high dimensional counterpart, mean curvature flow) in [43] is to use special solutions to the harmonic map heat flow in order to reparametrise the equations of motion. The reparametrisation by the harmonic map heat flow gives rise to tangential motions that can be exploited, from a numerical point of view, to yield a favourable redistribution of the mesh points. In [5] the convergence result of the finite element approximation of the curve shortening flow equation in [43] was extended to a coupled system comprising of forced curve shortening flow, with the forcing being a function of the solution of a reaction diffusion equation that holds on the evolving curve $\Gamma(t)$.

The derivation of the reparametrised mean curvature flow and curve shortening flow in [43] consists of two main steps. We outline the two steps in the case of curve shortening flow below, after first introducing some necessary notation. We then introduce forcing.

We introduce the parametrisation $\mathbf{x}(\cdot, t) : \mathbb{I} \rightarrow \mathbb{R}^2$, recalling that $\mathbb{I} := \mathbb{R}/(2\pi\mathbb{Z})$ is the periodic interval. Associated with this parametrisation is the unit tangent and the unit normal to $\Gamma(t)$, given respectively by

$$\boldsymbol{\tau} = \mathbf{x}_s = \frac{\mathbf{x}_\rho}{|\mathbf{x}_\rho|}, \quad \text{and} \quad \mathbf{n} = \boldsymbol{\tau}^\perp. \quad (2.1.2)$$

Here s is the arclength parameter on $\Gamma(t)$, $(\cdot)^\perp$ denotes a counter-clockwise rotation by $\frac{\pi}{2}$ and $\rho \in \mathbb{I}$. The relationship $\mathbf{x}_{ss} = \kappa \mathbf{n}$ gives rise to the following formulation of curve shortening flow,

$$\mathbf{x}_t = \mathbf{x}_{ss} = \frac{1}{|\mathbf{x}_\rho|} \left(\frac{\mathbf{x}_\rho}{|\mathbf{x}_\rho|} \right)_\rho. \quad (2.1.3)$$

On recalling (1.2.1) we see that taking the scalar product of (2.1.3) with \mathbf{n} yields $V = \kappa$.

The first step presented in [43] involves reparametrising \mathbf{x} by $\hat{\mathbf{x}}(t) = \mathbf{x}(\psi(t)^{-1})$ where $\psi(t)$ is the solution to the harmonic map heat flow, see Section 2.3 in [43], with constant diffusion coefficient $\omega > 0$. This yields the following reparametrised evolution equation of the curve shortening flow, see (2.16) in [43],

$$\begin{aligned} \hat{\mathbf{x}}_t &= |\hat{\mathbf{x}}_\rho|^{-2} \hat{\mathbf{x}}_{\rho\rho} - |\hat{\mathbf{x}}_\rho|^{-4} \hat{\mathbf{x}}_\rho \cdot \hat{\mathbf{x}}_{\rho\rho} \hat{\mathbf{x}}_\rho + \frac{1}{\omega} |\hat{\mathbf{x}}_\rho|^{-4} \hat{\mathbf{x}}_\rho \cdot \hat{\mathbf{x}}_{\rho\rho} \hat{\mathbf{x}}_\rho \\ &= \frac{1}{|\hat{\mathbf{x}}_\rho|} \left(\frac{\hat{\mathbf{x}}_\rho}{|\hat{\mathbf{x}}_\rho|} \right)_\rho + \frac{1}{\omega} |\hat{\mathbf{x}}_\rho|^{-4} \hat{\mathbf{x}}_\rho \cdot \hat{\mathbf{x}}_{\rho\rho} \hat{\mathbf{x}}_\rho. \end{aligned} \quad (2.1.4)$$

The additional term on the right hand side of (2.1.4) produces the tangential motion of the reparametrised flow, with the inverse diffusion constant determining the time scale on which these motions take place.

In their second step the authors split the time derivative, $\hat{\mathbf{x}}_t$ into weighted parts. Noting that

$$\frac{1}{|\hat{\mathbf{x}}_\rho|} \left(\frac{\hat{\mathbf{x}}_\rho}{|\hat{\mathbf{x}}_\rho|} \right)_\rho \cdot \boldsymbol{\tau} = 0 \quad \text{and} \quad |\hat{\mathbf{x}}_\rho|^{-4} \hat{\mathbf{x}}_\rho \cdot \hat{\mathbf{x}}_{\rho\rho} \hat{\mathbf{x}}_\rho \cdot \mathbf{n} = 0$$

we have

$$\frac{1}{|\hat{\mathbf{x}}_\rho|} \left(\frac{\hat{\mathbf{x}}_\rho}{|\hat{\mathbf{x}}_\rho|} \right)_\rho = \mathbf{n} \otimes \mathbf{n} \frac{1}{|\hat{\mathbf{x}}_\rho|} \left(\frac{\hat{\mathbf{x}}_\rho}{|\hat{\mathbf{x}}_\rho|} \right)_\rho = \mathbf{n} \otimes \mathbf{n} (|\hat{\mathbf{x}}_\rho|^{-2} \hat{\mathbf{x}}_{\rho\rho} - |\hat{\mathbf{x}}_\rho|^{-4} \hat{\mathbf{x}}_\rho \cdot \hat{\mathbf{x}}_{\rho\rho} \hat{\mathbf{x}}_\rho) = \mathbf{n} \otimes \mathbf{n} |\hat{\mathbf{x}}_\rho|^{-2} \hat{\mathbf{x}}_{\rho\rho}$$

and

$$\begin{aligned} \mathbf{0} &= \boldsymbol{\tau} \otimes \boldsymbol{\tau} \frac{1}{|\hat{\mathbf{x}}_\rho|} \left(\frac{\hat{\mathbf{x}}_\rho}{|\hat{\mathbf{x}}_\rho|} \right)_\rho = \boldsymbol{\tau} \otimes \boldsymbol{\tau} (|\hat{\mathbf{x}}_\rho|^{-2} \hat{\mathbf{x}}_{\rho\rho} - |\hat{\mathbf{x}}_\rho|^{-4} \hat{\mathbf{x}}_\rho \cdot \hat{\mathbf{x}}_{\rho\rho} \hat{\mathbf{x}}_\rho) \\ &\Rightarrow |\hat{\mathbf{x}}_\rho|^{-4} \hat{\mathbf{x}}_\rho \cdot \hat{\mathbf{x}}_{\rho\rho} \hat{\mathbf{x}}_\rho = \boldsymbol{\tau} \otimes \boldsymbol{\tau} |\hat{\mathbf{x}}_\rho|^{-4} \hat{\mathbf{x}}_\rho \cdot \hat{\mathbf{x}}_{\rho\rho} \hat{\mathbf{x}}_\rho = \boldsymbol{\tau} \otimes \boldsymbol{\tau} |\hat{\mathbf{x}}_\rho|^{-2} \hat{\mathbf{x}}_{\rho\rho}. \end{aligned}$$

Here \otimes is the tensor product. Thus (2.1.4) can be reformulated as

$$\hat{\mathbf{x}}_t = \mathbf{n} \otimes \mathbf{n} |\hat{\mathbf{x}}_\rho|^{-2} \hat{\mathbf{x}}_{\rho\rho} + \frac{1}{\omega} \boldsymbol{\tau} \otimes \boldsymbol{\tau} |\hat{\mathbf{x}}_\rho|^{-2} \hat{\mathbf{x}}_{\rho\rho}.$$

Since $\boldsymbol{\tau} \otimes \boldsymbol{\tau} = Id - \mathbf{n} \otimes \mathbf{n}$, where Id is the identity matrix, we conclude that

$$\hat{\mathbf{x}}_t = \left(\mathbf{n} \otimes \mathbf{n} + \frac{1}{\omega} (Id - \mathbf{n} \otimes \mathbf{n}) \right) |\hat{\mathbf{x}}_\rho|^{-2} \hat{\mathbf{x}}_{\rho\rho}.$$

Noting that

$$\left(\mathbf{n} \otimes \mathbf{n} + \frac{1}{\omega} (Id - \mathbf{n} \otimes \mathbf{n}) \right)^{-1} = (\omega Id + (1 - \omega) \mathbf{n} \otimes \mathbf{n})$$

we obtain the reparametrised curve shortening flow

$$(\omega Id + (1 - \omega) \mathbf{n} \otimes \mathbf{n}) \hat{\mathbf{x}}_t = |\hat{\mathbf{x}}_\rho|^{-2} \hat{\mathbf{x}}_{\rho\rho}.$$

For forced curve shortening flow, $V = \kappa + f$, (2.1.3) is replaced by

$$\mathbf{x}_t = \frac{1}{|\mathbf{x}_\rho|} \left(\frac{\mathbf{x}_\rho}{|\mathbf{x}_\rho|} \right)_\rho + f(\mathbf{x}) \mathbf{n}.$$

Using the techniques outlined above, the evolution equation for reparametrised forced curve shortening flow takes the form

$$(\omega Id + (1 - \omega)\mathbf{n} \otimes \mathbf{n}) \hat{\mathbf{x}}_t = (|\hat{\mathbf{x}}_\rho|^{-2} \hat{\mathbf{x}}_{\rho\rho} + f(\hat{\mathbf{x}})\mathbf{n}).$$

Thus we obtain the following reparametrisation for the velocity law $V = \beta\kappa + \frac{1}{\alpha}u$,

$$(\omega Id + (1 - \omega)\mathbf{n} \otimes \mathbf{n}) \hat{\mathbf{x}}_t = \left(\beta |\hat{\mathbf{x}}_\rho|^{-2} \hat{\mathbf{x}}_{\rho\rho} + \frac{u(\hat{\mathbf{x}})}{\alpha} \mathbf{n} \right). \quad (2.1.5)$$

For simplicity of notation we now set $\hat{\mathbf{x}} = \mathbf{x}$. Multiplying (2.1.5) by a test function $\boldsymbol{\xi} \in [H^1(\mathbb{I})]^2$ as well as by the density function $|\mathbf{x}_\rho|^2$, integrating over \mathbb{I} , and applying integration by parts yields

$$\int_{\mathbb{I}} |\mathbf{x}_\rho|^2 (\omega \mathbf{x}_t + (1 - \omega)(\mathbf{x}_t \cdot \mathbf{n})\mathbf{n}) \cdot \boldsymbol{\xi} d\rho + \beta \int_{\mathbb{I}} \mathbf{x}_\rho \cdot \boldsymbol{\xi}_\rho d\theta = \frac{1}{\alpha} \int_{\mathbb{I}} |\mathbf{x}_\rho|^2 u(\mathbf{x}) \mathbf{n} \cdot \boldsymbol{\xi} d\rho. \quad (2.1.6)$$

Combining (2.1.1) and (2.1.6) we arrive at the following problem.

Problem \mathbb{P}_{SI} Given an initial closed curve $\Gamma(0) \in \mathbb{R}^2$ and $\omega \in (0, 1]$, find (u, \mathbf{x}) such that for all $t \in (0, T)$,

$$\int_{\Omega(t)} \nabla u \cdot \nabla \phi dv + \frac{1}{\alpha} \int_{\Gamma(t)} u \phi ds + \int_{\Omega(t)} \phi dv = \int_{\Gamma(t)} Q \phi ds, \quad \forall \phi \in H^1(\Omega(t)) \quad (2.1.7)$$

and for all $\boldsymbol{\xi} \in H^1(\mathbb{I})$,

$$\int_{\mathbb{I}} |\mathbf{x}_\rho|^2 (\omega \mathbf{x}_t + (1 - \omega)(\mathbf{x}_t \cdot \mathbf{n})\mathbf{n}) \cdot \boldsymbol{\xi} d\rho + \beta \int_{\mathbb{I}} \mathbf{x}_\rho \cdot \boldsymbol{\xi}_\rho d\theta = \frac{1}{\alpha} \int_{\mathbb{I}} |\mathbf{x}_\rho|^2 u(\mathbf{x}) \mathbf{n} \cdot \boldsymbol{\xi} d\rho, \quad (2.1.8)$$

where $\Gamma(t)$ is parametrised by $\mathbf{x}(\rho, t)$, and $\Omega(t)$ is the interior of $\Gamma(t)$.

Remark

We note that the above problem is strongly coupled, as $\Gamma(t)$ is parametrised by \mathbf{x} , which is a function over \mathbb{I} , and thus the domain of the integrals in (2.1.7) depends upon the solution of (2.1.8).

2.2 Finite element scheme

We now introduce a finite element approximation of \mathbb{P}_{SI} . We partition the time interval $[0, T]$ into $N + 1$ steps: $0 = t_0 < t_1 < \dots < t_{N-1} < t_N = T$. These are evenly spaced, so that $\Delta t = t_{i+1} - t_i$. We introduce the decomposition $\mathbb{I} = \cup_{j=1}^J \bar{\sigma}_j$, where $\sigma_j := (\rho_{j-1}, \rho_j)$.

We define $W_h(\mathbb{I}) := [V_h(\mathbb{I})]^2$ where

$$V_h(\mathbb{I}) := \{ \rho_h \in C^0(\mathbb{I}) \mid \rho_h|_{\sigma_j} \text{ is affine for } j = 1, \dots, J \},$$

and we set $I^h : C(\mathbb{I}) \rightarrow V_h$ to be the standard Lagrange interpolation operator such that $(I^h \eta)(\rho_j) = \eta(\rho_j)$, $j = 1, \dots, J$. In addition we define the local interpolation operator $I_j^h := I_h|_{\sigma_j}$ for $j = 1, \dots, J$, and we define the discrete inner product $(\cdot, \cdot)^h$ by

$$(\eta_1, \eta_2)^h := \sum_{j=1}^J \int_{\sigma_j} I_j^h(\eta_1 \eta_2),$$

where η_i are piecewise continuous functions on the partition $\cup_{j=1}^J \bar{\sigma}_j$ of \mathbb{I} . We define the standard $L^2(\mathbb{I})$ inner product by (\cdot, \cdot) .

Let $\mathbf{X}_h^n \in W_h(\mathbb{I})$ parametrise a closed polyhedral curve, denoted by Γ_h^n . This will be an approximation to $\Gamma(t_n)$. We assign to an element $\mathbf{X}_h^n \in W_h(\mathbb{I})$ a piecewise constant discrete unit tangent and normal by

$$\boldsymbol{\tau}_h^n = \frac{\mathbf{X}_{h,\rho}^n}{|\mathbf{X}_{h,\rho}^n|}, \quad \text{and} \quad \mathbf{n}_h^n = (\boldsymbol{\tau}_h^n)^\perp, \quad \text{on } \sigma_j, \quad j = 1, \dots, J. \quad (2.2.1)$$

We denote the collection of straight line segments that constitute Γ_h^n by $\mathcal{T}_\Gamma^h := \{\psi_j^n\}_{j=1}^J$, where for simplicity of notation we write \mathcal{T}_Γ^h as opposed to $\mathcal{T}_{\Gamma_h^n}^h$.

We denote the interior of Γ_h^n by Ω_h^n and we triangulate it with a conforming mesh that we denote by $\mathcal{T}_\Omega^h := \{\mu_l^n\}_{l=1}^L$, where again, for simplicity of notation, we write \mathcal{T}_Ω^h as opposed to $\mathcal{T}_{\Omega_h^n}^h$. Here \mathcal{T}_Ω^h is a family of disjoint open triangles with vertices $\{\mathbf{p}_i^n\}_{i=1}^I$ and $\bar{\Omega}_h^n := \cup_{l=1}^L \bar{\mu}_l^n$. The mesh \mathcal{T}_Ω^h is such that the nodes and edges that make up the boundary of Ω_h^n coincide with the nodes and edges of \mathcal{T}_Γ^h , this set up can be seen in Figure 2.1.

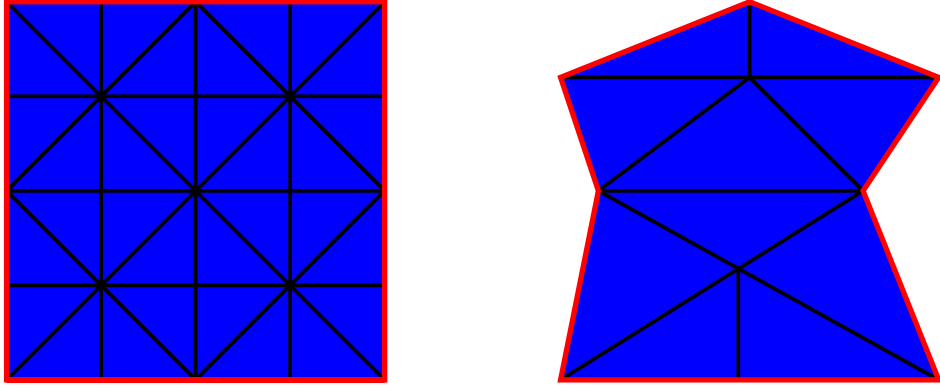


Figure 2.1: Two illustrations of the fitted meshes with \mathcal{T}_Ω^h in blue and \mathcal{T}_Γ^h in red.

We define the finite element space

$$S_h(\Omega_h^n) := \left\{ \phi_h \in C^0(\overline{\Omega}_h^n) \mid \phi_h|_\mu \text{ is linear } \forall \mu \in \mathcal{T}_\Omega^h \right\}$$

and we let $\hat{I}_h : C^0(\overline{\Omega}_h^n) \rightarrow S_h(\Omega_h^n)$ denote the interpolation operator onto $S_h(\Omega_h^n)$, such that $(\hat{I}_h \eta)(\mathbf{p}_i) = \eta(\mathbf{p}_i)$, $i = 1, \dots, I$.

Following [5], a finite element scheme for the weak form \mathbb{P}_{SI} , is given by the coupled system

Problem \mathbb{P}_{SI}^h For $\omega \in (0, 1]$, given $\mathbf{X}_h^0 = I^h \mathbf{x}(\cdot, 0) \in W_h(\mathbb{I})$, for $n = 0, \dots, N - 1$, find $\{u_h^n, \mathbf{X}_h^{n+1}\} \in S_h(\Omega_h^n) \times W_h(\mathbb{I})$ such that

$$\int_{\Omega_h^n} \nabla u_h^n \cdot \nabla \phi_h \, dv + \frac{1}{\alpha} \int_{\Gamma_h^n} \hat{I}_h(u_h^n \phi_h) \, ds + \int_{\Omega_h^n} \phi_h \, dv = Q \int_{\Gamma_h^n} \phi_h \, ds, \quad \forall \phi_h \in S_h(\Omega_h^n), \quad (2.2.2)$$

and

$$\begin{aligned} & \left(|\mathbf{X}_{h,\rho}^n|^2 (\omega D_t \mathbf{X}_h^{n+1} + (1 - \omega)(D_t \mathbf{X}_h^{n+1} \cdot \mathbf{n}_h^n) \mathbf{n}_h^n), \boldsymbol{\xi}_h \right)^h + \beta(\mathbf{X}_{h,\rho}^{n+1}, \boldsymbol{\xi}_{h,\rho}) \\ & = \frac{1}{\alpha} (|\mathbf{X}_{h,\rho}^n|^2 u_h^n(\mathbf{X}_h^n) \mathbf{n}_h^n, \boldsymbol{\xi}_h)^h, \quad \forall \boldsymbol{\xi}_h \in W_h(\mathbb{I}). \end{aligned} \quad (2.2.3)$$

Here $D_t \mathbf{X}_h^{n+1} := \frac{\mathbf{X}_h^{n+1} - \mathbf{X}_h^n}{\Delta t}$, Γ_h^n is given by $\mathbf{X}_h^n(\mathbb{I})$, and Ω_h^n is the interior of Γ_h^n .

Recall that the parameter ω controls the amount of mesh smoothing, such that the smaller the value of ω the greater the amount of mesh smoothing. Evolution via curve shortening flow, such that the right hand side of (2.2.3) is set to zero, can be seen, with different values of ω , in Figure 2.2. As $\omega \rightarrow 0$, the spacing of the nodes improves.

Since this only smooths the mesh \mathcal{T}_Γ^h , additional mesh smoothing methods are required for \mathcal{T}_Ω^h . These will be discussed in Section 2.3.

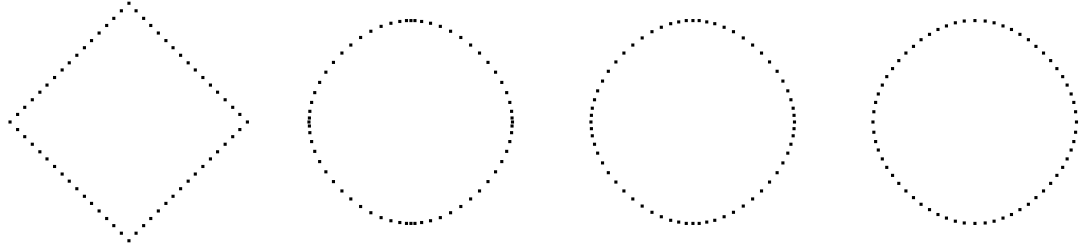


Figure 2.2: Evolution via mean curvature at $t = 0.8$, with the initial condition on the left. Middle left: $\omega = 0.1$. Middle right: $\omega = 0.01$. Right: $\omega = 0.001$.

2.3 Fitted mesh smoothing

As Γ_h^n is evolving in time, we need to implement a number of techniques in order to maintain well structured meshes for both Γ_h^n (denoted by \mathcal{T}_Γ^h) and Ω_h^n (denoted by \mathcal{T}_Ω^h) throughout the simulation. This is of importance to \mathcal{T}_Γ^h , but of even higher importance to \mathcal{T}_Ω^h . Not smoothing \mathcal{T}_Γ^h will lead to a suboptimal arrangement of vertices. Not smoothing \mathcal{T}_Ω^h will (within a very short time frame) lead to the nodes of \mathcal{T}_Ω^h that are fitted to \mathcal{T}_Γ^h moving such that \mathcal{T}_Ω^h has stretched and overlapping elements, thus making it unusable.

If we use the intrinsic mesh smoothing present in (2.2.3) for ω sufficiently small, then \mathcal{T}_Γ^h will remain smooth for $[0, T]$. There are then two approaches open to us in order to deal with \mathcal{T}_Ω^h : generate an entirely new mesh at each time step, or try and improve the mesh at time step n in order to yield an improved mesh at time step $n + 1$. Generating an entirely new mesh at each time step is not feasible, as the computational time to generate a new mesh and integrate it into the running program is too high. That leaves us with improving the mesh at time step n in order to yield an improved mesh at time step $n + 1$.

In order to smooth \mathcal{T}_Ω^h we first, in Section 2.3.1, describe a simple technique for generating a velocity field on \mathcal{T}_Ω^h ; this velocity field is denoted by \mathbf{W}_h^n . This technique gives a small amount of mesh smoothing when applied to the nodes of \mathcal{T}_Ω^h , however it does not “see” the nodes of \mathcal{T}_Γ^h , so it is unable to provide intelligent smoothing.

In Section 2.3.2 we introduce Algorithm 1 from [42], which provides intelligent smoothing of \mathcal{T}_Ω^h . Since this approach smooths both the nodes of \mathcal{T}_Ω^h and of \mathcal{T}_Γ^h , it is unnecessary

to take $\omega < 1$, and so we set $\omega = 1$. We present Algorithm 1 from [42] simplified to our particular set up; the algorithm takes \mathbf{W}_h^n as an input.

After large deformations \mathcal{T}_Ω^h may have a significantly reduced quality. If this is the case, then we use the re-meshing software GMSH [52], introduced in Section 2.3.3, to construct an entirely new mesh.

2.3.1 Harmonic extension method

We first present a simple technique for generating a velocity field on Ω_h^n such that, if we move the nodes of \mathcal{T}_Ω^h and \mathcal{T}_Γ^h with this velocity field, then we will achieve a reasonable level of mesh smoothing. Note that our model does not prescribe a velocity on Ω_h^n , so we are free to define this velocity. Note also that this technique works well with the inherent mesh smoothing in (2.2.3) which acts upon \mathcal{T}_Γ^h .

The velocity field that we generate is denoted by \mathbf{W}_h^n , with $\mathbf{W}_h^n|_{\Gamma_h^n}$ equivalent to the velocity $D_t \mathbf{X}_h^n$ of Γ_h^n . We then move the nodes of \mathcal{T}_Ω^h by the velocity \mathbf{W}_h^n . We calculate \mathbf{W}_h^n by solving a standard finite element approximation to

$$\begin{cases} \Delta \mathbf{w} = \mathbf{0}, & \text{in } \Omega(t), \\ \mathbf{w} = \mathbf{v}, & \text{on } \Gamma(t), \end{cases} \quad (2.3.1)$$

where \mathbf{v} is the velocity of $\Gamma(t)$. Note that \mathbf{v} is not necessarily normal to $\Gamma(t)$, as it can have an additional tangential component.

A simple example with a growing circle can be seen in Figure 2.3. Note that the mesh grows smoothly with Γ_h^n .

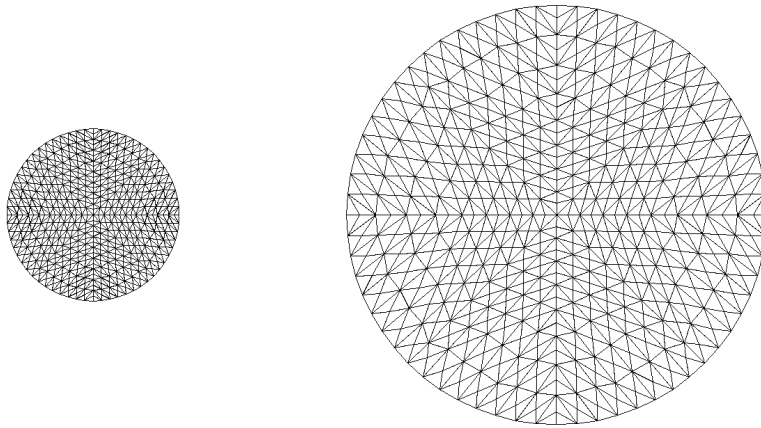


Figure 2.3: Evolution via an outward normal velocity, with mesh smoothing via the harmonic extension method detailed in Section 2.3.1. Left: $t = 0$. Right: $t = 10$.

2.3.2 DeTurck method

In [42] a general approach is introduced to obtain numerical schemes with good mesh properties for evolving submanifolds with boundaries. The approach is based on a variant of the so-called DeTurck trick whereby the authors apply the harmonic map heat flow on manifolds with boundaries. They assume that the submanifold $\Omega(t)$ is given as the image of a time-dependent embedding $\mathbf{s} : \mathcal{M} \times [0, T) \rightarrow \cup_{t \in [0, T)} \Omega(t) \times \{t\}$ of some reference manifold \mathcal{M} with boundary $\partial\mathcal{M}$ such that $\partial\Omega(t) = \mathbf{s}(\partial\mathcal{M}, t)$. Here we adopt the notation \mathbf{s} rather than \mathbf{x} , which is used in [42], to avoid confusion with the notation introduced in Section 2.1. The time-dependent embedding $\mathbf{s}(t)$ is reparametrised by the solution $\psi : \mathcal{M} \times [0, T) \rightarrow \mathcal{M}$ to the harmonic map heat flow on the reference manifold. We define $\hat{\mathbf{s}}(t) := \mathbf{s}(\psi(t)^{-1})$, with the inverse of the embedding $\hat{\mathbf{s}}$ denoted by $\hat{\mathbf{y}}(t) := \hat{\mathbf{s}}(t)^{-1}$, see Figure 2.4, in which our particular set up in \mathbb{R}^2 is shown with the reference manifold \mathcal{M} taken to be the half sphere in \mathbb{R}^3 , denoted by \mathbb{H} . In the discrete setting it transpires that the discrete embeddings corresponding to $\hat{\mathbf{s}}(t)$ can be totally gotten rid of and the resulting numerical scheme is written in terms of \mathbf{Y}_h^n , which is an approximation to $\hat{\mathbf{y}}(t)$. Throughout this thesis we refer to the approach in [42] as the DeTurck method.

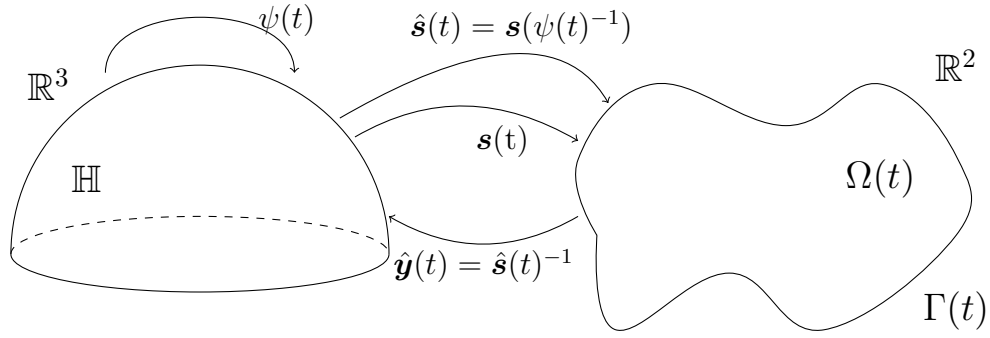


Figure 2.4: Schematic of the reparametrization of the time-dependent embedding $\mathbf{s}(t)$ by the solution $\psi(t)$ of the harmonic map heat flow.

In Section 3.2.1 of [42] the authors present an algorithm for the computation of the numerical scheme for this DeTurck reparametrization. Below we write out the simplified form of this algorithm for our particular set up of a simply connected domain $\Omega_h^n \subset \mathbb{R}^2$, with the boundary given by a closed curve Γ_h^n and the reference manifold, \mathbb{H} , being the half sphere in \mathbb{R}^3 . The reason that the reference manifold must be in \mathbb{R}^3 even though $\Omega(t)$ is in \mathbb{R}^2 is because the reference manifold must have a totally geodesic boundary. Since geodesics in an Euclidean space are straight lines, there is no bounded domain in \mathbb{R}^2 that has a smooth totally geodesic boundary, and can thus be used as a reference manifold.

Since the algorithm in [42] requires a velocity for the nodes of Ω_h^n , we use the harmonic extension method, detailed in Section 2.3.1, to extend the velocity, $D_t \mathbf{X}_h^n$, of Γ_h^n to a velocity $\mathbf{W}_h^n \in [S_h(\Omega_h^n)]^2$ that is defined on Ω_h^n .

Following [42], for the simplified set up of $\Omega \subset \mathbb{R}^2$, we assume that the reference manifold \mathbb{H} is approximated by a piecewise linear polyhedral manifold, denoted $\mathbb{H}_h := \cup_{\pi \in \mathcal{T}_{\mathbb{H}}^h} \pi \subset \mathbb{R}^3$, where $\mathcal{T}_{\mathbb{H}}^h$ is an admissible triangulation consisting of non-degenerate triangles. The finite element space $S_h(\mathbb{H}_h)$ is defined by

$$S_h(\mathbb{H}_h) := \left\{ \eta_h \in C^0(\mathbb{H}_h) \mid \eta_h|_{\pi} \text{ is a linear polynomial } \forall \pi \in \mathcal{T}_{\mathbb{H}}^h \right\}.$$

We seek approximations $\bar{\Omega}_h^n := \cup_{l=1}^L \bar{\mu}_l^n$ with $\Omega_h^n = \hat{\mathbf{S}}_h^n(\mathbb{H}_h)$, for some $\hat{\mathbf{S}}_h^n \in [S_h(\mathbb{H}_h)]^2$. Here the map $\hat{\mathbf{S}}_h^n$ is supposed to be a homeomorphism of \mathbb{H}_h onto Ω_h^n , with the inverse $\hat{\mathbf{Y}}_h^n := (\hat{\mathbf{S}}_h^n)^{-1} \in [S_h(\Omega_h^n)]^3$. Since the triangles of $\mathcal{T}_{\mathbb{H}}^h$ are affine to the standard simplex in \mathbb{R}^2 , the only remnant of the embedding is that the vertices of the mesh \mathcal{T}_{Ω}^h have position vectors into \mathbb{R}^3 .

We define

$$S_h^0(\Omega_h^n) := \{ \phi_h \in S_h(\Omega_h^n) \mid \phi_h|_{\Gamma_h^n} = 0 \}.$$

We use the notation \otimes for the tensor product.

As noted in [42], a natural way to define the discrete embeddings $\hat{\mathbf{S}}_h^{n+1}$ would be $\hat{\mathbf{S}}_h^{n+1} := \mathbf{Z}_h^{n+1}(\hat{\mathbf{S}}_h^n)$, where \mathbf{Z}_h^{n+1} is the update of the mesh for Ω_h^n to a mesh for Ω_h^{n+1} , and is given in Algorithm 1. Since $\hat{\mathbf{Y}}_h^{n+1} := (\hat{\mathbf{S}}_h^{n+1})^{-1}$, this would imply that $\hat{\mathbf{Y}}_h^{n+1} := (\hat{\mathbf{S}}_h^n)^{-1}((\mathbf{Z}_h^{n+1})^{-1})$, and thus $\hat{\mathbf{Y}}_h^{n+1} := \hat{\mathbf{Y}}_h^n((\mathbf{Z}_h^{n+1})^{-1})$. Thus the map $\hat{\mathbf{S}}_h^n$ can be totally gotten rid of for all time steps $n \geq 1$, resulting in Algorithm 1.

Algorithm 1 This algorithm corresponds to Algorithm 1 in [42]. Let $\bar{\omega} \in (0, \infty)$. Given $\Omega_h^0 \subset \mathbb{R}^2$, with $\hat{\mathbf{S}}_h^0 \in [S_h(\mathbb{H}_h)]^2$, set $\hat{\mathbf{Y}}_h^0 := (\hat{\mathbf{S}}_h^0)^{-1} \in [S_h(\Omega_h^0)]^3$. For $n = 0, \dots, N-1$, perform this algorithm.

1: **for** $j = 1, 2$ **do**

2: Find $\zeta_h^{n,j} \in S_h(\Omega_h^n)$ such that

$$\int_{\Omega_h^n} \zeta_h^{n,j} \phi_h \, dv = - \int_{\Omega_h^n} \nabla \hat{\mathbf{Y}}_h^{n,j} \cdot \nabla \phi_h \, dv, \quad \forall \phi_h \in S_h(\Omega_h^n).$$

3: Find $\zeta_h^{n,3} \in S_h^0(\Omega_h^n)$ such that

$$\int_{\Omega_h^n} \zeta_h^{n,3} \phi_h \, dv = - \int_{\Omega_h^n} \nabla \hat{\mathbf{Y}}_h^{n,3} \cdot \nabla \phi_h \, dv, \quad \forall \phi_h \in S_h^0(\Omega_h^n).$$

4: Define $I_{\Omega_h^n}$ as the identity map on Ω_h^n . We also define $\hat{\mathbf{H}}_h^n$ by

$$\hat{\mathbf{H}}_h^n := (\nabla \hat{\mathbf{Y}}_h^n)^T \nabla \hat{\mathbf{Y}}_h^n.$$

5: Define \mathbf{T}_h^n on vertex $\rho_j \in \mathcal{T}_\Gamma^h$ by

$$\mathbf{T}_h^n(\rho_j) := \frac{\mathbf{t}_h^n(\sigma_j) + \mathbf{t}_h^n(\sigma_{j+1})}{|\mathbf{t}_h^n(\sigma_j) + \mathbf{t}_h^n(\sigma_{j+1})|} \otimes \frac{\mathbf{t}_h^n(\sigma_j) + \mathbf{t}_h^n(\sigma_{j+1})}{|\mathbf{t}_h^n(\sigma_j) + \mathbf{t}_h^n(\sigma_{j+1})|},$$

where $\sigma_j, \sigma_{j+1} \in \mathcal{T}_\Gamma^h$ and σ_j, σ_{j+1} are adjacent to vertex ρ_j . Here $\mathbf{t}_h^n(\sigma)$ is a unit tangent vector to σ , where all tangent vectors are chosen such that $\mathbf{t}_h^n(\sigma_j) \cdot \mathbf{t}_h^n(\sigma_{j+1}) \geq 0$.

6: Define $\tilde{\zeta}_h^n$ on vertex $\rho_j \in \mathcal{T}_\Omega^h$ by

$$\tilde{\zeta}_h^n := P_{\mathbb{H}}(\hat{\mathbf{Y}}_h^n(\rho_j)) \zeta_h^n(\rho_j),$$

where $P_{\mathbb{H}}(\hat{\mathbf{Y}}_h^n(\rho_j))$ is the tangential projection onto the tangent space of \mathbb{H} at the point $\hat{\mathbf{Y}}_h^n(\rho_j)$.

7: Solve for $\mathbf{Z}_h^{n+1} \in [S_h(\Omega_h^n)]^2$, where

$$\begin{aligned} & \int_{\Omega_h^n} \left(\frac{1}{\Delta t} I_h(\mathbf{Z}_h^{n+1} \cdot \boldsymbol{\varphi}_h) + \frac{1}{\bar{\omega}} \sum_{i=1}^2 \sum_{j=1}^3 ((\hat{\mathbf{H}}_h^n)^{-1} \nabla \hat{\mathbf{Y}}_{h,j}^n)_i I_h(\tilde{\boldsymbol{\zeta}}_h^{n,j} \boldsymbol{\varphi}_h^i) \right) d\mathbf{x} \\ &= \int_{\Omega_h^n} \left(I_h(\mathbf{W}_h^n \cdot \boldsymbol{\varphi}_h) + \frac{1}{\Delta t} I_h(I_{\Omega_h^n} \cdot \boldsymbol{\varphi}_h) \right) d\mathbf{x}, \quad \forall \boldsymbol{\varphi}_h \in [S_h^0(\Omega_h^n)]^2, \end{aligned}$$

and

$$\begin{aligned} & \int_{\Gamma_h^n} \left(\frac{1}{\Delta t} I_h(\mathbf{Z}_h^{n+1} \cdot \boldsymbol{\eta}_h) + \frac{1}{\bar{\omega}} \sum_{i=1}^2 \sum_{j=1}^3 ((\hat{\mathbf{H}}_h^n)^{-1} \nabla \hat{\mathbf{Y}}_{h,j}^n)_i I_h(\tilde{\boldsymbol{\zeta}}_h^{n,j} (\mathbf{T}_h^n \boldsymbol{\eta}_h)^i) \right) d\mathbf{x} \\ &= \int_{\Gamma_h^n} \left(I_h(\mathbf{W}_h^n \cdot \boldsymbol{\eta}_h) + \frac{1}{\Delta t} I_h(I_{\Omega_h^n} \cdot \boldsymbol{\eta}_h) \right) d\mathbf{x}, \quad \forall \boldsymbol{\eta}_h \in [S_h(\Gamma_h^n)]^2. \end{aligned}$$

8: Let $\Omega_h^{n+1} := \mathbf{Z}_h^{n+1}(\Omega_h^n)$ (where we are mapping the mesh itself).

9: Let $\hat{\mathbf{Y}}_h^{n+1} := \hat{\mathbf{Y}}_h^n ((\mathbf{Z}_h^{n+1})^{-1})$.

Note that the projection \mathbf{T}_h^n onto the tangent space of Γ_h^n is introduced in [42] for stability reasons.

Remark As noted in [42], an important feature of the scheme is that it is not necessary to compute the inverse of \mathbf{Z}_h^{n+1} , since the components of the map $\hat{\mathbf{Y}}_h^n$ with respect to the Lagrange basis on Ω_h^n are given by the position vectors of the vertices of \mathbb{H}_h , which are constant. Therefore $\hat{\mathbf{Y}}_h^n$ is described by a component vector which is independent of n . However, the map $\hat{\mathbf{Y}}_h^n$ changes in time, since the finite element basis changes when Ω_h^n is updated.

We note that the parameter $\bar{\omega} > 0$ in Algorithm 1 is the inverse of the diffusion coefficient in the harmonic map heat flow. It corresponds to having differing time scales for the reparametrisation and for the evolution of the surface, and is important in applications where the submanifold $\Gamma(t)$ moves very fast and the time scale $\bar{\omega}$, on which the redistribution of the mesh nodes takes place, has to be very small.

For the simple evolution of a circle, similar to the one presented in Figure 2.3, the mesh smoothing obtained using the DeTurck method is virtually identical to the one obtained

using the harmonic extension method. If, however, we prescribe a normal velocity of

$$V := 2 \sin(3t), \quad (2.3.2)$$

to a circle (so that the radius is oscillating), then the harmonic extension method slowly degrades, while the DeTurck method does not. This is demonstrated in Figures 2.5 and 2.6. The simulation is run with an initial circle of radius 1.0, and from $t = 0$ to $t = 100$. In Figure 2.5 we see a comparison of coarse meshes at $t = 0$ and at $t = 100$. In Figure 2.6 we see a graph that shows the degradation of \mathcal{T}_Ω^h over time. The mesh quality is measured by

$$q := \max_{\mu \in \mathcal{T}_\Omega^h} \frac{H(\mu)}{h(\mu)}, \quad (2.3.3)$$

where $H(\mu)$ is the length of μ 's longest edge, and $h(\mu)$ is the length of μ 's shortest edge.

A comparison with and without the DeTurck method can also be seen in Figure 4.7, with the initial condition given by Figure 4.6. We can also see an example with $\bar{\omega} = 0.1$ in Figure 4.8.

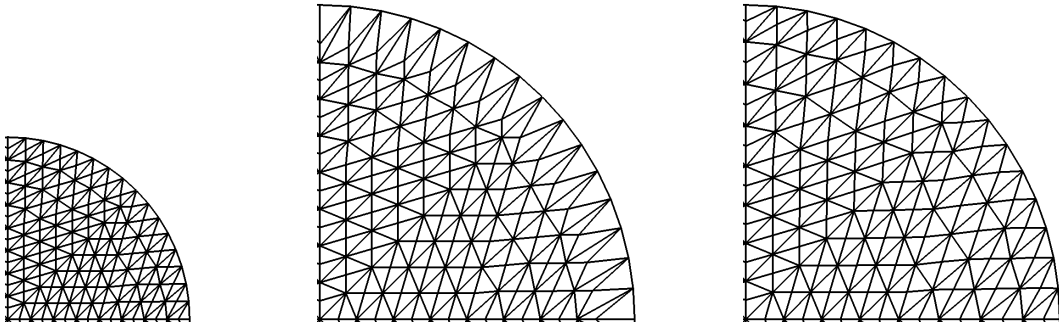


Figure 2.5: Snapshots of a single quadrant of \mathcal{T}_Ω^h , showing the difference in mesh quality between the harmonic extension method, and the DeTurck method. The left image is the initial condition. The center image is taken at $t = 100$, and shows the mesh under the harmonic extension method (Section 2.3.1). The right image is also taken at $t = 100$, and shows the mesh under the DeTurck method (Section 2.3.2). The evolution of the circle is given by the outward normal velocity (2.3.2). The DeTurck method appears significantly more effective.

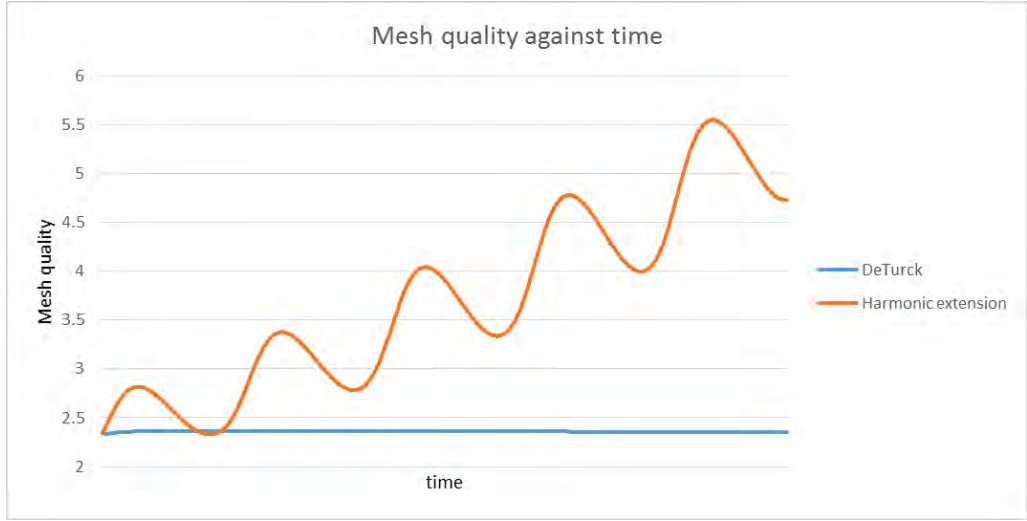


Figure 2.6: Graph showing the difference in mesh quality between the harmonic extension method (Section 2.3.1), and the DeTurck method (Section 2.3.2), measured by (2.3.3). A quality of $q = 1.0$ is ideal (this corresponds to a mesh consisting of equilateral triangles), and higher values imply a worse mesh. The evolution of the circle is given by the outward normal velocity (2.3.2). The simulation was run from $t = 0$ until $t = 100$, and at $t = 0$ we had $h := \max_{\mu \in \mathcal{T}_\Omega^h} H(\mu) \approx 0.05$ and $\Delta t = 10^{-2}$. We can see that the DeTurck method maintains the quality of the initial mesh, while the harmonic extension method degrades as time goes by. The quality oscillates with the velocity (2.3.2) (and thus with the radius of the circle).

2.3.3 Re-meshing via GMSH

Despite the effectiveness of the DeTurck method, a large deformation can leave the mesh in an irreparable state. When such a state arises, we employ the re-meshing software GMSH [52]. We use \mathcal{T}_Γ^h as an input to GMSH. The mesh \mathcal{T}_Ω^h is then rebuilt by GMSH. Figure 2.7 shows an example mesh created by GMSH, next to a mesh created by ALBERTA for comparison.

Since the re-meshing procedure is computationally expensive, we only perform it when

$$q := \max_{\mu \in \mathcal{T}_\Omega^h} \frac{H(\mu)}{h(\mu)} \geq \text{tol} := 5.$$

If tol is chosen too high, then the mesh degrades to a point where it is negatively impacting the accuracy of the solution. If it is chosen too small then the re-meshing happens too often, and the computational time increases drastically.

When using this technique with the DeTurck method, care must be taken to redefine \mathbf{Y}_h^n (defined in Section 2.3.2) on the new mesh.

Remark We stress that re-meshing is only strictly necessary for large deformations, although we choose to re-mesh more often, in order to maintain the quality of the mesh.

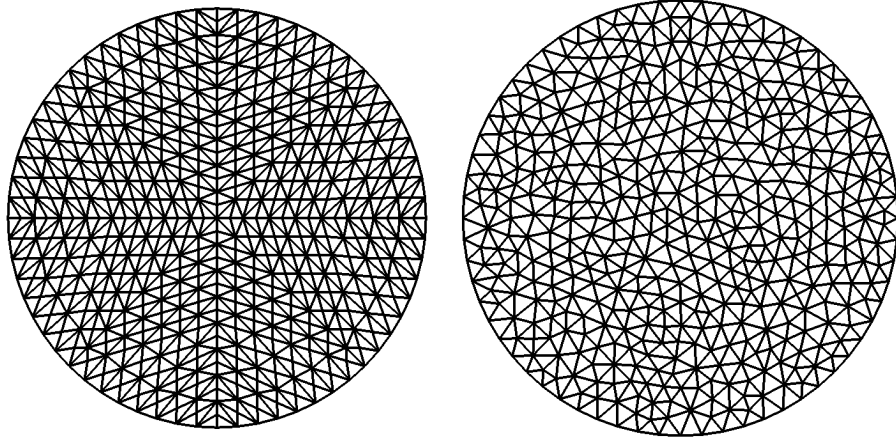


Figure 2.7: Comparison of a coarse mesh created by ALBERTA (left) and a coarse mesh created by GMSH (right).

2.4 Unfitted finite element approximation of (\mathbb{M}) in \mathbb{R}^2

This section introduces an unfitted finite element approximation of (\mathbb{M}) , restricted to \mathbb{R}^2 . We follow the techniques given in [8], with help from [6, 7, 41].

Let Γ_h^n be defined as in Section 2.2 such that it is a closed polyhedral curve, parametrised by a piecewise linear function \mathbf{X}_h^n . We introduce a domain $D \subset \mathbb{R}^2$ such that $\Gamma_h^n \subset D$ for $n = 0, \dots, N$. We triangulate D by a family of conforming disjoint open triangles, $\mathcal{T}_D^h := \{\pi_l\}_{l=1}^L$, with vertices $\{\mathbf{p}_m\}_{m=1}^M$. Thus we have $D := \cup_{l=1}^L \bar{\pi}_l$. We denote the interior of Γ_h^n by $(\Omega_h^n)^+$ and the exterior by $(\Omega_h^n)^-$ and we assume that Γ_h^n crosses any one triangle edge at most twice and each triangle contains at most one edge that is crossed twice.

We split the triangles of \mathcal{T}_D^h into the mutually exclusive classes *interior*, *exterior*, and *cut*. For the majority of triangles, the *interior* triangles are those that lie fully within $(\Omega_h^n)^+$, the *exterior* triangles are those that lie fully inside $(\Omega_h^n)^-$, and the *cut* triangles are those for which the intersection with Γ_h^n is non empty. This is illustrated in Figure 2.8, where Γ_h^n is denoted by the black line, with $(\Omega_h^n)^+$ to its left, the *interior* triangles are blue, the *exterior* triangles are green, and the *cut* triangles are red. There are some

triangles that are intersected by Γ_h^n that are not included in the class of *cut* triangles, these triangles are ones in which Γ_h^n only intersects one side of the triangle, see the left hand image in Figure 2.9. Such triangles are classed as *interior* if the two sides that are not intersected by Γ_h^n lie in $(\Omega_h^n)^+$ and *exterior* otherwise.

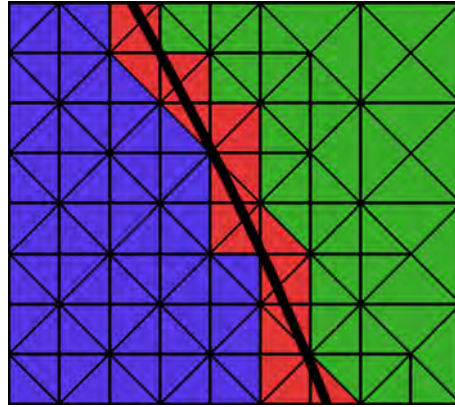


Figure 2.8: This figure displays an illustration of the unfitted finite element mesh \mathcal{T}_D^h . Γ_h^n is the bold black line, with $(\Omega_h^n)^+$ to its left, the *interior* triangles are in blue, the *exterior* triangles are in green, and the *cut* triangles are in red.

In each cut triangle, π , we approximate Γ_h^n by a chord, $[\mathbf{r}_1, \mathbf{r}_2]$. Here the \mathbf{r}_i are two intersections between Γ_h^n and the boundary of π . In the event of there being more than two intersections, we choose the chord to be the one that joins the points of intersection on the two sides that are cut only once by Γ_h^n , see the centre and right hand images in Figure 2.9. We denote the approximation of Γ_h^n given by these chords by $\tilde{\Gamma}_h^n$, and the region that lies in the interior of $\tilde{\Gamma}_h^n$ by $(\tilde{\Omega}_h^n)^+$, see Figure 2.10.

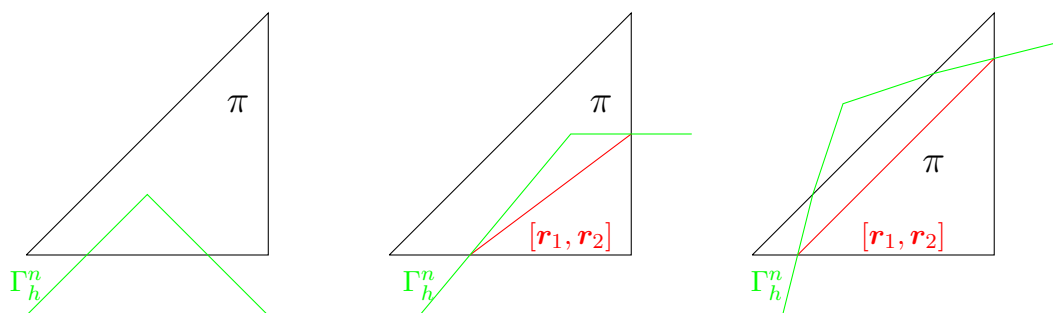


Figure 2.9: The left hand image is an example of an element, π , that is intersected by Γ_h^n but is not classified as *cut*. The centre and right hand images display different possibilities for Γ_h^n (in green) intersecting $\pi \in \mathcal{T}_D^h$ (in black), and the choice of $[\mathbf{r}_1, \mathbf{r}_2]$ (in red).

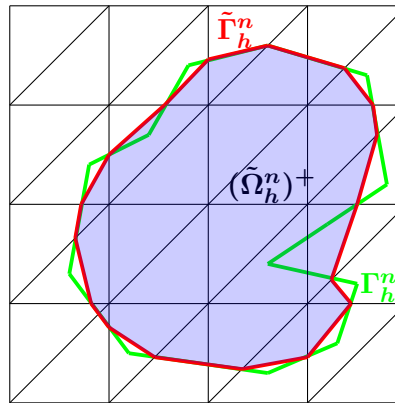


Figure 2.10: This image displays an illustration of Γ_h^n (in green) overlaid by $\tilde{\Gamma}_h^n$ (in red), and $(\tilde{\Omega}_h^n)^+$ (blue region).

Algorithms that allow quick and efficient splitting of the domain into *interior*, *exterior*, and *cut* elements are taken directly from [68]. They are copied out here for completeness in Algorithms 2 - 6. Note that Algorithm 6 is a modified version of the algorithm in [68], as it includes a reclassification of triangles that are *cut* on only one side as *interior* or *exterior*. This algorithm is modified because in [68] they do not consider integrals over the interface Γ_h^n when computing the bulk quantities. For the purpose of these algorithms, we have constructed \mathcal{T}_D^h as a hierarchical mesh with L levels, denoted $\mathcal{T}_{D,0}^h, \dots, \mathcal{T}_{D,L}^h$. Here $\mathcal{T}_{D,0}^h$ is the top level mesh, and $\mathcal{T}_{D,L}^h$ is the bottom level mesh, so that $\mathcal{T}_D = \mathcal{T}_{D,L}^h$. The triangles of mesh $\mathcal{T}_{D,l}^h$ are refined either zero or one times to give the mesh $\mathcal{T}_{D,l+1}^h$. Triangles in the mesh $\mathcal{T}_{D,L}^h$ are called leaf triangles. We start with Algorithm 2, which detects if a given triangle is intersected by a given line segment. This is used in Algorithms 3 and 4, which mark all triangles that are intersected by Γ_h^n as *cut*. We then use Algorithm 5 to mark all *exterior* triangles. Finally we use Algorithm 6 to mark all triangles that are neither *cut* nor *exterior* as *interior* and then to reassign the *cut* triangles that are cut on one side only as either *interior* or *exterior*.

Algorithm 2 This algorithm detects if a triangle is intersected by a line segment. The triangle is denoted π , and has edges e_1 , e_2 and e_3 . The line segment is denoted L , and has end points q_1 and q_2 . The algorithm returns *true* if there is an intersection, *false* otherwise.

```

1: for  $i = 1, 2$  do
2:   if  $q_i \in \pi$  then
3:     Return true
4: for  $i = 1, 2, 3$  do
5:   if  $L$  intersects  $e_i$  then
6:     Return true
7: Return false

```

Algorithm 3 Hierarchical search to mark all triangles intersected by Γ_h^n as *cut*. The set of triangles at the top level of the hierarchical mesh \mathcal{T}_D^h is denoted by $\mathcal{T}_{D,0}^h$.

```

1: for  $\sigma \in \mathcal{T}_\Gamma^h$  do
2:   for  $\pi \in \mathcal{T}_{D,0}^h$  do
3:     Algorithm 4 ( $\sigma, \pi$ )

```

Algorithm 4 Hierarchical search to mark all children of a given triangle that are intersected by $\sigma \in \mathcal{T}_\Gamma^h$ as *cut* if they are leaf triangles. Here $\pi \in \mathcal{T}_{D,l}^h$ for some mesh level l , where $0 \leq l \leq L$.

```

1: if  $l = L$  then
2:   Mark  $\pi$  as cut
3: for  $\pi_i$  child of  $\pi$  do
4:   if Algorithm 2 ( $\sigma, \pi_i$ ) then
5:     Algorithm 4 ( $\sigma, \pi_i$ )

```

Algorithm 5 Mark all triangles that are outside Γ_h^n as *exterior*. Γ_h^n must not intersect triangles on ∂D , the boundary of D . The algorithm needs the *cut* triangles to be marked, using Algorithm 3.

```

1: Mark all triangles in  $\mathcal{T}_D^h$  as clear
2: Mark all triangles on  $\partial D$  as exterior, and put them in currentFront
3: while currentFront is not empty do
4:   for  $\pi \in \text{currentFront}$  do
5:     for  $\pi_i$  neighbour of  $\pi$  do
6:       if  $\pi_i$  is clear, and is not cut then
7:         Put  $\pi_i$  in newFront
8:         Mark  $\pi_i$  as exterior
9:   Let currentFront = newFront
10:  Clear newFront

```

Algorithm 6 Mark all triangles that are neither *cut* nor *exterior* as *interior*. Mark triangles that are cut on one side only as either *interior* or *exterior*. Here $\#Cut(\pi)$ is the number of edges of π that are cut by Γ_h^n .

```

1: for  $\pi \in \mathcal{T}_D^h$  do
2:   if  $\pi$  is neither cut nor exterior then
3:     Set  $\pi$  as interior
4:   if  $\pi$  is cut and  $\#Cut(\pi) = 1$  then
5:     if the edges of  $\pi$  that are not cut belong to  $(\Omega_h^n)^+$  then
6:       Set  $\pi$  as interior
7:     else
8:       Set  $\pi$  as exterior

```

We propose the following unfitted finite element approximation of (\mathbb{M})

Problem \mathbb{P}_{SIU}^h For $\omega \in (0, 1]$, given $\mathbf{X}_h^0 = I^h \mathbf{x}^0 \in W_h(\mathbb{I})$, for $n = 0, \dots, N - 1$, find $\{u_h^n, \mathbf{X}_h^{n+1}\} \in S_h(D) \times W_h(\mathbb{I})$ such that

$$(\nabla u_h^n, \nabla \phi_h)_{(\tilde{\Omega}_h^n)^+} + \frac{1}{\alpha} (u_h^n, \phi_h)_{\tilde{\Gamma}_h^n}^h + (1, \phi_h)_{(\tilde{\Omega}_h^n)^+} = (Q, \phi_h)_{\tilde{\Gamma}_h^n}^h, \quad \forall \phi_h \in S_h(D), \quad (2.4.1)$$

and

$$\begin{aligned} & \left(|\mathbf{X}_{h,\rho}^n|^2 (\omega D_t \mathbf{X}_h^{n+1} + (1-\omega)(D_t \mathbf{X}_h^{n+1} \cdot \mathbf{n}_h^n) \mathbf{n}_h^n), \boldsymbol{\xi}_h \right)^h + \beta(\mathbf{X}_{h,\rho}^{n+1}, \boldsymbol{\xi}_{h,\rho}) \\ &= \frac{1}{\alpha} \left(|\mathbf{X}_{h,\rho}^n|^2 u_h^n(\mathbf{X}_h^n) \mathbf{n}_h^n, \boldsymbol{\xi}_h \right)^h, \quad \forall \boldsymbol{\xi}_h \in W_h(\mathbb{I}). \end{aligned} \quad (2.4.2)$$

Here $D_t \mathbf{X}_h^{n+1} := \frac{\mathbf{X}_h^{n+1} - \mathbf{X}_h^n}{\Delta t}$, Γ_h^n is given by $\mathbf{X}_h^n(\mathbb{I})$, and the inner products $(\cdot, \cdot)_{(\tilde{\Omega}_h^n)^+}$ and $(\cdot, \cdot)_{\tilde{\Gamma}_h^n}^h$ are defined below.

In (2.4.2) we need to sample u_h^n at point $\mathbf{q} \in \pi \in \mathcal{T}_D^h$ with barycentric coordinates $\mathbf{b}(\mathbf{q})$, where the i^{th} coordinate of \mathbf{b} is given by $\mathbf{b}_i(\mathbf{q})$. In order to do this, we take

$$u_h^n(\mathbf{q}) = \sum_{i=1}^3 \mathbf{b}_i(\mathbf{q}) u_h^n(\mathbf{p}_i).$$

Here \mathbf{p}_i is the vertex of π that corresponds to the barycentric coordinate $\mathbf{b}_i(\mathbf{q})$.

We define the inner product over $\tilde{\Gamma}_h^n$ by

$$(\eta_h, \zeta_h)_{\tilde{\Gamma}_h^n}^h := \frac{1}{2} \sum_{\pi \in \mathcal{T}_D^{h,cut}} |\mathbf{r}_1 - \mathbf{r}_2| \sum_{l=1}^2 \eta_h(\mathbf{r}_l) \zeta_h(\mathbf{r}_l), \quad \forall \eta_h, \zeta_h \in S_h(D),$$

where $\mathcal{T}_D^{h,cut}$ is the set of $\pi \in \mathcal{T}_D^h$ where π is *cut*, and the \mathbf{r}_i correspond to the given π . In order to define $(\cdot, \cdot)_{(\tilde{\Omega}_h^n)^+}$ we introduce the weight function $\mathcal{F}(\pi_l)$, for $\pi_l \in \mathcal{T}_D^h$. If π_l is *interior* then $\mathcal{F}(\pi_l) = 1$, and if π_l is *exterior*, then $\mathcal{F}(\pi_l) = 0$. If, however, π_l is *cut*, we take $\mathcal{F}(\pi_l)$ as the fraction of π_l that lies inside $(\tilde{\Omega}_h^n)^+$. We now define the inner products over $(\tilde{\Omega}_h^n)^+$ by

$$(\nabla u_h^n, \nabla \phi_h)_{(\tilde{\Omega}_h^n)^+} = \sum_{l=1}^L \int_{\pi_l} \mathcal{F}(\pi_l) \nabla u_h^n \cdot \nabla \phi_h \, d\mathbf{x}, \quad \text{and} \quad (1, \phi_h)_{(\tilde{\Omega}_h^n)^+} := \sum_{l=1}^L \int_{\pi_l} \mathcal{F}(\pi_l) \phi_h \, d\mathbf{x}.$$

2.5 Fitted sharp interface finite element scheme in \mathbb{R}^3

First, we partition the time interval $[0, T]$ into $N + 1$ steps: $0 = t_0 < t_1 < \dots < t_{N-1} < t_N = T$. We assume that these are evenly spaced, so that $\Delta t := t_{i+1} - t_i$. Let Γ_h^n be a closed polyhedral surface, consisting of triangles, parametrised by $\mathbf{X}_h^n : \Gamma_h^{n-1} \rightarrow \mathbb{R}^3$.

In a slight abuse of notation, we denote this collection of triangles by $\mathcal{T}_\Gamma^h := \{\eta_j^n\}_{j=1}^J$ (where, as before, we write \mathcal{T}_Γ^h as opposed to $\mathcal{T}_{\Gamma_h^0}$). The initial surface, Γ_h^0 , is a polyhedral approximation to $\Gamma(0)$. We define

$$Y_h(\Gamma_h^{n-1}) := \left\{ \boldsymbol{\xi}_h \in C^0(\Gamma_h^{n-1}, \mathbb{R}^3) \mid \boldsymbol{\xi}_h|_{\eta_j^n} \text{ is affine } \forall \eta_j^n \in \mathcal{T}_\Gamma^h \right\}.$$

As in Section 2.2, we mesh the interior of Γ_h^n , denoted by Ω_h^n , with a conforming mesh, this time consisting of tetrahedrons. In a slight abuse of notation, this mesh is denoted by $\mathcal{T}_\Omega^h := \{\mu_l^n\}_{l=1}^L$ (where, as before, we write \mathcal{T}_Ω^h as opposed to $\mathcal{T}_{\Omega_h^n}$), where the μ_l^n are tetrahedrons, with vertices $\{\mathbf{p}_i^n\}_{i=1}^I$. Thus we have $\Omega_h^n := \cup_{l=1}^L \bar{\mu}_l^n$, and Ω_h^n is such that the edge nodes are fitted to the corresponding nodes in Γ_h^n .

We define the tangential gradient of a function f , which is differential in an open neighbourhood of Γ , by $\nabla_\Gamma f := \nabla f - (\mathbf{n} \cdot \nabla f)\mathbf{n}$. From Lemma 2.4 in [40], we see that $\nabla_\Gamma f(\mathbf{x})$ only depends on the values of f on $\Gamma \cap U$, where $U \subset \mathbb{R}^3$ is a neighbourhood of \mathbf{x} .

Following [37], a sharp interface finite element scheme for (M), in \mathbb{R}^3 , with initial condition Γ_h^0 , is given by

Problem $\mathbb{P}_{SI\mathbb{R}^3}^h$ Given Γ_h^0 and the identity function $\mathbf{X}_h^0 \in Y_h(\Gamma_h^0)$, then for $n = 0, \dots, N$, find $\{u_h^n, \mathbf{X}_h^{n+1}\} \in S_h(\Omega_h^n) \times Y_h(\Gamma_h^n)$ such that

$$\int_{\Omega_h^n} \nabla u_h^n \cdot \nabla \phi_h \, dv + \frac{1}{\alpha} \int_{\Gamma_h^n} I_h(u_h^n \phi_h) \, ds + \int_{\Omega_h^n} \phi_h \, dv = Q \int_{\Gamma_h^n} \phi_h \, ds, \quad \forall \phi_h \in S_h(\Omega_h^n), \quad (2.5.1)$$

(where Γ_h^n is given by $\mathbf{X}_h^n(\Gamma_h^{n-1})$, and Ω_h^n is the interior of Γ_h^n) and

$$\int_{\Gamma_h^n} D_t \mathbf{X}_h^{n+1} \cdot \boldsymbol{\xi}_h \, ds + \beta \int_{\Gamma_h^n} \nabla_{\Gamma_h^n} \mathbf{X}_h^{n+1} \cdot \nabla_{\Gamma_h^n} \boldsymbol{\xi}_h \, ds = \frac{1}{\alpha} \int_{\Gamma_h^n} u_h^n \mathbf{n}_h^n \cdot \boldsymbol{\xi}_h \, ds, \quad \forall \boldsymbol{\xi}_h \in Y_h(\Gamma_h^n). \quad (2.5.2)$$

Here $D_t \mathbf{X}_h^{n+1} := \frac{\mathbf{X}_h^{n+1} - \mathbf{X}_h^n}{\Delta t}$ and, following [37],

$$\nabla_{\Gamma_h^n} \mathbf{X}_h^{n+1} \cdot \nabla_{\Gamma_h^n} \boldsymbol{\xi}_h = \sum_{i=1}^3 \nabla_{\Gamma_h^n} \mathbf{X}_{h,i}^{n+1} \cdot \nabla_{\Gamma_h^n} \boldsymbol{\xi}_{h,i},$$

where $\mathbf{X}_{h,i}^{n+1}$ and $\boldsymbol{\xi}_{h,i}$ denote the i^{th} component of \mathbf{X}_h^{n+1} and $\boldsymbol{\xi}_h$, respectively. We note that for $n \geq 1$, $\mathbf{X}_h^n \in Y_h(\Gamma_h^{n-1})$ and we abuse notation by also denoting the identity function on Γ_h^n as \mathbf{X}_h^n for $n \geq 0$.

Unlike the scheme in \mathbb{R}^2 (given by \mathbb{P}_{SI}^h), the scheme in \mathbb{R}^3 has no intrinsic mesh smoothing on \mathcal{T}_Γ^h . This is in contrast to the approach introduced in [43], in which there is an intrinsic mesh smoothing on \mathcal{T}_Γ^h . We did not implement this scheme due to the additional programming complexity.

Chapter 3

Applied and numerical analysis of a diffuse interface model

This chapter concerns itself with the diffuse interface approach. In this approach, we approximate $\Gamma(t)$ by a diffuse interface of width $\mathcal{C}\varepsilon$, where \mathcal{C} is a positive constant. Here we choose $\varepsilon > 0$ as small as needed, thus allowing us to resolve $\Gamma(t)$ to the desired accuracy. Doing this comes at the price of a finer mesh (and associated smaller time step). In order to define the diffuse interface, we introduce a phase field variable $\varphi(\mathbf{x}, t) : D \times [0, T] \rightarrow \mathbb{R}$, such that $\varphi = 1$ inside the interface, $\varphi = -1$ outside the interface, and φ varies smoothly over the interface (note that we consider a double obstacle potential, defined later). As φ evolves we keep track of its zero level set; this is our approximation of $\Gamma(t)$. We write the diffuse interfacial region as

$$\Gamma_\varepsilon(t) := \{ \mathbf{x} \in D \mid |\varphi(\mathbf{x}, t)| < 1 \},$$

where $D \subset \mathbb{R}^2$ is a bounded domain, large enough to contain $\Gamma_\varepsilon(t)$, for all $t \in [0, T]$, with outward unit normal $\boldsymbol{\nu}$.

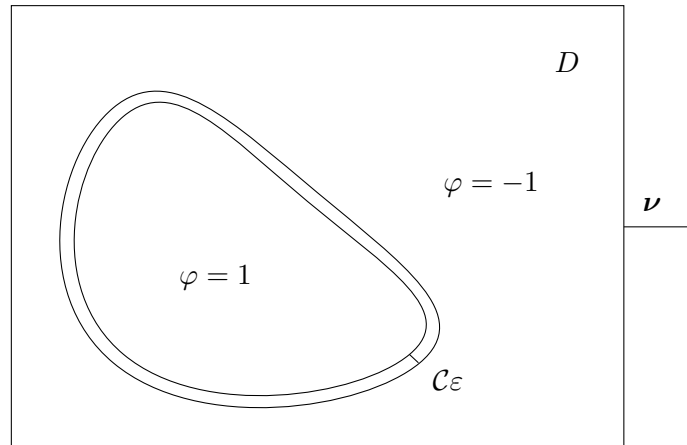


Figure 3.1: The diffuse interfacial region $\Gamma_\varepsilon(t)$ in D , with outward unit normal ν . Here $\Gamma(t)$ is approximated by the zero level set of φ .

The diffuse interface approach has a number of advantages over the sharp interface approach used in Chapter 2, the most notable being a natural and smooth handling of topology change. Although recent advances, for example [18], allow us to perform topology changes on a fitted mesh, these can be challenging to implement, and they are not integrated naturally into the model. We also do not need to maintain an evolving mesh. These two advantages (topology change and mesh simplicity) mean that the numerical simulations are able to run for significantly longer times. The diffuse interface approach also has a few disadvantages that the sharp interface approach does not, the biggest of which is execution time. The introduction of the phase field variable φ increases the dimension of the problem by one, which has a large impact on the simulation's execution time. By representing $\Gamma(t)$ as a diffuse interface, the approach also loses some accuracy. This can be offset, at the cost of execution time, by taking ε smaller. The diffuse interface approach is also less able to simulate more extreme values of α and β . For example, taking α smaller in the diffuse interface paradigm requires us to take ε smaller, causing us to reduce h and Δt , and thus increasing the execution time.

This chapter starts, in Section 3.1, by writing (M) in the diffuse interface paradigm, the resulting diffuse interface model is then regularised in time in order to establish the analytical results in the subsequent sections of the chapter. In Sections 3.2 and 3.3 we respectively show the existence and uniqueness of the solution to the weak formulation of the regularised diffuse interface model. We then present a finite element approximation

of the model in Section 3.4, and in Section 3.5 we show the existence and uniqueness of a solution to the finite element approximation. We follow this with a convergence result.

Throughout this chapter, we use the notation $C^k(D)$ to denote functions that are k times continuously differentiable over D and $C_0^k(D)$ to denote functions that are k times continuously differentiable over D and have compact support.

3.1 Diffuse interface formulation

The diffuse interface approach is different to the sharp interface approach, as we deal with $\Gamma(t)$ and $\Omega(t)$ implicitly; thus, the model (M) must be altered to account for this.

The velocity law (Mc) is mean curvature flow with a forcing term. This means that we can approximate it, as per the techniques in [37], with the Allen-Cahn equation. Using the double obstacle potential [15],

$$W(s) := \frac{1}{2}(1 - s^2) + I_{[-1,1]}(s),$$

where

$$I_{[-1,1]}(s) := \begin{cases} \infty, & \text{for } |s| > 1, \\ 0, & \text{for } |s| \leq 1, \end{cases}$$

yields the Allen-Cahn equation

$$\varepsilon\varphi_t - \beta\varepsilon\Delta\varphi - \frac{\beta}{\varepsilon}W'(\varphi) = \frac{\pi u}{4\alpha}, \quad \text{in } D \times (0, T), \quad (3.1.1)$$

which we supplement with the homogeneous Neumann boundary conditions

$$\nabla\varphi \cdot \nu = 0, \quad \text{on } \partial D \times (0, T). \quad (3.1.2)$$

We consider the sub-differential of $\partial I_{[-1,1]}(s)$ to interpret $W'(s)$ as

$$W'(s) = \begin{cases} (-\infty, 1], & \text{if } s = -1, \\ -s, & \text{if } |s| < 1, \\ [-1, \infty), & \text{if } s = 1. \end{cases}$$

In (3.1.1) u is the solution to (3.1.4) or (3.1.6) (both diffuse interface approximations to (Ma) with (Mb), given later) and the factor of $\frac{\pi}{4}$ on the right hand side of (3.1.1) is chosen such that as $\varepsilon \rightarrow 0$ we recover the sharp interface equation (Mc). In [67] the authors show, in the case of a smooth evolution of the forced mean curvature flow, that the Hausdorff distance between the zero level set of φ and the interface of the flow is of order $\mathcal{O}(\varepsilon^2)$.

We note that since we are using the double obstacle energy we have $\varphi \in [-1, 1]$, and $|\varphi| < 1$ only in the diffuse interfacial region $\Gamma_\varepsilon(t)$.

To construct the initial condition $\varphi(\mathbf{x}, 0) = \varphi_0(\mathbf{x})$, we first define a distance function from \mathbf{x} to $\Gamma(0)$, denoted by $d_\Gamma(\mathbf{x})$. This is such that it is positive for \mathbf{x} inside $\Gamma(0)$, and negative outside. We now define the initial condition by

$$\varphi(\mathbf{x}, 0) = \varphi_0(\mathbf{x}) := \begin{cases} 1, & \text{if } d_\Gamma(\mathbf{x}) \geq \frac{\varepsilon\pi}{2}, \\ \sin\left(\frac{d_\Gamma(\mathbf{x})}{\varepsilon}\right), & \text{if } -\frac{\varepsilon\pi}{2} < d_\Gamma(\mathbf{x}) < \frac{\varepsilon\pi}{2}, \\ -1, & \text{if } d_\Gamma(\mathbf{x}) \leq -\frac{\varepsilon\pi}{2}. \end{cases} \quad (3.1.3)$$

This initial condition corresponds to a diffuse interface of width $\varepsilon\pi$, and its zero level set coincides with $\Gamma(0)$. This is constructed to have a sinusoidal profile, as the double obstacle energy naturally leads to φ taking this profile.

For a diffuse interface approximation of (Ma) with (Mb) we follow the techniques described in [1, 64] to obtain

$$-\nabla(\zeta(\varphi)\nabla u) + \frac{1}{\alpha\varepsilon}\delta(\varphi)u = -\zeta(\varphi) + \frac{Q}{\varepsilon}\delta(\varphi), \quad \text{in } D \times (0, T), \quad (3.1.4)$$

$$\zeta(\varphi)\nabla u \cdot \boldsymbol{\nu} = 0, \quad \text{on } \partial D \times (0, T) \quad (3.1.5)$$

where

$$\zeta(s) := \frac{1+s}{2}, \quad \text{and} \quad \delta(s) := \frac{2}{\pi}(1-s^2).$$

We note that since $\varphi \equiv -1$ in the region exterior to the diffuse interfacial region, $\Gamma_\varepsilon(t)$, and $\varphi \equiv 1$ in the region in the interior of $\Gamma_\varepsilon(t)$, it follows that $\zeta(\varphi) \equiv 1$ in the interior region and $\zeta(\varphi) \equiv 0$ in the exterior region. Similarly as $|\varphi| < 1$ only in the diffuse interfacial region it follows that $\delta(\varphi) \equiv 0$ outside this region and hence we can view the terms in

(3.1.4) that contain $\delta(\varphi)$ as an approximation to the Robin boundary conditions. The convergence, as $\varepsilon \rightarrow 0$, of (3.1.4) to (Ma) with boundary condition (Mb) is proved in [1, 64].

To aid the analysis in Sections 3.2 and 3.3, and the numerical analysis results in Section 3.5, we regularise (3.1.4) by introducing the time derivative of u (this aids as we use Theorem 3.2.1, given later, which requires bounds on the time derivative of u). This yields the following regularised diffuse interface model

$$\varepsilon^2 u_t - \nabla(\zeta(\varphi)\nabla u) + \frac{1}{\alpha\varepsilon}\delta(\varphi)u = -\zeta(\varphi) + \frac{Q}{\varepsilon}\delta(\varphi), \quad \text{in } D \times (0, T). \quad (3.1.6)$$

Here, for simplicity of presentation, in an abuse of notation, we denote the solution of this regularised diffuse interface model by u . We compliment (3.1.6) with the Neumann boundary condition (3.1.5), and the initial condition

$$u(\mathbf{x}, 0) = u_0(\mathbf{x}), \quad \text{in } D. \quad (3.1.7)$$

To determine the natural choice for the initial data, u_0 , we note that in the region exterior to the diffuse interface, where $\varphi = -1$, there should be no contribution from u . Thus, setting $u_0(\mathbf{x}) \equiv 0$ would be a good way to approximate this.

Remark We introduce the $\varepsilon^2 u_t$ regularisation in the diffuse interface model purely for analytical purposes, however, using formally matched asymptotic expansions, as $\varepsilon \rightarrow 0$ we expect to recover (Ma) with boundary condition (Mb) from (3.1.6).

The weak formulation for (3.1.1) coupled with (3.1.6), together with the associated boundary and initial conditions (3.1.2), (3.1.3), (3.1.5), and (3.1.7) is given by

Problem \mathbb{P}_{DI} Find $(\varphi, u) \in X_1 \times X_2$, $\varphi(t) \in K(D)$, such that φ and u satisfy the initial conditions (3.1.3) and (3.1.7) respectively and, for all $t \in (0, T)$,

$$\begin{aligned} \int_D \varphi_t(\rho - \varphi) \, d\mathbf{x} + \beta \int_D \nabla\varphi \cdot \nabla(\rho - \varphi) \, d\mathbf{x} - \frac{\beta}{\varepsilon^2} \int_D \varphi(\rho - \varphi) \, d\mathbf{x} \\ \geq \frac{C_w}{\alpha\varepsilon} \int_D u(\rho - \varphi) \, d\mathbf{x}, \quad \forall \rho \in K(D), \end{aligned} \quad (3.1.8)$$

and

$$\begin{aligned} \varepsilon^2 \int_D u_t \phi \, d\mathbf{x} + \int_D \zeta(\varphi) \nabla u \cdot \nabla \phi \, d\mathbf{x} + \frac{1}{\alpha \varepsilon} \int_D \delta(\varphi) u \phi \, d\mathbf{x} \\ = \frac{1}{\varepsilon} \int_D \delta(\varphi) Q \phi \, d\mathbf{x} - \int_D \zeta(\varphi) \phi \, d\mathbf{x}, \quad \forall \phi \in H^1(D), \end{aligned} \quad (3.1.9)$$

where

$$K(D) := \{ \rho \in H^1(D) \mid |\rho| \leq 1 \text{ in } D \},$$

$$X_1 := \{ \phi \in L^\infty(0, T; L^\infty(D)) \mid \nabla \phi \in L^2(0, T; H^1(D) \cap L^\infty(D)), \phi_t \in L^2(0, T; H^1(D)) \},$$

and

$$X_2 := H^1(0, T; L^2(D)) \cap L^2(0, T; H^1(D)).$$

3.2 Existence of a solution to \mathbb{P}_{DI} for $D \subset \mathbb{R}^2$

In this section we restrict $D \subset \mathbb{R}^2$ and show the existence of a solution to the regularised system \mathbb{P}_{DI} . This section is inspired by [38]; we closely follow many of the proofs therein.

The plan of this section is as follows. We first regularise the system by a parameter $\gamma > 0$ to yield $\mathbb{P}_{DI\gamma}$. This regularisation is performed for a number of reasons. It first removes the degeneracy in the coefficients of (3.1.6), by introducing regularised versions of the weight functions ζ and δ . Secondly, the complex nature of (3.1.1) is reduced to a standard parabolic equation. The first step in the proof is to show the existence of a solution $(\varphi_\gamma, u_\gamma)$ to a regularised system, $\mathbb{P}_{DI\gamma}$, introduced later. We then derive bounds on φ_γ and u_γ , which allow us to show that the solution $(\varphi_\gamma, u_\gamma)$ is unique, and that φ_γ converges to φ and u_γ converges to u as $\gamma \rightarrow 0$, where (φ, u) solve \mathbb{P}_{DI} .

Definitions

We assume, in Sections 3.2 and 3.3, that D is a bounded convex domain, whose boundary $\partial D \in C^3$.

We take $0 < \varepsilon \leq 1$ as fixed and we introduce a regularising parameter $\gamma \in \mathbb{R}$, such that $0 < \gamma \leq \varepsilon$. We define the functions $\delta_\gamma(s)$, $\zeta_\gamma(s)$ and $\chi_\gamma^\varepsilon(s)$ such that

$$\gamma \leq \delta_\gamma(s) \leq C, \quad \text{and} \quad \frac{\gamma}{2} \leq \zeta_\gamma(s) \leq C^*, \quad \text{for } s \in \mathbb{R}, \quad (3.2.1)$$

$$\delta_\gamma(s) := \frac{2}{\pi}((1+2\gamma)^2 - s^2), \quad \text{if } |s| \leq 1 + \gamma, \quad (3.2.2)$$

$$\zeta_\gamma(s) := \frac{1}{2}(1+2\gamma+s), \quad \text{if } |s| \leq 1 + \gamma, \quad (3.2.3)$$

and

$$\chi_\gamma^\varepsilon(s) := \begin{cases} \frac{\beta}{\varepsilon}s + \frac{C_w}{\alpha} \max(\alpha Q, \|u_0\|_{L^\infty(D)}), & \text{for } s \geq 1 + \gamma, \\ 0, & \text{for } s \in [-1, 1], \\ \frac{\beta}{\varepsilon}s - \|u_0\|_{L^\infty(D)} - \frac{C^*t}{\varepsilon^2} & \text{for } s \leq -1 - \gamma. \end{cases} \quad (3.2.4)$$

We fill in the gaps in χ_γ^ε by letting it be continuous and monotone over $(1, 1 + \gamma) \cup (-1 - \gamma, -1)$. We assume that the initial data is such that

$$\|u_0\|_{L^\infty(D)} \leq C, \quad |\varphi_0| \leq 1, \quad \text{and} \quad \|\varphi_0\|_{H^2(D)} \leq C. \quad (3.2.5)$$

We now present a regularised version of (3.1.1) and (3.1.6) together with the associated boundary and initial conditions (3.1.2), (3.1.3), (3.1.5), and (3.1.7).

Problem $\mathbb{P}_{DI\gamma}$ Find $(u_\gamma, \varphi_\gamma)$ such that

$$\varepsilon \varphi_{\gamma,t} - \beta \varepsilon \Delta \varphi_\gamma - \frac{\beta}{\varepsilon} \varphi_\gamma + \chi_\gamma^\varepsilon(\varphi_\gamma) - \frac{C_w}{\alpha} u_\gamma = 0, \quad \text{in } D \times (0, T), \quad (3.2.6)$$

$$\nabla \varphi_\gamma \cdot \boldsymbol{\nu} = 0, \quad \text{on } \partial D \times (0, T), \quad (3.2.7)$$

$$\varphi_\gamma(\mathbf{x}, 0) = \varphi_0, \quad \text{in } D, \quad (3.2.8)$$

$$\varepsilon^2 u_{\gamma,t} - \nabla \cdot (\zeta_\gamma(\varphi_\gamma) \nabla u_\gamma) + \frac{1}{\alpha \varepsilon} \delta_\gamma(\varphi_\gamma) u_\gamma = \frac{Q}{\varepsilon} \delta_\gamma(\varphi_\gamma) - \zeta_\gamma(\varphi_\gamma), \quad \text{in } D \times (0, T), \quad (3.2.9)$$

$$\nabla u_\gamma \cdot \boldsymbol{\nu} = 0, \quad \text{on } \partial D \times (0, T), \quad (3.2.10)$$

$$u_\gamma(\mathbf{x}, 0) = u_0, \quad \text{in } D. \quad (3.2.11)$$

For use later on we note that multiplying (3.2.6) by a smooth test function ρ , integrating over D , using integration by parts, and noting (3.2.7) yields

$$\varepsilon \int_D \varphi_{\gamma,t} \rho \, d\mathbf{x} + \beta \varepsilon \int_D \nabla \varphi_\gamma \cdot \nabla \rho \, d\mathbf{x} - \frac{\beta}{\varepsilon} \int_D \varphi_\gamma \rho \, d\mathbf{x} + \int_D \chi_\gamma^\varepsilon(\varphi_\gamma) \rho \, d\mathbf{x} = \frac{C_w}{\alpha} \int_D u_\gamma \rho \, d\mathbf{x}, \quad (3.2.12)$$

and similarly multiplying (3.2.9) by a smooth test function ϕ , integrating over D , using

integration by parts, and noting (3.2.10) yields

$$\varepsilon^2 \int_D u_{\gamma,t} \phi \, d\mathbf{x} + \int_D \zeta_\gamma(\varphi_\gamma) \nabla u_\gamma \cdot \nabla \phi \, d\mathbf{x} + \frac{1}{\varepsilon} \int_D \delta_\gamma(\varphi_\gamma) \left(\frac{u_\gamma}{\alpha} - Q \right) \phi \, d\mathbf{x} = - \int_D \zeta_\gamma(\varphi_\gamma) \phi \, d\mathbf{x}. \quad (3.2.13)$$

Theorem 3.2.1 Let X , B and Y be Banach spaces with $X \hookrightarrow B \hookrightarrow Y$, the injection $X \hookrightarrow B$ being compact. Assume that the sequence $(f_k)_{k \in \mathbb{N}}$ is bounded in $L^p(0, T; X) \cap W^{s,r}(0, T; Y)$, where $s > 0$ if $r \geq p$ and where $s > 1/r - 1/p$ if $r \leq p$. Then there exists a subsequence $(f_{k_j})_{j \in \mathbb{N}}$, which converges in $L^p(0, T; B)$ and in $C(0, T; B)$ if $p = \infty$.

Proof. See Corollary 5, Section 8 in [70]. \square

Theorem 3.2.2 There exists a solution $(u_\gamma, \varphi_\gamma)$ to the system $\mathbb{P}_{DI\gamma}$.

Proof. This proof follows the proof of Theorem 2.2 in [38].

We use the Leray-Schauder theorem (see, for example, [53], Theorem 11.3). Define

$$\mathbb{X} := L^2(0, T; L^2(D)) \times L^2(0, T; L^2(D)),$$

and

$$F := \mathbb{X} \rightarrow \mathbb{X}, \quad F(\varphi, u) = (\psi, v),$$

where (ψ, v) solve an uncoupled linear version of system $\mathbb{P}_{DI\gamma}$, namely

$$\varepsilon \psi_t - \beta \varepsilon \Delta \psi - \frac{\beta}{\varepsilon} \psi = \frac{C_w}{\alpha} u - \chi_\gamma^\varepsilon(\varphi), \quad \text{in } D \times (0, T), \quad (3.2.14)$$

$$\varepsilon^2 v_t - \nabla \cdot (\zeta_\gamma(\varphi) \nabla v) + \frac{1}{\alpha} v \delta_\gamma(\varphi) = -\zeta_\gamma(\varphi) + Q \delta_\gamma(\varphi), \quad \text{in } D \times (0, T), \quad (3.2.15)$$

with boundary conditions

$$\nabla v \cdot \boldsymbol{\nu} = \nabla \psi \cdot \boldsymbol{\nu} = 0, \quad \text{on } \partial D \times (0, T), \quad (3.2.16)$$

and initial conditions

$$v(\mathbf{x}, 0) = u_0, \quad \text{and} \quad \psi(\mathbf{x}, 0) = \varphi_0, \quad \text{in } D. \quad (3.2.17)$$

Note that if $\psi = \varphi$ and $v = u$ (i.e. F has a fixed point), then we recover the system $\mathbb{P}_{DI\gamma}$.

We want to show that F is a compact mapping. By standard parabolic theory (and the properties of δ_γ , ζ_γ , and χ_γ^ε), we infer that F is well defined and compact. The compactness follows from Theorem 3.2.1, with $p = r = 2$, $s = 1$, $X = H^1(D)$, $Y = (H^1(D))'$ and $B = L^2(D)$, since, for every sequence (φ_n, u_n) that is bounded in \mathbb{X} , the corresponding solutions $(\psi_n, v_n) = F(\varphi_n, u_n)$ are bounded in $L^2(0, T; H^1(D))$, with $(\psi_{n,t}, v_{n,t})$ bounded in $L^2(0, T; (H^1(D))')$. This means that the image (under F) of a bounded sequence has a convergent subsequence, and thus F is compact. The notation $(H^1(D))'$ denotes the dual space of $H^1(D)$. Finally, we want to show that there exists a constant C such that

$$\|(\varphi, u)\|_{\mathbb{X}}^2 := \int_0^T \left(\|\varphi\|_{L^2(D)}^2 + \|u\|_{L^2(D)}^2 \right) dt \leq C,$$

holds on the set $\{(\varphi, u) \in \mathbb{X} \mid (\varphi, u) = \sigma F(\varphi, u) \text{ for some } \sigma \in [0, 1]\}$.

If we take (3.2.15), multiply it by v , and integrate over D , we achieve

$$\frac{\varepsilon^2}{2} \frac{d}{dt} \|v\|_{L^2(D)}^2 \leq \left| \int_D \zeta_\gamma(\varphi) v \, d\mathbf{x} \right| + Q \left| \int_D \delta_\gamma(\varphi) v \, d\mathbf{x} \right| \leq C + C \|v\|_{L^2(D)}^2,$$

where we used Young's inequality. Following this with Gronwall's inequality we have, since $\sigma \leq 1$ and $u = \sigma v$,

$$\sup_{t \in [0, T]} \|u\|_{L^2(D)}^2 \leq \sup_{t \in [0, T]} \|v\|_{L^2(D)}^2 \leq C(\gamma, \varepsilon, D, T).$$

Similarly for (3.2.14), we multiply by ψ and integrate over D to obtain

$$\frac{\varepsilon}{2} \frac{d}{dt} \|\psi\|_{L^2(D)}^2 \leq \frac{\beta}{\varepsilon} \|\psi\|_{L^2(D)}^2 + \frac{C_w}{\alpha} \left| \int_D u \psi \, d\mathbf{x} \right| + \left| \int_D \chi_\gamma^\varepsilon(\varphi) \psi \, d\mathbf{x} \right|.$$

Since $(u, \varphi) \in \mathbb{X}$ (and $\chi_\gamma^\varepsilon(\varphi) \leq C + C|\varphi|$), we have $\chi_\gamma^\varepsilon(\varphi) \in L^2(0, T; L^2(D))$. Using Young's inequality followed by Gronwall's inequality we conclude that

$$\sup_{t \in [0, T]} \|\varphi\|_{L^2(D)}^2 \leq \sup_{t \in [0, T]} \|\psi\|_{L^2(D)}^2 \leq C(\gamma, \varepsilon, D, T).$$

We infer from this that, by the Leray-Schauder theorem, F has a fixed point $(\varphi, u) \in \mathbb{X}$, which is a weak solution to system $\mathbb{P}_{DI\gamma}$.

□

The following lemma, Lemma 3.2.3, along with Lemmas 3.2.4 and 3.2.5, will be used to show uniqueness of the solution $(u_\gamma, \varphi_\gamma)$ (see Theorem 3.2.6). Lemmas 3.2.3 and 3.2.4 will then also be used in Lemma 3.2.7 in order to establish a number of stability bounds. These, along with Theorem 3.2.1, give us the convergence results (3.2.36) - (3.2.44), from which it follows that a subsequence of $(u_\gamma, \varphi_\gamma)$ converges to (u, φ) as $\gamma \rightarrow 0$.

Lemma 3.2.3 We have

$$- \|u_0\|_{L^\infty(D)} - \frac{C^*t}{\varepsilon^2} \leq u_\gamma \leq \max(\alpha Q, \|u_0\|_{L^\infty(D)}), \quad \forall t \in (0, T). \quad (3.2.18)$$

Proof. This proof uses the techniques used in the proof of Lemma 2.3 in [38].

We show the upper bound first. Setting $\phi = u_\gamma^+ := \max(0, u_\gamma - k)$ in (3.2.13), where $k := \max(\alpha Q, \|u_0\|_{L^\infty(D)})$, yields

$$\begin{aligned} \frac{\varepsilon^2}{2} \frac{d}{dt} \|u_\gamma^+\|_{L^2(D)}^2 + \|[\zeta_\gamma(\varphi_\gamma)]^{\frac{1}{2}} \nabla u_\gamma^+\|_{L^2(D)}^2 + \frac{1}{\alpha\varepsilon} \|[\delta_\gamma(\varphi_\gamma)]^{\frac{1}{2}} u_\gamma^+\|_{L^2(D)}^2 \\ = \frac{1}{\varepsilon} \left(Q - \frac{k}{\alpha} \right) \int_D u_\gamma^+ \delta_\gamma(\varphi_\gamma) \, d\mathbf{x} - \int_D u_\gamma^+ \zeta_\gamma(\varphi_\gamma) \, d\mathbf{x} \leq 0. \end{aligned}$$

Integrating over $(0, t)$ yields

$$\frac{\varepsilon^2}{2} \|u_\gamma^+\|_{L^2(D)}^2 \leq \frac{\varepsilon}{2} \|u^+(\mathbf{x}, 0)\|_{L^2(D)}^2 = 0,$$

and thus $u_\gamma \leq k = \max(\alpha Q, \|u_0\|_{L^\infty(D)})$.

We now show the lower bound. Setting $\phi = u_\gamma^- := \min(0, u_\gamma + \frac{C^*}{\varepsilon^2}t + \|u_0\|_{L^\infty(D)})$ in (3.2.13) gives

$$\begin{aligned} \varepsilon^2 \int_D u_{\gamma,t} u_\gamma^- \, d\mathbf{x} + \|[\zeta_\gamma(\varphi_\gamma)]^{\frac{1}{2}} \nabla u_\gamma^-\|_{L^2(D)}^2 + \frac{1}{\alpha\varepsilon} \|[\delta_\gamma(\varphi_\gamma)]^{\frac{1}{2}} u_\gamma^-\|_{L^2(D)}^2 \\ \leq \frac{1}{\varepsilon} \left(\frac{C^*}{\varepsilon^2\alpha}t + \frac{1}{\alpha} \|u_0\|_{L^\infty(D)} + Q \right) \int_D u_\gamma^- \delta_\gamma(\varphi_\gamma) \, d\mathbf{x} - \int_D \zeta_\gamma(\varphi_\gamma) u_\gamma^- \, d\mathbf{x}, \end{aligned}$$

and thus, using (3.2.1),

$$\begin{aligned} \varepsilon^2 \int_D u_{\gamma,t} u_\gamma^- \, d\mathbf{x} &\leq \frac{1}{\varepsilon} \left(\frac{C^*}{\varepsilon^2\alpha}t + \frac{1}{\alpha} \|u_0\|_{L^\infty(D)} + Q \right) \int_D u_\gamma^- \delta_\gamma(\varphi_\gamma) \, d\mathbf{x} - \int_D \zeta_\gamma(\varphi_\gamma) u_\gamma^- \, d\mathbf{x} \\ &\leq \frac{\gamma}{\varepsilon} \left(\frac{C^*}{\varepsilon^2\alpha}t + \frac{1}{\alpha} \|u_0\|_{L^\infty(D)} + Q \right) \int_D u_\gamma^- \, d\mathbf{x} - C^* \int_D u_\gamma^- \, d\mathbf{x}, \end{aligned}$$

which we re-arrange to give

$$\begin{aligned} \frac{\varepsilon^2}{2} \frac{d}{dt} \int_D (u_\gamma^-)^2 d\mathbf{x} &= \int_D (\varepsilon^2 u_{\gamma,t} u_\gamma^- + C^* u_\gamma^-) d\mathbf{x} \\ &\leq \frac{\gamma}{\varepsilon} \left(\frac{C^*}{\varepsilon^2 \alpha} t + \frac{1}{\alpha} \|u_0\|_{L^\infty(D)} + Q \right) \int_D u_\gamma^- d\mathbf{x} \leq 0. \end{aligned}$$

Integrating over $(0, t)$ yields

$$\frac{\varepsilon^2}{2} \|u_\gamma^-\|_{L^2(D)}^2 \leq \frac{\varepsilon^2}{2} \|u_0^-\|_{L^2(D)}^2 = 0,$$

and thus $u_\gamma \geq -\|u_0\|_{L^\infty(D)} - \frac{C^* t}{\varepsilon^2}$.

□

Lemma 3.2.4 We have

$$|\varphi_\gamma| \leq 1 + \gamma, \quad (3.2.19)$$

and

$$\int_0^T \left(\|\varphi_\gamma\|_{W^{2,p}(D)}^p + \|\varphi_{\gamma,t}\|_{L^p(D)}^p \right) dt \leq C, \quad \text{for } 1 \leq p < \infty. \quad (3.2.20)$$

Proof. This proof follows the proof of Lemma 2.4 in [38].

We first show that $\varphi_\gamma \leq 1 + \gamma$. Setting $\rho = \varphi_\gamma^+ := \max(0, \varphi_\gamma - 1 - \gamma)$ in (3.2.12) and noting (3.2.4) and (3.2.18), we obtain

$$\begin{aligned} \frac{\varepsilon}{2} \frac{d}{dt} \|\varphi_\gamma^+\|_{L^2(D)}^2 + \beta \varepsilon \|\nabla \varphi_\gamma^+\|_{L^2(D)}^2 + \int_D \chi_\gamma^\varepsilon(\varphi_\gamma) \varphi_\gamma^+ d\mathbf{x} \\ = \frac{\beta}{\varepsilon} \int_D \varphi_\gamma \varphi_\gamma^+ d\mathbf{x} + \frac{C_w}{\alpha} \int_D u_\gamma \varphi_\gamma^+ d\mathbf{x} \\ \leq \int_D \left(\frac{\beta}{\varepsilon} \varphi_\gamma + \frac{C_w}{\alpha} \max(\alpha Q, \|u_0\|_{L^\infty(D)}) \right) \varphi_\gamma^+ d\mathbf{x} \\ = \int_D \chi_\gamma^\varepsilon(\varphi_\gamma) \varphi_\gamma^+ d\mathbf{x}. \end{aligned}$$

Where in the final step we use the fact that if $\varphi_\gamma < 1 + \gamma$ then $\varphi_\gamma^+ = 0$.

We now integrate over time. Recalling the initial condition (3.2.8), in which $|\varphi_0| \leq 1$, we have

$$\|\varphi_\gamma^+\|_{L^2(D)}^2 = 0, \quad \text{for } t \geq 0,$$

and hence $\varphi_\gamma \leq 1 + \gamma$. Now setting $\rho = \varphi_\gamma^- := \min(0, \varphi_\gamma + 1 + \gamma)$ in (3.2.12), we argue

similarly to show that $\varphi_\gamma \geq -1 - \gamma$, and thus $|\varphi_\gamma| < 1 + \gamma$.

In order to prove the second result, we define

$$F_\gamma := \varepsilon \varphi_{\gamma,t} - \beta \varepsilon \Delta \varphi_\gamma = \frac{\beta}{\varepsilon} \varphi_\gamma - \chi_\gamma^\varepsilon(\varphi_\gamma) + \frac{C_w}{\alpha} u_\gamma. \quad (3.2.21)$$

Since $|\varphi_\gamma| \leq 1 + \gamma$, $\gamma \leq \varepsilon \leq 1$, recalling (3.2.4), we have $|\chi_\gamma^\varepsilon(\varphi_\gamma)| \leq C$ for $t \in [0, T]$. Using this together with (3.2.18) and (3.2.19) we conclude that

$$|F_\gamma| \leq C, \quad \text{in } D \times (0, T). \quad (3.2.22)$$

Recalling (3.2.5), by parabolic L^p -theory (the result is proved for Dirichlet boundary conditions in Theorem 9.1 of [63], where a remark is made at the end of Chapter 4, Section 9, stating that an analogous result holds for Neumann boundary conditions) we have the result;

$$\int_0^T \left(\|\varphi_\gamma\|_{W^{2,p}(D)}^p + \|\varphi_{\gamma,t}\|_{L^p(D)}^p \right) dt \leq C(\varepsilon, p, \|\varphi_0\|_{H^2(D)}), \quad \text{for } 1 \leq p < \infty.$$

□

Remark We require the result with $p > 2$ at the end of Lemma 3.2.7, see (3.2.35), in order to bound $\|\nabla \varphi_\gamma\|_{L^\infty(D)}$.

Lemma 3.2.5 We have

$$u_\gamma \in L^2(0, T; W^{1,\infty}(D)). \quad (3.2.23)$$

Proof. This proof follows the result that is outlined at the end of the proof of Theorem 2.2 in [38]. From the proof of Theorem 3.2.2 we have that $\varphi_\gamma, u_\gamma \in L^2(0, T; H^1(D))$, this combined with (3.2.18) yields that $C_w u_\gamma / \alpha - \chi_\gamma^\varepsilon(\varphi_\gamma) \in L^2(0, T; H^1(D))$, and from parabolic theory (see Theorem 9.1 in [63]), we conclude $\varphi_{\gamma,t} \in L^2(0, T; H^1(D))$ and $\varphi_\gamma \in L^\infty(0, T; H^2(D)) \cap L^2(0, T; H^3(D))$. Finally noting (3.2.20), and using parabolic theory, we have $u_\gamma \in L^2(0, T; H^3(D))$ and the desired result follows since $H^3(D) \hookrightarrow W^{1,\infty}(D)$. □

We note that, as mentioned in the proof of Lemma 3.2.4, the parabolic theory result is proved for Dirichlet boundary conditions in Theorem 9.1 of [63] where a remark is made

at the end of Chapter 4, Section 9, stating that an analogous result holds for Neumann boundary conditions.

Theorem 3.2.6 The solution $(u_\gamma, \varphi_\gamma)$ to system $\mathbb{P}_{DI\gamma}$ is unique.

Proof. We let the pairs $(u_{\gamma,1}, \varphi_{\gamma,1})$ and $(u_{\gamma,2}, \varphi_{\gamma,2})$ be solutions to system $\mathbb{P}_{DI\gamma}$. Let $v := u_{\gamma,1} - u_{\gamma,2}$ and $\psi := \varphi_{\gamma,1} - \varphi_{\gamma,2}$. We aim to show that $v = \psi = 0$, for all $t \in [0, T)$. We set $u_\gamma = u_{\gamma,1}$, $\varphi_\gamma = \varphi_{\gamma,1}$, and $\rho = \psi$ in (3.2.12) and then $u_\gamma = u_{\gamma,2}$, $\varphi_\gamma = \varphi_{\gamma,2}$, and $\rho = \psi$ in (3.2.12), we then subtract the resulting equations. Similarly we set $u_\gamma = u_{\gamma,1}$, $\varphi_\gamma = \varphi_{\gamma,1}$, and $\phi = v$ in (3.2.13) and then $u_\gamma = u_{\gamma,2}$, $\varphi_\gamma = \varphi_{\gamma,2}$, and $\phi = v$ in (3.2.13), we then subtract the resulting equations.

Adding these two resulting equations, we arrive at

$$\begin{aligned} \frac{\varepsilon}{2} \frac{d}{dt} \left(\|\psi\|_{L^2(D)}^2 + \varepsilon \|v\|_{L^2(D)}^2 \right) &+ \beta \varepsilon \|\nabla \psi\|_{L^2(D)}^2 + \|\zeta_\gamma(\varphi_{\gamma,1})\|_{L^2(D)}^{\frac{1}{2}} \|\nabla v\|_{L^2(D)}^2 \\ &+ \frac{1}{\alpha \varepsilon} \|\delta_\gamma(\varphi_{\gamma,1})\|_{L^2(D)}^{\frac{1}{2}} \|v\|_{L^2(D)}^2 + \int_D (\chi_\gamma^\varepsilon(\varphi_{\gamma,1}) - \chi_\gamma^\varepsilon(\varphi_{\gamma,2})) \psi \, d\mathbf{x} \\ &= \frac{\beta}{\varepsilon} \|\psi\|_{L^2(D)}^2 + \left(\frac{C_w}{\alpha} - \frac{1}{2} \right) \int_D \psi v \, d\mathbf{x} - \frac{1}{2} \int_D \psi \nabla u_{\gamma,2} \cdot \nabla v \, d\mathbf{x} \\ &\quad - \frac{2Q}{\varepsilon \pi} \int_D \psi v (\varphi_{\gamma,1} + \varphi_{\gamma,2}) \, d\mathbf{x} + \frac{2}{\varepsilon \pi \alpha} \int_D \psi v u_{\gamma,2} (\varphi_{\gamma,1} + \varphi_{\gamma,2}) \, d\mathbf{x}. \end{aligned}$$

We note that (3.2.1) gives $\zeta_\gamma \geq \frac{\gamma}{2}$, and that the monotonicity of χ_γ^ε gives $(\chi_\gamma^\varepsilon(\varphi_{\gamma,1}) - \chi_\gamma^\varepsilon(\varphi_{\gamma,2})) \psi \geq 0$. Using these facts, together with Young's inequality, Hölder's inequality and Lemmas 3.2.3 and 3.2.4, we arrive at

$$\begin{aligned} \frac{\varepsilon}{2} \frac{d}{dt} \left(\|\psi\|_{L^2(D)}^2 + \varepsilon \|v\|_{L^2(D)}^2 \right) &+ \beta \varepsilon \|\nabla \psi\|_{L^2(D)}^2 + \frac{\gamma}{2} \|\nabla v\|_{L^2(D)}^2 + \frac{1}{\alpha \varepsilon} \|\delta_\gamma(\varphi_{\gamma,1})\|_{L^2(D)}^{\frac{1}{2}} \|v\|_{L^2(D)}^2 \\ &\leq C \|\psi\|_{L^2(D)}^2 + C \|v\|_{L^2(D)}^2 + \frac{1}{2} \|\nabla u_{\gamma,2}\|_{L^\infty(D)} \|\psi\|_{L^2(D)} \|\nabla v\|_{L^2(D)} \\ &\leq C \left(1 + \frac{1}{\gamma} \|\nabla u_{\gamma,2}\|_{L^\infty(D)}^2 \right) \|\psi\|_{L^2(D)}^2 + C \|v\|_{L^2(D)}^2 + \frac{\gamma}{4} \|\nabla v\|_{L^2(D)}^2 \end{aligned}$$

and thus

$$\begin{aligned} \frac{\varepsilon}{2} \frac{d}{dt} \left(\|\psi\|_{L^2(D)}^2 + \varepsilon \|v\|_{L^2(D)}^2 \right) &+ \beta \varepsilon \|\nabla \psi\|_{L^2(D)}^2 + \frac{\gamma}{4} \|\nabla v\|_{L^2(D)}^2 + \frac{1}{\alpha \varepsilon} \|\delta_\gamma(\varphi_{\gamma,1})\|_{L^2(D)}^{\frac{1}{2}} \|v\|_{L^2(D)}^2 \\ &\leq C \left(1 + \frac{1}{\gamma} \|\nabla u_{\gamma,2}\|_{L^\infty(D)}^2 \right) \|\psi\|_{L^2(D)}^2 + C \|v\|_{L^2(D)}^2. \end{aligned}$$

We now use Gronwall's inequality together with (3.2.23) and the fact that $\psi(\mathbf{x}, 0) = 0$ and

$v(\mathbf{x}, 0) = 0$, to conclude that $\psi = v = 0$, for all $t \in [0, T]$.

□

The following lemma gives the bounds required to show the convergence, as $\gamma \rightarrow 0$, of a subsequence of $(u_\gamma, \varphi_\gamma)$ to functions (u, φ) that we show satisfy \mathbb{P}_{DI} .

Lemma 3.2.7 We have

$$\begin{aligned} \sup_{t \in [0, T]} \|\nabla u_\gamma\|_{L^2(D)}^2 + \sup_{t \in [0, T]} \|\zeta_\gamma(\varphi_\gamma)^{\frac{1}{2}} \nabla u_\gamma\|_{L^2(D)}^2 + \sup_{t \in [0, T]} \|\varphi_{\gamma, t}\|_{L^2(D)}^2 \\ + \int_0^T \left(\|u_{\gamma, t}\|_{L^2(D)}^2 + \|\zeta_\gamma(\varphi_\gamma)^{\frac{1}{2}} D^2 u_\gamma\|_{L^2(D)}^2 \right. \\ \left. + \frac{1}{\varepsilon} \|\delta_\gamma(\varphi_\gamma)^{\frac{1}{2}} \nabla u_\gamma\|_{L^2(D)}^2 + \|\nabla \varphi_{\gamma, t}\|_{L^2(D)}^2 \right) dt \leq C, \end{aligned}$$

uniformly in γ .

Proof. This proof follows the proof of Lemma 2.5 in [38].

Noting that

$$\frac{\varepsilon^2}{2} \frac{d}{dt} \|\nabla u_\gamma\|_{L^2(D)}^2 = \varepsilon^2 \int_D \nabla u_\gamma \cdot \nabla u_{\gamma, t} \, d\mathbf{x},$$

and using (3.2.9) and (3.2.10), we have

$$\begin{aligned} \frac{\varepsilon^2}{2} \frac{d}{dt} \|\nabla u_\gamma\|_{L^2(D)}^2 = \underbrace{\int_D \nabla u_\gamma \cdot \nabla (\nabla \cdot (\zeta_\gamma(\varphi_\gamma) \nabla u_\gamma)) \, d\mathbf{x}}_{(1)} - \underbrace{\frac{1}{\alpha \varepsilon} \int_D \nabla u_\gamma \cdot \nabla (\delta_\gamma(\varphi_\gamma) u_\gamma) \, d\mathbf{x}}_{(2)} \\ + \underbrace{\int_D \Delta u_\gamma \zeta_\gamma(\varphi_\gamma) \, d\mathbf{x}}_{(3)} + \underbrace{\frac{Q}{\varepsilon} \int_D \nabla u_\gamma \cdot \nabla \delta_\gamma(\varphi_\gamma) \, d\mathbf{x}}_{(4)}. \end{aligned}$$

We consider the terms (1) - (4) individually, starting by splitting term (1) into two terms

$$(1) = - \underbrace{\sum_{i, k=1}^2 \int_D u_{\gamma, x_k, x_i} (\zeta_\gamma(\varphi_\gamma) u_{\gamma, x_k})_{x_i} \, d\mathbf{x}}_{(1_1)} + \underbrace{\sum_{i, k=1}^2 \int_{\partial D} u_{\gamma, x_i} (\zeta_\gamma(\varphi_\gamma) u_{\gamma, x_k})_{x_i} \boldsymbol{\nu}_k \, d\mathbf{x}}_{(1_2)}.$$

The subscripts of x_i or x_k denote differentiation with respect to the i^{th} or k^{th} coordinate.

Bounding (1₁) first, we recall the definition of F_γ , (3.2.21), and the bound on it given in

(3.2.22). Using this, we compute

$$\begin{aligned}
(1_1) &= - \int_D \zeta_\gamma(\varphi_\gamma) |D^2 u_\gamma|^2 \, d\mathbf{x} - \frac{1}{2} \sum_{i,k=1}^2 \int_D u_{\gamma,x_k,x_i} \varphi_{\gamma,x_i} u_{x_k} \, d\mathbf{x} \\
&= - \| [\zeta_\gamma(\varphi_\gamma)]^{\frac{1}{2}} D^2 u_\gamma \|_{L^2(D)}^2 - \frac{1}{4} \sum_{i=1}^2 \int_D \varphi_{\gamma,x_i} (|\nabla u_\gamma|^2)_{x_i} \, d\mathbf{x} \\
&= - \| [\zeta_\gamma(\varphi_\gamma)]^{\frac{1}{2}} D^2 u_\gamma \|_{L^2(D)}^2 + \frac{1}{4} \int_D \Delta \varphi_\gamma |\nabla u_\gamma|^2 \, d\mathbf{x} \\
&= - \| [\zeta_\gamma(\varphi_\gamma)]^{\frac{1}{2}} D^2 u_\gamma \|_{L^2(D)}^2 + \frac{1}{4\beta} \int_D \varphi_{\gamma,t} |\nabla u_\gamma|^2 \, d\mathbf{x} - \frac{1}{4\epsilon\beta} \int_D F_\gamma |\nabla u_\gamma|^2 \, d\mathbf{x} \\
&\leq - \| [\zeta_\gamma(\varphi_\gamma)]^{\frac{1}{2}} D^2 u_\gamma \|_{L^2(D)}^2 + \frac{1}{4\beta} \int_D \varphi_{\gamma,t} |\nabla u_\gamma|^2 \, d\mathbf{x} + C \| \nabla u_\gamma \|_{L^2(D)}^2.
\end{aligned}$$

Now considering (1₂), in order to investigate the boundary integral, we will choose a counter-clockwise arc-length parametrisation of ∂D , denoted by $\boldsymbol{\sigma} : [0, L] \rightarrow \partial D$. This is such that $\boldsymbol{\sigma}(0) = \boldsymbol{\sigma}(L)$. For $s \in [0, L]$, we let

$$\boldsymbol{\tau}(s) := \boldsymbol{\sigma}'(s), \quad \text{and} \quad \boldsymbol{\nu}(s) := (\boldsymbol{\tau}_2(s), -\boldsymbol{\tau}_1(s))$$

be a unit tangent and the outward unit normal to ∂D at the point $\boldsymbol{\sigma}(s)$. Recall the Frenet formulae

$$\frac{d}{ds} \boldsymbol{\tau}(s) = \kappa(s) \boldsymbol{\nu}(s), \quad \text{and} \quad \frac{d}{ds} \boldsymbol{\nu}(s) = -\kappa(s) \boldsymbol{\tau}(s), \quad (3.2.24)$$

where $\kappa(s)$ is the curvature of ∂D at $\boldsymbol{\sigma}(s)$ with respect to $\boldsymbol{\nu}$. Since D is convex, we have $\kappa \leq 0$. We also introduce the short hand

$$f_\tau := \nabla f \cdot \boldsymbol{\tau}, \quad \text{and} \quad f_\nu := \nabla f \cdot \boldsymbol{\nu}.$$

Differentiating (3.2.10) in the $\boldsymbol{\tau}$ direction and noting (3.2.24) gives

$$\sum_{i,k=1}^2 u_{\gamma,x_i,x_k} \boldsymbol{\nu}_k \boldsymbol{\tau}_i = \kappa u_{\gamma,\tau}. \quad (3.2.25)$$

Using this, and noting both $\sum_{k=1}^2 u_{\gamma,x_k} \boldsymbol{\nu}_k = u_{\gamma,\nu} = 0$ and $\nabla u_\gamma = u_{\gamma,\nu} \boldsymbol{\nu} + u_{\gamma,\tau} \boldsymbol{\tau} = u_{\gamma,\tau} \boldsymbol{\tau}$, we

have

$$\begin{aligned}
(1_2) &= \frac{1}{2} \sum_{i,k=1}^2 \int_{\partial D} u_{\gamma,x_i} \varphi_{\gamma,x_i} u_{\gamma,x_k} \boldsymbol{\nu}_k \, d\mathbf{x} + \sum_{i,k=1}^2 \int_{\partial D} u_{\gamma,x_i} \zeta_{\gamma}(\varphi_{\gamma}) u_{\gamma,x_i,x_k} \boldsymbol{\nu}_k \, d\mathbf{x} \\
&= \sum_{i,k=1}^2 \int_{\partial D} \zeta_{\gamma}(\varphi_{\gamma}) u_{\gamma,\tau} u_{\gamma,x_i,x_k} \boldsymbol{\nu}_k \boldsymbol{\tau}_i \, d\mathbf{x} = \int_{\partial D} \zeta_{\gamma}(\varphi_{\gamma}) (u_{\gamma,\tau})^2 \kappa \, d\mathbf{x} \leq 0.
\end{aligned}$$

Combining the bounds for (1₁) and (1₂), we have

$$(1) \leq -\|[\zeta_{\gamma}(\varphi_{\gamma})]^{\frac{1}{2}} D^2 u_{\gamma}\|_{L^2(D)}^2 + \frac{1}{4\beta} \int_D \varphi_{\gamma,t} |\nabla u_{\gamma}|^2 \, d\mathbf{x} + C \|\nabla u_{\gamma}\|_{L^2(D)}^2.$$

For term (2) we use the bound on the L^{∞} norms of u_{γ} and φ_{γ} , along with Young's inequality, to compute

$$\begin{aligned}
(2) &= -\frac{1}{\alpha\varepsilon} \|\delta_{\gamma}(\varphi_{\gamma})\|^{\frac{1}{2}} \|\nabla u_{\gamma}\|_{L^2(D)}^2 - \frac{1}{\alpha\varepsilon} \int_D \nabla \delta_{\gamma}(\varphi_{\gamma}) \cdot \nabla u_{\gamma} u_{\gamma} \, d\mathbf{x} \\
&= -\frac{1}{\alpha\varepsilon} \|\delta_{\gamma}(\varphi_{\gamma})\|^{\frac{1}{2}} \|\nabla u_{\gamma}\|_{L^2(D)}^2 + \frac{4}{\varepsilon\pi\alpha} \int_D \varphi_{\gamma} u_{\gamma} \nabla \varphi_{\gamma} \cdot \nabla u_{\gamma} \, d\mathbf{x} \\
&\leq C - \frac{1}{\alpha\varepsilon} \|\delta_{\gamma}(\varphi_{\gamma})\|^{\frac{1}{2}} \|\nabla u_{\gamma}\|_{L^2(D)}^2 + C \|\nabla u_{\gamma}\|_{L^2(D)}^2 + C \|\nabla \varphi_{\gamma}\|_{L^2(D)}^2.
\end{aligned}$$

Upon noting that we have $\zeta_{\gamma} \leq C$, we bound term (3) by an application of Young's inequality,

$$(3) \leq C + \frac{1}{2} \|[\zeta_{\gamma}(\varphi_{\gamma})]^{\frac{1}{2}} D^2 u_{\gamma}\|_{L^2(D)}^2.$$

Similarly, for term (4), we have

$$(4) \leq \frac{Q}{2} \|\nabla u_{\gamma}\|_{L^2(D)}^2 + \frac{Q}{2\varepsilon^2} \|\nabla \delta_{\gamma}(\varphi_{\gamma})\|_{L^2(D)}^2 \leq C \|\nabla u_{\gamma}\|_{L^2(D)}^2 + C \|\nabla \varphi_{\gamma}\|_{L^2(D)}^2.$$

Combining the above bounds for (1) - (4) yields

$$\begin{aligned}
\frac{\varepsilon^2}{2} \frac{d}{dt} \|\nabla u_{\gamma}\|_{L^2(D)}^2 + \frac{1}{2} \|[\zeta_{\gamma}(\varphi_{\gamma})]^{\frac{1}{2}} D^2 u_{\gamma}\|_{L^2(D)}^2 + \frac{1}{\alpha\varepsilon} \|\delta_{\gamma}(\varphi_{\gamma})\|^{\frac{1}{2}} \|\nabla u_{\gamma}\|_{L^2(D)}^2 & \quad (3.2.26) \\
\leq C + C \|\nabla u_{\gamma}\|_{L^2(D)}^2 + C \|\nabla \varphi_{\gamma}\|_{L^2(D)}^2 + \frac{1}{4\beta} \int_D \varphi_{\gamma,t} |\nabla u_{\gamma}|^2 \, d\mathbf{x}.
\end{aligned}$$

Setting $\phi = u_{\gamma,t}$ in (3.2.13) gives

$$\begin{aligned} \varepsilon^2 \|u_{\gamma,t}\|_{L^2(D)}^2 + \int_D \zeta_\gamma(\varphi_\gamma) \nabla u_\gamma \cdot \nabla u_{\gamma,t} \, d\mathbf{x} + \frac{1}{\alpha\varepsilon} \int_D \delta_\gamma(\varphi_\gamma) u_\gamma u_{\gamma,t} \, d\mathbf{x} \\ = \frac{Q}{\varepsilon} \int_D \delta_\gamma(\varphi_\gamma) u_{\gamma,t} \, d\mathbf{x} - \int_D \zeta_\gamma(\varphi_\gamma) u_{\gamma,t} \, d\mathbf{x}. \end{aligned}$$

Once again using that $\|u_\gamma\|_{L^\infty(D)} \leq C$, $\|\delta_\gamma(\varphi_\gamma)\|_{L^\infty(D)} \leq C$, and $\|\zeta_\gamma(\varphi_\gamma)\|_{L^\infty(D)} \leq C$, Young's inequality gives us

$$\varepsilon^2 \|u_{\gamma,t}\|_{L^2(D)}^2 \leq C + \frac{\varepsilon^2}{2} \|u_{\gamma,t}\|_{L^2(D)}^2 - \frac{1}{2} \int_D \zeta_\gamma(\varphi_\gamma) \frac{d}{dt} |\nabla u_\gamma|^2 \, d\mathbf{x}.$$

so that

$$\frac{\varepsilon^2}{2} \|u_{\gamma,t}\|_{L^2(D)}^2 \leq C + \frac{1}{4} \int_D \varphi_{\gamma,t} |\nabla u_\gamma|^2 \, d\mathbf{x} - \frac{1}{2} \frac{d}{dt} \int_D \zeta_\gamma(\varphi_\gamma) |\nabla u_\gamma|^2 \, d\mathbf{x},$$

and thus

$$\frac{\varepsilon^2}{2} \|u_{\gamma,t}\|_{L^2(D)}^2 + \frac{1}{2} \frac{d}{dt} \|\zeta_\gamma(\varphi_\gamma)\|_{L^2(D)}^2 \|\nabla u_\gamma\|_{L^2(D)}^2 \leq C + \frac{1}{4} \int_D \varphi_{\gamma,t} |\nabla u_\gamma|^2 \, d\mathbf{x}.$$

Combining this with (3.2.26) yields

$$\begin{aligned} \frac{\varepsilon^2}{2} \|u_{\gamma,t}\|_{L^2(D)}^2 + \frac{1}{2} \frac{d}{dt} \|\zeta_\gamma(\varphi_\gamma)\|_{L^2(D)}^2 \|\nabla u_\gamma\|_{L^2(D)}^2 + \frac{\varepsilon^2}{2} \frac{d}{dt} \|\nabla u_\gamma\|_{L^2(D)}^2 + \frac{1}{2} \|\zeta_\gamma(\varphi_\gamma)\|_{L^2(D)}^2 \|D^2 u_\gamma\|_{L^2(D)}^2 \\ + \frac{1}{\alpha\varepsilon} \|\delta_\gamma(\varphi_\gamma)\|_{L^2(D)}^2 \|\nabla u_\gamma\|_{L^2(D)}^2 \\ \leq C + C \|\nabla u_\gamma\|_{L^2(D)}^2 + C \|\nabla \varphi_\gamma\|_{L^2(D)}^2 + \left(\frac{1}{4\beta} + \frac{1}{4}\right) \int_D \varphi_{\gamma,t} |\nabla u_\gamma|^2 \, d\mathbf{x}. \end{aligned} \tag{3.2.27}$$

We now differentiate (3.2.6) with respect to t , multiply by $\varphi_{\gamma,t}$, and integrate over D to obtain

$$\begin{aligned} \frac{\varepsilon}{2} \frac{d}{dt} \|\varphi_{\gamma,t}\|_{L^2(D)}^2 + \beta\varepsilon \|\nabla \varphi_{\gamma,t}\|_{L^2(D)}^2 + \int_D (\chi_\gamma^\varepsilon)'(\varphi_\gamma) |\varphi_{\gamma,t}|^2 \, d\mathbf{x} \\ \leq C \|\varphi_{\gamma,t}\|_{L^2(D)}^2 + \frac{C_w}{\alpha} \int_D |u_{\gamma,t} \varphi_{\gamma,t}| \, d\mathbf{x}. \end{aligned}$$

The fact that $(\chi_\gamma^\varepsilon)'(\varphi_\gamma) \geq 0$, along with Young's inequality, gives

$$\frac{\varepsilon}{2} \frac{d}{dt} \|\varphi_{\gamma,t}\|_{L^2(D)}^2 + \beta\varepsilon \|\nabla\varphi_{\gamma,t}\|_{L^2(D)}^2 \leq C\|\varphi_{\gamma,t}\|_{L^2(D)}^2 + \frac{\varepsilon^2}{4} \|u_{\gamma,t}\|_{L^2(D)}^2.$$

We add the above equation to (3.2.27),

$$\begin{aligned} \frac{\varepsilon}{2} \frac{d}{dt} \|\varphi_{\gamma,t}\|_{L^2(D)}^2 + \frac{1}{2} \frac{d}{dt} \|\zeta_\gamma(\varphi_\gamma)\|_{L^2(D)}^2 + \frac{\varepsilon^2}{2} \frac{d}{dt} \|\nabla u_\gamma\|_{L^2(D)}^2 + \frac{\varepsilon^2}{4} \|u_{\gamma,t}\|_{L^2(D)}^2 \\ + \frac{1}{2} \|\zeta_\gamma(\varphi_\gamma)\|_{L^2(D)}^2 + \frac{1}{\alpha\varepsilon} \|\delta_\gamma(\varphi_\gamma)\|_{L^2(D)}^2 + \beta\varepsilon \|\nabla\varphi_{\gamma,t}\|_{L^2(D)}^2 \\ \leq C + C\|\varphi_{\gamma,t}\|_{L^2(D)}^2 + C\|\nabla u_\gamma\|_{L^2(D)}^2 + C\|\nabla\varphi_\gamma\|_{L^2(D)}^2 \\ + \left(\frac{1}{4\beta} + \frac{1}{4}\right) \int_D \varphi_{\gamma,t} |\nabla u_\gamma|^2 \, d\mathbf{x}. \end{aligned} \quad (3.2.28)$$

We now derive a bound for the last term in (3.2.28). Using (3.2.9), we write

$$\begin{aligned} \frac{\varepsilon^2}{2} \frac{d}{dt} \|\varphi_\gamma |\nabla u_\gamma|\|_{L^2(D)}^2 &= \varepsilon^2 \int_D \varphi_\gamma \varphi_{\gamma,t} |\nabla u_\gamma|^2 \, d\mathbf{x} + \varepsilon^2 \int_D \varphi_\gamma^2 \nabla u_\gamma \cdot \nabla u_{\gamma,t} \, d\mathbf{x} \\ &= \varepsilon^2 \int_D \varphi_\gamma \varphi_{\gamma,t} |\nabla u_\gamma|^2 \, d\mathbf{x} - \underbrace{\frac{1}{\alpha\varepsilon} \int_D \varphi_\gamma^2 \nabla u_\gamma \cdot \nabla(\delta_\gamma(\varphi_\gamma) u_\gamma) \, d\mathbf{x}}_{(1)} \\ &\quad + \underbrace{\int_D \varphi_\gamma^2 \nabla u_\gamma \cdot \nabla(-\zeta_\gamma(\varphi_\gamma) + \frac{Q}{\varepsilon} \delta_\gamma(\varphi_\gamma)) \, d\mathbf{x}}_{(2)} \\ &\quad + \underbrace{\int_D \varphi_\gamma^2 \nabla u_\gamma \cdot \nabla(\nabla \cdot (\zeta_\gamma(\varphi_\gamma) \nabla u_\gamma)) \, d\mathbf{x}}_{(3)}. \end{aligned}$$

Bounding each of these terms individually, we start with (1), and use Young's inequality along with the bounds on the L^∞ norms of u_γ and φ_γ to yield

$$\begin{aligned} (1) &= -\frac{1}{\alpha\varepsilon} \int_D \varphi_\gamma^2 \left(\delta_\gamma(\varphi_\gamma) |\nabla u_\gamma|^2 - \frac{4}{\pi} u_\gamma \varphi_\gamma \nabla \varphi_\gamma \cdot \nabla u_\gamma \right) \, d\mathbf{x} \\ &\leq C\|\nabla u_\gamma\|_{L^2(D)}^2 + C\|\nabla\varphi_\gamma\|_{L^2(D)}^2. \end{aligned} \quad (3.2.29)$$

Term (2) is similar,

$$\begin{aligned} (2) &= \int_D \varphi_\gamma^2 \nabla u_\gamma \cdot \left(-\frac{1}{2} \nabla \varphi_\gamma - \frac{4Q}{\varepsilon\pi} \varphi_\gamma \nabla \varphi_\gamma \right) \, d\mathbf{x} \\ &\leq C\|\nabla u_\gamma\|_{L^2(D)}^2 + C\|\nabla\varphi_\gamma\|_{L^2(D)}^2. \end{aligned} \quad (3.2.30)$$

We split term (3) into three terms

$$\begin{aligned}
(3) &= - \underbrace{\sum_{i,k=1}^2 \int_D (\varphi_\gamma^2)_{x_k} u_{\gamma,x_i} (\zeta_\gamma(\varphi_\gamma) u_{\gamma,x_k})_{x_i} \, d\mathbf{x}}_{(3_1)} - \underbrace{\sum_{i,k=1}^2 \int_D \varphi_\gamma^2 u_{\gamma,x_i,x_k} (\zeta_\gamma(\varphi_\gamma) u_{\gamma,x_k})_{x_i} \, d\mathbf{x}}_{(3_2)} \\
&\quad + \underbrace{\sum_{i,k=1}^2 \int_{\partial D} \varphi_\gamma^2 u_{\gamma,x_i} (\zeta_\gamma(\varphi_\gamma) u_{\gamma,x_k})_{x_i} \boldsymbol{\nu}_k \, d\mathbf{x}}_{(3_3)}.
\end{aligned}$$

Starting with (3₁), we use Young's inequality, with $a \in \mathbb{R}$, $a > 0$, which will be determined later, to give (using the bound on the L^∞ norm of φ_γ)

$$\begin{aligned}
(3_1) &= - \sum_{i,k=1}^2 \int_D \varphi_\gamma \varphi_{\gamma,x_k} u_{\gamma,x_i} \varphi_{\gamma,x_i} u_{\gamma,x_k} \, d\mathbf{x} - 2 \sum_{i,k=1}^2 \int_D \varphi_\gamma \varphi_{\gamma,x_k} u_{\gamma,x_i} u_{\gamma,x_k,x_i} \zeta_\gamma(\varphi_\gamma) \, d\mathbf{x} \\
&\leq C \int_D |\nabla \varphi_\gamma|^2 |\nabla u_\gamma|^2 \, d\mathbf{x} + C \int_D |\nabla \varphi_\gamma| |\nabla u_\gamma| |D^2 u_\gamma| \zeta_\gamma(\varphi_\gamma) \, d\mathbf{x} \\
&\leq C \int_D |\nabla \varphi_\gamma|^2 |\nabla u_\gamma|^2 \, d\mathbf{x} + a \|\zeta_\gamma(\varphi_\gamma)\|_{L^\infty(D)}^{\frac{1}{2}} \|D^2 u_\gamma\|_{L^2(D)}^2.
\end{aligned}$$

For term (3₂), we use (3.2.21) and the bounds on the L^∞ norms of F_γ and φ_γ to obtain

$$\begin{aligned}
(3_2) &= - \int_D \varphi_\gamma^2 \zeta_\gamma(\varphi_\gamma) |D^2 u_\gamma|^2 \, d\mathbf{x} - \frac{1}{2} \sum_{i,k=1}^2 \int_D \varphi_\gamma^2 u_{\gamma,x_i,x_k} u_{\gamma,x_k} \varphi_{\gamma,x_i} \, d\mathbf{x} \\
&\leq -\frac{1}{4} \sum_{i=1}^2 \int_D \varphi_\gamma^2 (|\nabla u_\gamma|^2)_{x_i} \varphi_{\gamma,x_i} \, d\mathbf{x} \\
&\leq C \int_D |\varphi_\gamma| |\nabla \varphi_\gamma|^2 |\nabla u_\gamma|^2 \, d\mathbf{x} + \frac{1}{4} \int_D \varphi_\gamma^2 |\nabla u_\gamma|^2 \Delta \varphi_\gamma \, d\mathbf{x} \\
&\leq C \int_D |\nabla \varphi_\gamma|^2 |\nabla u_\gamma|^2 \, d\mathbf{x} + \frac{1}{4\beta} \int_D \varphi_\gamma^2 |\nabla u_\gamma|^2 \varphi_{\gamma,t} \, d\mathbf{x} - \frac{1}{4\beta\varepsilon} \int_D \varphi_\gamma^2 F_\gamma |\nabla u_\gamma|^2 \, d\mathbf{x} \\
&\leq C \int_D |\nabla \varphi_\gamma|^2 |\nabla u_\gamma|^2 \, d\mathbf{x} + C \int_D |\zeta_\gamma(\varphi_\gamma)| |\nabla u_\gamma|^2 |\varphi_{\gamma,t}| \, d\mathbf{x} + C \|\nabla u_\gamma\|_{L^2(D)}^2.
\end{aligned}$$

For term (3₃) we use the fact that $\kappa \leq 0$, (3.2.10), and (3.2.25), to estimate that

$$\begin{aligned}
(3_3) &= \frac{1}{2} \sum_{i,k=1}^2 \int_{\partial D} \varphi_\gamma^2 u_{\gamma,x_i} \varphi_{\gamma,x_i} u_{\gamma,x_k} \boldsymbol{\nu}_k \, d\mathbf{x} + \sum_{i,k=1}^2 \int_{\partial D} \varphi_\gamma^2 u_{\gamma,x_i} \zeta_\gamma(\varphi_\gamma) u_{\gamma,x_k,x_i} \boldsymbol{\nu}_k \, d\mathbf{x} \\
&= \sum_{i,k=1}^2 \int_{\partial D} \varphi_\gamma^2 \zeta_\gamma(\varphi_\gamma) u_{\gamma,x_k,x_i} u_{\gamma,\tau} \boldsymbol{\nu}_k \boldsymbol{\tau}_i \, d\mathbf{x} \\
&= \int_{\partial D} \varphi_\gamma^2 \zeta_\gamma(\varphi_\gamma) (u_{\gamma,\tau})^2 \kappa \, d\mathbf{x} \leq 0.
\end{aligned}$$

Combining the bounds (3₁) - (3₃) gives

$$(3) \leq C \int_D |\nabla \varphi_\gamma|^2 |\nabla u_\gamma|^2 \, d\mathbf{x} + a \|\zeta_\gamma(\varphi_\gamma)\|^{\frac{1}{2}} \|D^2 u_\gamma\|_{L^2(D)}^2 \\ + C \|\nabla u_\gamma\|_{L^2(D)}^2 + C \int_D |\zeta_\gamma(\varphi_\gamma)| |\nabla u_\gamma|^2 |\varphi_{\gamma,t}| \, d\mathbf{x},$$

while combining the bounds for (1) - (3) gives

$$\frac{\varepsilon^2}{2} \frac{d}{dt} \|\varphi_\gamma |\nabla u_\gamma|\|_{L^2(D)}^2 \leq C \|\nabla \varphi_\gamma\|_{L^2(D)}^2 + C \|\nabla u_\gamma\|_{L^2(D)}^2 + a \|\zeta_\gamma(\varphi_\gamma)\|^{\frac{1}{2}} \|D^2 u_\gamma\|_{L^2(D)}^2 \\ + C \int_D |\nabla \varphi_\gamma|^2 |\nabla u_\gamma|^2 \, d\mathbf{x} + C \int_D \zeta_\gamma(\varphi_\gamma) |\nabla u_\gamma|^2 |\varphi_{\gamma,t}| \, d\mathbf{x} \\ + \varepsilon^2 \int_D \varphi_\gamma \varphi_{\gamma,t} |\nabla u_\gamma|^2 \, d\mathbf{x}. \quad (3.2.31)$$

Note that if $\tilde{a} := (1 + 2\gamma)$, then

$$\varphi_\gamma = 2\zeta_\gamma(\varphi_\gamma) - \tilde{a}.$$

Substituting this into the last term of (3.2.31) yields

$$\frac{\varepsilon^2}{2} \frac{d}{dt} \|\varphi_\gamma |\nabla u_\gamma|\|_{L^2(D)}^2 \leq C \|\nabla \varphi_\gamma\|_{L^2(D)}^2 + C \|\nabla u_\gamma\|_{L^2(D)}^2 + a \|\zeta_\gamma(\varphi_\gamma)\|^{\frac{1}{2}} \|D^2 u_\gamma\|_{L^2(D)}^2 \\ + C \int_D |\nabla \varphi_\gamma|^2 |\nabla u_\gamma|^2 \, d\mathbf{x} + C \int_D \zeta_\gamma(\varphi_\gamma) |\nabla u_\gamma|^2 |\varphi_{\gamma,t}| \, d\mathbf{x} \\ - \varepsilon^2 \tilde{a} \int_D \varphi_{\gamma,t} |\nabla u_\gamma|^2 \, d\mathbf{x}. \quad (3.2.32)$$

Dividing (3.2.32) by $\tilde{\beta}$, where $\tilde{\beta} := \frac{1}{\frac{1}{4\tilde{\beta}} + \frac{1}{4}}$, and multiplying (3.2.28) by $\varepsilon^2 \tilde{a}$, we add these equations to yield

$$\frac{\varepsilon^2}{2\tilde{\beta}} \frac{d}{dt} \|\varphi_\gamma |\nabla u_\gamma|\|_{L^2(D)}^2 + \frac{\varepsilon^3 \tilde{a}}{2} \frac{d}{dt} \|\varphi_{\gamma,t}\|_{L^2(D)}^2 + \frac{\varepsilon^2 \tilde{a}}{2} \frac{d}{dt} \|\zeta_\gamma(\varphi_\gamma)\|^{\frac{1}{2}} \|\nabla u_\gamma\|_{L^2(D)}^2 + \frac{\varepsilon^4 \tilde{a}}{2} \frac{d}{dt} \|\nabla u_\gamma\|_{L^2(D)}^2 \\ + \frac{\varepsilon^4 \tilde{a}}{4} \|u_{\gamma,t}\|_{L^2(D)}^2 + \frac{3\varepsilon^2 \tilde{a}}{4} \|\zeta_\gamma(\varphi_\gamma)\|^{\frac{1}{2}} \|D^2 u_\gamma\|_{L^2(D)}^2 \\ + \frac{\varepsilon \tilde{a}}{\alpha} \|\delta_\gamma(\varphi_\gamma)\|^{\frac{1}{2}} \|\nabla u_\gamma\|_{L^2(D)}^2 + \beta \varepsilon^3 \tilde{a} \|\nabla \varphi_{\gamma,t}\|_{L^2(D)}^2 \\ \leq C + C \|\varphi_{\gamma,t}\|_{L^2(D)}^2 + C \|\nabla \varphi_\gamma\|_{L^2(D)}^2 + C \|\nabla u_\gamma\|_{L^2(D)}^2 \\ + C \int_D |\nabla \varphi_\gamma|^2 |\nabla u_\gamma|^2 \, d\mathbf{x} + C \int_D \zeta_\gamma(\varphi_\gamma) |\nabla u_\gamma|^2 |\varphi_{\gamma,t}| \, d\mathbf{x}. \quad (3.2.33)$$

where we have chosen $a = \frac{\varepsilon^2 \tilde{a} \tilde{\beta}}{4}$. In order to bound the last term in (3.2.33) we use the

fact that, in \mathbb{R}^2 , $\|f\|_{L^2(D)} \leq C\|f\|_{W^{1,1}(D)}$. Thus, using the bound on the L^∞ norm of φ_γ , we have

$$\begin{aligned}
\int_D \zeta_\gamma(\varphi_\gamma) |\nabla u_\gamma|^2 |\varphi_{\gamma,t}| \, d\mathbf{x} &\leq C \|\varphi_{\gamma,t}\|_{L^2(D)} \|\zeta_\gamma(\varphi_\gamma) |\nabla u_\gamma|^2\|_{L^2(D)} \\
&\leq C \|\varphi_{\gamma,t}\|_{L^2(D)} \|\zeta_\gamma(\varphi_\gamma) |\nabla u_\gamma|^2\|_{W^{1,1}(D)} \\
&\leq C \|\varphi_{\gamma,t}\|_{L^2(D)} \int_D \zeta_\gamma(\varphi_\gamma) |\nabla u_\gamma|^2 \, d\mathbf{x} \\
&\quad + C \|\varphi_{\gamma,t}\|_{L^2(D)} \int_D |\nabla \varphi_\gamma| |\nabla u_\gamma|^2 \, d\mathbf{x} \\
&\quad + C \|\varphi_{\gamma,t}\|_{L^2(D)} \int_D \zeta_\gamma(\varphi_\gamma) |\nabla u_\gamma| |D^2 u_\gamma| \, d\mathbf{x} \\
&\leq C \left(1 + \|\varphi_{\gamma,t}\|_{L^2(D)}^2 + \|\nabla \varphi_\gamma\|_{L^\infty(D)}^2\right) \|\nabla u_\gamma\|_{L^2(D)}^2 \\
&\quad + \frac{\varepsilon^2 \tilde{a}}{8} \|\zeta_\gamma(\varphi_\gamma)\|_{L^2(D)}^{\frac{1}{2}} \|D^2 u_\gamma\|_{L^2(D)}^2.
\end{aligned}$$

Using this, we write (3.2.33) as

$$\begin{aligned}
\frac{\varepsilon^2}{2\tilde{\beta}} \frac{d}{dt} \|\varphi_\gamma |\nabla u_\gamma|\|_{L^2(D)}^2 &+ \frac{\varepsilon^3 \tilde{a}}{2} \frac{d}{dt} \|\varphi_{\gamma,t}\|_{L^2(D)}^2 + \frac{\varepsilon^2 \tilde{a}}{2} \frac{d}{dt} \|\zeta_\gamma(\varphi_\gamma)\|_{L^2(D)}^{\frac{1}{2}} \|\nabla u_\gamma\|_{L^2(D)}^2 + \frac{\varepsilon^4 \tilde{a}}{2} \frac{d}{dt} \|\nabla u_\gamma\|_{L^2(D)}^2 \\
&+ \frac{\varepsilon^4 \tilde{a}}{4} \|u_{\gamma,t}\|_{L^2(D)}^2 + \frac{5\varepsilon^2 \tilde{a}}{8} \|\zeta_\gamma(\varphi_\gamma)\|_{L^2(D)}^{\frac{1}{2}} \|D^2 u_\gamma\|_{L^2(D)}^2 \\
&+ \frac{\varepsilon \tilde{a}}{\alpha} \|\delta_\gamma(\varphi_\gamma)\|_{L^2(D)}^{\frac{1}{2}} \|\nabla u_\gamma\|_{L^2(D)}^2 + \beta \varepsilon^3 \tilde{a} \|\nabla \varphi_{\gamma,t}\|_{L^2(D)}^2 \\
&\leq C + C \left(1 + \|\varphi_{\gamma,t}\|_{L^2(D)}^2 + \|\nabla \varphi_\gamma\|_{L^\infty(D)}^2\right) \|\nabla u_\gamma\|_{L^2(D)}^2 \\
&\quad + C \|\varphi_{\gamma,t}\|_{L^2(D)}^2 + C \|\nabla \varphi_\gamma\|_{L^2(D)}^2. \tag{3.2.34}
\end{aligned}$$

Since $W^{2,p}(D) \hookrightarrow C^1(\overline{D})$ (where $p > 2$), Lemma 3.2.4 gives that

$$\int_0^T \left(1 + \|\varphi_{\gamma,t}\|_{L^2(D)}^2 + \|\nabla \varphi_\gamma\|_{L^\infty(D)}^2\right) dt \leq C \tag{3.2.35}$$

uniformly with respect to γ . We use Gronwall's inequality on (3.2.34) to yield the required result. \square

By Theorem 3.2.1, with $p = r = 2$, $s = 1$, $X = H^2(D)$, $Y = B = H^1(D)$, Theorem 3.2.1 with $p = r = 2$, $s = 1$, $X = H^1(D)$, $Y = B = L^2(D)$, and Lemmas 3.2.3, 3.2.4, and

3.2.7, there exist subsequences, with $\gamma \rightarrow 0$ (after re-indexing), such that

$$\varphi_\gamma \rightharpoonup \varphi^* \quad \text{in } L^2(0, T; H^2(D)), \quad (3.2.36)$$

$$\varphi_{\gamma,t} \rightharpoonup \varphi_t^* \quad \text{in } L^2(0, T; H^1(D)), \quad (3.2.37)$$

$$\varphi_\gamma \rightarrow \varphi^* \quad \text{in } L^2(0, T; H^1(D)), \quad (3.2.38)$$

$$\nabla u_\gamma \rightharpoonup \nabla u^* \quad \text{in } L^2(0, T; [L^2(D)]^2), \quad (3.2.39)$$

$$u_{\gamma,t} \rightharpoonup u_t^* \quad \text{in } L^2(0, T; L^2(D)), \quad (3.2.40)$$

$$u_\gamma \rightarrow u^* \quad \text{in } L^2(0, T; L^2(D)). \quad (3.2.41)$$

Combining (3.2.36) with Agmon's inequality, [46], $\|f\|_{C^0(D)} \leq \|f\|_{L^2(D)}^{\frac{1}{2}} \|f\|_{H^2(D)}^{\frac{1}{2}}$, we have

$$\varphi_\gamma \rightarrow \varphi^* \quad \text{in } L^2(0, T; C^0(D)), \quad (3.2.42)$$

$$\zeta_\gamma(\varphi_\gamma) \rightarrow \zeta(\varphi^*) \quad \text{in } L^2(0, T; C^0(D)). \quad (3.2.43)$$

Noting from (3.2.2) that as $\gamma \rightarrow 0$,

$$|\delta_\gamma(\varphi_\gamma) - \delta(\varphi^*)| \leq \frac{8\gamma}{\pi} |1 + \gamma| + \frac{2}{\pi} |\varphi^* - \varphi_\gamma| |\varphi^* + \varphi_\gamma| \rightarrow 0$$

we conclude that

$$\delta_\gamma(\varphi_\gamma) \rightarrow \delta(\varphi^*) \quad \text{in } L^2(0, T; C^0(D)). \quad (3.2.44)$$

Convergences (3.2.42) and (3.2.41), together with (3.2.8) and (3.2.11), imply that

$$\varphi^*(\mathbf{x}, 0) = \varphi_0, \quad \text{and} \quad u^*(\mathbf{x}, 0) = u_0,$$

while Lemmas 3.2.3, 3.2.4 and 3.2.7 imply that $|\varphi^*| \leq 1$,

$$\varphi^* \in L^2(0, T; H^2(D) \cap W^{1,\infty}(D)), \quad \varphi_t^* \in L^2(0, T; H^1(D)), \quad (3.2.45)$$

$$u^* \in L^\infty(0, T; H^1(D)) \cap H^1(0, T; L^2(D)). \quad (3.2.46)$$

and, since in the limit as $\gamma \rightarrow 0$ we have $C^* = 1$, we write

$$-\|u_0\|_{L^\infty(D)} - \frac{t}{\varepsilon^2} \leq u^* \leq \max(\alpha Q, \|u_0\|_{L^\infty(D)}), \quad \forall t \in (0, T).$$

Theorem 3.2.8 We have that φ^* and u^* solve the following system, for almost every $t \in (0, T)$, and for all $\rho \in K(D)$,

$$\begin{aligned} \int_D \varphi_t^*(\rho - \varphi^*) \, d\mathbf{x} + \beta \int_D \nabla \varphi^* \cdot \nabla(\rho - \varphi^*) \, d\mathbf{x} - \frac{\beta}{\varepsilon^2} \int_D \varphi^*(\rho - \varphi^*) \, d\mathbf{x} \\ - \frac{C_w}{\alpha \varepsilon} \int_D u^*(\rho - \varphi^*) \, d\mathbf{x} \geq 0, \end{aligned} \quad (3.2.47)$$

and for all $\phi \in H^1(D)$,

$$\begin{aligned} \varepsilon^2 \int_D u_t^* \phi \, d\mathbf{x} + \int_D \zeta(\varphi^*) \nabla u^* \cdot \nabla \phi \, d\mathbf{x} + \frac{1}{\alpha \varepsilon} \int_D \delta(\varphi^*) u^* \phi \, d\mathbf{x} \\ = \frac{Q}{\varepsilon} \int_D \delta(\varphi^*) \phi \, d\mathbf{x} - \int_D \zeta(\varphi^*) \phi \, d\mathbf{x}. \end{aligned} \quad (3.2.48)$$

Proof. This proof follows arguments made on page 1336 of [38].

We multiply (3.2.6) by $\rho - \varphi_\gamma$, where $\rho \in K(D)$. Integrating this over D yields

$$\begin{aligned} \varepsilon \int_D \varphi_{\gamma,t}(\rho - \varphi_\gamma) \, d\mathbf{x} + \beta \varepsilon \int_D \nabla \varphi_\gamma \cdot \nabla(\rho - \varphi_\gamma) \, d\mathbf{x} - \frac{\beta}{\varepsilon} \int_D \varphi_\gamma(\rho - \varphi_\gamma) \, d\mathbf{x} \\ - \frac{C_w}{\alpha} \int_D u_\gamma(\rho - \varphi_\gamma) \, d\mathbf{x} = - \int_D \chi_\gamma^\varepsilon(\varphi_\gamma)(\rho - \varphi_\gamma) \, d\mathbf{x} \\ = - \int_D (\chi_\gamma^\varepsilon(\rho) - \chi_\gamma^\varepsilon(\varphi_\gamma))(\rho - \varphi_\gamma) \, d\mathbf{x} \geq 0, \end{aligned} \quad (3.2.49)$$

where we have used that $\chi_\gamma^\varepsilon(\rho) = 0$ and χ_γ^ε is non-decreasing. Using (3.2.37), (3.2.38), and (3.2.41), (3.2.49) converges to (3.2.47) as $\gamma \rightarrow 0$ for almost every $t \in (0, T)$.

Using (3.2.39) - (3.2.41), (3.2.43), (3.2.44), and (3.2.13), we see that u^* solves (3.2.48). □

Corollary 3.2.8.1 There exist solutions φ and u to the weak form \mathbb{P}_{DI} . These solutions are such that

$$|\varphi| \leq 1, \quad \varphi \in L^2(0, T; H^2(D) \cap W^{1,\infty}(D)), \quad \varphi_t \in L^2(0, T; H^1(D)), \quad (3.2.50)$$

$$-\|u_0\|_{L^\infty(D)} - \frac{t}{\varepsilon^2} \leq u \leq \max(\alpha Q, \|u_0\|_{L^\infty(D)}), \quad \forall t \in (0, T), \quad (3.2.51)$$

and

$$u \in L^\infty(0, T; H^1(D)) \cap H^1(0, T; L^2(D)). \quad (3.2.52)$$

Proof. Theorem 3.2.2 gives us the existence of $(\varphi_\gamma, u_\gamma)$, Theorem 3.2.6 gives us uniqueness, and Theorem 3.2.8 tells us that $(\varphi_\gamma, u_\gamma) \rightarrow (\varphi^*, u^*)$ as $\gamma \rightarrow 0$, where (φ^*, u^*) solve the system (3.2.47) with (3.2.48). The rest of the corollary follows from (3.2.45) and (3.2.46). \square

3.3 Uniqueness of a solution to \mathbb{P}_{DI} for $D \subset \mathbb{R}^2$

In this section we restrict $D \subset \mathbb{R}^2$ and show that the solution (u, φ) to the regularised system \mathbb{P}_{DI} is unique. Recall that we assume, in Sections 3.2 and 3.3, that D is a bounded convex domain, whose boundary $\partial D \in C^3$.

In order to prove uniqueness we assume additional regularity on φ ,

$$\Delta \varphi \in L^1(0, T; L^\infty(D)). \quad (3.3.1)$$

We also assume additional regularity on u , namely

$$\nabla u \in L^\infty(0, T; L^\infty(D)). \quad (3.3.2)$$

We let φ_1 and φ_2 be solutions to (3.1.8), and let $\psi := \varphi_1 - \varphi_2$. Similarly, we let u_1 and u_2 be solutions to (3.1.9) and define $w := u_1 - u_2$. We also let

$$\bar{\varphi} := \frac{\varphi_1 + \varphi_2}{2}, \quad \bar{\zeta}(\varphi_1, \varphi_2) := \frac{\zeta(\varphi_1) + \zeta(\varphi_2)}{2}, \quad \text{and} \quad \bar{\delta}(\varphi_1, \varphi_2) := \frac{\delta(\varphi_1) + \delta(\varphi_2)}{2}.$$

The uniqueness result is presented later in Theorem 3.3.3, after we establish a result in Lemma 3.3.2. In the first stage of the proof of Theorem 3.3.3, see (3.3.12), we see that we need to bound $\int_D \psi w \, d\mathbf{x}$. To this end we introduce a function v that solves the backwards degenerate parabolic equation over the time interval $(0, t_0)$,

$$-\varepsilon^2 v_t - \nabla \cdot (\bar{\zeta}(\varphi_1, \varphi_2) \nabla v) + \frac{1}{\alpha \varepsilon} \bar{\delta}(\varphi_1, \varphi_2) v = \psi, \quad \text{in } D, \quad (3.3.3)$$

with $v(\mathbf{x}, t_0) = 0$ in D , and $\bar{\zeta}(\varphi_1, \varphi_2)\nabla v \cdot \boldsymbol{\nu} = 0$ on ∂D .

The reason that we take v to be the solution of the above backwards degenerate parabolic equation is because later on, in Lemma 3.3.2, we multiply (3.3.3) by w , integrate over $D \times (0, t_0)$, and use integration by parts, with respect to t , on the first term. This then enables us to use (3.1.9) with $u = u_1$ and $\varphi = \varphi_1$, and with $u = u_2$ and $\varphi = \varphi_2$, to bound $\int_0^{t_0} \int_D \psi w \, d\mathbf{x} \, dt$ by norms of ψ .

The following lemma is the first step in bounding $\int_0^{t_0} \int_D \psi w \, d\mathbf{x} \, dt$, in particular we use its result in the proof of Lemma 3.3.2.

Lemma 3.3.1 There exists a unique v solving (3.3.3), and we have

$$\sup_{t \in [0, t_0]} \|v\|_{L^2(D)}^2 \leq C \int_0^{t_0} \|\psi\|_{L^2(D)}^2 \, dt, \quad (3.3.4)$$

and

$$\sup_{t \in [0, t_0]} \|\nabla v\|_{L^2(D)}^2 \leq C \int_0^{t_0} \|\psi\|_{H^1(D)}^2 \, dt. \quad (3.3.5)$$

Proof. This proof follows the techniques in the proof of Lemma 3.3 and arguments of equation (3.6) in Theorem 3.1 in [38].

In order to conveniently prove the existence and uniqueness of v (this is convenient as it allows us to directly follow the techniques used in Section 3.2), we formulate (3.3.3) as an (equivalent) forward equation. This is given by

$$\varepsilon^2 v_t - \nabla \cdot (\bar{\zeta}(\varphi_1, \varphi_2)\nabla v) + \frac{1}{\alpha\varepsilon} \bar{\delta}(\varphi_1, \varphi_2)v = \psi, \quad \text{in } D \times (0, t_0), \quad (3.3.6)$$

with $v(\mathbf{x}, 0) = 0$ in D and $\bar{\zeta}(\varphi_1, \varphi_2)\nabla v \cdot \boldsymbol{\nu} = 0$ on ∂D . Here we abuse notation in writing v , φ , and ψ for $v(t_0 - t)$, $\varphi(t_0 - t)$, and $\psi(t_0 - t)$.

We show uniqueness first, using a simple energy argument. Let $\tilde{w} := v_1 - v_2$ where v_1 and v_2 are solutions to (3.3.6). Subtracting (3.3.6) with $v = v_2$ from (3.3.6) with $v = v_1$, multiplying by \tilde{w} and integrating over D , we have

$$\frac{\varepsilon^2}{2} \frac{d}{dt} \|\tilde{w}\|_{L^2(D)}^2 + \|\bar{\zeta}(\varphi_1, \varphi_2)\|_{L^2(D)}^{\frac{1}{2}} \|\nabla \tilde{w}\|_{L^2(D)}^2 + \frac{1}{\alpha\varepsilon} \|\bar{\delta}(\varphi_1, \varphi_2)\|_{L^2(D)}^{\frac{1}{2}} \|\tilde{w}\|_{L^2(D)}^2 = 0,$$

after integrating over $(0, t_0)$ and recalling that $v(\mathbf{x}, 0) = 0$, it follows that $\tilde{w} = 0$, and thus

$v_1 = v_2$.

To show existence we regularise (3.3.6) with $\gamma \in \mathbb{R}$, $\gamma \in (0, 1]$. The regularised system is then

$$\varepsilon^2 v_t^\gamma - \nabla \cdot ((\bar{\zeta}(\varphi_1, \varphi_2) + \gamma) \nabla v^\gamma) + \frac{1}{\alpha} (\varepsilon^{-1} \bar{\delta}(\varphi_1, \varphi_2) + \gamma) v^\gamma = \psi, \quad \text{on } D \times (0, t_0), \quad (3.3.7)$$

with $v^\gamma(\mathbf{x}, 0) = 0$ and $\nabla v^\gamma \cdot \boldsymbol{\nu} = 0$ on ∂D . Since this is a parabolic equation with non-degenerate coefficients, we have existence and uniqueness of v^γ for some time $(0, t_0)$ (see, for example, Theorem 5.3 in [63]).

We want to take $\gamma \rightarrow 0$ in order to show the existence of a solution to (3.3.3). First we derive an estimate in the L^2 norm by multiplying (3.3.7) by v^γ , integrating over D , using Hölder's inequality, and then using Gronwall's inequality, to give

$$\sup_{t \in [0, t_0]} \|v^\gamma\|_{L^2(D)}^2 \leq C \int_0^{t_0} \|\psi\|_{L^2(D)}^2 dt. \quad (3.3.8)$$

We now want an estimate in the H^1 norm. Using (3.3.7), we calculate that

$$\begin{aligned} \frac{\varepsilon^2}{2} \frac{d}{dt} \|\nabla v^\gamma\|_{L^2(D)}^2 &= \varepsilon^2 \int_D \nabla v^\gamma \cdot \nabla v_t^\gamma d\mathbf{x} \\ &= \underbrace{\int_D \nabla v^\gamma \cdot \nabla \psi d\mathbf{x}}_{(1)} + \underbrace{\int_D \nabla v^\gamma \cdot \nabla (\nabla \cdot ((\bar{\zeta}(\varphi_1, \varphi_2) + \gamma) \nabla v^\gamma)) d\mathbf{x}}_{(2)} \\ &\quad - \underbrace{\frac{1}{\alpha} \int_D \nabla v^\gamma \cdot \nabla ((\varepsilon^{-1} \bar{\delta}(\varphi_1, \varphi_2) + \gamma) v^\gamma) d\mathbf{x}}_{(3)}. \end{aligned}$$

Considering each term individually, we start with (1) and use Hölder's inequality to obtain

$$(1) \leq \|\nabla v^\gamma\|_{L^2(D)} \|\nabla \psi\|_{L^2(D)} \leq \|v^\gamma\|_{H^1(D)} \|\psi\|_{H^1(D)}.$$

We split term (2) into two integrals, which we bound separately

$$(2) \leq - \underbrace{\sum_{i,k=1}^2 \int_D v_{x_i, x_k}^\gamma ((\bar{\zeta}(\varphi_1, \varphi_2) + \gamma) v_{x_k}^\gamma)_{x_i} d\mathbf{x}}_{(2_1)} + \underbrace{\sum_{i,k=1}^2 \int_{\partial D} v_{x_i}^\gamma ((\bar{\zeta}(\varphi_1, \varphi_2) + \gamma) v_{x_k}^\gamma)_{x_i} \boldsymbol{\nu}_k d\mathbf{x}}_{(2_2)}.$$

We bound (2₁) as follows, noting that $\nabla\varphi \cdot \boldsymbol{\nu} = 0$ on ∂D ,

$$\begin{aligned}
(2_1) &= -\|[(\bar{\zeta}(\varphi_1, \varphi_2) + \gamma)]^{\frac{1}{2}} D^2 v^\gamma\|_{L^2(D)}^2 - \sum_{i,k=1}^2 \int_D v_{x_i, x_k}^\gamma (\bar{\zeta}(\varphi_1, \varphi_2))_{x_i} v_{x_k}^\gamma \, d\mathbf{x} \\
&= -\|[(\bar{\zeta}(\varphi_1, \varphi_2) + \gamma)]^{\frac{1}{2}} D^2 v^\gamma\|_{L^2(D)}^2 - \frac{1}{2} \sum_{i=1}^2 \int_D (|\nabla v^\gamma|^2)_{x_i} (\bar{\zeta}(\varphi_1, \varphi_2))_{x_i} \, d\mathbf{x} \\
&= -\|[(\bar{\zeta}(\varphi_1, \varphi_2) + \gamma)]^{\frac{1}{2}} D^2 v^\gamma\|_{L^2(D)}^2 + \frac{1}{2} \int_D |\nabla v^\gamma|^2 \Delta \bar{\zeta}(\varphi_1, \varphi_2) \, d\mathbf{x} \\
&\leq -\|[(\bar{\zeta}(\varphi_1, \varphi_2) + \gamma)]^{\frac{1}{2}} D^2 v^\gamma\|_{L^2(D)}^2 + C \|\Delta \bar{\zeta}(\varphi_1, \varphi_2)\|_{L^\infty(D)} \|\nabla v^\gamma\|_{L^2(D)}^2 \\
&\leq -\|[(\bar{\zeta}(\varphi_1, \varphi_2) + \gamma)]^{\frac{1}{2}} D^2 v^\gamma\|_{L^2(D)}^2 + C \|\Delta \bar{\varphi}\|_{L^\infty(D)} \|\nabla v^\gamma\|_{L^2(D)}^2.
\end{aligned}$$

For term (2₂) we use (3.2.25), the fact that $\nabla v^\gamma \cdot \boldsymbol{\nu} = 0$ on ∂D , and that $\kappa \leq 0$ (since D is convex), to yield

$$\begin{aligned}
(2_2) &= \sum_{i,k=1}^2 \int_{\partial D} v_{x_i}^\gamma (\bar{\zeta}(\varphi_1, \varphi_2))_{x_i} v_{x_k}^\gamma \boldsymbol{\nu}_k \, d\mathbf{x} + \sum_{i,k=1}^2 \int_{\partial D} v_{x_i}^\gamma (\bar{\zeta}(\varphi_1, \varphi_2) + \gamma) v_{x_k, x_i}^\gamma \boldsymbol{\nu}_k \, d\mathbf{x} \\
&= \sum_{i,k=1}^2 \int_{\partial D} v_\tau^\gamma (\bar{\zeta}(\varphi_1, \varphi_2) + \gamma) v_{x_k, x_i}^\gamma \boldsymbol{\nu}_k \boldsymbol{\tau}_i \, d\mathbf{x} \\
&= \int_{\partial D} (v_\tau^\gamma)^2 (\bar{\zeta}(\varphi_1, \varphi_2) + \gamma) \kappa \, d\mathbf{x} \leq 0.
\end{aligned}$$

Combining (2₁) and (2₂), we have

$$(2) \leq -\|[(\bar{\zeta}(\varphi_1, \varphi_2) + \gamma)]^{\frac{1}{2}} D^2 v^\gamma\|_{L^2(D)}^2 + C \|\Delta \bar{\varphi}\|_{L^\infty(D)} \|\nabla v^\gamma\|_{L^2(D)}^2.$$

We bound (3) similarly to (2₁),

$$\begin{aligned}
(3) &= -\frac{1}{\alpha} \left\| [(\varepsilon^{-1} \bar{\delta}(\varphi_1, \varphi_2) + \gamma)]^{\frac{1}{2}} \nabla v^\gamma \right\|_{L^2(D)}^2 + \frac{4}{\pi \varepsilon \alpha} \int_D v^\gamma \nabla v^\gamma \cdot (\bar{\varphi} \nabla \bar{\varphi}) \, d\mathbf{x} \\
&\leq -\frac{1}{\alpha} \left\| [(\varepsilon^{-1} \bar{\delta}(\varphi_1, \varphi_2) + \gamma)]^{\frac{1}{2}} \nabla v^\gamma \right\|_{L^2(D)}^2 + \frac{2}{\pi \varepsilon \alpha} \int_D \nabla((v^\gamma)^2) \cdot (\bar{\varphi} \nabla \bar{\varphi}) \, d\mathbf{x} \\
&\leq -\frac{1}{\alpha} \left\| [(\varepsilon^{-1} \bar{\delta}(\varphi_1, \varphi_2) + \gamma)]^{\frac{1}{2}} \nabla v^\gamma \right\|_{L^2(D)}^2 - \frac{2}{\pi \varepsilon \alpha} \int_D (v^\gamma)^2 |\nabla \bar{\varphi}|^2 \, d\mathbf{x} \\
&\quad - \frac{2}{\pi \varepsilon \alpha} \int_D (v^\gamma)^2 \bar{\varphi} \Delta \bar{\varphi} \, d\mathbf{x} + \frac{2}{\pi \varepsilon \alpha} \int_{\partial D} (v^\gamma)^2 \bar{\varphi} \nabla \bar{\varphi} \cdot \boldsymbol{\nu} \, d\mathbf{x} \\
&\leq -\frac{1}{\alpha} \left\| [(\varepsilon^{-1} \bar{\delta}(\varphi_1, \varphi_2) + \gamma)]^{\frac{1}{2}} \nabla v^\gamma \right\|_{L^2(D)}^2 + C \|\Delta \bar{\varphi}\|_{L^\infty(D)} \|v^\gamma\|_{L^2(D)}^2 \\
&\quad + C \|v^\gamma\|_{L^4(D)}^2 \|\nabla \bar{\varphi}\|_{L^4(D)}^2 \\
&\leq -\frac{1}{\alpha} \left\| [(\varepsilon^{-1} \bar{\delta}(\varphi_1, \varphi_2) + \gamma)]^{\frac{1}{2}} \nabla v^\gamma \right\|_{L^2(D)}^2 + C \|\Delta \bar{\varphi}\|_{L^\infty(D)} \|v^\gamma\|_{L^2(D)}^2 \\
&\quad + C \|v^\gamma\|_{H^1(D)}^2 \|\nabla \bar{\varphi}\|_{H^1(D)}^2.
\end{aligned}$$

Combining (1), (2), and (3), we have

$$\begin{aligned}
&\frac{\varepsilon^2}{2} \frac{d}{dt} \|\nabla v^\gamma\|_{L^2(D)}^2 + \left\| [(\bar{\zeta}(\varphi_1, \varphi_2) + \gamma)]^{\frac{1}{2}} D^2 v^\gamma \right\|_{L^2(D)}^2 + \frac{1}{\alpha} \left\| [(\varepsilon^{-1} \bar{\delta}(\varphi_1, \varphi_2) + \gamma)]^{\frac{1}{2}} \nabla v^\gamma \right\|_{L^2(D)}^2 \\
&\leq C \|v^\gamma\|_{H^1(D)} \|\psi\|_{H^1(D)} + C \|\Delta \bar{\varphi}\|_{L^\infty(D)} \|v^\gamma\|_{H^1(D)}^2 \\
&\quad + C \|v^\gamma\|_{H^1(D)}^2 \|\nabla \bar{\varphi}\|_{H^1(D)}^2.
\end{aligned}$$

Using (3.3.1), (3.3.8), noting from (3.2.50) that $\bar{\varphi} \in L^2(0, T; H^2(D))$, and using a Gronwall argument, we have

$$\sup_{t \in [0, t_0]} \|\nabla v^\gamma\|_{L^2(D)}^2 \leq C \int_0^{t_0} \|\psi\|_{H^1(D)}^2 \, dt, \quad (3.3.9)$$

and we have

$$\int_0^{t_0} \left(\left\| [(\bar{\zeta}(\varphi_1, \varphi_2) + \gamma)]^{\frac{1}{2}} D^2 v^\gamma \right\|_{L^2(D)}^2 + \frac{1}{\alpha} \left\| [(\varepsilon^{-1} \bar{\delta}(\varphi_1, \varphi_2) + \gamma)]^{\frac{1}{2}} \nabla v^\gamma \right\|_{L^2(D)}^2 \right) dt \leq C, \quad (3.3.10)$$

uniformly with respect to γ .

We now need a bound on $\int_0^{t_0} \|v_t^\gamma\|_{L^2(D)}^2 \, dt$. This follows from (3.3.7) and (3.3.10), and noting that

$$\int_0^{t_0} \|\nabla(\bar{\zeta}(\varphi_1, \varphi_2) + \gamma) \cdot \nabla v^\gamma\|_{L^2(D)}^2 \, dt = \frac{1}{2} \int_0^{t_0} \|\nabla \bar{\varphi} \cdot \nabla v^\gamma\|_{L^2(D)}^2 \, dt \leq C.$$

The solution v is now obtained by a simple convergence argument, similar to the one in the proof of Theorem 3.2.8.

We obtain (3.3.4) and (3.3.5) from (3.3.8), (3.3.9), and the weak lower semi-continuity of the norm. □

We now bound $\int_0^{t_0} \int_D \psi w \, d\mathbf{x} \, dt$. This bound will then be used in the proof of the uniqueness result, Theorem 3.3.3.

Lemma 3.3.2 We have

$$\int_0^{t_0} \int_D \psi w \, d\mathbf{x} \, dt \leq \frac{\varepsilon \alpha \beta}{2C_w} \int_0^{t_0} \|\nabla \psi\|_{L^2(D)}^2 \, dt + C \int_0^{t_0} \|\psi\|_{L^2(D)}^2 \, dt,$$

for $\psi := \varphi_1 - \varphi_2$ and $w := u_1 - u_2$, where (φ_1, u_1) and (φ_2, u_2) are solutions to (\mathbb{P}_{DI}) .

Proof. This proof follows arguments made in the proof of Theorem 3.1 of [38].

Multiplying (3.3.3) by w and integrating over D and then $(0, t_0)$ yields

$$\begin{aligned} \int_0^{t_0} \int_D \psi w \, d\mathbf{x} \, dt &= -\varepsilon^2 \int_0^{t_0} \int_D v_t w \, d\mathbf{x} \, dt + \int_0^{t_0} \int_D \bar{\zeta}(\varphi_1, \varphi_2) \nabla v \cdot \nabla w \, d\mathbf{x} \, dt \\ &\quad + \frac{1}{\alpha \varepsilon} \int_0^{t_0} \int_D \bar{\delta}(\varphi_1, \varphi_2) v w \, d\mathbf{x} \, dt \\ &= \varepsilon^2 \int_0^{t_0} \int_D v w_t \, d\mathbf{x} \, dt + \int_0^{t_0} \int_D \bar{\zeta}(\varphi_1, \varphi_2) \nabla v \cdot \nabla w \, d\mathbf{x} \, dt \\ &\quad + \frac{1}{\alpha \varepsilon} \int_0^{t_0} \int_D \bar{\delta}(\varphi_1, \varphi_2) v w \, d\mathbf{x} \, dt, \end{aligned}$$

since $w(\mathbf{x}, 0) = v(\mathbf{x}, t_0) = 0$. We now substitute in (3.1.9), with $u = u_1$ and $\varphi = \varphi_1$, and with $u = u_2$ and $\varphi = \varphi_2$. This yields

$$\begin{aligned} \int_0^{t_0} \int_D \psi w \, d\mathbf{x} \, dt &= \frac{Q}{\varepsilon} \int_0^{t_0} \int_D (\delta(\varphi_1) - \delta(\varphi_2)) v \, d\mathbf{x} \, dt + \int_0^{t_0} \int_D (\zeta(\varphi_2) - \zeta(\varphi_1)) v \, d\mathbf{x} \, dt \\ &\quad + \frac{1}{2\alpha \varepsilon} \int_0^{t_0} \int_D v (\delta(\varphi_2) - \delta(\varphi_1)) (u_1 + u_2) \, d\mathbf{x} \, dt \tag{3.3.11} \\ &\quad + \frac{1}{2} \int_0^{t_0} \int_D (\zeta(\varphi_2) - \zeta(\varphi_1)) \nabla v \cdot \nabla (u_1 + u_2) \, d\mathbf{x} \, dt. \end{aligned}$$

Using Hölder's inequality and the bounds on the L^∞ norms for u and φ given in (3.2.50)

and (3.2.51) we have, after using (3.3.2),

$$\begin{aligned}
\int_0^{t_0} \int_D \psi w \, d\mathbf{x} \, dt &\leq C \int_0^{t_0} \|v\|_{L^2(D)} \|\psi\|_{L^2(D)} \, dt \\
&\quad + C \|\nabla(u_1 + u_2)\|_{L^\infty(D)} \int_0^{t_0} \|\nabla v\|_{L^2(D)} \|\psi\|_{L^2(D)} \, dt \\
&\leq C \underbrace{\int_0^{t_0} \|v\|_{L^2(D)} \|\psi\|_{L^2(D)} \, dt}_{(1)} + C \underbrace{\int_0^{t_0} \|\nabla v\|_{L^2(D)} \|\psi\|_{L^2(D)} \, dt}_{(2)}.
\end{aligned}$$

Starting with term (1) we calculate, using (3.3.4) and Hölder's inequality, that

$$\begin{aligned}
(1) &\leq \left(\int_0^{t_0} \|\psi\|_{L^2(D)}^2 \, dt \right)^{\frac{1}{2}} \left(\int_0^{t_0} \|v\|_{L^2(D)}^2 \, dt \right)^{\frac{1}{2}} \\
&\leq C \left(\int_0^{t_0} \|\psi\|_{L^2(D)}^2 \, dt \right)^{\frac{1}{2}} \left(\sup_{t \in [0, t_0]} \|v\|_{L^2(D)}^2 \right)^{\frac{1}{2}} \\
&\leq C \left(\int_0^{t_0} \|\psi\|_{L^2(D)}^2 \, dt \right)^{\frac{1}{2}} \left(\int_0^{t_0} \|\psi\|_{L^2(D)}^2 \, dt \right)^{\frac{1}{2}} \\
&\leq C \int_0^{t_0} \|\psi\|_{L^2(D)}^2 \, dt.
\end{aligned}$$

In order to bound (2) we use (3.3.5), and Young's inequality with $a \in \mathbb{R}$, $a > 0$, where a is then chosen as $a = \frac{\varepsilon\alpha\beta}{2Cw}$. Thus

$$\begin{aligned}
(2) &\leq Ca \sup_{t \in [0, t_0]} \|\nabla v\|_{L^2(D)}^2 + C \int_0^{t_0} \|\psi\|_{L^2(D)}^2 \, dt \\
&\leq Ca \int_0^{t_0} \|\psi\|_{H^1(D)}^2 \, dt + C \int_0^{t_0} \|\psi\|_{L^2(D)}^2 \, dt \\
&\leq \frac{\varepsilon\alpha\beta}{2Cw} \int_0^{t_0} \|\psi\|_{H^1(D)}^2 \, dt + C \int_0^{t_0} \|\psi\|_{L^2(D)}^2 \, dt.
\end{aligned}$$

Combining the bounds for (1) and (2) yields the desired result. □

We now prove the main result of this section.

Theorem 3.3.3 If φ and u solve the weak form \mathbb{P}_{DI} , then φ and u are unique. Here (and throughout this section) $\psi := \varphi_1 - \varphi_2$ and $w := u_1 - u_2$, where (φ_1, u_1) and (φ_2, u_2) are solutions to (\mathbb{P}_{DI}) .

Proof. This proof follows arguments made in the proof of Theorem 3.1 of [38].

Starting with (3.1.8), we first set $\rho = \varphi_2$ in the inequality for φ_1 , and set $\rho = \varphi_1$ in the inequality for φ_2 . Then we add the resulting inequalities for φ_1 and φ_2 , yielding

$$\frac{1}{2} \frac{d}{dt} \|\psi\|_{L^2(D)}^2 + \beta \|\nabla \psi\|_{L^2(D)}^2 \leq \frac{\beta}{\varepsilon^2} \|\psi\|_{L^2(D)}^2 + \frac{C_w}{\varepsilon \alpha} \int_D w \psi \, d\mathbf{x}. \quad (3.3.12)$$

Integrating over $(0, t_0)$ and using Lemma 3.3.2 gives (since $\psi(\mathbf{x}, 0) = 0$)

$$\frac{1}{2} \|\psi(\mathbf{x}, t_0)\|_{L^2(D)}^2 + \beta \int_0^{t_0} \|\nabla \psi\|_{L^2(D)}^2 \, dt \leq C \int_0^{t_0} \|\psi\|_{L^2(D)}^2 \, dt + \frac{\beta}{2} \int_0^{t_0} \|\nabla \psi\|_{L^2(D)}^2 \, dt.$$

Rearranging, we have

$$\|\psi(\mathbf{x}, t_0)\|_{L^2(D)}^2 \leq C \int_0^{t_0} \|\psi\|_{L^2(D)}^2 \, dt.$$

Using Gronwall's inequality, and the fact that $\psi(\mathbf{x}, 0) = 0$, we have $\psi = 0$, and thus $\varphi_1 = \varphi_2$, $\forall t \in [0, t_0]$.

Now considering (3.1.9), we test both the u_1 and u_2 equations with $\phi = w$. We then subtract the two resulting equations, giving

$$\begin{aligned} \frac{\varepsilon^2}{2} \frac{d}{dt} \|w\|_{L^2(D)}^2 + \int_D (\zeta(\varphi_1) \nabla u_1 - \zeta(\varphi_2) \nabla u_2) \cdot \nabla w \, d\mathbf{x} + \frac{1}{\alpha \varepsilon} \int_D (\delta(\varphi_1) u_1 - \delta(\varphi_2) u_2) w \, d\mathbf{x} \\ = \int_D (\zeta(\varphi_2) - \zeta(\varphi_1)) w \, d\mathbf{x} + \frac{Q}{\varepsilon} \int_D (\delta(\varphi_1) - \delta(\varphi_2)) w \, d\mathbf{x} \\ = -\frac{1}{2} \int_D \psi w \, d\mathbf{x} - \frac{2Q}{\pi \varepsilon} \int_D \psi (\varphi_1 + \varphi_2) w \, d\mathbf{x} = 0, \end{aligned}$$

where $\psi = 0$ is given by the first part of this proof. Again using $\psi = 0$, we have

$$\begin{aligned} \int_D (\zeta(\varphi_1) \nabla u_1 - \zeta(\varphi_2) \nabla u_2) \cdot \nabla w \, d\mathbf{x} \\ = \int_D ((\zeta(\varphi_1) - \zeta(\varphi_2)) \nabla u_1 + \zeta(\varphi_2) (\nabla u_1 - \nabla u_2)) \cdot \nabla w \, d\mathbf{x} \\ = \frac{1}{2} \int_D \psi \nabla u_1 \cdot \nabla w \, d\mathbf{x} + \|\zeta(\varphi_2)\|_{L^2(D)}^{\frac{1}{2}} \|\nabla w\|_{L^2(D)}^2 \geq 0, \end{aligned}$$

and

$$\begin{aligned} \int_D (\delta(\varphi_1) u_1 - \delta(\varphi_2) u_2) w \, d\mathbf{x} = \int_D ((\delta(\varphi_1) - \delta(\varphi_2)) u_1 + \delta(\varphi_2) (u_1 - u_2)) w \, d\mathbf{x} \\ = -\frac{2}{\pi} \int_D \psi (\varphi_1 + \varphi_2) u_1 w \, d\mathbf{x} + \|\delta(\varphi_2)\|_{L^2(D)}^{\frac{1}{2}} \|w\|_{L^2(D)}^2 \geq 0. \end{aligned}$$

Hence, by Gronwall's inequality,

$$\|w(\mathbf{x}, t)\|_{L^2(D)}^2 \leq C \|w(\mathbf{x}, 0)\|_{L^2(D)}^2 = 0,$$

as $w(\mathbf{x}, 0) = 0$. Thus $w = 0$, and so $u_1 = u_2, \forall t \in [0, t_0]$.

□

3.4 Finite element scheme

We partition the time interval $[0, T]$ into $N + 1$ time steps: $0 = t_0 < t_1 < \dots < t_{N-1} < t_N = T$. These time steps are evenly spaced, so that $\Delta t := t_{i+1} - t_i$ for $i = 0, \dots, N - 1$. We assume that D is bounded and polygonal. Let $\{\mathcal{T}_D^h\}_{h>0}$ be a family of conforming partitions of D into disjoint open simplices σ , with $h_\sigma := \text{diam}(\sigma)$ and $h := \max_{\sigma \in \mathcal{T}_D^h} h_\sigma$, so that $\bar{D} = \cup_{\sigma \in \mathcal{T}_D^h} \bar{\sigma}$. We denote the outward unit normal to ∂D by $\boldsymbol{\nu}$. This set up can be seen in Figure 3.2.

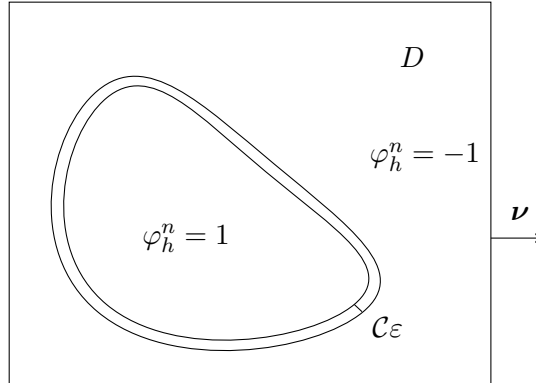


Figure 3.2: The polyhedral domain D . Here $\boldsymbol{\nu}$ is the outward unit normal to ∂D , the boundary of D .

We define the spaces

$$U_h(D) := \left\{ \phi_h \in C^0(\bar{D}) \mid \phi_h|_\sigma \text{ is linear } \forall \sigma \in \mathcal{T}_D^h \right\},$$

and

$$K_h(D) := \{ \rho_h \in U_h(D) \mid |\rho_h| \leq 1 \}.$$

Let \mathcal{I} be the set of nodes of \mathcal{T}_D^h , with $|\mathcal{I}| = I$, and let $\{\mathbf{q}_i\}_{i \in \mathcal{I}}$ be the coordinates of these nodes. Let $\{\phi_i\}_{i \in \mathcal{I}}$ be the standard basis functions for $U_h(D)$. We denote by

$I_h : C^0(\overline{D}) \rightarrow U_h(D)$ the Lagrange interpolation operator onto $U_h(D)$. For simplicity of notation we extend I_h to encompass $I_h : C^0(\overline{D}) \rightarrow K_h(D)$ the Lagrange interpolation operator onto $K_h(D)$.

We assume that \mathcal{T}_D^h is of non-negative type, see [31], such that

$$\int_{\sigma} \nabla \phi_i \cdot \nabla \phi_j \, d\mathbf{x} \leq 0, \quad \text{for } i \neq j, \forall \sigma \in \mathcal{T}_D^h. \quad (3.4.1)$$

In addition, for the convergence results presented in Theorems 3.5.6 and 3.5.10, and the lemmas presented in Section 3.5.2, we assume that the family of partitions $\{\mathcal{T}_D^h\}_{h>0}$ is quasi-uniform, see Definition 4.4.13 in [16].

For the initial conditions, we take

$$\varphi_h^0 := I_h \varphi_0, \quad \text{in } D, \quad (3.4.2)$$

and

$$u_h^0 := I_h u_0, \quad \text{in } D. \quad (3.4.3)$$

Note that, by (3.2.5), it follows that

$$\|u_h^0\|_{L^\infty(D)} \leq C, \quad (3.4.4)$$

where the positive constant C does not depend on Δt , n , or h . We write $D_t \varphi_h^{n+1} := \frac{\varphi_h^{n+1} - \varphi_h^n}{\Delta t}$ and $D_t u_h^{n+1} := \frac{u_h^{n+1} - u_h^n}{\Delta t}$.

A finite element scheme for the weak form \mathbb{P}_{DI} , with initial conditions (3.4.2) and (3.4.3), is given by the coupled system

Problem \mathbb{P}_{DI}^h Given initial conditions (3.4.2) and (3.4.3), for $n = 0, \dots, N-1$, find $\{u_h^{n+1}, \varphi_h^{n+1}\} \in U_h(D) \times K_h(D)$ such that

$$\begin{aligned} \varepsilon^2 \int_D I_h (D_t u_h^{n+1} \phi_h) \, d\mathbf{x} + \int_D \zeta(\varphi_h^{n+1}) \nabla u_h^{n+1} \cdot \nabla \phi_h \, d\mathbf{x} + \frac{1}{\alpha \varepsilon} \int_D I_h (\delta(\varphi_h^{n+1}) u_h^{n+1} \phi_h) \, d\mathbf{x} \\ = \frac{Q}{\varepsilon} \int_D I_h (\delta(\varphi_h^{n+1}) \phi_h) \, d\mathbf{x} - \int_D I_h (\zeta(\varphi_h^{n+1}) \phi_h) \, d\mathbf{x}, \quad \forall \phi_h \in U_h(D), \end{aligned} \quad (3.4.5)$$

and

$$\begin{aligned} & \int_D I_h (D_t \varphi_h^{n+1} (\rho_h - \varphi_h^{n+1})) \, d\mathbf{x} + \beta \int_D \nabla \varphi_h^{n+1} \cdot \nabla (\rho_h - \varphi_h^{n+1}) \, d\mathbf{x} \\ & - \frac{\beta}{\varepsilon^2} \int_D I_h (\varphi_h^n (\rho_h - \varphi_h^{n+1})) \, d\mathbf{x} \geq \frac{C_w}{\alpha \varepsilon} \int_D I_h (u_h^n (\rho_h - \varphi_h^{n+1})) \, d\mathbf{x}, \quad \forall \rho_h \in K_h(D). \end{aligned} \quad (3.4.6)$$

In order to solve (3.4.6) we use the projected SOR algorithm given in Chapter 9 of [44].

Algorithm 7 This algorithm numerically solves the system given by (3.4.6) with initial guess \mathbf{x}^0 . Here A is the $I \times I$ square matrix given by the first two terms in (3.4.6) with components $a_{i,j}$, and \mathbf{x}^k and \mathbf{b} are vectors of length I with components \mathbf{x}_i^k and \mathbf{b}_i . Here \mathbf{x}^k corresponds to φ_h^{n+1} , and \mathbf{b} is given by the final two terms in (3.4.6). The algorithm takes as input a maximum number of loops, *loops*, and the tolerance, *tol*.

```

1: for  $k = 0$  to loops do
2:   for  $i = 1 \dots I$  do
3:     Set  $\mathbf{x}_i^{k+\frac{1}{2}} := \frac{\mathbf{b}_i - \sum_{j=1}^{i-1} a_{ij} \mathbf{x}_j^{k+\frac{1}{2}} - \sum_{j=i+1}^I a_{ij} \mathbf{x}_j^k}{a_{ii}}$ 
4:     Project  $\mathbf{x}_i^{k+1} := \min(\max(-1, \mathbf{x}_i^{k+\frac{1}{2}}), 1)$ 
5:   if  $\|\mathbf{x}^{k+1} - \mathbf{x}^k\| < \textit{tol}$  then
6:     Return  $\mathbf{x}^{k+1}$ 

```

3.5 Numerical analysis

This section is split in two. We first show the existence and uniqueness of a solution to the finite element scheme \mathbb{P}_{DI}^h . We then show the convergence (as $h \rightarrow 0$) of the solution to the finite element scheme \mathbb{P}_{DI}^h .

Throughout Section 3.5 we liberally use the standard inequality

$$\|v_h\|_{L^2(D)}^2 \leq \|v_h\|_{L_h^2(D)}^2 \leq C \|v_h\|_{L^2(D)}^2, \quad (3.5.1)$$

where

$$\|v_h\|_{L_h^2(D)}^2 := \int_D I_h(v_h^2) \, d\mathbf{x}.$$

Here $v_h \in U_h$.

3.5.1 Existence and uniqueness of the finite element scheme

Theorem 3.5.1 For $n = 0, \dots, N - 1$ there exists a unique pair of solutions u_h^{n+1} and φ_h^{n+1} to the coupled finite element scheme \mathbb{P}_{DI}^h .

Proof. We argue by induction over n . Clearly, by (3.4.2) and (3.4.3), the base case $n = 0$ is satisfied. Assuming that there exists a unique pair of solutions u_h^n and φ_h^n , we show that there exists a unique pair of solutions u_h^{n+1} and φ_h^{n+1} .

Starting with φ_h^{n+1} , we follow [10]. There exists a unique $\varphi_h^{n+1} \in K_h(D)$ solving (3.4.6), since this is the Euler-Lagrange variational inequality of the strictly convex minimization problem,

$$\min_{z_h \in K_h(D)} \left\{ \frac{\varepsilon\beta}{2} \|\nabla z_h\|_{L^2(D)}^2 + \frac{\varepsilon}{2\Delta t} \|I_h(z_h - \varphi_h^n)\|_{L^2(D)}^2 - \int_D I_h \left(\frac{\beta}{\varepsilon} \varphi_h^n z_h + \frac{C_w}{\alpha} u_h^n z_h \right) d\mathbf{x} \right\}.$$

We will now consider u_h^{n+1} . We note that (3.4.5) is a linear system, $\mathbf{A}\mathbf{x} = \mathbf{b}$, for matrix \mathbf{A} and vectors \mathbf{x} and \mathbf{b} . If we set $\mathbf{b} = \mathbf{0}$, then we need only show that $\mathbf{x} = \mathbf{0}$. Setting $\mathbf{b} = \mathbf{0}$ in (3.4.5), we have

$$\frac{\varepsilon^2}{\Delta t} \int_D I_h(u_h^{n+1} \phi_h) d\mathbf{x} + \int_D \zeta(\varphi_h^{n+1}) \nabla u_h^{n+1} \cdot \nabla \phi_h d\mathbf{x} + \frac{1}{\alpha\varepsilon} \int_D I_h(\delta(\varphi_h^{n+1}) u_h^{n+1} \phi_h) d\mathbf{x} = 0.$$

We now let $\phi_h = u_h^{n+1}$, to yield

$$\frac{\varepsilon^2}{\Delta t} \|u_h^{n+1}\|_{L_h^2(D)}^2 + \|\zeta(\varphi_h^{n+1})\|_{L^2(D)}^{\frac{1}{2}} \|\nabla u_h^{n+1}\|_{L^2(D)}^2 + \frac{1}{\alpha\varepsilon} \|\delta(\varphi_h^{n+1})\|_{L_h^2(D)}^{\frac{1}{2}} \|u_h^{n+1}\|_{L_h^2(D)}^2 = 0,$$

which then implies, noting (3.5.1), that $u_h^{n+1} = 0$ almost everywhere. □

3.5.2 Convergence of the finite element scheme

In this section, which is adapted from [39], we prove the convergence of the solution of the finite element scheme \mathbb{P}_{DI}^h as $h \rightarrow 0$. Here we fix ε , and assume that $\Delta t \leq Ch^2$. All limits are taken as $h \rightarrow 0$ (and thus $\Delta t \rightarrow 0$). All positive constants C do not depend on h or Δt .

The convergence result given in this section only holds if $D \subset \mathbb{R}^2$, however the stability bounds hold if $D \subset \mathbb{R}^d$, for $d \geq 2$.

Definition 3.5.1 Extension of discrete functions to be continuous in time. For $t \in (t_n, t_{n+1}]$, we define

$$\varphi_h(t) := \frac{t - t_n}{\Delta t} \varphi_h^{n+1} + \frac{t_{n+1} - t}{\Delta t} \varphi_h^n, \quad (3.5.2)$$

$$\varphi_h^+(t) := \varphi_h^{n+1}, \quad \varphi_h^-(t) := \varphi_h^n, \quad (3.5.3)$$

and

$$u_h(t) := \frac{t - t_n}{\Delta t} u_h^{n+1} + \frac{t_{n+1} - t}{\Delta t} u_h^n, \quad (3.5.4)$$

$$u_h^+(t) := u_h^{n+1}, \quad u_h^-(t) := u_h^n. \quad (3.5.5)$$

Rewriting (3.4.6) and (3.4.5) using the above notation gives, for $t \in (t_n, t_{n+1})$,

$$\begin{aligned} & \int_D I_h(\varphi_{h,t}(t)(\rho_h - \varphi_h^+(t))) \, d\mathbf{x} + \beta \int_D \nabla \varphi_h^+(t) \cdot \nabla(\rho_h - \varphi_h^+(t)) \, d\mathbf{x} \\ & - \frac{\beta}{\varepsilon^2} \int_D I_h(\varphi_h^-(t)(\rho_h - \varphi_h^+(t))) \, d\mathbf{x} \geq \frac{C_w}{\alpha\varepsilon} \int_D I_h(u_h^-(t)(\rho_h - \varphi_h^+(t))) \, d\mathbf{x}, \quad \forall \rho_h \in K_h(D), \end{aligned} \quad (3.5.6)$$

and

$$\begin{aligned} & \varepsilon^2 \int_D I_h(u_{h,t}(t)\phi_h) \, d\mathbf{x} + \int_D \zeta(\varphi_h^+(t)) \nabla u_h^+(t) \cdot \nabla \phi_h \, d\mathbf{x} + \frac{1}{\alpha\varepsilon} \int_D I_h(\delta(\varphi_h^+(t))u_h^+(t)\phi_h) \, d\mathbf{x} \\ & = \frac{Q}{\varepsilon} \int_D I_h(\delta(\varphi_h^+(t))\phi_h) \, d\mathbf{x} - \int_D I_h(\zeta(\varphi_h^+(t))\phi_h) \, d\mathbf{x}, \quad \forall \phi_h \in U_h(D). \end{aligned} \quad (3.5.7)$$

This arguments in this section are split into two main steps. In the first step we show the convergence of φ_h , and in the second we show the convergence of u_h , both as $h \rightarrow 0$.

We begin, in Lemma 3.5.2, by proving a bound on $\|u_h^{n+1}\|_{L^\infty(D)}$. This is then used in Lemmas 3.5.3 and 3.5.4 order to prove a number of bounds on φ_h and u_h , respectively. The results of Lemma 3.5.4 allow us to prove a bound on $u_{h,t}$ in Lemma 3.5.5. Collectively, Lemmas 3.5.2 - 3.5.5, along with Theorem 3.2.1, give us the convergence results 3.5.18 - 3.5.25, which are required in Theorem 3.5.6 to prove the convergence of φ_h .

In the second part of this section, we use the results of Lemmas 3.5.2 - 3.5.5 in order to prove a convergence result for $\delta(\varphi_h)u_h$, see Lemma 3.5.7. This is used when showing the convergence of u_h . We then show a convergence result for $\zeta(\varphi_h)u_h$ in Lemma 3.5.8. This

is used in Lemma 3.5.9, where we identify F , which is the limit of $\zeta(\varphi_h^+) \nabla u_h^+$ as $h \rightarrow 0$. Using the results from Lemmas 3.5.7, and 3.5.9 in Theorem 3.5.10, we are able to show the convergence of u_h .

Lemma 3.5.2 If u_h^{n+1} is the solution to (3.4.5), then for $j \in \mathcal{I}$ we have

$$-\|u_h^0\|_{L^\infty(D)} - \frac{n\Delta t}{\varepsilon^2} \leq u_j^{n+1} \leq \max(\alpha Q, \|u_h^0\|_{L^\infty(D)}),$$

where the u_j^{n+1} are the components of u_h^{n+1} , so that

$$u_h^{n+1} = \sum_{j \in \mathcal{I}} u_j^{n+1} \phi_j, \quad \text{for } n = -1, \dots, N-1,$$

for the linear basis functions ϕ_j . Recall that (3.4.4) gives us that $\|u_h^0\|_{L^\infty(D)} \leq C$.

Proof. This proof follows the proof of Lemma 4.1 in [39].

We will use an induction argument, starting with the maximum bound. Assume that $u_{j_0}^n \leq \max(\alpha Q, \|u_h^0\|_{L^\infty(D)})$. If the maximum occurs when $|\varphi_{j_0}^{n+1}| = 1$ (where the φ_j^{n+1} are the components of φ_h^{n+1}) then setting $u_{j_0}^{n+1} := \max_{j \in \mathcal{I}} u_j^{n+1}$ and testing (3.4.5) with $\phi_h = \phi_{j_0}$ (where ϕ_{j_0} is the linear basis function associated with $u_{j_0}^{n+1}$) yields

$$\begin{aligned} \frac{\varepsilon^2}{\Delta t} (u_{j_0}^{n+1} - u_{j_0}^n) \int_D \phi_{j_0} \, d\mathbf{x} + \sum_{\sigma \in \mathcal{T}_D^h} \sum_{i \in \mathcal{I}} u_i^{n+1} \nabla \phi_i|_\sigma \cdot \nabla \phi_{j_0}|_\sigma \int_\sigma \zeta(\varphi_h^{n+1}) \, d\mathbf{x} \\ = -\zeta(\varphi_{j_0}^{n+1}) \int_D \phi_{j_0} \, d\mathbf{x} \leq 0. \end{aligned}$$

Since \mathcal{T}_D^h is of non-negative type, noting (3.4.1) we have

$$\sum_{\sigma \in \mathcal{T}_D^h} \sum_{i \in \mathcal{I}} u_i^{n+1} \nabla \phi_i|_\sigma \cdot \nabla \phi_{j_0}|_\sigma \geq \sum_{\sigma \in \mathcal{T}_D^h} u_{j_0}^{n+1} \sum_{i \in \mathcal{I}} \nabla \phi_i|_\sigma \cdot \nabla \phi_{j_0}|_\sigma. \quad (3.5.8)$$

Since $\sum_{i \in \mathcal{I}} \phi_i = 1$ in D , it follows that $\sum_{\sigma \in \mathcal{T}_D^h} \sum_{i \in \mathcal{I}} \nabla \phi_i|_\sigma \cdot \nabla \phi_{j_0}|_\sigma = 0$, and hence we have $u_{j_0}^{n+1} \leq u_{j_0}^n \leq \max(\alpha Q, \|u_h^0\|_{L^\infty(D)})$.

If the maximum occurs when $|\varphi_{j_0}^{n+1}| < 1$ then using (3.5.8), and testing (3.4.5) with

$\phi_h = \phi_{j_0}$, we have

$$\begin{aligned} \frac{\varepsilon^2}{\Delta t}(u_{j_0}^{n+1} - u_{j_0}^n) \int_D \phi_{j_0} \, d\mathbf{x} &\leq \left(-\zeta(\varphi_{j_0}^{n+1}) + \delta(\varphi_{j_0}^{n+1}) \frac{1}{\varepsilon} \left(Q - \frac{u_{j_0}^{n+1}}{\alpha} \right) \right) \int_D \phi_{j_0} \, d\mathbf{x} \\ &\leq \delta(\varphi_{j_0}^{n+1}) \frac{1}{\varepsilon} \left(Q - \frac{u_{j_0}^{n+1}}{\alpha} \right) \int_D \phi_{j_0} \, d\mathbf{x}. \end{aligned}$$

If $u_{j_0}^{n+1} > \max(\alpha Q, \|u_h^0\|_{L^\infty(D)})$, then we have $u_{j_0}^{n+1} < u_{j_0}^n \leq \max(\alpha Q, \|u_h^0\|_{L^\infty(D)})$. This is a contradiction, and thus $u_{j_0}^{n+1} \leq \max(\alpha Q, \|u_h^0\|_{L^\infty(D)})$.

For the minimum bound, we will again use an induction argument. Assume that $u_{j_0}^n \geq -\frac{n\Delta t}{\varepsilon^2} - \|u_h^0\|_{L^\infty(D)}$. If the minimum occurs when $|\varphi_{j_0}^{n+1}| < 1$ then, letting $u_{j_0}^{n+1} := \min_{j \in \mathcal{I}} u_j^{n+1}$ and testing (3.4.5) with $\phi_h = \phi_{j_0}$, we have

$$\frac{\varepsilon^2}{\Delta t}(u_{j_0}^{n+1} - u_{j_0}^n) \int_D \phi_{j_0} \, d\mathbf{x} \geq \left(-\zeta(\varphi_{j_0}^{n+1}) + \delta(\varphi_{j_0}^{n+1}) \frac{1}{\varepsilon} \left(Q - \frac{u_{j_0}^{n+1}}{\alpha} \right) \right) \int_D \phi_{j_0} \, d\mathbf{x},$$

where we used a similar argument to (3.5.8). If $u_{j_0}^{n+1} \geq 0$, then clearly $u_{j_0}^{n+1} \geq -\frac{(n+1)\Delta t}{\varepsilon^2} - \|u_h^0\|_{L^\infty(D)}$. This means that we need only consider $u_{j_0}^{n+1} < 0$, which implies that $Q - \frac{u_{j_0}^{n+1}}{\alpha} > 0$. Thus

$$\frac{\varepsilon^2}{\Delta t}(u_{j_0}^{n+1} - u_{j_0}^n) \int_D \phi_{j_0} \, d\mathbf{x} \geq -\zeta(\varphi_{j_0}^{n+1}) \int_D \phi_{j_0} \, d\mathbf{x} \geq -\int_D \phi_{j_0} \, d\mathbf{x},$$

and hence we have

$$u_{j_0}^{n+1} \geq -\frac{(n+1)\Delta t}{\varepsilon^2} + u_{j_0}^0 \geq -\frac{(n+1)\Delta t}{\varepsilon^2} - \|u_h^0\|_{L^\infty(D)}.$$

If the minimum occurs when $|\varphi_{j_0}^{n+1}| = 1$, then we test (3.4.5) with $\phi_h = \phi_{j_0}$, and use a similar argument to (3.5.8), to yield

$$\frac{\varepsilon^2}{\Delta t}(u_{j_0}^{n+1} - u_{j_0}^n) \int_D \phi_{j_0} \, d\mathbf{x} \geq -\zeta(\varphi_{j_0}^{n+1}) \int_D \phi_{j_0} \, d\mathbf{x}. \quad (3.5.9)$$

If $\varphi_{j_0}^{n+1} = -1$, then $\zeta(\varphi_{j_0}^{n+1}) = 0$, and so

$$u_{j_0}^{n+1} \geq u_{j_0}^n \geq -\frac{n\Delta t}{\varepsilon^2} - \|u_h^0\|_{L^\infty(D)} \geq -\frac{(n+1)\Delta t}{\varepsilon^2} - \|u_h^0\|_{L^\infty(D)}.$$

If $\varphi_{j_0}^{n+1} = 1$, then $\zeta(\varphi_{j_0}^{n+1}) = 1$. Arguing by contradiction, we assume that $u_{j_0}^{n+1} <$

$-\frac{(n+1)\Delta t}{\varepsilon^2} - \|u_h^0\|_{L^\infty(D)}$. Since $u_{j_0}^n \geq -\frac{n\Delta t}{\varepsilon^2} - \|u_h^0\|_{L^\infty(D)}$, using (3.5.9) we have

$$-\int_D \phi_{j_0} \, d\mathbf{x} = \frac{\varepsilon^2}{\Delta t} \left(-\frac{(n+1)\Delta t}{\varepsilon^2} + \frac{n\Delta t}{\varepsilon^2} \right) \int_D \phi_{j_0} \, d\mathbf{x} > -\int_D \phi_{j_0} \, d\mathbf{x},$$

which is a contradiction, so $u_{j_0}^{n+1} \geq -\frac{(n+1)\Delta t}{\varepsilon^2} - \|u_h^0\|_{L^\infty(D)}$. □

The result given in Lemma 3.5.2 now enables us to prove the bounds on φ_h and u_h given in the following two lemmas.

Lemma 3.5.3 We have that

$$\sup_{t \in [0, T]} \|\nabla \varphi_h\|_{L^2(D)}^2 + \int_0^T \|\varphi_{h,t}\|_{L^2(D)}^2 \, dt \leq C, \quad (3.5.10)$$

and

$$\int_0^T \|\nabla(\varphi_h^+ - \varphi_h^-)\|_{L^2(D)}^2 \, dt \leq C\Delta t. \quad (3.5.11)$$

Proof. This proof follows the proof of Lemma 4.1 in [39].

We show (3.5.10) first, and use this to show (3.5.11). First, test (3.4.6) with $\rho_h = \varphi_h^n \in K_h(D)$, re-arrange, and use (3.5.1) to achieve

$$\begin{aligned} \Delta t \left\| \frac{\varphi_h^{n+1} - \varphi_h^n}{\Delta t} \right\|_{L_h^2(D)}^2 &+ \frac{\beta}{2} \left(\|\nabla \varphi_h^{n+1}\|_{L^2(D)}^2 - \|\nabla \varphi_h^n\|_{L^2(D)}^2 \right) + \frac{\beta}{2} \|\nabla(\varphi_h^{n+1} - \varphi_h^n)\|_{L^2(D)}^2 \\ &+ \frac{\beta}{2\varepsilon^2} \left(\|\varphi_h^n\|_{L_h^2(D)}^2 - \|\varphi_h^{n+1}\|_{L_h^2(D)}^2 \right) + \frac{\beta\Delta t^2}{2\varepsilon^2} \left\| \frac{\varphi_h^{n+1} - \varphi_h^n}{\Delta t} \right\|_{L_h^2(D)}^2 \\ &\leq C_w \frac{\Delta t}{\varepsilon\alpha} \int_D I_h \left(u_h^n \frac{\varphi_h^{n+1} - \varphi_h^n}{\Delta t} \right) \, d\mathbf{x}. \end{aligned}$$

Here we have used that

$$a(a-b) = \frac{1}{2}a^2 - \frac{1}{2}b^2 + \frac{1}{2}(a-b)^2. \quad (3.5.12)$$

Removing terms on the left hand side, we have

$$\begin{aligned} \Delta t \left\| \frac{\varphi_h^{n+1} - \varphi_h^n}{\Delta t} \right\|_{L_h^2(D)}^2 + \frac{\beta}{2} \left(\|\nabla \varphi_h^{n+1}\|_{L^2(D)}^2 - \|\nabla \varphi_h^n\|_{L^2(D)}^2 \right) \\ + \frac{\beta}{2\varepsilon^2} \left(\|\varphi_h^n\|_{L_h^2(D)}^2 - \|\varphi_h^{n+1}\|_{L_h^2(D)}^2 \right) \\ \leq C_w \frac{\Delta t}{\varepsilon \alpha} \int_D I_h \left(u_h^n \frac{\varphi_h^{n+1} - \varphi_h^n}{\Delta t} \right) d\mathbf{x}. \end{aligned}$$

We use Young's inequality with $\gamma \in \mathbb{R}$, $\gamma > 0$, on the right hand side to give

$$\begin{aligned} \Delta t \left\| \frac{\varphi_h^{n+1} - \varphi_h^n}{\Delta t} \right\|_{L_h^2(D)}^2 + \frac{\beta}{2} \left(\|\nabla \varphi_h^{n+1}\|_{L^2(D)}^2 - \|\nabla \varphi_h^n\|_{L^2(D)}^2 \right) \\ + \frac{\beta}{2\varepsilon^2} \left(\|\varphi_h^n\|_{L_h^2(D)}^2 - \|\varphi_h^{n+1}\|_{L_h^2(D)}^2 \right) \\ \leq C \Delta t \left(\gamma \|u_h^n\|_{L_h^2(D)}^2 + \frac{1}{\gamma} \left\| \frac{\varphi_h^{n+1} - \varphi_h^n}{\Delta t} \right\|_{L_h^2(D)}^2 \right). \end{aligned}$$

We now, by choosing $\gamma = 2C$, move the last term on to the left hand side. Summing over $n = 0, \dots, N - 1$ and noting (3.5.1) and Lemma 3.5.2 yields (3.5.10).

In order to show (3.5.11), we consider the inverse estimate, see [30],

$$\Delta t \|\nabla(\varphi_h^{n+1} - \varphi_h^n)\|_{L^2(D)}^2 \leq Ch^{-2} \Delta t \|\varphi_h^{n+1} - \varphi_h^n\|_{L^2(D)}^2 \leq Ch^{-2} (\Delta t)^3 \left\| \frac{\varphi_h^{n+1} - \varphi_h^n}{\Delta t} \right\|_{L^2(D)}^2.$$

Summing the above inequality for $n = 0, \dots, N - 1$ and noting (3.5.10) yields

$$\int_0^T \|\nabla(\varphi_h^+ - \varphi_h^-)\|_{L^2(D)}^2 dt \leq C \frac{\Delta t^2}{h^2} \int_0^T \left\| \frac{\varphi_h^+ - \varphi_h^-}{\Delta t} \right\|_{L^2(D)}^2 dt \leq C \Delta t,$$

by the properties of φ_h^+ and φ_h^- .

□

Lemma 3.5.4 We have

$$\sup_{t \in [0, T]} \|u_h(t)\|_{L^2(D)}^2 \leq C, \quad (3.5.13)$$

$$\int_0^T \left(\left\| [\zeta(\varphi_h^+)]^{\frac{1}{2}} \nabla u_h^+ \right\|_{L^2(D)}^2 + \frac{1}{\alpha \varepsilon} \left\| [\delta(\varphi_h^+)]^{\frac{1}{2}} u_h^+ \right\|_{L^2(D)}^2 \right) dt \leq C, \quad (3.5.14)$$

and

$$\int_0^T \|u_h^+ - u_h^-\|_{L^2(D)}^2 dt \leq C \Delta t. \quad (3.5.15)$$

Proof. This proof follows the proof of Lemma 4.1 in [39].

The bound (3.5.13) follows directly from Lemma 3.5.2. For (3.5.14) and (3.5.15), test (3.4.5) with $\phi_h = \Delta t u_h^{n+1}$, and note (3.5.12), to obtain

$$\begin{aligned} & \frac{\varepsilon^2}{2} \|u_h^{n+1} - u_h^n\|_{L_h^2(D)}^2 + \frac{\varepsilon^2}{2} \left(\|u_h^{n+1}\|_{L_h^2(D)}^2 - \|u_h^n\|_{L_h^2(D)}^2 \right) \\ & \quad + \Delta t \| [\zeta(\varphi_h^{n+1})]^{\frac{1}{2}} \nabla u_h^{n+1} \|_{L^2(D)}^2 + \frac{\Delta t}{\alpha \varepsilon} \| [\delta(\varphi_h^{n+1})]^{\frac{1}{2}} u_h^{n+1} \|_{L_h^2(D)}^2 \\ & = -\Delta t \int_D I_h(\zeta(\varphi_h^{n+1})u_h^{n+1}) \, d\mathbf{x} + \frac{Q\Delta t}{\varepsilon} \int_D I_h(\delta(\varphi_h^{n+1})u_h^{n+1}) \, d\mathbf{x}. \end{aligned}$$

Summing over $n = 0, \dots, N-1$ and recalling Lemma 3.5.2 gives

$$\begin{aligned} & \frac{\varepsilon^2}{2} \sum_{n=0}^{N-1} \|u_h^{n+1} - u_h^n\|_{L_h^2(D)}^2 + \frac{\varepsilon^2}{2} \|u_h^N\|_{L_h^2(D)}^2 + \Delta t \sum_{n=0}^{N-1} \| [\zeta(\varphi_h^{n+1})]^{\frac{1}{2}} \nabla u_h^{n+1} \|_{L^2(D)}^2 \\ & \quad + \Delta t \sum_{n=0}^{N-1} \frac{1}{\alpha \varepsilon} \| [\delta(\varphi_h^{n+1})]^{\frac{1}{2}} u_h^{n+1} \|_{L_h^2(D)}^2 \\ & \leq C \sum_{n=0}^{N-1} \Delta t + \frac{\varepsilon^2}{2} \|u_h^0\|_{L_h^2(D)}^2. \end{aligned} \tag{3.5.16}$$

By the properties of u_h , u_h^+ , and u_h^- , the last two terms on the left hand side of (3.5.16) give us (3.5.14); while considering the first term on the left hand side of (3.5.16), and multiplying through by Δt , gives us (3.5.15). □

We are now able, with the results of Lemma 3.5.4, to show a bound on $u_{h,t}$.

Lemma 3.5.5 We have

$$\int_0^T \|u_{h,t}\|_{(H^1(D))'}^2 \, dt \leq C.$$

Proof. This proof follows the proof of Lemma 4.2 in [39].

Let $\psi \in H^1(D)$ be arbitrary, and let $J_h \psi \in U_h(D)$ be its L^2 -projection such that

$$\int_D v_h \psi \, d\mathbf{x} = \int_D I_h(v_h J_h \psi) \, d\mathbf{x}, \quad \forall v_h \in U_h(D).$$

Testing (3.4.5) with $\phi_h = J_h \psi$ and noting that

$$\varepsilon^2 \left(\frac{u_h^{n+1} - u_h^n}{\Delta t}, \psi \right)_{((H^1)')', H^1} := \varepsilon^2 \int_D u_{h,t} \psi \, d\mathbf{x} = \varepsilon^2 \int_D I_h(u_{h,t} J_h \psi) \, d\mathbf{x},$$

yields,

$$\begin{aligned} \varepsilon^2 \left(\frac{u_h^{n+1} - u_h^n}{\Delta t}, \psi \right)_{((H^1)', H^1)} &= - \int_D \zeta(\varphi_h^{n+1}) \nabla u_h^{n+1} \cdot \nabla (J_h \psi) \, d\mathbf{x} - \int_D I_h (\zeta(\varphi_h^{n+1}) J_h \psi) \, d\mathbf{x} \\ &\quad - \frac{1}{\alpha \varepsilon} \int_D I_h (\delta(\varphi_h^{n+1}) u_h^{n+1} J_h \psi) \, d\mathbf{x} + \frac{Q}{\varepsilon} \int_D I_h (\delta(\varphi_h^{n+1}) J_h \psi) \, d\mathbf{x}. \end{aligned}$$

It can be shown that $\|J_h \psi\|_{H^1(D)} \leq C \|\psi\|_{H^1(D)}$, $\forall \psi \in H^1(D)$ (see, for example, [4]). Using this fact, as well as the bounds on the L^∞ norms of $\delta(\varphi_h^{n+1})$, $\zeta(\varphi_h^{n+1})$, and u_h^{n+1} , we have the following for all $\psi \in H^1(D)$, and for (t_n, t_{n+1}) ,

$$\begin{aligned} \varepsilon^2 \left(\frac{u_h^{n+1} - u_h^n}{\Delta t}, \psi \right)_{((H^1)', H^1)} &\leq C \left\| [\zeta(\varphi_h^{n+1})]^{\frac{1}{2}} \nabla u_h^{n+1} \right\|_{L^2(D)} \|\nabla (J_h \psi)\|_{L^2(D)} + C \|\psi\|_{L^2(D)} \\ &\leq C \left(1 + \left\| [\zeta(\varphi_h^{n+1})]^{\frac{1}{2}} \nabla u_h^{n+1} \right\|_{L^2(D)} \right) \|\psi\|_{H^1(D)}. \quad (3.5.17) \end{aligned}$$

We conclude that, for $t \in (t_n, t_{n+1})$,

$$\left\| \frac{u_h^{n+1} - u_h^n}{\Delta t} \right\|_{(H^1(D))'} \leq C + C \left\| [\zeta(\varphi_h^{n+1})]^{\frac{1}{2}} \nabla u_h^{n+1} \right\|_{L^2(D)}.$$

Squaring, multiplying by Δt , and summing from $n = 0, \dots, N-1$ yields, in light of Lemma 3.5.4, the required result. □

From Lemmas 3.5.2 - 3.5.5 (and recalling Theorem 3.2.1, with $p = r = 2$, $s = 1$, $X = H^1(D)$ and $Y = B = L^2(D)$) we have (after possibly re-indexing from subsequences),

as $h \rightarrow 0$,

$$\varphi_h, \varphi_h^-, \varphi_h^+ \rightharpoonup \varphi \quad \text{in } L^2(0, T; H^1(D)), \quad (3.5.18)$$

$$\varphi_{h,t} \rightharpoonup \varphi_t \quad \text{in } L^2(0, T; L^2(D)), \quad (3.5.19)$$

$$\varphi_h, \varphi_h^-, \varphi_h^+ \rightarrow \varphi \quad \text{in } L^2(0, T; L^2(D)), \quad (3.5.20)$$

$$\zeta(\varphi_h), \zeta(\varphi_h^-), \zeta(\varphi_h^+) \rightarrow \zeta(\varphi) \quad \text{in } L^2(0, T; L^2(D)), \quad (3.5.21)$$

$$\delta(\varphi_h), \delta(\varphi_h^-), \delta(\varphi_h^+) \rightharpoonup \delta(\varphi) \quad \text{in } L^2(0, T; L^2(D)), \quad (3.5.22)$$

$$u_h, u_h^-, u_h^+ \overset{*}{\rightharpoonup} u \quad \text{in } L^\infty(D \times (0, T)), \quad (3.5.23)$$

$$u_{h,t} \rightharpoonup u_t \quad \text{in } L^2(0, T; (H^1(D))'), \quad (3.5.24)$$

$$\zeta(\varphi_h^+) \nabla u_h^+ \rightharpoonup F \quad \text{in } L^2(0, T; [L^2(D)]^2). \quad (3.5.25)$$

Here (3.5.25) follows directly from (3.5.14) and the bound on the L^∞ norm of $\zeta(\varphi_h^+)$. The function F will be identified later, see Lemma 3.5.9.

Theorem 3.5.6 For $D \subset \mathbb{R}^2$, the functions φ and u in (3.5.18) - (3.5.24) satisfy, for almost every $t \in (0, T)$,

$$\begin{aligned} \int_D \varphi_t(\rho - \varphi) \, d\mathbf{x} + \beta \int_D \nabla \varphi \cdot \nabla(\rho - \varphi) \, d\mathbf{x} - \frac{\beta}{\varepsilon^2} \int_D \varphi(\rho - \varphi) \, d\mathbf{x} \\ \geq \frac{C_w}{\alpha \varepsilon} \int_D u(\rho - \varphi) \, d\mathbf{x}, \quad \forall \rho \in K(D). \end{aligned}$$

Proof. This proof follows the proof of Theorem 1 in [39].

Multiply (3.5.6) by an arbitrary $\psi \in C_0^\infty(0, T)$, $\psi \geq 0$, and integrate over $t \in (0, T)$,

$$\begin{aligned} \int_0^T \psi \int_D I_h(\varphi_{h,t}(\rho_h - \varphi_h^+)) \, d\mathbf{x} \, dt + \beta \int_0^T \psi \int_D \nabla \varphi_h^+ \cdot \nabla \rho_h \, d\mathbf{x} \, dt \\ - \frac{\beta}{\varepsilon^2} \int_0^T \psi \int_D I_h(\varphi_h^-(\rho_h - \varphi_h^+)) \, d\mathbf{x} \, dt - \frac{C_w}{\varepsilon \alpha} \int_0^T \psi \int_D I_h(u_h^-(\rho_h - \varphi_h^+)) \, d\mathbf{x} \, dt \\ \geq \beta \int_0^T \psi \int_D |\nabla \varphi_h^+|^2 \, d\mathbf{x} \, dt. \end{aligned}$$

Let $\rho \in K(D)$, there exists a sequence $\rho_h \in K_h(D)$ such that $\rho_h \rightarrow \rho$ in $H^1(D)$ as $h \rightarrow 0$. We use the well known inequality, see [30],

$$\left| \int_D \eta \chi \, dx - \int_D I_h(\eta \chi) \, dx \right| \leq Ch \|\nabla \eta\|_{L^2(D)} \|\chi\|_{L^2(D)}, \quad \text{for } \eta, \chi \in U_h(D). \quad (3.5.26)$$

We also consider (3.5.18) - (3.5.20) and (3.5.23), and use the weak lower semi-continuity of the L^2 norm (which gives that $\|\nabla\varphi\|_{L^2(D)}^2 \leq \liminf_{h \rightarrow 0} \|\nabla\varphi_h^+\|_{L^2(D)}^2$), to yield

$$\begin{aligned} \int_0^T \psi \int_D \varphi_t(\rho - \varphi) \, d\mathbf{x} \, dt + \beta \int_0^T \psi \int_D \nabla\varphi \cdot \nabla\rho \, d\mathbf{x} \, dt - \frac{\beta}{\varepsilon^2} \int_0^T \psi \int_D \varphi(\rho - \varphi) \, d\mathbf{x} \, dt \\ - \frac{C_w}{\alpha\varepsilon} \int_0^T \psi \int_D u(\rho - \varphi) \, d\mathbf{x} \, dt \geq \beta \int_0^T \psi \int_D |\nabla\varphi|^2 \, d\mathbf{x} \, dt, \end{aligned}$$

as $h \rightarrow 0$. Since $\psi \geq 0$ is arbitrary, this gives us the required result. \square

The convergence result given in the following lemma is used directly when proving the convergence result in Theorem 3.5.10.

Lemma 3.5.7 For $D \subset \mathbb{R}^2$, we have $\delta(\varphi)u \in L^2(0, T; H^1(D))$ and (after possibly re-indexing from subsequences), as $h \rightarrow 0$,

$$\delta(\varphi_h)u_h \rightarrow \delta(\varphi)u \quad \text{in } L^2(0, T; L^2(D)). \quad (3.5.27)$$

Proof. This proof follows the proof of Lemma 4.3 in [39].

We first obtain a bound on $\delta(\varphi_h)u_h$ in $L^2(0, T; H^1(D))$ and then we obtain a bound on $(\delta(\varphi_h)u_h)_t$ in $L^2(0, T; (W^{1,q}(D))')$, $q > 2$. Combining these bounds and using Theorem 3.2.1 will then yield the desired result. To bound $\|\nabla(\delta(\varphi_h)u_h)\|_{L^2(D)}^2$ we first note that from Lemma 3.5.3 we have $\|\nabla\delta(\varphi_h)\|_{L^2(D)}^2 \leq C$, and thus

$$\begin{aligned} \|\nabla(\delta(\varphi_h)u_h)\|_{L^2(D)}^2 &\leq C\|\nabla\delta(\varphi_h)\|_{L^2(D)}^2\|u_h\|_{L^\infty(D)}^2 + C \int_D \delta(\varphi_h)^2 |\nabla u_h|^2 \, d\mathbf{x} \\ &\leq C + C \int_D \delta(\varphi_h)^2 |\nabla u_h|^2 \, d\mathbf{x}. \end{aligned}$$

For $t \in (t_n, t_{n+1})$

$$\delta(\varphi_h) \leq \delta(\varphi_h^{n+1}) + C|\varphi_h^{n+1} - \varphi_h^n|,$$

we square both sides to yield

$$\delta(\varphi_h)^2 \leq C\delta(\varphi_h^{n+1})^2 + C|\varphi_h^{n+1} - \varphi_h^n|^2.$$

We also note that

$$|\nabla u_h|^2 \leq C|\nabla u_h^{n+1}|^2 + C|\nabla(u_h^{n+1} - u_h^n)|^2.$$

Using the previous two inequalities and the bound on the L^∞ norm of $\delta_h(\varphi_h^{n+1})$, for $t \in (t_n, t_{n+1})$, we have

$$\begin{aligned} \int_D \delta(\varphi_h)^2 |\nabla u_h|^2 \, d\mathbf{x} &\leq C \int_D \delta(\varphi_h^{n+1})^2 |\nabla u_h|^2 \, d\mathbf{x} + C \int_D |\varphi_h^{n+1} - \varphi_h^n|^2 |\nabla u_h|^2 \, d\mathbf{x} \\ &\leq C \int_D \delta(\varphi_h^{n+1})^2 |\nabla u_h^{n+1}|^2 \, d\mathbf{x} + C \int_D \delta(\varphi_h^{n+1})^2 |\nabla(u_h^{n+1} - u_h^n)|^2 \, d\mathbf{x} \\ &\quad + C \int_D |\varphi_h^{n+1} - \varphi_h^n|^2 |\nabla u_h|^2 \, d\mathbf{x} \\ &\leq C \|\delta(\varphi_h^{n+1})\|_{L^2(D)}^{\frac{1}{2}} \|\nabla u_h^{n+1}\|_{L^2(D)}^2 + Ch^{-2} \|u_h^{n+1} - u_h^n\|_{L^2(D)}^2 \\ &\quad + Ch^{-2} \|u_h\|_{L^\infty(D)}^2 \|\varphi_h^{n+1} - \varphi_h^n\|_{L^2(D)}^2, \end{aligned}$$

where we have applied Hölder's inequality and, noting that we are restricting ourselves to $D \subset \mathbb{R}^2$, the inverse estimate, see [30],

$$\|\nabla u_h\|_{L^p(D)} \leq Ch^{-1} \|u_h\|_{L^p(D)}, \quad (3.5.28)$$

for $p = 2$ and $p = \infty$. Summing over n and multiplying by Δt yields, in light of the properties of u_h^+ , u_h^- , φ_h^+ , and φ_h^- ,

$$\begin{aligned} \int_0^T \int_D \delta(\varphi_h)^2 |\nabla u_h|^2 \, d\mathbf{x} \, dt &\leq C \int_0^T \|\zeta(\varphi_h^+)\|_{L^2(D)}^{\frac{1}{2}} \|\nabla u_h^+\|_{L^2(D)}^2 \, dt + Ch^{-2} \int_0^T \|u_h^+ - u_h^-\|_{L^2(D)}^2 \, dt \\ &\quad + Ch^{-2} \int_0^T \|\varphi_h^+ - \varphi_h^-\|_{L^2(D)}^2 \, dt \\ &\leq C + Ch^{-2} \Delta t \leq C, \end{aligned}$$

where we used the fact that $\delta(\varphi_h^+) = \frac{2}{\pi}(1 - (\varphi_h^+)^2) = \frac{2}{\pi}(1 + \varphi_h^+)(1 - \varphi_h^+) \leq C\zeta(\varphi_h^+)$, and bounds from Lemmas 3.5.3 and 3.5.4.

Fix $q > 2$, we now bound

$$\int_0^T \|(\delta(\varphi_h)u_h)_t\|_{(W^{1,q}(D))'} \, dt. \quad (3.5.29)$$

Let $\psi \in W^{1,q}(D)$ be arbitrary. Then for $t \in (t_n, t_{n+1})$ we have

$$\begin{aligned}
((\delta(\varphi_h)u_h)_t, \psi)_{((W^{1,q})', W^{1,q})} &= \int_D (\delta(\varphi_h)u_h)_t \psi \, d\mathbf{x} \\
&\leq C \left| \int_D \varphi_h \varphi_{h,t} u_h \psi \, d\mathbf{x} \right| + C \left| \int_D \delta(\varphi_h) u_{h,t} \psi \, d\mathbf{x} \right| \\
&\leq C \|\psi\|_{L^2(D)} \|\varphi_{h,t}\|_{L^2(D)} + \|u_{h,t}\|_{(H^1(D))'} \|\psi \delta(\varphi_h)\|_{H^1(D)} \\
&\leq C \|\psi\|_{L^2(D)} \|\varphi_{h,t}\|_{L^2(D)} \\
&\quad + \|u_{h,t}\|_{(H^1(D))'} (\|\psi\|_{H^1(D)} + \|\psi\|_{L^\infty(D)} \|\delta(\varphi_h)\|_{H^1(D)}) \\
&\leq C \|\psi\|_{W^{1,q}(D)} \left(\|\varphi_{h,t}\|_{L^2(D)} + \|u_{h,t}\|_{(H^1(D))'} \right. \\
&\quad \left. + \|u_{h,t}\|_{(H^1(D))'} \|\varphi_h\|_{H^1(D)} \right).
\end{aligned}$$

Using bounds from Lemmas 3.5.3 and 3.5.5, and the continuous embedding $W^{1,q}(D) \hookrightarrow C^0(\overline{D})$, we deduce a bound on (3.5.29). This, combined with the bound $\|\nabla(\delta(\varphi_h)u_h)\|_{L^2(D)}^2 \leq C$ and Theorem 3.2.1, with $p = r = 2$, $s = 1$, $X = H^1(D)$, $Y = (W^{1,q}(D))'$, and $B = L^2(D)$ yields the required result. \square

The convergence result given in the following lemma is not used directly in Theorem 3.5.10, however it is used in the subsequent lemma, Lemma 3.5.9, in which we identify F .

Lemma 3.5.8 For $D \subset \mathbb{R}^2$ we have, after possibly re-indexing from sub-sequences, as $h \rightarrow 0$,

$$\zeta(\varphi_h)u_h \rightarrow \zeta(\varphi)u \quad \text{in } L^2(0, T; L^2(D)). \quad (3.5.30)$$

Proof. This proof follows the proof of Lemma 4.3 in [39].

Similar to the proof of Lemma 3.5.7 we first obtain a bound on $\zeta(\varphi_h)u_h$ in $L^2(0, T; H^1(D))$ and then we obtain a bound on $(\zeta(\varphi_h)u_h)_t$ in $L^2(0, T; (W^{1,q}(D))')$. Combining these bounds and using Theorem 3.2.1 will then yield the desired result. Following a similar argument to the one in the proof of Lemma 3.5.7 we have, using the inverse estimate

(3.5.28), Hölder's inequality, and Lemma 3.5.2, for $t \in (t_n, t_{n+1})$,

$$\begin{aligned}
\|\nabla(\zeta(\varphi_h)u_h)\|_{L^2(D)}^2 &\leq C\|\nabla\varphi_h\|_{L^2(D)}^2\|u_h\|_{L^\infty(D)}^2 + C\int_D \zeta(\varphi_h)^2|\nabla u_h|^2 \, d\mathbf{x} \\
&\leq C\|\nabla\varphi_h\|_{L^2(D)}^2 + C\int_D \zeta(\varphi_h^{n+1})|\nabla u_h|^2 \, d\mathbf{x} \\
&\quad + C\int_D |\nabla u_h|^2|\varphi_h^{n+1} - \varphi_h^n|^2 \, d\mathbf{x} \\
&\leq C\|\nabla\varphi_h\|_{L^2(D)}^2 + C\int_D \zeta(\varphi_h^{n+1})|\nabla u_h^{n+1}|^2 \, d\mathbf{x} \\
&\quad + C\int_D \zeta(\varphi_h^{n+1})|\nabla(u_h^{n+1} - u_h^n)|^2 \, d\mathbf{x} \\
&\quad + C\int_D |\nabla u_h|^2|\varphi_h^{n+1} - \varphi_h^n|^2 \, d\mathbf{x} \\
&\leq C\|\nabla\varphi_h\|_{L^2(D)}^2 + C\|\zeta(\varphi_h^{n+1})\|_{L^2(D)}^{\frac{1}{2}}\|\nabla u_h^{n+1}\|_{L^2(D)}^2 + Ch^{-2}\|u_h^{n+1} - u_h^n\|_{L^2(D)} \\
&\quad + C\|\nabla u_h\|_{L^\infty(D)}^2\|\varphi_h^{n+1} - \varphi_h^n\|_{L^2(D)}^2 \\
&\leq C\|\nabla\varphi_h\|_{L^2(D)}^2 + C\|\zeta(\varphi_h^{n+1})\|_{L^2(D)}^{\frac{1}{2}}\|\nabla u_h^{n+1}\|_{L^2(D)}^2 + Ch^{-2}\|u_h^{n+1} - u_h^n\|_{L^2(D)} \\
&\quad + Ch^{-2}\|\varphi_h^{n+1} - \varphi_h^n\|_{L^2(D)}^2.
\end{aligned}$$

Multiplying by Δt , summing over n , and using results from Lemmas 3.5.3 and 3.5.4, yields

$$\begin{aligned}
\int_0^T \|\nabla(\zeta(\varphi_h)u_h)\|_{L^2(D)}^2 \, dt &\leq C\int_0^T \|\nabla\varphi_h\|_{L^2(D)}^2 \, dt + C\int_0^T \|\zeta(\varphi_h^+)\|_{L^2(D)}^{\frac{1}{2}}\|\nabla u_h^+\|_{L^2(D)}^2 \, dt \\
&\quad + Ch^{-2}\int_0^T \|u_h^+ - u_h^-\|_{L^2(D)}^2 \, dt \\
&\quad + Ch^{-2}\int_0^T \|\varphi_h^+ - \varphi_h^-\|_{L^2(D)}^2 \, dt \\
&\leq C + Ch^{-2}\Delta t \leq C.
\end{aligned} \tag{3.5.31}$$

Fix $q > 2$. Now we bound

$$\int_0^T \|(\zeta(\varphi_h)u_h)_t\|_{(W^{1,q}(D))'} \, dt. \tag{3.5.32}$$

Let $\psi \in W^{1,q}(D)$ be arbitrary, then for $t \in (t_n, t_{n+1})$ we have

$$\begin{aligned}
((\zeta(\varphi_h)u_h)_t, \psi)_{(W^{1,q})', W^{1,q}} &= \int_D (\zeta(\varphi_h)u_h)_t \psi \, d\mathbf{x} \\
&= \int_D (\zeta(\varphi_h))_t u_h \psi \, d\mathbf{x} + \int_D \zeta(\varphi_h) u_{h,t} \psi \, d\mathbf{x} \\
&\leq C \|\varphi_{h,t}\|_{L^2(D)} \|\psi\|_{L^2(D)} + C \|u_{h,t}\|_{(H^1(D))'} \|\zeta(\varphi_h)\psi\|_{H^1(D)} \\
&\leq C \|\varphi_{h,t}\|_{L^2(D)} \|\psi\|_{L^2(D)} \\
&\quad + C \|u_{h,t}\|_{(H^1(D))'} (\|\psi\|_{H^1(D)} + \|\psi\|_{L^\infty(D)} \|\zeta(\varphi_h)\|_{H^1(D)}) \\
&\leq C \|\psi\|_{W^{1,q}(D)} \left(\|\varphi_{h,t}\|_{L^2(D)} + \|u_{h,t}\|_{(H^1(D))'} \right. \\
&\quad \left. + \|u_{h,t}\|_{(H^1(D))'} \|\varphi_h\|_{H^1(D)} \right),
\end{aligned}$$

where we used Hölder's inequality and Lemma 3.5.2. Using Lemmas 3.5.3 and 3.5.5, and the continuous embedding $W^{1,q}(D) \hookrightarrow C^0(\overline{D})$, we deduce the bound on (3.5.32). This, along with the bound $\|\nabla(\zeta_h u_h)\|_{L^2(D)}^2 \leq C$, gives us (3.5.30) by Theorem 3.2.1, with $p = r = 2$, $s = 1$, $X = H^1(D)$, $Y = (W^{1,q}(D))'$ and $B = L^2(D)$.

□

In order to identify F , we define the set

$$U := \{ (\mathbf{x}, t) \in D \times (0, T) \mid \zeta(\varphi(\mathbf{x}, t)) > 0 \}.$$

By the convergence result (3.5.23) we see that u belongs to $L^\infty(D \times (0, T))$. Regularity theory for parabolic variational inequalities (see [49]) gives us

$$\varphi \in L^p(0, T; W^{2,p}(D)), \quad \text{and} \quad \varphi_t \in L^p(0, T; L^p(D)), \quad \forall p < \infty.$$

Thus, by standard embedding results, $\varphi \in C^0(\overline{D \times (0, T)})$. This tells us that the set U is open.

Lemma 3.5.9 For $D \subset \mathbb{R}^2$, the F in (3.5.25) satisfies $F = \chi(U)\zeta(\varphi)\nabla u$ almost everywhere in $D \times (0, T)$, where $\chi(U)$ is the characteristic function of U .

Proof. This proof follows the proof of Lemma 4.4 in [39].

In order to identify F on U we show that $(\zeta(\varphi)^2 u)_{x_i} \in L^2(0, T; L^2(D))$ and

$$(\zeta(\varphi)^2 u)_{x_i} = \zeta(\varphi) u_{\varphi_{x_i}} + F_i \zeta(\varphi). \quad (3.5.33)$$

By Lemma 3.5.8 we have $\zeta(\varphi_h) u_h \rightarrow \zeta(\varphi) u$ in $L^2(0, T; L^2(D))$, so that (noting (3.5.21))

$$\int_0^T \int_D \zeta(\varphi)^2 u \psi_{x_i} \, d\mathbf{x} \, dt = \lim_{h \rightarrow 0} \int_0^T \int_D \zeta(\varphi_h)^2 u_h \psi_{x_i} \, d\mathbf{x} \, dt, \quad \forall \psi \in C_0^\infty(D \times (0, T)).$$

Using integration by parts on the right hand side integral we have

$$\begin{aligned} \int_0^T \int_D \zeta(\varphi_h)^2 u_h \psi_{x_i} \, d\mathbf{x} \, dt &= - \int_0^T \int_D \zeta(\varphi_h)^2 u_{h,x_i} \psi \, d\mathbf{x} \, dt - \int_0^T \int_D (\zeta(\varphi_h)^2)_{x_i} u_h \psi \, d\mathbf{x} \, dt \\ &= - \int_0^T \int_D \zeta(\varphi_h) (\zeta(\varphi_h) u_{h,x_i}) \psi \, d\mathbf{x} \, dt \\ &\quad - \int_0^T \int_D \zeta(\varphi_h) u_h \varphi_{h,x_i} \psi \, d\mathbf{x} \, dt. \end{aligned}$$

Since $\zeta(\varphi_h) u_h \rightarrow \zeta(\varphi) u$ in $L^2(0, T; L^2(D))$ (by (3.5.30)), the dominated convergence theorem implies that $\zeta(\varphi_h) u_h \psi \rightarrow \zeta(\varphi) u \psi$ in $L^2(0, T; L^2(D))$. Using this, and $\nabla \varphi_h \rightarrow \nabla \varphi$ in $L^2(0, T; [L^2(D)]^2)$ from (3.5.18), we have

$$\int_0^T \int_D \zeta(\varphi_h) u_h \varphi_{h,x_i} \psi \, d\mathbf{x} \, dt \rightarrow \int_0^T \int_D \zeta(\varphi) u \varphi_{x_i} \psi \, d\mathbf{x} \, dt, \quad \forall \psi \in C_0^\infty(D \times (0, T)).$$

By (3.5.25) and (3.5.21) we have

$$\int_0^T \int_D \zeta(\varphi_h) (\zeta(\varphi_h) u_{h,x_i}) \psi \, d\mathbf{x} \, dt \rightarrow \int_0^T \int_D \zeta(\varphi) F_i \psi \, d\mathbf{x} \, dt, \quad \forall \psi \in C_0^\infty(D \times (0, T)).$$

Thus, as ψ is arbitrary, we have (3.5.33) almost everywhere.

We now identify F on U . Let $\psi \in C_0^\infty(U)$ be arbitrary. Using integration by parts we have

$$\begin{aligned} - \int_U u_{x_i} \psi \, d\mathbf{x} &= \int_U u \psi_{x_i} \, d\mathbf{x} = \int_U \zeta(\varphi)^2 u \frac{1}{\zeta(\varphi)^2} \psi_{x_i} \, d\mathbf{x} \\ &= - \int_U (\zeta(\varphi)^2 u)_{x_i} \frac{\psi}{\zeta(\varphi)^2} \, d\mathbf{x} + \int_U \frac{1}{\zeta(\varphi)} u \varphi_{x_i} \psi \, d\mathbf{x}. \end{aligned}$$

Substituting in (3.5.33), we have

$$-\int_U u_{x_i} \psi \, d\mathbf{x} = -\int_U F_i \frac{1}{\zeta(\varphi)} \psi \, d\mathbf{x}.$$

Since ψ is arbitrary, this gives us that $u_{x_i} \zeta(\varphi) = F_i$ almost everywhere on U .

It remains to identify F on U^c , where $U^c := D \times (0, T) \setminus U$. Let $\psi \in C_0^\infty(D \times (0, T))$ be arbitrary. We use that $1 - \chi(U) = 0$ on U to give

$$\begin{aligned} \left| \int_{U^c} \zeta(\varphi_h^+) u_{h,x_i}^+ \psi \, d\mathbf{x} \, dt \right| &= \left| \int_0^T \int_D \zeta(\varphi_h^+) u_{h,x_i}^+ (1 - \chi(U)) \psi \, d\mathbf{x} \, dt \right| \\ &\leq \left(\int_0^T \int_D \zeta(\varphi_h^+) |\nabla u_h^+|^2 \, d\mathbf{x} \, dt \right)^{\frac{1}{2}} \left(\int_0^T \int_D \zeta(\varphi_h^+) (1 - \chi(U))^2 \psi^2 \, d\mathbf{x} \, dt \right)^{\frac{1}{2}}. \end{aligned} \quad (3.5.34)$$

We know from (3.5.14) that

$$\left(\int_0^T \int_D \zeta(\varphi_h^+) |\nabla u_h^+|^2 \, d\mathbf{x} \, dt \right)^{\frac{1}{2}} \leq C.$$

Considering the second term on the right hand side of (3.5.34), we use the fact that $\zeta(\varphi)(1 - \chi(U)) = 0$ almost everywhere in $D \times (0, T)$, along with (3.5.21), to see that, as $h \rightarrow 0$,

$$\left(\int_0^T \int_D \zeta(\varphi_h^+) (1 - \chi(U))^2 \psi^2 \, d\mathbf{x} \, dt \right)^{\frac{1}{2}} \rightarrow \left(\int_0^T \int_D \zeta(\varphi) (1 - \chi(U))^2 \psi^2 \, d\mathbf{x} \, dt \right)^{\frac{1}{2}} = 0.$$

Thus, from (3.5.34), we have

$$\int_{U^c} \zeta(\varphi_h^+) u_{h,x_i}^+ \psi \, d\mathbf{x} \, dt \rightarrow 0, \quad \text{as } h \rightarrow 0.$$

Recalling (3.5.25), we have

$$\int_0^T \int_D \zeta(\varphi_h^+) u_{h,x_i}^+ \psi \, d\mathbf{x} \, dt \rightarrow \int_0^T \int_D F_i \psi \, d\mathbf{x} \, dt.$$

We conclude that $F_i = 0$ almost everywhere in U^c . □

Lemma 3.5.9 and (3.5.25) give us, as $h \rightarrow 0$ (after possibly re-indexing from subse-

quences)

$$\zeta(\varphi_h^+) \nabla u_h^+ \rightharpoonup \chi(U) \zeta(\varphi) \nabla u \quad \text{in } L^2(0, T; [L^2(D)]^2). \quad (3.5.35)$$

Theorem 3.5.10 For $D \subset \mathbb{R}^2$, the functions φ and u in (3.5.18) - (3.5.24), (3.5.27), and (3.5.35) satisfy

$$\begin{aligned} & \varepsilon^2 \int_0^T \psi(u_t, \phi)_{((H^1)', H^1)} dt + \int_{\{\zeta(\varphi) > 0\}} \psi \zeta(\varphi) \nabla u \cdot \nabla \phi \, d\mathbf{x} \, dt \\ & + \frac{1}{\alpha \varepsilon} \int_0^T \psi \int_D \delta(\varphi) u \phi \, d\mathbf{x} \, dt = \frac{Q}{\varepsilon} \int_0^T \psi \int_D \delta(\varphi) \phi \, d\mathbf{x} \, dt - \int_0^T \psi \int_D \zeta(\varphi) \phi \, d\mathbf{x} \, dt, \end{aligned} \quad (3.5.36)$$

for arbitrary $\phi \in H^1(D)$ and $\psi \in C_0^\infty(0, T)$.

Proof. This proof follows arguments made on page 16 of [39].

Multiply (3.5.7) by $\psi \in C_0^\infty(0, T)$, and integrate over t , to yield

$$\begin{aligned} & \underbrace{\varepsilon^2 \int_0^T \psi \int_D I_h(u_{h,t} \phi_h) \, d\mathbf{x} \, dt}_{(1)} + \underbrace{\int_0^T \psi \int_D \zeta(\varphi_h^+) \nabla u_h^+ \cdot \nabla \phi_h \, d\mathbf{x} \, dt}_{(2)} \\ & + \frac{1}{\alpha \varepsilon} \underbrace{\int_0^T \psi \int_D I_h(\delta(\varphi_h^+) u_h^+ \phi_h) \, d\mathbf{x} \, dt}_{(3)} \\ & = \frac{Q}{\varepsilon} \underbrace{\int_0^T \psi \int_D I_h(\delta(\varphi_h^+) \phi_h) \, d\mathbf{x} \, dt}_{(4)} \\ & - \underbrace{\int_0^T \psi \int_D I_h(\zeta(\varphi_h^+) \phi_h) \, d\mathbf{x} \, dt}_{(5)}. \end{aligned} \quad (3.5.37)$$

We consider the convergence of the integrals in (3.5.37), as $h \rightarrow 0$, to the corresponding terms in (3.5.36). For $\phi \in H^1(D)$ there exists a sequence $\phi_h \in U_h(D)$ such that $\phi_h \rightarrow \phi$ in $H^1(D)$. For integrals (1), (3), (4), and (5) we use (3.5.26). For integral (1), we use (3.5.24). For integral (2) we use (3.5.35). For integral (3) we use (3.5.27). For integral (4) we use (3.5.22). For integral (5) we use (3.5.21). This yields the required result. \square

Chapter 4

Numerical simulations

In this chapter we first reformulate and regularise (1.1.13a) - (1.1.13c) to obtain an alternative model, $(\tilde{\mathbb{M}})$, to (\mathbb{M}) . We present finite element approximations of these alternative models, and also a finite element approximation of a diffuse interface approximation to (\mathbb{M}) that does not include the regularising $\varepsilon^2 u_t$ term introduced in Chapter 3. We follow this with a summary of the implementations of the different finite element schemes. We then present a number of numerical simulations obtained from these finite element approximations, together with the finite element approximations of (\mathbb{M}) introduced in Chapter 2.

We begin the numerical simulations by testing the accuracy of the numerical schemes, we do this by considering a radially symmetric geometry, which enables us to compute analytic solutions of (\mathbb{M}) . At the start of Section 4.4 we present a number of graphs in which we compare the analytic radius with the computed radius, and compare the profile of the analytic solution u with the numerical solution u_h , computed with sharp interface and diffuse interface finite element schemes, where appropriate. This is done in both \mathbb{R}^2 and \mathbb{R}^3 . We then, in Section 4.4.1, use the analytic solution to compute the experimental order of convergence for the sharp interface finite element approximations of (\mathbb{M}) . We then show some radially symmetric simulations in \mathbb{R}^3 in Section 4.4.2.

The next section, Section 4.4.3, shows that for small enough γ the effect of the regularising term $\gamma \nabla u \cdot \mathbf{n}$ (that is introduced in $(\tilde{\mathbb{M}})$) is negligible.

In Section 4.4.4, we investigate the effect of the parameters on the morphological stability of the geometries arising in the radially symmetric sharp interface simulations of

(M). In particular we investigate in which parameter regimes spheroids become unstable and lose their radial symmetry.

In Section 4.5 we present simulations in \mathbb{R}^2 . In Sections 4.5.1 - 4.5.3, we fix $Q = 1.0$ and investigate the relationship between α and β . In particular we consider the parameter spaces $\alpha < \beta$, $\alpha > \beta$, and $\alpha, \beta \ll 1.0$. The simulations presented include a number of complex initial geometries, comparisons between the alternate formulations of the model, and formally setting $\alpha = 0$. The section concludes with the presentation of a number of *in vivo* tumours.

In the final section, Section 4.6, we present simulations in \mathbb{R}^3 . In these simulations we restrict ourselves to the original model (M). Similar to in Section 4.5, we start by fixing $Q = 1.25$ in order to investigate the relationship between α and β . In particular, Sections 4.6.1 and 4.6.2 investigate the cases $\alpha > \beta$ and $\alpha, \beta \ll 1.0$. We do not investigate $\beta > \alpha$, as we found that, similar to in \mathbb{R}^2 , our simulations tend to a spherical steady state with a small radius. Section 4.6 includes a comparison between the sharp interface and diffuse interface schemes, run with a number of different initial geometries. The section concludes with the presentation of a number of *in vivo* tumours.

Throughout this chapter we use u_h to mean both $u_h := \{u_h^n\}_{n=0}^N$, and $u_h := u_h^n$ for some n . We use a similar notation for \mathbf{X}_h , φ_h , Γ_h , and Ω_h . For a function f that is continuous in time we write $f^n := f(t_n)$.

4.1 Alternate formulation of the model

In Section 1.1 we derive the system (1.1.13a) - (1.1.13c), which we then regularise to yield (M). We now arrange (1.1.13a) - (1.1.13c) in a different way and then regularise as before, in order to obtain an alternative formulation.

Our reason for considering this alternative formulation is that it enables us to set $\alpha = 0$, which is clearly not possible for (M).

For the alternative formulation we take (1.1.13c) as the boundary condition for (1.1.13a), and substitute (1.1.13c) into (1.1.13b) to yield a velocity law for $\Gamma(t)$. Then for ease of computation, we regularise the boundary condition (1.1.13c) with a $\gamma \nabla u \cdot \mathbf{n}$ term, where $\gamma \in \mathbb{R}$ taken small and positive. This is done in order to maintain Robin boundary conditions, so that only a minor modification of the computer program for the original

formulation is necessary. In addition we regularise the velocity law with a $\beta\kappa$ term. This results in the following model

$$\Delta u = 1, \quad \text{in } \Omega(t), \quad (\tilde{\mathbb{M}}\text{a})$$

$$\gamma \nabla u \cdot \mathbf{n} + u = \alpha V, \quad \text{on } \Gamma(t), \quad (\tilde{\mathbb{M}}\text{b})$$

$$V = Q - \nabla u \cdot \mathbf{n} + \beta\kappa, \quad \text{on } \Gamma(t). \quad (\tilde{\mathbb{M}}\text{c})$$

In Section 4.4.3 we computationally show that for $\gamma \leq 10^{-4}$ the Robin boundary regularisation has a negligible effect, and we found computationally that we need $\alpha \lesssim 0.01$ in order for the evolution to be stable.

Following Sections 2.1 and 2.2, the weak form for $(\tilde{\mathbb{M}})$ and the corresponding finite element approximation are given by:

Problem $\tilde{\mathbb{P}}_{SI}$ Given an initial closed curve $\Gamma(0) \in \mathbb{R}^2$ and $\omega \in (0, 1]$, find (u, \mathbf{x}) such that, for all $t \in (0, T)$,

$$\int_{\Omega(t)} \nabla u \cdot \nabla \phi \, dv + \frac{1}{\gamma} \int_{\Gamma(t)} u \phi \, ds + \int_{\Omega(t)} \phi \, dv = \frac{\alpha}{\gamma} \int_{\Gamma(t)} \mathbf{x}_t \cdot \mathbf{n} \phi \, ds, \quad \forall \phi \in H^1(\Omega(t)), \quad (4.1.2)$$

and, for all $\boldsymbol{\xi} \in H^1(\mathbb{I})$,

$$\int_{\mathbb{I}} |\mathbf{x}_\rho|^2 (\omega \mathbf{x}_t + (1 - \omega)(\mathbf{x}_t \cdot \mathbf{n})\mathbf{n}) \cdot \boldsymbol{\xi} \, d\theta + \beta \int_{\mathbb{I}} \mathbf{x}_\rho \cdot \boldsymbol{\xi}_\rho \, d\theta = \int_{\mathbb{I}} |\mathbf{x}_\rho|^2 (Q - \nabla u(\mathbf{x}) \cdot \mathbf{n}) \mathbf{n} \cdot \boldsymbol{\xi} \, d\theta. \quad (4.1.3)$$

Here $\Gamma(t)$ is parametrised by $\mathbf{x}(\mathbb{I}, t)$, and $\Omega(t)$ is the interior of $\Gamma(t)$.

Problem $\tilde{\mathbb{P}}_{SI}^h$ For $\omega \in (0, 1]$, given $\mathbf{X}_h^0 = I^h \mathbf{x}(\cdot, 0) \in W_h(\mathbb{I})$, with $\mathbf{X}_h^{-1} := \mathbf{X}_h^0$, for $n = 0, \dots, N - 1$, find $\{u_h^n, \mathbf{X}_h^{n+1}\} \in S_h(\Omega_h^n) \times W_h(\mathbb{I})$ such that, for all $\phi_h \in S_h(\Omega_h^n)$,

$$\int_{\Omega_h^n} \nabla u_h^n \cdot \nabla \phi_h \, dv + \frac{1}{\gamma} \int_{\Gamma_h^n} \hat{I}_h(u_h^n \phi_h) \, ds + \int_{\Omega_h^n} \phi_h \, dv = \frac{\alpha}{\gamma} \left(|\mathbf{X}_{h,\rho}^n| D_t \mathbf{X}_h^n \cdot \mathbf{n}_h^n, \phi_h \right)^h, \quad (4.1.4)$$

and

$$\begin{aligned} & \left(|\mathbf{X}_{h,\rho}^n|^2 (\omega D_t \mathbf{X}_h^{n+1} + (1-\omega)(D_t \mathbf{X}_h^{n+1} \cdot \mathbf{n}_h^n) \mathbf{n}_h^n), \boldsymbol{\xi}_h \right)^h + \beta(\mathbf{X}_{h,\rho}^{n+1}, \boldsymbol{\xi}_{h,\rho}) \\ &= \frac{1}{\alpha} \left(|\mathbf{X}_{h,\rho}^n|^2 (Q - \nabla u_h^n(\mathbf{X}_h^n) \cdot \mathbf{n}_h^n) \mathbf{n}_h^n, \boldsymbol{\xi}_h \right)^h, \quad \forall \boldsymbol{\xi}_h \in W_h(\mathbb{I}). \end{aligned} \quad (4.1.5)$$

Here $D_t \mathbf{X}_h^{n+1} := \frac{\mathbf{X}_h^{n+1} - \mathbf{X}_h^n}{\Delta t}$ (and similarly for $D_t \mathbf{X}_h^n$), Γ_h^n is given by $\mathbf{X}_h^n(\mathbb{I})$, Ω_h^n is the interior of Γ_h^n , and $\nabla u_h^n(\mathbf{X}_h^n)|_{\sigma_j}$, for $j = 1, \dots, J$, is piecewise constant for $\sigma_j \in \mathcal{T}_\Gamma^h$, with

$$\nabla u_h^n(\mathbf{X}_h^n)|_{\sigma_j} = \nabla u_h^n|_{\mu_l}, \quad \text{for } j = 1, \dots, J,$$

where μ_l is the element in \mathcal{T}_Ω^h that has the line joining \mathbf{X}_{j-1}^n and \mathbf{X}_j^n as one of its edges.

4.2 Diffuse interface without regularisation

In Chapter 3 we introduce a diffuse interface approximation of (\mathbb{M}) that is regularised in time by $\varepsilon^2 u_t$. We also present a finite element scheme for this model. We now introduce an unregularised diffuse interface weak form and finite element scheme that we will use to obtain the simulations presented in this chapter.

4.2.1 Weak form

Using the notation in Section 3.1, we have that the weak formulation for (3.1.1) coupled with (3.1.4), with initial condition (3.1.3), is given by

Problem $\tilde{\mathbb{P}}_{DI}$ Given initial condition (3.1.3) for $\varphi_0 \in K(D)$, find (φ, u) , with $\varphi(t) \in K(D)$, such that, for all $t \in (0, T)$,

$$\int_D \zeta(\varphi) \nabla u \cdot \nabla \phi \, d\mathbf{x} + \frac{1}{\alpha \varepsilon} \int_D \delta(\varphi) u \phi \, d\mathbf{x} = \frac{Q}{\varepsilon} \int_D \delta(\varphi) \phi \, d\mathbf{x} - \int_D \zeta(\varphi) \phi \, d\mathbf{x}, \quad \forall \phi \in H^1(D), \quad (4.2.1)$$

and, for all $\rho \in K(D)$,

$$\int_D \varepsilon \varphi_t (\rho - \varphi) \, d\mathbf{x} + \beta \varepsilon \int_D \nabla \varphi \cdot \nabla (\rho - \varphi) \, d\mathbf{x} - \frac{\beta}{\varepsilon} \int_D \varphi (\rho - \varphi) \, d\mathbf{x} \geq \frac{\pi}{4\alpha} \int_D u (\rho - \varphi) \, d\mathbf{x}. \quad (4.2.2)$$

4.2.2 Finite element scheme

Similar to Section 3.4, we write a finite element scheme for the weak form $\tilde{\mathbb{P}}_{DI}$, with initial data (3.4.2), in the following form

Problem $\tilde{\mathbb{P}}_{DI}^h$ Given an approximation $\varphi_h^0 = I_h \varphi_0 \in K_h(D)$, for $n = 0, \dots, N-1$, find $\{u_h^n, \varphi_h^{n+1}\} \in U_h(D) \times K_h(D)$ such that

$$\begin{aligned} \int_D \zeta(\varphi_h^n) \nabla u_h^n \cdot \nabla \phi_h \, d\mathbf{x} + \frac{1}{\alpha \varepsilon} \int_D I_h(\delta(\varphi_h^n) u_h^n \phi_h) \, d\mathbf{x} \\ = \frac{Q}{\varepsilon} \int_D I_h(\delta(\varphi_h^n) \phi_h) \, d\mathbf{x} - \int_D I_h(\zeta(\varphi_h^n) \phi_h) \, d\mathbf{x}, \quad \forall \phi_h \in U_h(D), \end{aligned} \quad (4.2.3)$$

and, for all $\rho_h \in K_h(D)$,

$$\begin{aligned} \varepsilon \int_D I_h(D_t \varphi_h^{n+1}(\rho_h - \varphi_h^{n+1})) \, d\mathbf{x} + \beta \varepsilon \int_D \nabla \varphi_h^{n+1} \cdot \nabla(\rho_h - \varphi_h^{n+1}) \, d\mathbf{x} \\ - \frac{\beta}{\varepsilon} \int_D I_h(\varphi_h^n(\rho_h - \varphi_h^{n+1})) \, d\mathbf{x} \geq \frac{\pi}{4\alpha} \int_D I_h(u_h^n(\rho_h - \varphi_h^{n+1})) \, d\mathbf{x}. \end{aligned} \quad (4.2.4)$$

Here, as in Chapter 3,

$$U_h(D) := \left\{ \phi_h \in C^0(\overline{D}) \mid \phi_h|_\sigma \text{ is linear } \forall \sigma \in \mathcal{T}_D^h \right\},$$

$$K_h(D) := \{ \rho_h \in U_h(D) \mid |\rho_h| \leq 1 \},$$

$I_h : C^0(\overline{D}) \rightarrow U_h(D)$ is the Lagrange interpolation operator onto $U_h(D)$, and for simplicity of notation we extend I_h to encompass $I_h : C^0(\overline{D}) \rightarrow K_h(D)$, the Lagrange interpolation operator onto $K_h(D)$.

In order to solve (4.2.4) we employ the projected SOR algorithm given in Algorithm 7.

4.2.3 Diffuse interface approximation to $(\tilde{\mathbb{M}})$

A natural diffuse interface approximation to the velocity law $(\tilde{\mathbb{M}}c)$ would take the form

$$\begin{aligned} \int_D \varepsilon \varphi_t (\rho - \varphi) \, d\mathbf{x} + \beta \varepsilon \int_D \nabla \varphi \cdot \nabla (\rho - \varphi) \, d\mathbf{x} - \frac{\beta}{\varepsilon} \int_D \varphi (\rho - \varphi) \, d\mathbf{x} \\ \geq \frac{\pi}{4} \int_D (Q - \nabla u \cdot \mathbf{n}_\varphi) (\rho - \varphi) \, d\mathbf{x}. \end{aligned} \quad (4.2.5)$$

where $\mathbf{n}_\varphi = \frac{\nabla \varphi}{|\nabla \varphi|}$. Coupling (4.2.5) to a diffuse interface approximation to $(\mathbb{M}a)$ with boundary condition $(\mathbb{M}b)$ (for example (4.2.1)) yields a diffuse interface approximation to $(\tilde{\mathbb{M}})$. When we implemented a finite element approximation of this diffuse interface approximation to $(\tilde{\mathbb{M}})$, we found that the numerical solutions that we obtained (in a radially symmetric setting) compared badly with the corresponding analytical solutions of $(\tilde{\mathbb{M}}c)$. We believe that this was not due to the finite element approximation, but is instead a limitation of the diffuse interface approximation that we used. In particular, we believe that although the diffuse interface approximation approximates the solution u well, it has difficulties approximating ∇u correctly within the interfacial region. Our reasoning for this can be seen in Figure 4.1, where the numerical approximation u_h is displayed alongside the analytical solution u . Here we have taken a radially symmetric setting in which $\Omega(t) \subset \mathbb{R}^2$ is a disk, centred at the origin with radius $R(t)$, and u is expressed in polar coordinates with $u(r, \theta) = u(r)$. The figure shows a plot of $u(r)$ (blue line) together with $u_h(r)$ restricted to the positive x -axis (red line), at $t = 0.8$. The vertical black lines denote the diffuse interfacial region. From these plots we see that although u_h is close to u , towards the right hand edge of the diffuse interfacial region ∇u_h diverges significantly from ∇u . Since ∇u appears in the velocity law for $(\tilde{\mathbb{M}})$, an alternative diffuse interface approximation for this model is required, however we do not suggest one here.

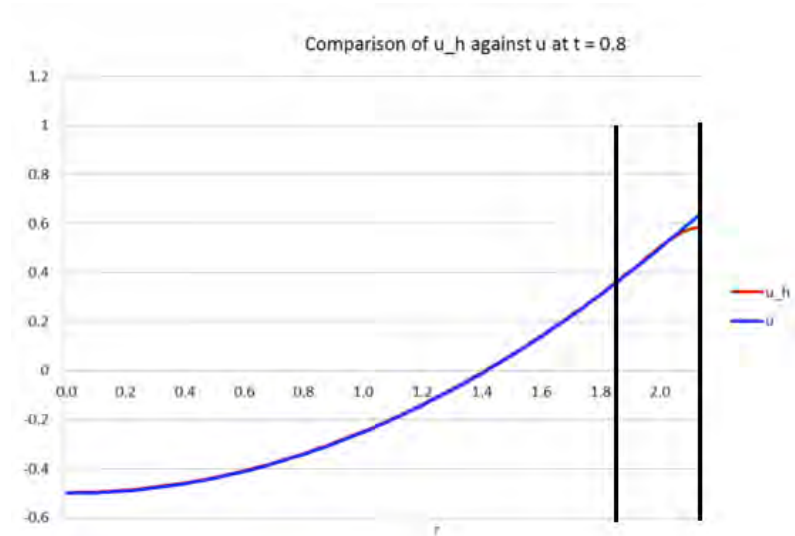


Figure 4.1: Comparison of the analytic solution $u(r)$ (blue line) and the diffuse interface approximation $u_h(r)$ (red line). The x -axis is the radius, r . The edges of the diffuse interfacial region are denoted by two black lines. The diffuse interfacial region is of approximate width 0.3, centred at $r = 2.0$.

4.3 Summary of the implementations

In this section we present a summary of the techniques used in the implementations of the finite element schemes that are used in the remainder of the chapter. We begin with the sharp interface scheme, in which we discuss the mesh smoothing, and refinement and coarsening scheme. We then turn our attention to the unfitted sharp interface scheme, where we discuss the mesh adaptivity used. We finally discuss the mesh adaptivity used in the diffuse interface case.

All finite element schemes are implemented in the programming language *c*, using the finite element toolbox ALBERTA [69]. The output files are visualised in Paraview [3].

4.3.1 Sharp interface

With regard to the finite element schemes introduced in Sections 2.2 and 4.1, maintaining a high quality mesh throughout the simulation is important. For this reason, when working in \mathbb{R}^2 , we choose to use the DeTurck method, described in Section 2.3.2, with $\bar{\omega} = 1$. This is coupled with the refinement and coarsening scheme suggested in [42], in which we seek

to refine element $\mu^n \in \mathcal{T}_\Omega^h$ if

$$|\mu^n| \geq 1.5\overline{|\mu^0|},$$

and seek to coarsen element $\mu^n \in \mathcal{T}_\Omega^h$ if

$$|\mu^n| \leq 0.5\overline{|\mu^0|},$$

where $\mu^0 \in \mathcal{T}_\Omega^h$ at $t = 0$, $|\mu^n|$ is the element area, and $\overline{|\mu^0|}$ is the mean area of all elements at time $t = 0$. We use ALBERTA's built in scheme for refining and coarsening.

We then, in \mathbb{R}^2 , couple this mesh maintenance algorithm with the re-meshing software GMSH, described in Section 2.3.3. We perform re-meshes sparingly, waiting until $q \geq 5$, where q is defined in (2.3.3). This allows the simulation to continue until it reaches a self intersection. Note that re-meshing is not required until a large transformation has occurred, however we re-mesh more often than is strictly necessary in order to maintain the accuracy of the solution.

With regard to the finite element scheme introduced in Section 2.5, when working in \mathbb{R}^3 , we did not implement the DeTurck method described in Section 2.3.2. This is because it would require a reference manifold in \mathbb{R}^4 , and ALBERTA does not allow dimensions above \mathbb{R}^3 . We also did not implement re-meshing via GMSH, due to the complexity of the programming task. In order to maintain a reasonable mesh for a short time we implemented the simpler harmonic extension method, described in Section 2.3.1.

4.3.2 Unfitted sharp interface scheme

The unfitted sharp interface scheme \mathbb{P}_{SIU}^h does not require any mesh smoothing on \mathcal{T}_D^h . We implemented an identical refining and coarsening algorithm to that of the sharp interface scheme, described in Section 4.3.1, on the mesh \mathcal{T}_Γ^h (with the only difference that we consider the length of the element, rather than the element area). In order to keep the execution time low, and the accuracy high, we ensure that the simplexes of the mesh \mathcal{T}_D^h that are either inside Γ_h^n or cut by Γ_h^n are refined a set number of times, whilst simplexes that are entirely outside of Γ_h^n are coarsened as much as possible. In all unfitted sharp interface simulations we take $\omega = 1$.

4.3.3 Diffuse interface

Similar to the unfitted sharp interface scheme, the diffuse interface finite element scheme $\tilde{\mathbb{P}}_{DI}^h$ does not need smoothing on the mesh \mathcal{T}_D^h . However, in order to keep the execution time low, and the accuracy high, the mesh is adaptively refined and coarsened so that it is well refined when $\varphi_h^n > -1$, and coarse otherwise.

When computing radially symmetric simulations, we use the symmetry of the system, of the initial conditions, and of D , to reduce the computation space to either a quadrant in \mathbb{R}^2 , or an octant in \mathbb{R}^3 .

4.4 Radially symmetric simulations

In this section we consider a radially symmetric geometry for $\Gamma(t)$. Thus, we set $\Gamma(t) \subset \mathbb{R}^d$ to be an d dimensional sphere, centred at the origin. We denote by $R = R(t)$ the radius of the sphere, and we express u in polar coordinates such that $u(r, \theta) = u(r)$. We now derive an analytic solution, starting by solving for u using (Ma) and (Mb). This gives

$$u(r) = \frac{1}{2d}r^2 + \alpha Q - \frac{\alpha}{d}R - \frac{1}{2d}R^2, \quad (4.4.1)$$

which means that (Mc) simplifies to

$$R'(t) = -\frac{d\beta}{2R} + \frac{1}{\alpha}u(r) = Q - \frac{d\beta}{2R} - \frac{1}{d}R, \quad (4.4.2)$$

with initial condition $R(0) := R_0$. Note that if we solve ($\tilde{\mathbb{M}}$) in a similar way, then we get a different expression for u , but the value of R' (and thus R) remains unchanged at time t (for $\gamma = 0$).

In Figure 4.2 we consider $d = 2$, and plot the radius for the sharp interface scheme \mathbb{P}_{SI}^h (blue line) together with the radius for the diffuse interface scheme $\tilde{\mathbb{P}}_{DI}^h$ (obtained from the zero level set of φ_h , red line) and the radius for the unfitted sharp interface scheme \mathbb{P}_{SIU}^h (green line). These are compared to the radius given by the analytic equation (4.4.2) (calculated numerically, dashed yellow line). In this example we set the initial radius $R_0 = 1.5$, $Q = 1.5$ and $\alpha = \beta = 1.0$. The diffuse interface solution was obtained with

$\varepsilon = 0.09$, $\Delta t = 5 \times 10^{-7}$, $h = 0.0048$ and $dofs \approx 1.7 \times 10^5$, the fitted sharp interface scheme with $\Delta t = 5 \times 10^{-4}$, $h = 0.0046$ and $dofs \approx 5.3 \times 10^5$, and the unfitted sharp interface scheme with $\Delta t = 10^{-4}$, $h = 0.00057$ and $dofs = 1.3 \times 10^5$, where $dofs$ is the number of degrees of freedom.

In Figure 4.2 we also plot the function u_h , for both the sharp interface and diffuse interface schemes, against u (here u solves (4.4.1), and is extended beyond $\Omega(t)$ by an extension of the formula). Once again, we use blue for the sharp interface scheme, red for the diffuse interface scheme, green for the unfitted sharp interface scheme, and dashed yellow for the analytical solution. This is plotted at $t = 0.5$. We see a good agreement between the two schemes.

In Figure 4.3 we display the influence of ε on the diffuse interface solution. We set $d = 2$, and plot the radius (top image) and the solution u_h (bottom image) obtained from the diffuse interface scheme using $\varepsilon = 0.39, 0.27, 0.19, 0.09$, and 0.049 , $h \approx 0.028, 0.020, 0.014, 0.0098$, and 0.0049 , $\Delta t = 9 \times 10^{-5}, 6 \times 10^{-5}, 2 \times 10^{-5}, 10^{-5}$, and 10^{-6} , and $dofs \approx 9.2 \times 10^3, 1.5 \times 10^4, 2.9 \times 10^4, 4.6 \times 10^4$, and 1.7×10^5 . From this figure we see the convergence of the radius and the solution u_h , to their analytical counterparts, as $\varepsilon \rightarrow 0$.

In Figure 4.4 we consider $d = 3$, and plot similarly to Figure 4.2 (omitting the unfitted sharp interface scheme, as this was not implemented in \mathbb{R}^3). In this example we set the initial radius $R_0 = 1.0$, the diffuse interface solution was obtained with $\varepsilon = 0.1$, $h = 0.014$, $\Delta t = 5 \times 10^{-6}$, $dofs = 8.2 \times 10^5$, and the sharp interface with $\Delta t = 1.0 \times 10^{-5}$, $h = 0.06$, $dofs = 1.5 \times 10^4$. We choose $Q = 1.666(\approx \frac{5}{3})$ and $\alpha = \beta = 1.0$. As in Figure 4.2 we also plot u_h , from both the sharp interface and diffuse interface schemes, against u (once again u solves (4.4.1), and is extended beyond $\Omega(t)$ by an extension of the formula). This is plotted at $t = 0.3$. Again, we see a good agreement between the two schemes.

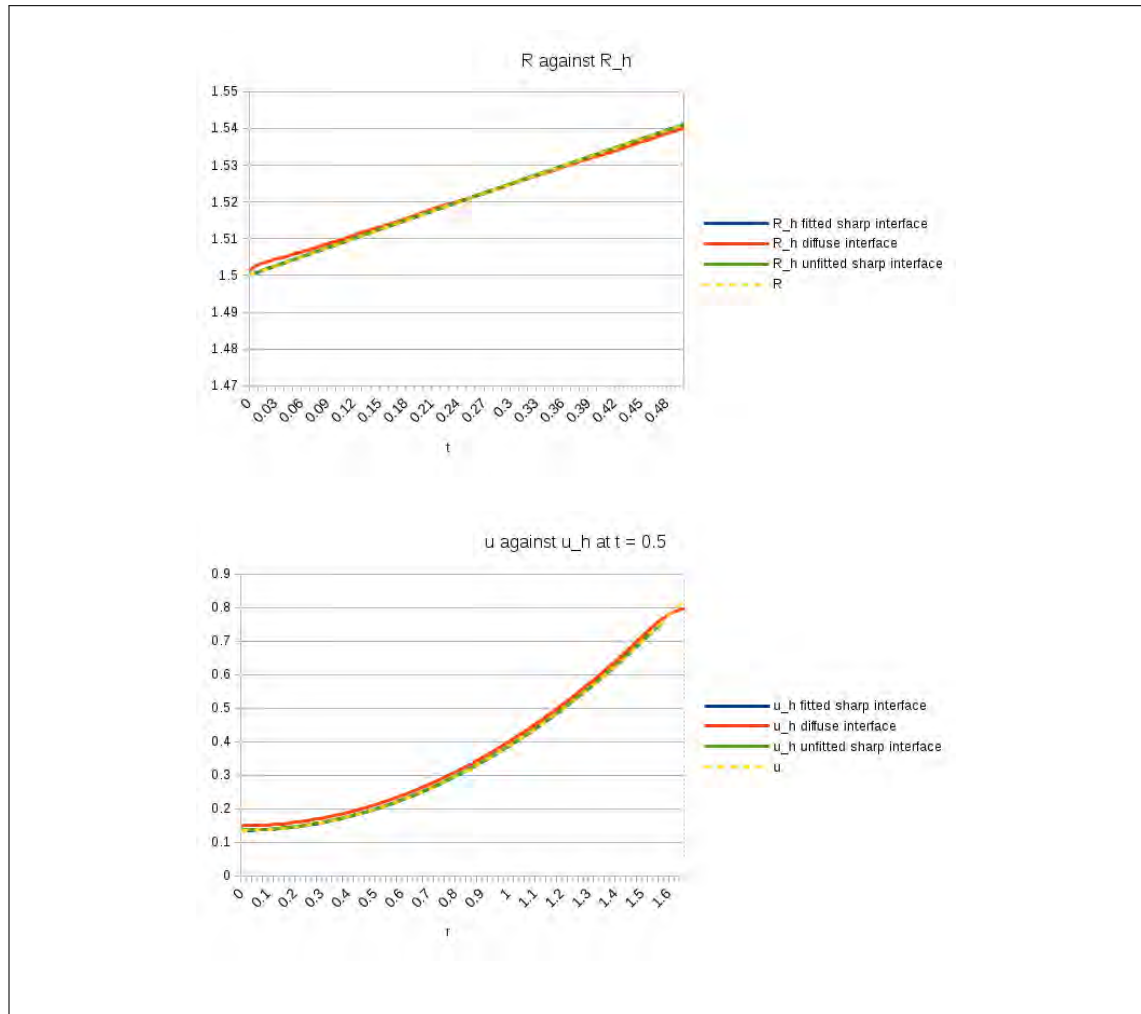


Figure 4.2: Top plot: comparison of the radius, in \mathbb{R}^2 , computed using the sharp interface scheme \mathbb{P}_{SI}^h (blue line), diffuse interface scheme $\tilde{\mathbb{P}}_{DI}^h$ (red line) and the unfitted sharp interface scheme \mathbb{P}_{SIU}^h (green line), with the analytical radius from (4.4.2) (dashed yellow line, computed numerically). Bottom plot: comparison of u_h from the sharp interface scheme (blue line), from the diffuse interface scheme (red line), and from the unfitted sharp interface scheme, with the extended analytic solution u from (4.4.1) (dashed yellow line), taken at $t = 0.5$. In both plots the blue line is behind the dashed yellow and solid green lines. The diffuse interface solution was obtained with $\varepsilon = 0.09$, $\Delta t = 5 \times 10^{-7}$, $h = 0.0048$ and $dofs \approx 1.7 \times 10^5$, the fitted sharp interface scheme with $\Delta t = 5 \times 10^{-4}$, $h = 0.0046$ and $dofs \approx 5.3 \times 10^5$ and the unfitted sharp interface scheme with $\Delta t = 10^{-4}$, $h = 0.00057$ and $dofs = 1.3 \times 10^5$.

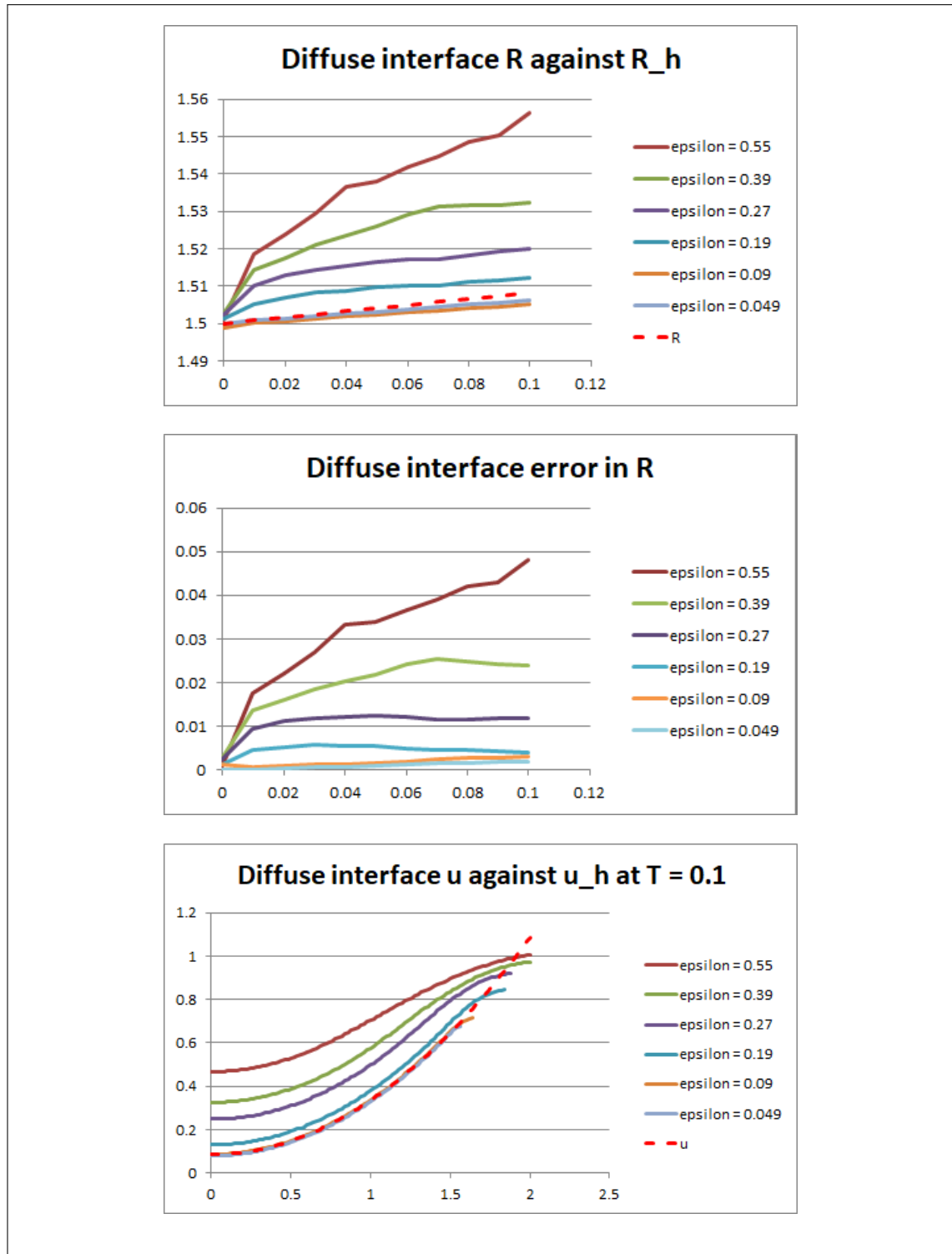


Figure 4.3: Top plot: comparison of the radius, in \mathbb{R}^2 , computed using the diffuse interface scheme $\tilde{\mathbb{P}}_{DI}^h$ and the analytical radius from (4.4.2) (dashed yellow line, computed numerically). Bottom plot: comparison of u_h from the diffuse interface scheme with the extended analytic solution u from (4.4.1) (dashed yellow line), taken at $t = 0.1$. Here we take $\varepsilon = 0.39, 0.27, 0.19, 0.09$, and 0.049 , $h \approx 0.028, 0.020, 0.014, 0.0098$, and 0.0049 , $\Delta t = 9 \times 10^{-5}, 6 \times 10^{-5}, 2 \times 10^{-5}, 10^{-5}$, and 10^{-6} , and $dofs \approx 9.2 \times 10^3, 1.5 \times 10^4, 2.9 \times 10^4, 4.6 \times 10^4$, and 1.7×10^5 .

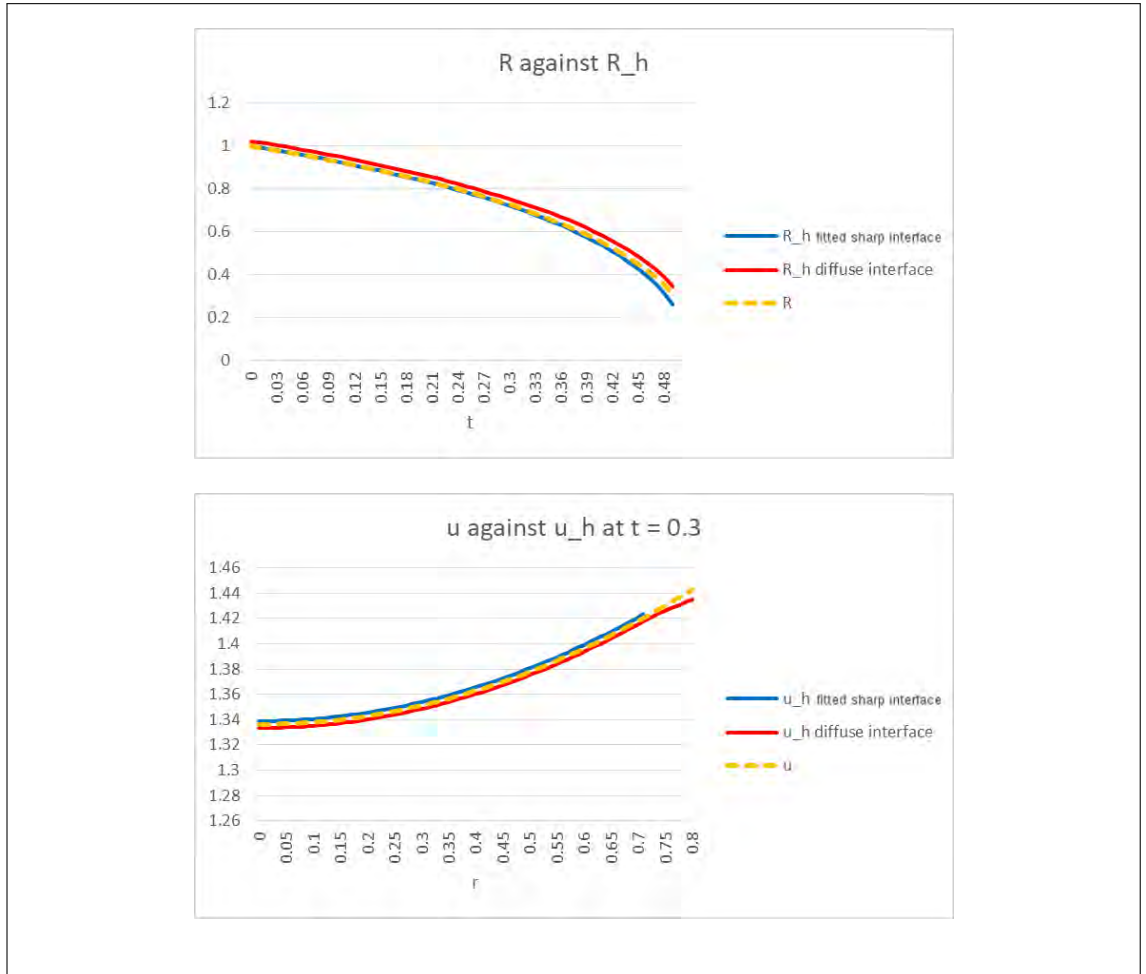


Figure 4.4: Top plot: comparison of the radius, in \mathbb{R}^3 , computed using the sharp interface scheme $\mathbb{P}_{SI\mathbb{R}^3}^h$ (blue line) and diffuse interface scheme $\tilde{\mathbb{P}}_{DI}^h$ (red line), with the analytical radius from (4.4.2) (dashed yellow line, computed numerically). Bottom plot: comparison of u_h from the sharp interface scheme (blue line), from the diffuse interface scheme (red line), and with the extended analytic solution u from (4.4.1) (dashed yellow line), taken at $t = 0.3$. For the diffuse interface scheme we choose $\varepsilon = 0.1$, $h = 0.014$, $\Delta t = 5 \times 10^{-6}$, $dofs = 8.2 \times 10^5$, and for the sharp interface scheme we choose $\Delta t = 1.0 \times 10^{-5}$, $h = 0.06$, $dofs = 1.5 \times 10^4$.

4.4.1 Sharp interface experimental order of convergence

Using the analytic solution to (4.4.1), and the numerically computed solution to (4.4.2), we compute the experimental orders of convergence for the sharp interface scheme \mathbb{P}_{SI}^h . This is done with both $\omega = 1$ and $\omega = 10^{-3}$. For each of these choices of ω , we smooth the bulk mesh with either the harmonic extension method, detailed in Section 2.3.1, or with the DeTurck method, detailed in Section 2.3.2.

We perform these simulations for both a uniform, and a non-uniform mesh. We addi-

tionally present experimental orders of convergence for the unfitted sharp interface scheme \mathbb{P}_{SIU}^h (for $\omega = 1$ since the mesh is uniform) with a uniform mesh.

Throughout the simulations in this section we take $\alpha = 1.0$, $\beta = 0.5$, $Q = 1.5$, $T = 2.0$, and the initial radius $R_0 = 1.5$. The values of Δt and h chosen are shown in the respective tables. In all cases h is the maximum over all time steps; in the case of the unfitted sharp interface scheme it is the mesh size for D (although the mesh size for Γ_h^n is reduced accordingly).

Uniform mesh

When constructing the uniform mesh, we choose

$$\mathbf{X}_h^0(q) = 1.5(\cos(q), \sin(q)), \quad (4.4.3)$$

for vertex q of the mesh for Γ_h^0 . This leads to the mesh shown in Figure 4.5.

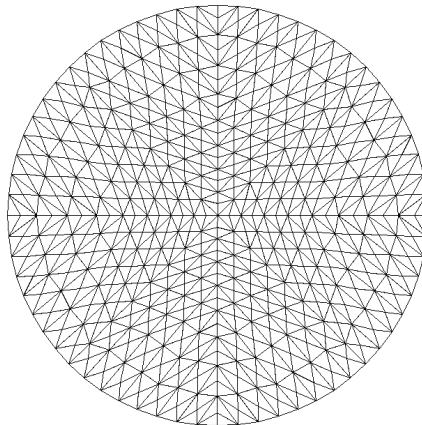


Figure 4.5: Uniform mesh, with Γ_h^0 given by (4.4.3).

Table 4.1 shows the errors and Table 4.2 shows the experimental order of convergence for the sharp interface scheme \mathbb{P}_{SI}^h , with $\omega = 1$, and the DeTurck method. Table 4.3 shows the errors and Table 4.4 shows the experimental order of convergence for the sharp interface scheme \mathbb{P}_{SI}^h , with $\omega = 10^{-3}$, and the DeTurck method. Table 4.5 shows the errors and Table 4.6 shows the experimental order of convergence for the sharp interface scheme \mathbb{P}_{SI}^h , with $\omega = 1$, and the harmonic extension method. Table 4.7 shows the errors and Table 4.8 shows the experimental order of convergence for the sharp interface scheme

\mathbb{P}_{SI}^h , with $\omega = 10^{-3}$, and the harmonic extension method. Table 4.9 shows the errors and Table 4.10 shows the experimental order of convergence for the unfitted sharp interface scheme \mathbb{P}_{SIU}^h , with $\omega = 1$, and the DeTurck method. We use the L^∞ in time norm when dealing with the unfitted sharp interface scheme.

We use the L^2 in time norm for the computations regarding the sharp interface scheme \mathbb{P}_{SI}^h . This is because it captures the effect of the mesh improving (whereas the L^∞ in time norm may have the largest error near to $t = 0$ when the mesh is at its least uniform). Since the mesh in this section is uniform, the improvement of the mesh has very little effect, however we choose the L^2 norm for consistency with the results regarding the non-uniform mesh given in Section 4.4.1. The experimental order of convergence in the H^1 norms of Ω_h^n and \mathbb{I} are approximately 2, while the L^2 norms of Ω_h^n and \mathbb{I} tend to give an experimental order convergence of approximately 2 or greater.

We see, by comparing Table 4.2 with Table 4.4, that we have almost identical experimental orders of convergence for $\omega = 1$ and $\omega = 10^{-3}$ when using the DeTurck scheme. This is due to the initial mesh being uniformly distributed, and so the boundary mesh cannot be significantly improved by taking smaller ω . Thus, as the circle grows we only have the effect of the DeTurck method, which is identical in these two cases. We have a similar effect when comparing Tables 4.6 and 4.8 (in which $\omega = 1$ or $\omega = 10^{-3}$, respectively, and we use the harmonic extension method). Again, the boundary mesh cannot be significantly improved by taking smaller ω .

We see only very slightly improved experimental orders of convergence for Table 4.2, in which we take $\omega = 1$ and use the DeTurck method, compared to Table 4.6, in which we again take $\omega = 1$ and this time use the harmonic extension method. This is because the initial mesh is uniform, and so the small amounts of improvement that can be done to the mesh can be carried out equally well by the DeTurck method as by the harmonic extension method. This is also reflected in results for $\omega = 10^{-3}$, when comparing the experimental orders of convergence for the DeTurck method (Table 4.4) with the harmonic extension method (Table 4.8), since they are almost identical.

With regard to the errors themselves, we see a similar effect as reported for the experimental orders of convergence. There is a slight improvement for $\omega = 1$ compared to $\omega = 10^{-3}$ when considering the DeTurck method, and identical results when comparing

$\omega = 1$ with $\omega = 10^{-3}$ and the harmonic extension method. Similarly the results are almost identical when comparing the DeTurck method with the harmonic extension method.

The experimental orders of convergence for the unfitted sharp interface scheme \mathbb{P}_{SIU}^h shown in Table 4.10 improve slightly upon the results for the sharp interface scheme \mathbb{P}_{SI}^h for all but the L^2 norm on \mathbf{X} . With regard to the errors, when comparing them for similar values of h and Δt , we see that the errors in the H^1 norms on u and \mathbf{X} for the unfitted sharp interface scheme are much smaller than the corresponding fitted errors, and that an experimental order of convergence of approximately 4 is seen for the errors for u_h in L^2 over Ω_h^n .

h	Δt	$L^2(u, \Omega_h^n)$	$H^1(u, \Omega_h^n)$	$L^2(\mathbf{X}, \mathbb{I})$	$H^1(\mathbf{X}, \mathbb{I})$
4.60E-01	7.40E-03	3.06E-04	4.09E-02	2.84E-05	3.48E-02
2.38E-01	3.90E-03	2.68E-05	1.04E-02	2.50E-06	8.63E-03
1.22E-01	2.00E-03	2.75E-06	2.62E-03	2.95E-07	2.16E-03
6.16E-02	1.00E-03	3.57E-07	6.58E-04	4.86E-08	5.40E-04
3.09E-02	5.20E-02	6.37E-08	1.63E-04	1.11E-09	1.34E-04

Table 4.1: Errors for the given norms, solving the sharp interface scheme \mathbb{P}_{SI}^h with $\omega = 1$, and the DeTurck method. With Γ_h^0 given by (4.4.3). Here $L^2(v, U)$ for function v and set U denotes the norm $\Delta t \sum_{n=0}^N \|v_h^n - v(t_n)\|_{L^2(U)}^2$, and $H^1(v, U)$ for function v and set U denotes the norm $\Delta t \sum_{n=0}^N |v_h^n - v(t_n)|_{H^1(U)}^2$.

h	Δt	$L^2(u, \Omega_h^n)$	$H^1(u, \Omega_h^n)$	$L^2(\mathbf{X}, \mathbb{I})$	$H^1(\mathbf{X}, \mathbb{I})$
4.60E-01	7.40E-03				
2.38E-01	3.90E-03	3.69	2.08	3.69	2.12
1.22E-01	2.00E-03	3.39	2.06	3.19	2.07
6.16E-02	1.00E-03	2.99	2.03	2.64	2.03
3.09E-02	5.20E-02	2.50	2.03	2.14	2.02

Table 4.2: Experimental order of convergence for the given norms, solving the sharp interface scheme \mathbb{P}_{SI}^h with $\omega = 1$, and the DeTurck method. With Γ_h^0 given by (4.4.3). Here $L^2(v, U)$ for function v and set U denotes the experimental orders of convergence for the norm $\Delta t \sum_{n=0}^N \|v_h^n - v(t_n)\|_{L^2(U)}^2$, and $H^1(v, U)$ for function v and set U denotes the experimental orders of convergence for the norm $\Delta t \sum_{n=0}^N |v_h^n - v(t_n)|_{H^1(U)}^2$.

h	Δt	$L^2(u, \Omega_h^n)$	$H^1(u, \Omega_h^n)$	$L^2(\mathbf{X}, \mathbb{I})$	$H^1(\mathbf{X}, \mathbb{I})$
4.59E-01	7.40E-03	2.98E-04	4.08E-02	2.83E-05	3.48E-02
2.38E-01	3.90E-03	2.66E-05	1.04E-02	2.49E-06	8.63E-03
1.22E-01	2.00E-03	2.74E-06	2.62E-03	2.95E-07	2.16E-03
6.16E-02	1.00E-03	3.56E-07	6.58E-04	4.85E-08	5.40E-04
3.09E-02	5.20E-04	6.42E-08	1.64E-04	1.12E-08	1.35E-04

Table 4.3: Errors for the given norms, solving the sharp interface scheme \mathbb{P}_{SI}^h with $\omega = 10^{-3}$, and the DeTurck method. With Γ_h^0 given by (4.4.3). Here $L^2(v, U)$ for function v and set U denotes the norm $\Delta t \sum_{n=0}^N \|v_h^n - v(t_n)\|_{L^2(U)}^2$, and $H^1(v, U)$ for function v and set U denotes the norm $\Delta t \sum_{n=0}^N |v_h^n - v(t_n)|_{H^1(U)}^2$.

h	Δt	$L^2(u, \Omega_h^n)$	$H^1(u, \Omega_h^n)$	$L^2(\mathbf{X}, \mathbb{I})$	$H^1(\mathbf{X}, \mathbb{I})$
4.59E-01	7.40E-03				
2.38E-01	3.90E-03	3.68	2.08	3.71	2.12
1.22E-01	2.00E-03	3.39	2.06	3.19	2.07
6.16E-02	1.00E-03	2.99	2.03	2.64	2.03
3.09E-02	5.20E-04	2.49	2.01	2.13	2.01

Table 4.4: Experimental order of convergence for the given norms, solving the sharp interface scheme \mathbb{P}_{SI}^h with $\omega = 10^{-3}$, and the DeTurck method. With Γ_h^0 given by (4.4.3). Here $L^2(v, U)$ for function v and set U denotes the experimental orders of convergence for the norm $\Delta t \sum_{n=0}^N \|v_h^n - v(t_n)\|_{L^2(U)}^2$, and $H^1(v, U)$ for function v and set U denotes the experimental orders of convergence for the norm $\Delta t \sum_{n=0}^N |v_h^n - v(t_n)|_{H^1(U)}^2$.

h	Δt	$L^2(u, \Omega_h^n)$	$H^1(u, \Omega_h^n)$	$L^2(\mathbf{X}, \mathbb{I})$	$H^1(\mathbf{X}, \mathbb{I})$
4.70E-01	7.40E-03	3.23E-04	4.10E-02	2.94E-05	3.47E-02
2.40E-01	3.90E-03	2.73E-05	1.04E-02	2.55E-06	8.63E-03
1.22E-01	2.00E-03	2.77E-06	2.62E-03	2.98E-07	2.16E-03
6.11E-02	1.00E-03	3.57E-07	6.57E-04	4.88E-08	5.39E-04
3.06E-02	5.20E-04	6.44E-08	1.64E-04	1.12E-08	1.35E-04

Table 4.5: Errors for the given norms, solving the sharp interface scheme \mathbb{P}_{SI}^h with $\omega = 1$, and the harmonic extension method. With Γ_h^0 given by (4.4.3). Here $L^2(v, U)$ for function v and set U denotes the norm $\Delta t \sum_{n=0}^N \|v_h^n - v(t_n)\|_{L^2(U)}^2$, and $H^1(v, U)$ for function v and set U denotes the norm $\Delta t \sum_{n=0}^N |v_h^n - v(t_n)|_{H^1(U)}^2$.

h	Δt	$L^2(u, \Omega_h^n)$	$H^1(u, \Omega_h^n)$	$L^2(\mathbf{X}, \mathbb{I})$	$H^1(\mathbf{X}, \mathbb{I})$
4.70E-01	7.40E-03				
2.40E-01	3.90E-03	3.69	2.04	3.65	2.08
1.22E-01	2.00E-03	3.35	2.02	3.15	2.03
6.11E-02	1.00E-03	2.98	2.01	2.63	2.01
3.06E-02	5.20E-04	2.48	2.01	2.13	2.01

Table 4.6: Experimental order of convergence for the given norms, solving the sharp interface scheme \mathbb{P}_{SI}^h with $\omega = 1$, and the harmonic extension method. With Γ_h^0 given by (4.4.3). Here $L^2(v, U)$ for function v and set U denotes the experimental orders of convergence for the norm $\Delta t \sum_{n=0}^N \|v_h^n - v(t_n)\|_{L^2(U)}^2$, and $H^1(v, U)$ for function v and set U denotes the experimental orders of convergence for the norm $\Delta t \sum_{n=0}^N |v_h^n - v(t_n)|_{H^1(U)}^2$.

h	Δt	$L^2(u, \Omega_h^n)$	$H^1(u, \Omega_h^n)$	$L^2(\mathbf{X}, \mathbb{I})$	$H^1(\mathbf{X}, \mathbb{I})$
4.68E-01	7.40E-03	3.23E-04	4.09E-02	2.95E-05	3.47E-02
2.40E-01	3.90E-03	2.73E-05	1.04E-02	2.55E-06	8.63E-03
1.21E-01	2.00E-03	2.77E-06	2.62E-03	2.98E-07	2.16E-03
6.11E-02	1.00E-03	3.57E-07	6.57E-04	4.88E-08	5.39E-04
3.06E-02	5.20E-04	6.44E-08	1.64E-04	1.12E-08	1.35E-04

Table 4.7: Errors for the given norms, solving the sharp interface scheme \mathbb{P}_{SI}^h with $\omega = 10^{-3}$, and the harmonic extension method. With Γ_h^0 given by (4.4.3). Here $L^2(v, U)$ for function v and set U denotes the norm $\Delta t \sum_{n=0}^N \|v_h^n - v(t_n)\|_{L^2(U)}^2$, and $H^1(v, U)$ for function v and set U denotes the norm $\Delta t \sum_{n=0}^N |v_h^n - v(t_n)|_{H^1(U)}^2$.

h	Δt	$L^2(u, \Omega_h^n)$	$H^1(u, \Omega_h^n)$	$L^2(\mathbf{X}, \mathbb{I})$	$H^1(\mathbf{X}, \mathbb{I})$
4.68E-01	7.40E-03				
2.40E-01	3.90E-03	3.70	2.05	3.66	2.08
1.21E-01	2.00E-03	3.36	2.02	3.15	2.04
6.11E-02	1.00E-03	2.98	2.01	2.63	2.02
3.06E-02	5.20E-04	2.48	2.01	2.13	2.01

Table 4.8: Experimental order of convergence for the given norms, solving the sharp interface scheme \mathbb{P}_{SI}^h with $\omega = 10^{-3}$, and the harmonic extension method. With Γ_h^0 given by (4.4.3). Here $L^2(v, U)$ for function v and set U denotes the experimental orders of convergence for the norm $\Delta t \sum_{n=0}^N \|v_h^n - v(t_n)\|_{L^2(U)}^2$, and $H^1(v, U)$ for function v and set U denotes the experimental orders of convergence for the norm $\Delta t \sum_{n=0}^N |v_h^n - v(t_n)|_{H^1(U)}^2$.

h	Δt	$L^2(u, \Omega_h^n)$	$H^1(u, \Omega_h^n)$	$L^2(\mathbf{X}, \mathbb{I})$	$H^1(\mathbf{X}, \mathbb{I})$
1.33E-01	1.30E-03	1.86E-06	1.76E-04	1.83E-06	2.53E-06
9.38E-02	9.40E-04	4.78E-07	8.46E-05	9.61E-07	1.13E-06
6.63E-02	6.60E-04	1.29E-07	4.04E-05	4.74E-07	5.18E-07
4.69E-02	4.70E-04	3.11E-08	1.94E-05	2.41E-07	2.51E-07
3.31E-02	3.30E-04	7.48E-09	9.41E-06	1.19E-07	1.21E-07

Table 4.9: Errors for the given norms, solving the unfitted sharp interface scheme \mathbb{P}_{SIU}^h with $\omega = 1$. With Γ_h^0 given by (4.4.3). Here $L^2(v, U)$ for function v and set U denotes the norm $\sup_{n=0, \dots, N} \|v_h^n - v(t_n)\|_{L^2(U)}^2$, and $H^1(v, U)$ for function v and set U denotes the norm $\sup_{n=0, \dots, N} |v_h^n - v(t_n)|_{H^1(U)}^2$.

h	Δt	$L^2(u, \Omega_h^n)$	$H^1(u, \Omega_h^n)$	$L^2(\mathbf{X}, \mathbb{I})$	$H^1(\mathbf{X}, \mathbb{I})$
1.33E-01	1.30E-03				
9.38E-02	9.40E-04	3.91	2.11	1.87	2.31
6.63E-02	6.60E-04	3.79	2.13	2.04	2.26
4.69E-02	4.70E-04	4.10	2.12	1.96	2.08
3.31E-02	3.30E-04	4.11	2.09	2.04	2.10

Table 4.10: Experimental order of convergence for the given norms, solving the unfitted sharp interface scheme \mathbb{P}_{SIU}^h with $\omega = 1$. With Γ_h^0 given by (4.4.3). Here $L^2(v, U)$ for function v and set U denotes the experimental orders of convergence for the norm $\sup_{n=0, \dots, N} \|v_h^n - v(t_n)\|_{L^2(U)}^2$, and $H^1(v, U)$ for function v and set U denotes the experimental orders of convergence for the norm $\sup_{n=0, \dots, N} |v_h^n - v(t_n)|_{H^1(U)}^2$.

Non-uniform mesh

When constructing the non-uniform mesh, we choose

$$\mathbf{X}_h^0(q) = 1.5(\cos(q + 0.9(q^3 - q)), \sin(q + 0.9(q^3 - q))), \quad (4.4.4)$$

for vertex q of the mesh for Γ_h^0 . This leads to the mesh shown in Figure 4.6.

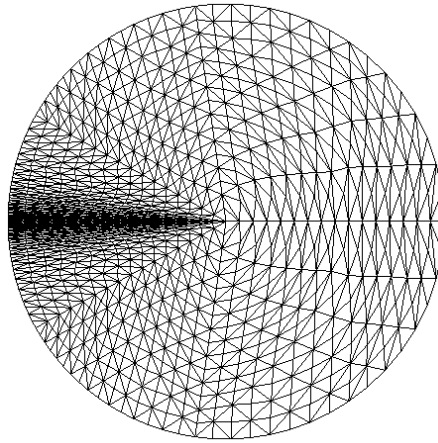


Figure 4.6: Non-uniform mesh, with Γ_h^0 given by (4.4.4).

Table 4.11 shows the errors and Table 4.12 shows the experimental order of convergence for the sharp interface scheme \mathbb{P}_{SI}^h , with $\omega = 1$, and the DeTurck method. Table 4.13 shows the errors and Table 4.14 shows the experimental order of convergence for the sharp interface scheme \mathbb{P}_{SI}^h , with $\omega = 10^{-3}$, and the DeTurck method. Table 4.15 shows the errors and Table 4.16 shows the experimental order of convergence for the sharp interface scheme \mathbb{P}_{SI}^h , with $\omega = 1$, and the harmonic extension method. Table 4.17 shows the errors and Table 4.18 shows the experimental order of convergence for the sharp interface scheme \mathbb{P}_{SI}^h , with $\omega = 10^{-3}$, and the harmonic extension method. In all cases the experimental orders of convergence for the H^1 errors (both in Ω_h^n and \mathbb{I}) are very similar to ones seen for the uniform initial mesh, yielding values of approximately 2. The experimental orders of convergence for the L^2 errors (both in Ω_h^n and \mathbb{I}) are slightly better than those for the uniform initial mesh, yielding values of 2 or greater.

It is not clear from tables 4.11 - 4.16 which mesh smoothing yields the best errors, since the difference between the errors is very small. It is also not clear because the errors at the start of the simulation, for small t , compound as t grows towards T . For this reason it is often the mesh smoothing technique that yields the quickest mesh smoothing (as opposed to the best mesh at time T) that also yields the best error values. Choosing $\omega = 10^{-3}$ (as opposed to $\omega = 1$) gives better errors for the L^2 norm of \mathbf{X}_h , this is as expected, since smaller values of ω lead to greater amounts of mesh smoothing. However, with $\omega = 10^{-3}$, the DeTurck mesh smoothing yields worse errors for the L^2 norm of \mathbf{X}_h than the harmonic extension method. This may be because the DeTurck method aims to improve the bulk

mesh as well as the boundary mesh; the optimum transformation to improve the boundary mesh may not be optimal when also considering the bulk mesh. The DeTurck method does not appear to improve the value of h significantly between Tables 4.11 and 4.15, and Tables 4.13 and 4.17 (here we compare tables with identical values of ω , as the mesh size is often greatest on the boundary, and thus is significantly different for different values of ω). This appears to be because, as discussed in [42], the DeTurck method aims to transform the triangles on the bulk mesh to triangles of a similar shape to those on the reference mesh, regardless of triangle size. This means that although the meshes generated by the DeTurck method have greatly improved meshes with regard to thin and distorted triangles, the value of h is not always significantly improved. This can be offset by the refinement and coarsening scheme introduced in [42], also detailed in Section 4.3.1; this scheme was not included in this section, as it has a significant effect on the value of h for a short time, thus causing issues with the experimental orders of convergence. The L^2 error for u_h is best for the DeTurck scheme with $\omega = 10^{-3}$; this agrees with what we would expect from the meshes shown in Figure 4.7. We stress again that the difference between the errors for different mesh smoothing techniques is very small; they are all of the same order, and often differ only after the first significant figure.

In Figure 4.7 we see the meshes at $t = 20$, under the four different mesh smoothing techniques discussed in this section. In order to reduce the time taken to improve the mesh, we can reduce $\bar{\omega}$ (the timescale parameter for the DeTurck method) to $\bar{\omega} = 0.1$. This yields the mesh shown in Figure 4.8 at time $t = 0.1$; note how it is almost identical to the image in Figure 4.7 with the DeTurck method and $\omega = 1$ at $t = 20$. In order to run this simulation, we had to significantly reduce Δt , thus greatly increasing the execution time. We use $\bar{\omega} = 1$ for the simulations in Sections 4.4 and 4.5 (as opposed to a smaller value for $\bar{\omega}$) since the mesh smoothing given by $\bar{\omega}$ is sufficient for our purposes, and allows for a much greater value of Δt .

It appears from Figure 4.7 that taking $\omega < 1$ speeds up the mesh smoothing given by the DeTurck method. We see a similar effect for $\bar{\omega} < 1$ in Figure 4.8. This is an advantage if the initial mesh is significantly sub-optimal, for example that in Figure 4.6. However, the simulations in the remainder of this chapter begin with a “good” mesh. Experimentally we find that our simulations evolve at such a speed that the DeTurck method is able to

maintain the mesh quality with $\omega = \bar{\omega} = 1$; we do not need the additional speeding up given by taking either $\omega < 1$ or $\bar{\omega} < 1$.

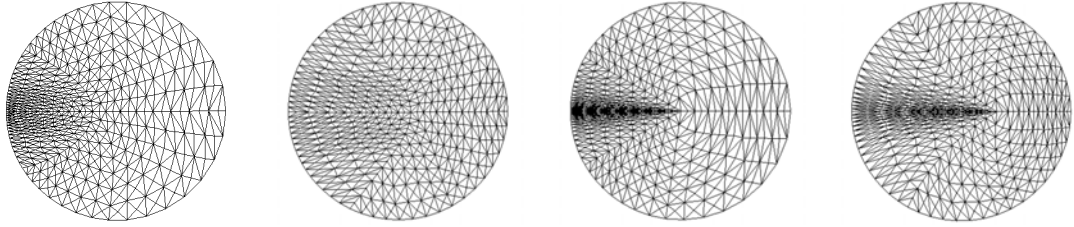


Figure 4.7: Left: the DeTurck method with $\omega = 1$. Center left: the DeTurck method with $\omega = 10^{-3}$. Center right: the harmonic extension method with $\omega = 1$. Right: the harmonic extension method with $\omega = 10^{-3}$. All at $t = 20$.

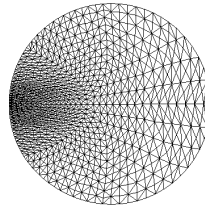


Figure 4.8: DeTurck method with $\omega = 1$, $\bar{\omega} = 0.1$ (recall that $\bar{\omega}$ is the timescale parameter for the DeTurck method). Taken at $t = 0.1$.

h	Δt	$L^2(u, \Omega_h^n)$	$H^1(u, \Omega_h^n)$	$L^2(\mathbf{X}, \mathbb{I})$	$H^1(\mathbf{X}, \mathbb{I})$
1.02E+00	7.40E-03	2.69E-03	1.03E-01	4.38E-04	1.13E-01
5.52E-01	3.90E-03	2.22E-04	2.90E-02	2.89E-05	2.82E-02
2.88E-01	2.00E-03	1.74E-05	7.63E-03	2.02E-06	7.06E-03
1.47E-01	1.00E-03	1.46E-06	1.95E-03	1.66E-07	1.77E-03
7.39E-02	5.20E-04	1.57E-07	4.89E-04	1.98E-08	4.42E-04

Table 4.11: Errors for the given norms, solving the sharp interface scheme \mathbb{P}_{SI}^h with $\omega = 1$, and the DeTurck method. With Γ_h^0 given by (4.4.4). Here $L^2(v, U)$ for function v and set U denotes the norm $\Delta t \sum_{n=0}^N \|v_h^n - v(t_n)\|_{L^2(U)}^2$, and $H^1(v, U)$ for function v and set U denotes the norm $\Delta t \sum_{n=0}^N |v_h^n - v(t_n)|_{H^1(U)}^2$.

h	Δt	$L^2(u, \Omega_h^n)$	$H^1(u, \Omega_h^n)$	$L^2(\mathbf{X}, \mathbb{I})$	$H^1(\mathbf{X}, \mathbb{I})$
1.02E+00	7.40E-03				
5.52E-01	3.90E-03	4.03	2.05	4.40	2.25
2.88E-01	2.00E-03	3.91	2.05	4.08	2.12
1.47E-01	1.00E-03	3.67	2.03	3.71	2.05
7.39E-02	5.20E-04	3.26	2.02	3.10	2.02

Table 4.12: Experimental order of convergence for the given norms, solving the sharp interface scheme \mathbb{P}_{SI}^h with $\omega = 1$, and the DeTurck method. With Γ_h^0 given by (4.4.4). Here $L^2(v, U)$ for function v and set U denotes the experimental orders of convergence for the norm $\Delta t \sum_{n=0}^N \|v_h^n - v(t_n)\|_{L^2(U)}^2$, and $H^1(v, U)$ for function v and set U denotes the experimental orders of convergence for the norm $\Delta t \sum_{n=0}^N |v_h^n - v(t_n)|_{H^1(U)}^2$.

h	Δt	$L^2(u, \Omega_h^n)$	$H^1(u, \Omega_h^n)$	$L^2(\mathbf{X}, \mathbb{I})$	$H^1(\mathbf{X}, \mathbb{I})$
7.85E-01	7.40E-03	1.63E-03	8.27E-02	3.10E-04	9.01E-02
4.81E-01	3.90E-03	1.65E-04	2.59E-02	2.29E-05	2.54E-02
2.69E-01	2.00E-03	1.49E-05	7.29E-03	1.73E-06	6.78E-03
1.42E-01	1.00E-03	1.35E-06	1.92E-03	1.50E-07	1.74E-03
7.30E-02	5.20E-04	1.51E-07	4.87E-04	1.88E-08	4.40E-04

Table 4.13: Errors for the given norms, solving the sharp interface scheme \mathbb{P}_{SI}^h with $\omega = 10^{-3}$, and the DeTurck method. With Γ_h^0 given by (4.4.4). Here $L^2(v, U)$ for function v and set U denotes the norm $\Delta t \sum_{n=0}^N \|v_h^n - v(t_n)\|_{L^2(U)}^2$, and $H^1(v, U)$ for function v and set U denotes the norm $\Delta t \sum_{n=0}^N |v_h^n - v(t_n)|_{H^1(U)}^2$.

h	Δt	$L^2(u, \Omega_h^n)$	$H^1(u, \Omega_h^n)$	$L^2(\mathbf{X}, \mathbb{I})$	$H^1(\mathbf{X}, \mathbb{I})$
7.85E-01	7.40E-03				
4.81E-01	3.90E-03	4.68	2.37	5.33	2.58
2.69E-01	2.00E-03	4.12	2.18	4.43	2.27
1.42E-01	1.00E-03	3.77	2.10	3.84	2.13
7.30E-02	5.20E-04	3.29	2.05	3.11	2.07

Table 4.14: Experimental order of convergence for the given norms, solving the sharp interface scheme \mathbb{P}_{SI}^h with $\omega = 10^{-3}$, and the DeTurck method. With Γ_h^0 given by (4.4.4). Here $L^2(v, U)$ for function v and set U denotes the experimental orders of convergence for the norm $\Delta t \sum_{n=0}^N \|v_h^n - v(t_n)\|_{L^2(U)}^2$, and $H^1(v, U)$ for function v and set U denotes the experimental orders of convergence for the norm $\Delta t \sum_{n=0}^N |v_h^n - v(t_n)|_{H^1(U)}^2$.

h	Δt	$L^2(u, \Omega_h^n)$	$H^1(u, \Omega_h^n)$	$L^2(\mathbf{X}, \mathbb{I})$	$H^1(\mathbf{X}, \mathbb{I})$
7.85E-01	7.40E-03	1.63E-03	8.27E-02	3.10E-04	9.01E-02
4.81E-01	3.90E-03	1.65E-04	2.59E-02	2.29E-05	2.54E-02
2.69E-01	2.00E-03	1.49E-05	7.29E-03	1.73E-06	6.78E-03
1.42E-01	1.00E-03	1.35E-06	1.92E-03	1.50E-07	1.74E-03
7.30E-02	5.20E-04	1.51E-07	4.87E-04	1.88E-08	4.40E-04

Table 4.15: Errors for the given norms, solving the sharp interface scheme \mathbb{P}_{SI}^h with $\omega = 1$, and the harmonic extension method. With Γ_h^0 given by (4.4.4). Here $L^2(v, U)$ for function v and set U denotes the norm $\Delta t \sum_{n=0}^N \|v_h^n - v(t_n)\|_{L^2(U)}^2$, and $H^1(v, U)$ for function v and set U denotes the norm $\Delta t \sum_{n=0}^N |v_h^n - v(t_n)|_{H^1(U)}^2$.

h	Δt	$L^2(u, \Omega_h^n)$	$H^1(u, \Omega_h^n)$	$L^2(\mathbf{X}, \mathbb{I})$	$H^1(\mathbf{X}, \mathbb{I})$
7.85E-01	7.40E-03				
4.81E-01	3.90E-03	4.68	2.37	5.33	2.58
2.69E-01	2.00E-03	4.12	2.18	4.43	2.27
1.42E-01	1.00E-03	3.77	2.10	3.84	2.13
7.30E-02	5.20E-04	3.29	2.05	3.11	2.07

Table 4.16: Experimental order of convergence for the given norms, solving the sharp interface scheme \mathbb{P}_{SI}^h with $\omega = 1$, and the harmonic extension method. With Γ_h^0 given by (4.4.4). Here $L^2(v, U)$ for function v and set U denotes the experimental orders of convergence for the norm $\Delta t \sum_{n=0}^N \|v_h^n - v(t_n)\|_{L^2(U)}^2$, and $H^1(v, U)$ for function v and set U denotes the experimental orders of convergence for the norm $\Delta t \sum_{n=0}^N |v_h^n - v(t_n)|_{H^1(U)}^2$.

h	Δt	$L^2(u, \Omega_h^n)$	$H^1(u, \Omega_h^n)$	$L^2(\mathbf{X}, \mathbb{I})$	$H^1(\mathbf{X}, \mathbb{I})$
8.18E-01	7.40E-03	2.22E-03	9.68E-02	2.56E-04	9.06E-02
4.85E-01	3.90E-03	1.96E-04	2.77E-02	1.98E-05	2.55E-02
2.69E-01	2.00E-03	1.65E-05	7.46E-03	1.56E-06	6.78E-03
1.42E-01	1.00E-03	1.45E-06	1.93E-03	1.43E-07	1.74E-03
7.29E-02	5.20E-04	1.58E-07	4.88E-04	1.88E-08	4.40E-04

Table 4.17: Errors for the given norms, solving the sharp interface scheme \mathbb{P}_{SI}^h with $\omega = 10^{-3}$, and the harmonic extension method. With Γ_h^0 given by (4.4.4). Here $L^2(v, U)$ for function v and set U denotes the norm $\Delta t \sum_{n=0}^N \|v_h^n - v(t_n)\|_{L^2(U)}^2$, and $H^1(v, U)$ for function v and set U denotes the norm $\Delta t \sum_{n=0}^N |v_h^n - v(t_n)|_{H^1(U)}^2$.

h	Δt	$L^2(u, \Omega_h^n)$	$H^1(u, \Omega_h^n)$	$L^2(\mathbf{X}, \mathbb{I})$	$H^1(\mathbf{X}, \mathbb{I})$
8.18E-01	7.40E-03				
4.85E-01	3.90E-03	4.64	2.40	4.90	2.43
2.69E-01	2.00E-03	4.21	2.23	4.32	2.25
1.42E-01	1.00E-03	3.81	2.11	3.74	2.12
7.29E-02	5.20E-04	3.32	2.06	3.04	2.06

Table 4.18: Experimental order of convergence for the given norms, solving the sharp interface scheme \mathbb{P}_{SI}^h with $\omega = 10^{-3}$, and the harmonic extension method. With Γ_h^0 given by (4.4.4). Here $L^2(v, U)$ for function v and set U denotes the experimental orders of convergence for the norm $\Delta t \sum_{n=0}^N \|v_h^n - v(t_n)\|_{L^2(U)}^2$, and $H^1(v, U)$ for function v and set U denotes the experimental orders of convergence for the norm $\Delta t \sum_{n=0}^N |v_h^n - v(t_n)|_{H^1(U)}^2$.

4.4.2 Comparison of the radius in \mathbb{R}^3

In this section we compare the radii of spheres in \mathbb{R}^3 , evolving under the sharp interface scheme $\mathbb{P}_{SI\mathbb{R}^3}^h$ in Figure 4.9, and the diffuse interface scheme $\tilde{\mathbb{P}}_{DI}^h$ in Figure 4.10. We take a number of values of h in order to see how it affects the error. We chose $\alpha = \beta = 1.0$, $Q = 1.66$, and the initial radius $R_0 = 1.0$. In the sharp interface simulations we take $h \approx 0.45, 0.35$, and 0.21 , we take $\Delta t = 5 \times 10^{-3}, 2.5 \times 10^{-3}$, and 1.25×10^{-3} , and the number of degrees of freedom *dofs* are *dofs* $\approx 3.9 \times 10^3, 1.5 \times 10^4$, and 6.3×10^4 . In the diffuse interface simulations we take $\varepsilon = 0.151, 0.125$, and 0.1 for the values $h \approx 0.027, 0.024$, and 0.014 , $\Delta t = 5 \times 10^{-5}, 10^{-5}$, and 5×10^{-6} , and the number of degrees of freedom *dofs*, at $t = 0$, are *dofs* $\approx 1.1 \times 10^5, 2.6 \times 10^5$, and 8.2×10^5 .

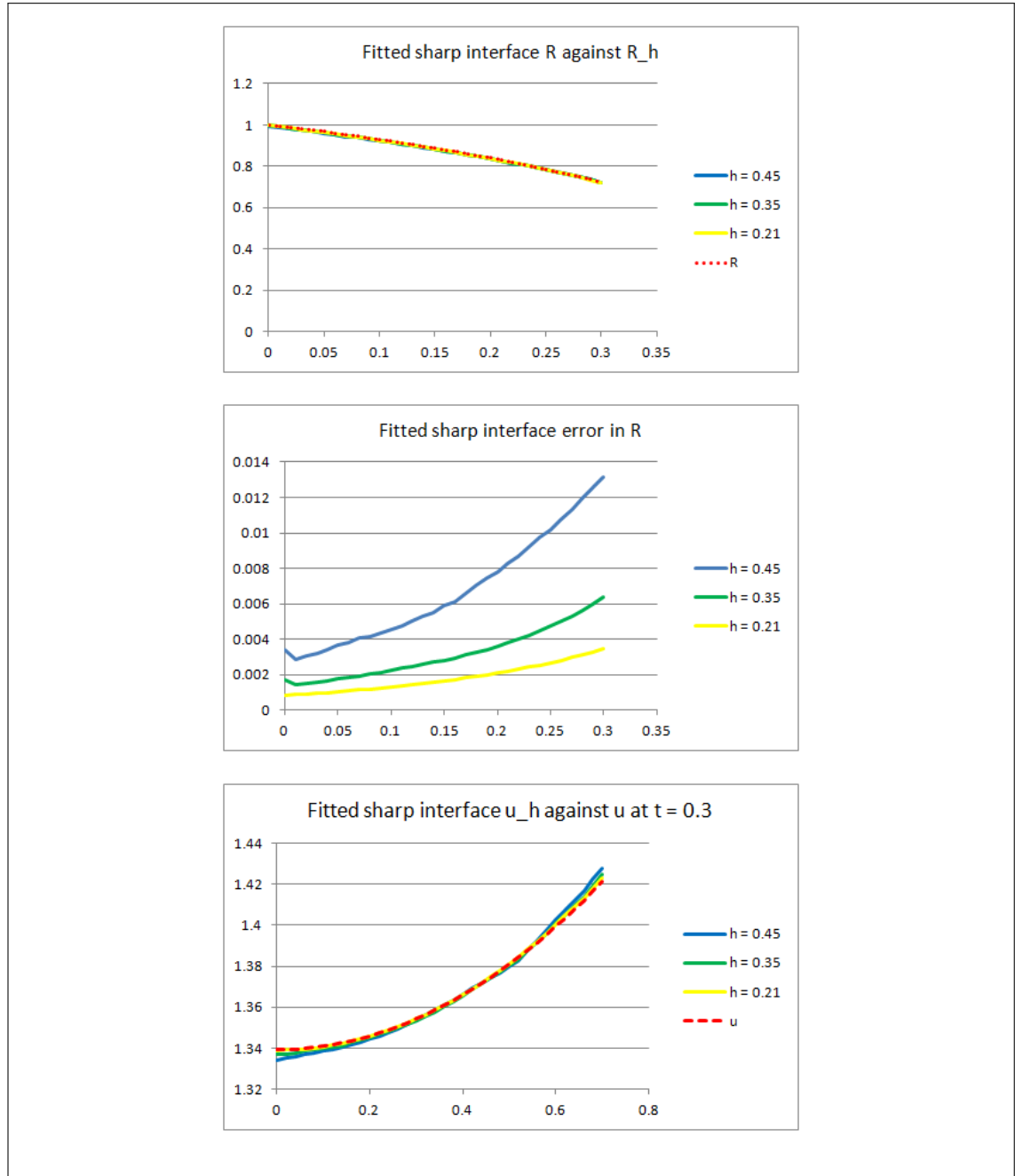


Figure 4.9: Top plot: comparison of the radius, in \mathbb{R}^3 , computed using the sharp interface scheme $\mathbb{P}_{SI\mathbb{R}^3}^h$, with varying values of h , and the analytical radius (dashed red line). Center plot: the error $|R - R_h|$ for different values of h . Bottom plot: Comparison of u_h from the sharp interface scheme, with the extended analytical solution u (dashed red), taken at $t = 0.3$. We take $h \approx 0.45, 0.35$, and 0.21 , we take $\Delta t = 5 \times 10^{-3}, 2.5 \times 10^{-3}$, and 1.25×10^{-3} , and the number of degrees of freedom $dofs$ are $dofs \approx 3.9 \times 10^3, 1.5 \times 10^4$, and 6.3×10^4 .

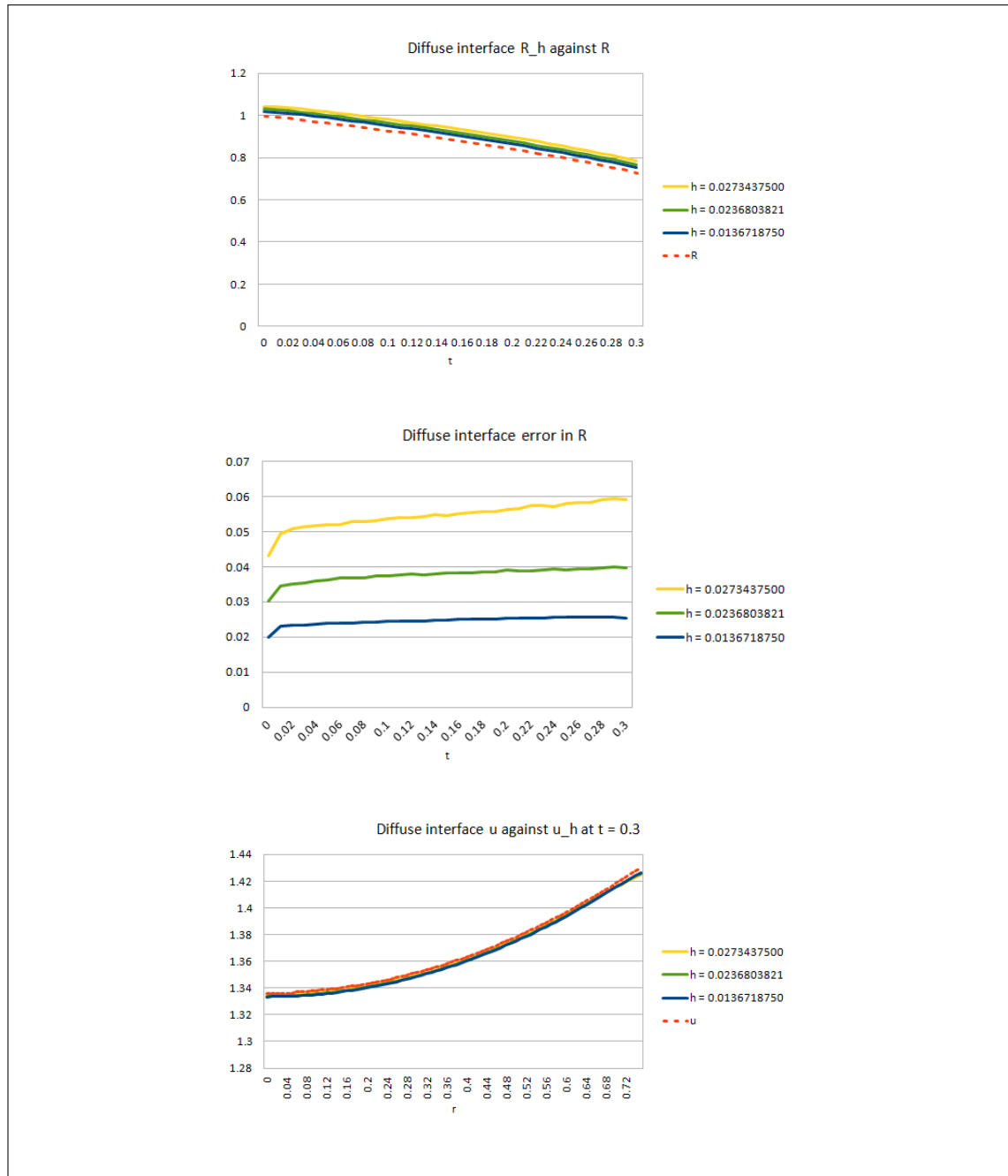


Figure 4.10: Top plot: comparison of the radius, in \mathbb{R}^3 , computed using the diffuse interface scheme \mathbb{P}_{DI}^h , with varying values of h , and the analytical radius (dashed red line). Center plot: the error $|R - R_h|$ for different values of h . Bottom plot: comparison of u_h from the diffuse interface scheme, with the extended analytical solution u (dashed red line), taken at $t = 0.3$. We take $\varepsilon = 0.151, 0.125$, and 0.1 for the values $h \approx 0.027, 0.024$, and 0.014 , $\Delta t = 5 \times 10^{-5}, 10^{-5}$, and 5×10^{-6} , and the number of degrees of freedom $dofs$, at $t = 0$, are $dofs \approx 1.1 \times 10^5, 2.6 \times 10^5$, and 8.2×10^5 .

4.4.3 Effect of the regularisation parameter γ in $(\tilde{\mathbb{M}})$

In $(\tilde{\mathbb{M}}b)$, $\gamma \nabla u \cdot \mathbf{n}$ was introduced in order to give both formulations of the model Robin boundary conditions. The effect of adding this term is not clear, although for a small γ we show the effect to be negligible. In order to investigate this we consider the radially symmetric case, and compute the error. We consider the steady state with $R_0 = R(t) = 2.0$. This corresponds to $\beta = 1.0$ and $Q = 1.5$, and we choose $\alpha = 0.01$, $\Delta t = 10^{-4}$, $T = 1.0$, and $h \approx 0.03$.

The results of the simulations are displayed in Table 4.19. We can see that for $\gamma \leq 10^{-4}$ there is a negligible change in the error. For this reason we take $\gamma = 10^{-5}$ for all other simulations. It is interesting to note that the error only changes in the $L^2(0, T; L^2(\Omega_h^n))$ norm. This is because, in the stationary radially symmetric case, changing γ only serves to translate u to $u + c$ for some constant c (so the gradient remains unchanged). Importantly, the gradient only remains unaffected in this special case; we are not able to take γ large if $\Omega(t)$ is not radially symmetric. The velocity law $(\tilde{\mathbb{M}}c)$ is only forced by the gradient of u , so this is unaffected.

γ	$\ u_h - u\ _{L^2(L^2(\Omega_h^n))}$	$\ u_h - u\ _{L^2(H^1(\Omega_h^n))}$	$\ \mathbf{X}_h - \mathbf{X}\ _{L^2(L^2(\mathbb{I}))}$	$\ \mathbf{X}_h - \mathbf{X}\ _{L^2(H^1(\mathbb{I}))}$
1	12.5048958	0.000106	0.00032	9.13E-05
10^{-1}	0.1292175	0.000106	0.000332	0.000104
10^{-2}	0.00175579	0.000106	0.000335	0.000106
10^{-3}	0.00011647	0.000106	0.000336	0.000109
10^{-4}	6.3455E-05	0.000106	0.000337	0.00011
10^{-5}	5.9258E-05	0.000106	0.000337	0.00011
10^{-6}	5.8849E-05	0.000106	0.000337	0.00011

Table 4.19: Comparison of errors for different values of γ when solving $\tilde{\mathbb{P}}_{SI}^h$ with $h \approx 0.03$ and $\Delta t = 10^{-4}$. Here $\|f\|_{L^2(L^2(U))} := \Delta t \sum_{n=0}^N \|f^n\|_{L^2(U)}^2$, and $\|f\|_{L^2(H^1(U))} := \Delta t \sum_{n=0}^N \|f^n\|_{H^1(U)}^2$ for a set U and function f .

4.4.4 Diverging from radial symmetry: reducing invasion

Spheroid models are often used as a bridge between *in vivo* and *in vitro* tumours, for example in [56], as they are relatively easy to cultivate in a laboratory [12, 14], and they occur naturally *in vivo*, see for example Figure 4.11 and [34]. They are also useful as an

intermediary between mathematical models and physical tumours [20], as the mathematics can often be simplified to one space dimension. The diameter of the spheroids is limited by the distance that nutrients are able to diffuse, often reaching a diameter of around $1-2\text{mm}$ [14, 23], and page 25 of [34]. Research into spheroids is ongoing, as the applications include, among others, drug testing [60] and photodynamic therapy (activating a drug with a specific wavelength of light) [35]. Running simulations using our model, we see that many non trivial geometries converge to a spheroid, for example Figure 4.12 shows a rounded star shape converging to a circle. This section, however, investigates the converse of this: spheroids becoming unstable and losing their symmetry.



Figure 4.11: Two examples of slices of spheroids *in vivo* (outlined in red). The images are taken from the database used in [22, 29]. There is more information on the database in Section 4.5.4. The tumour type (both meningiomas), file number, and patient ID are written above the images.

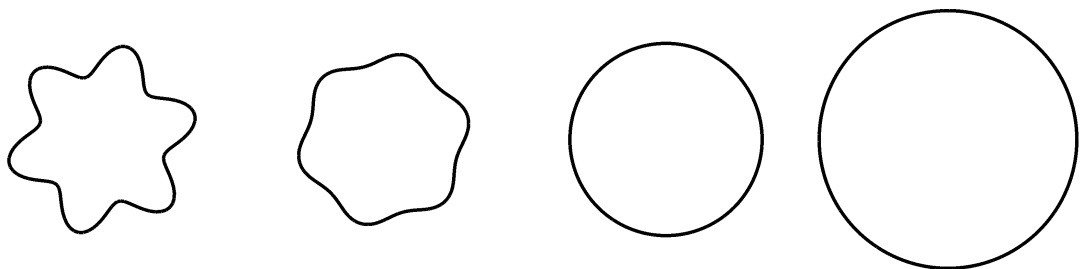


Figure 4.12: This figure shows a rounded star shape converging to a spheroid steady state. Here we solve the sharp interface scheme \mathbb{P}_{SI}^h , with $Q = 1.0$, $\beta = 0.3$, $\alpha = 1.0$, $h \approx 0.075$ and $\Delta t = 10^{-2}$. From left to right we have $t = 0, 0.1, 1$, and 10 . The geometry does not change significantly for $t > 10$. The initial geometry is formed by distorting a circle of initial radius $R_0 = 1.0$ in the normal direction by $0.2 \sin(6\theta)$, where θ is the polar angle.

Behaviour similar to that which we are trying to reproduce (instability in a spheroid,

also called unstable budding) is seen in [24]. In this paper they discuss possible therapies that would inhibit morphological instability (and thus reduce the chance of metastasis and invasion). In particular, they provide evidence that morphological instability could be suppressed in vivo by inducing a spatially homogeneous oxygen and nutrient supply. Note that in our simulations the nutrient supply is homogeneous, so something else is driving the instability, possibly the initial mesh.

We focus on choosing parameter values that cause the radially symmetric steady state to become morphologically unstable. Figure 4.13 is an example of the eventual morphology if we allow the tumour to continue evolving. In our model we can see from (4.4.2) that (for fixed dimension d) Q and β determine the radius at which a steady state lies, and whether the steady state is stable or unstable (when assuming that the solution is constrained to radial symmetry); α has no effect on the radius of the steady state.

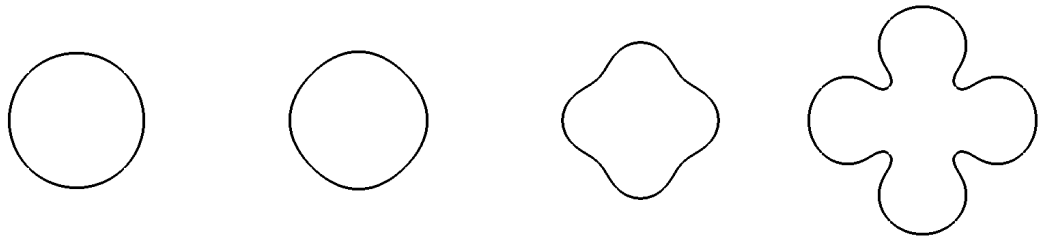


Figure 4.13: Solving the finite element scheme \mathbb{P}_{SI}^h with $\alpha = 10^{-2}$, $\beta = 0.5$, $Q = 1.5$, and initial radius $R_0 = 2.62$. Taken at $t = 0, 11, 16$, and 21 . We choose $\Delta t = 10^{-3}$ and $h \approx 0.076$. We can see that at $t = 11$ the radial symmetry begins to break.

The effect in Figure 4.13 is not caused by a lack of refinement in the mesh, as simulations with $\alpha = 10^{-2}$, $\beta = 0.5$, and $Q = 1.5$ were run with h as small as 4×10^{-4} , with no change in the behaviour (Δt was reduced in proportion to h). We believe, instead, that it is caused by the slight instabilities in the initial meshes. This instability has not been replicated in the diffuse interface paradigm, as the diffuse nature of the interface makes any differences in the mesh negligible. The nature of the diffuse interface ensures a significantly “smoother” initial circle.

The times at which the solutions of the model diverge from a circle are given in Tables 4.20, 4.21, and 4.22, in which we fix $\alpha = 10^{-2}$, $Q = 1.4$, and $\beta = 0.6$, respectively. Here we start each simulation at the radially symmetric stable steady state, the radius of which can be found in Table 4.24 (recall that this depends only on β and Q , not α). The simulation

is run until the $L^2(\mathbb{I})$ error of \mathbf{X}_h is greater than 0.1. This is an effective proxy for telling us when the radial symmetry is lost. The values of h for the initial meshes are given in Table 4.23 (again, note that this depends only on the initial radius, which itself depends only on β and Q , not α).

Our simulations show that lower values of β lead to greater instability, which makes sense physically as the $\beta\kappa$ term physically pertains to cell-cell adhesion, and if this is reduced we would expect to see instabilities form in the tumour. Our simulations seem to suggest that larger values of Q (the surface source nutrient term) also lead to instabilities. Additionally we see that smaller values of α lead to instabilities. This agrees with [47], since the authors note that α has a regularising effect.

		β					
		0.4	0.5	0.6	0.7	0.8	0.9
Q	1.6	6.501	8.616	13.926	68.912	>100	>100
	1.5	7.627	11.799	43.513	95.509	>100	>100
	1.4	9.74	24.59	90.66	>100	>100	>100
	1.3	15.663	82.154	>100	>100	>100	
	1.2	78.771	>100	>100	>100		
	1.1	>100	>100	>100			

Table 4.20: Time at which the $L^2(\mathbb{I})$ error in \mathbf{X}_h for the finite element scheme \mathbb{P}_{SI}^h is first greater than 0.1. Here $\alpha = 10^{-2}$, $\Delta t = 10^{-3}$, and the values of h can be found in Table 4.23. The initial shape is a circle, with initial radius given in Table 4.24. For entries of > 100 the error did not diverge for $t \in [0, 100]$. We did not use GMSH. The blank entries have no steady state.

		α			
		0.005	0.01	0.025	0.05
β	0.4	9.538	9.74	10.366	11.522
	0.5	23.143	24.59	30.127	48.107
	0.6	89.428	90.66	96.173	98.543
	0.7	>100	>100	>100	>100
	0.8	>100	>100	>100	>100
	0.9	>100	>100	>100	>100

Table 4.21: Time at which the $L^2(\mathbb{I})$ error in \mathbf{X}_h for the finite element scheme \mathbb{P}_{SI}^h is first greater than 0.1. Here $Q = 1.4$, $\Delta t = 10^{-3}$, and the values of h can be found in Table 4.23. The initial shape is a circle, with initial radius given in Table 4.24. Recall that R_0 (and thus h) depends only on β and Q . For entries of > 100 the error did not diverge for $t \in [0, 100]$. We did not use GMSH.

		α			
		0.005	0.01	0.025	0.05
Q	1.6	13.53	13.926	15.21	17.821
	1.5	38.857	43.513	66.409	70.972
	1.4	89.428	90.66	96.173	98.543
	1.3	>100	>100	>100	>100
	1.2	>100	>100	>100	>100
	1.1	>100	>100	>100	>100

Table 4.22: Time at which the $L^2(\mathbb{I})$ error in \mathbf{X}_h for the finite element scheme \mathbb{P}_{SI}^h is first greater than 0.1. Here $\beta = 0.6$, $\Delta t = 10^{-3}$, and the values of h can be found in Table 4.23. The initial shape is a circle, with initial radius given in Table 4.24. Recall that R_0 (and thus h) depends only on β and Q . For entries of > 100 the error did not diverge for $t \in [0, 100]$. We did not use GMSH.

		β					
		0.4	0.5	0.6	0.7	0.8	0.9
Q	1.6	0.084	0.082	0.080	0.078	0.074	0.071
	1.5	0.078	0.076	0.073	0.070	0.067	0.063
	1.4	0.072	0.069	0.066	0.062	0.058	0.052
	1.3	0.065	0.062	0.058	0.053	0.046	
	1.2	0.058	0.054	0.049	0.041		
	1.1	0.050	0.045	0.036			

Table 4.23: This table shows the values of h (to 3 decimal places) for the initial meshes used in the simulations of Section 4.4.4. The values of h are different for each initial radius, as we generate the mesh by refining a triangulation of a circle a fixed number of times. These initial radii can be found in Table 4.24. The blank entries have no steady state.

		β					
		0.4	0.5	0.6	0.7	0.8	0.9
Q	1.6	2.93	2.85	2.77	2.68	2.58	2.47
	1.5	2.70	2.62	2.52	2.42	2.31	2.17
	1.4	2.48	2.38	2.27	2.15	2.00	1.80
	1.3	2.24	2.13	2.00	1.84	1.60	
	1.2	2.00	1.86	1.69	1.40		
	1.1	1.74	1.56	1.20			

Table 4.24: Here we show the radius of the radially symmetric stable steady state for the given Q and β . These are shown to 2 decimal places. The blank entries have no steady state.

4.5 Simulations in \mathbb{R}^2

In this section we restrict the simulations to \mathbb{R}^2 . Sections 4.5.1 - 4.5.3 start by fixing $Q = 1.0$ and investigating the relationship between α and β . We start with the parameter space $\alpha < \beta$, followed by $\alpha > \beta$, and then $\alpha, \beta \ll 1$. These investigations include complex initial geometries, and the effect of taking $\alpha = 0$. This section concludes with the presentation of a number of *in vivo* tumours.

4.5.1 The parameter space $\alpha < \beta$

Our simulations show that for $\beta \gtrsim 0.3$ the geometry tends to a radially symmetric steady state, with the radius shrinking as β grows. This radius can be calculated by setting $R'(t) = 0$ in (4.4.2). This holds for $\alpha \in [0.1, 1]$, and initial geometry given by an ellipse of width 0.5 and height 1.0.

For the choice of $\beta = 1.0$ and $\alpha = 0.1$, our simulations show Γ_h transforming from an ellipse towards a circle, which then shrinks until it is too small for the mesh to resolve it. The time at which the interface produced by the sharp interface scheme \mathbb{P}_{SI}^h , with $h \approx 0.03$ and $\Delta t = 10^{-3}$, reached what visually looked like a point was $t \approx 0.4004$, the time at which the interfacial region produced by the diffuse interface scheme $\tilde{\mathbb{P}}_{DI}^h$, with $\varepsilon = 0.075$, $h \approx 0.06$ and $\Delta t = 10^{-4}$ reached a similar geometry was $t \approx 0.4443$, while the time associated with the unfitted sharp interface scheme \mathbb{P}_{SIU}^h , with $h \approx 0.05$ and $\Delta t = 5 \times 10^{-3}$ was $t \approx 0.43$. The discrepancy between the sharp interface and diffuse interface schemes is due to the fact that the imposed interfacial thickness in the diffuse interface scheme means that it is only an approximation of mean curvature flow.

4.5.2 The parameter space $\alpha > \beta$

We first investigate the parameter choice $\alpha > \beta$ with a simple initial geometry: an ellipse of width 0.5 and height 1.0. We choose $\alpha = 1.0$, $\beta = 0.1$, and $Q = 1.0$. We use the sharp interface schemes \mathbb{P}_{SI}^h and \mathbb{P}_{SIU}^h , and the diffuse interface scheme $\tilde{\mathbb{P}}_{DI}^h$. For the diffuse interface scheme we choose $\varepsilon = 0.075$, $\Delta t = 10^{-4}$, and $h \approx 0.07$. For the sharp interface scheme we take $\Delta t = 10^{-3}$ and $h \approx 0.03$. For the unfitted sharp interface scheme we take $\Delta t = 5 \times 10^{-3}$ and $h \approx 0.05$. The results of the simulations can be seen in Figure 4.14, where we see very good agreement between the schemes.

Figure 4.15 extends Figure 4.14 in time, and displays the evolution of the diffuse interface scheme. We see topological changes occurring beyond $t = 45$. Although from a purely mathematical standpoint the model holds when “holes” such as those visible in Figure 4.15 occur, this is not biologically realistic.

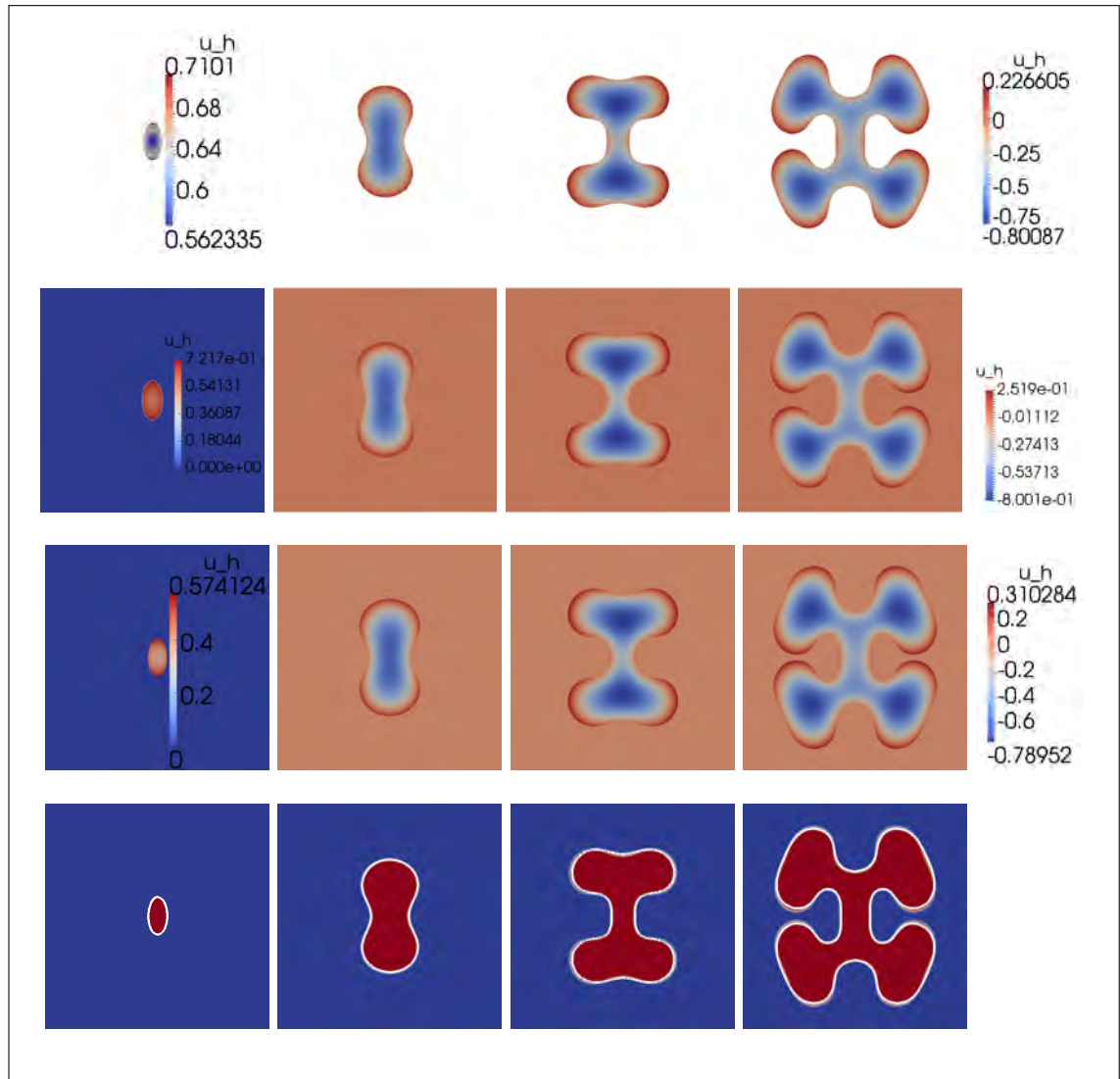


Figure 4.14: Solution u_h from the sharp interface scheme \mathbb{P}_{SI}^h (top row) with $h \approx 0.03$ and $\Delta t = 10^{-3}$ (top row), from the unfitted sharp interface scheme \mathbb{P}_{SIU}^h with $h \approx 0.05$ and $\Delta t = 5 \times 10^{-3}$ (second row), and from the diffuse interface scheme $\tilde{\mathbb{P}}_{DI}^h$, with $\varepsilon = 0.075$, $h \approx 0.07$ and $\Delta t = 10^{-4}$ (third row). On the fourth row: a comparison between \mathbf{X}_h from the sharp interface scheme (in white), \mathbf{X}_h from the unfitted sharp interface scheme (in black), and φ_h from the diffuse interface scheme (in red and blue). The black line is covered by the white line. With $\alpha = 1.0$, $\beta = 0.1$, and $Q = 1.0$. Taken at $t = 0, 15, 30$, and 45 .

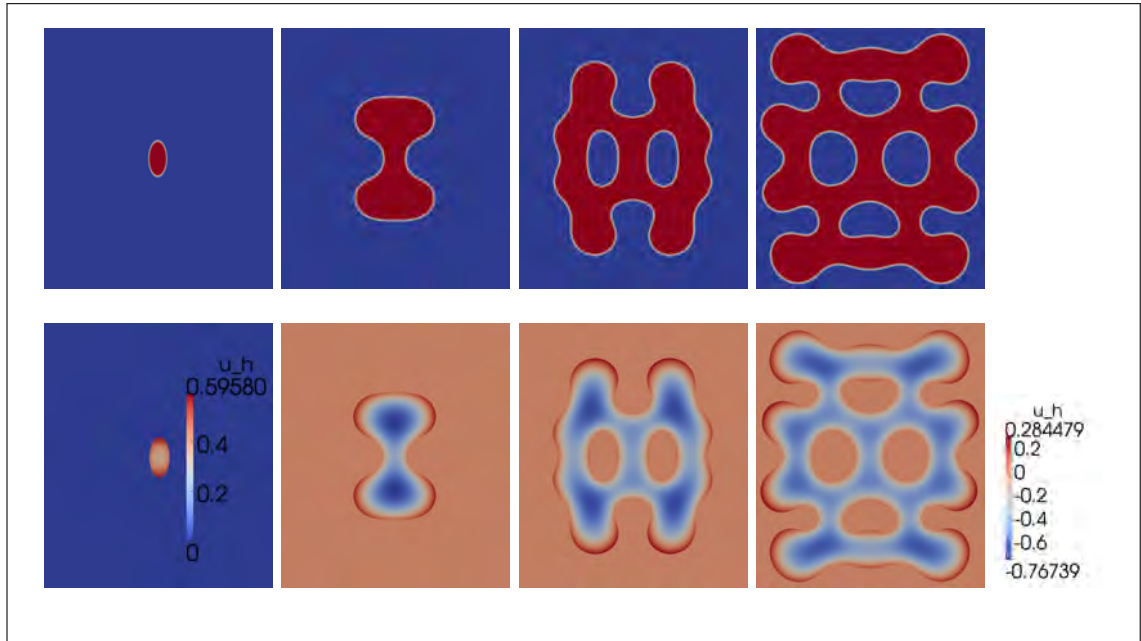


Figure 4.15: φ_h from the diffuse interface scheme $\tilde{\mathbb{P}}_{DI}^h$ (red and blue, top row). Diffuse interface solution u_h (bottom row). Taken at $t = 0, 25, 50,$ and 75 , with $\alpha = 1.0, \beta = 0.1, Q = 1.0, \varepsilon = 0.075, h \approx 0.07,$ and $\Delta t = 10^{-4}$. This extends Figure 4.14 in time.

More complex initial geometries

In Figure 4.16 we display two results from simulations using the sharp interface scheme \mathbb{P}_{SI}^h , in which the initial geometries Γ_h^0 are chosen to reduce symmetry. We choose $\alpha = 1.0, \beta = 0.1, Q = 1.0, \Delta t = 10^{-3},$ and $h \approx 0.017$. To create the initial geometries we perturb a point \mathbf{X}_h on an ellipse of width 0.5 and height 1.0 by a distance of either $0.2 \sin(5\theta)$ or $0.2 \sin(6\theta)$ in the direction $\frac{\mathbf{X}_h}{|\mathbf{X}_h|}$, where θ is the polar angle of \mathbf{X}_h . We present the solutions at $t = 0, 14, 29,$ and 46 . Beyond $t = 46$ we would see a change of topology due to merging.

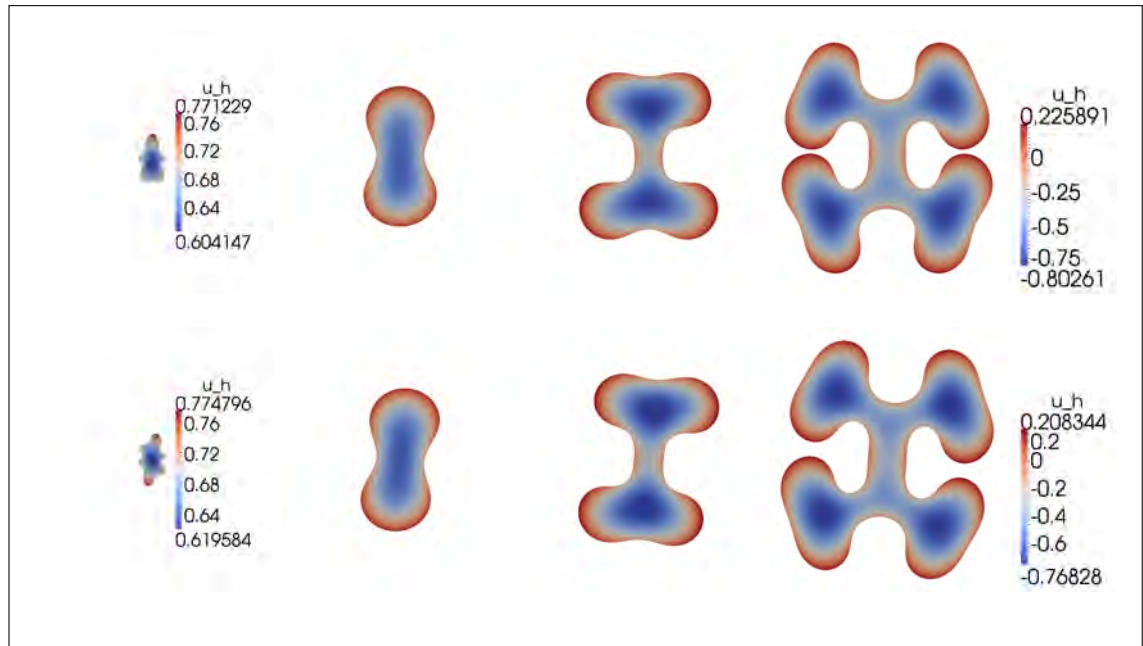


Figure 4.16: Two simulations (top row and bottom row) using the sharp interface scheme \mathbb{P}_{SI}^h with different initial geometries. The initial geometries are created by distorting an ellipse of width 0.5 and height 1.0 in the $\frac{\mathbf{x}_h}{|\mathbf{x}_h|}$ direction, by a distance of either $0.2 \sin(5\theta)$ on the top row, or $0.2 \sin(6\theta)$ on the bottom row. We choose $\alpha = 1.0$, $\beta = 0.1$, $Q = 1.0$, $\Delta t = 10^{-3}$, and $h \approx 0.017$. The snapshots are at $t = 0, 14, 29$, and 46.

Colliding circles

Figure 4.17 displays a simulation of two circles colliding, using the diffuse interface scheme $\tilde{\mathbb{P}}_{DI}^h$ with $\alpha = 1.0$, $\beta = 0.1$, $Q = 1.0$, $\varepsilon = 0.07$, $\Delta t = 5 \times 10^{-4}$, and $h \approx 0.03$, taken at $t = 0, 1, 6, 20, 30$, and 40. The initial geometry is given by two circles of radius 1.0, with centres at $(1.3, 0)$ and $(-1.3, 0)$. As they evolve, the circles grow and merge. Recall that the model is not biologically valid once “holes” have formed.

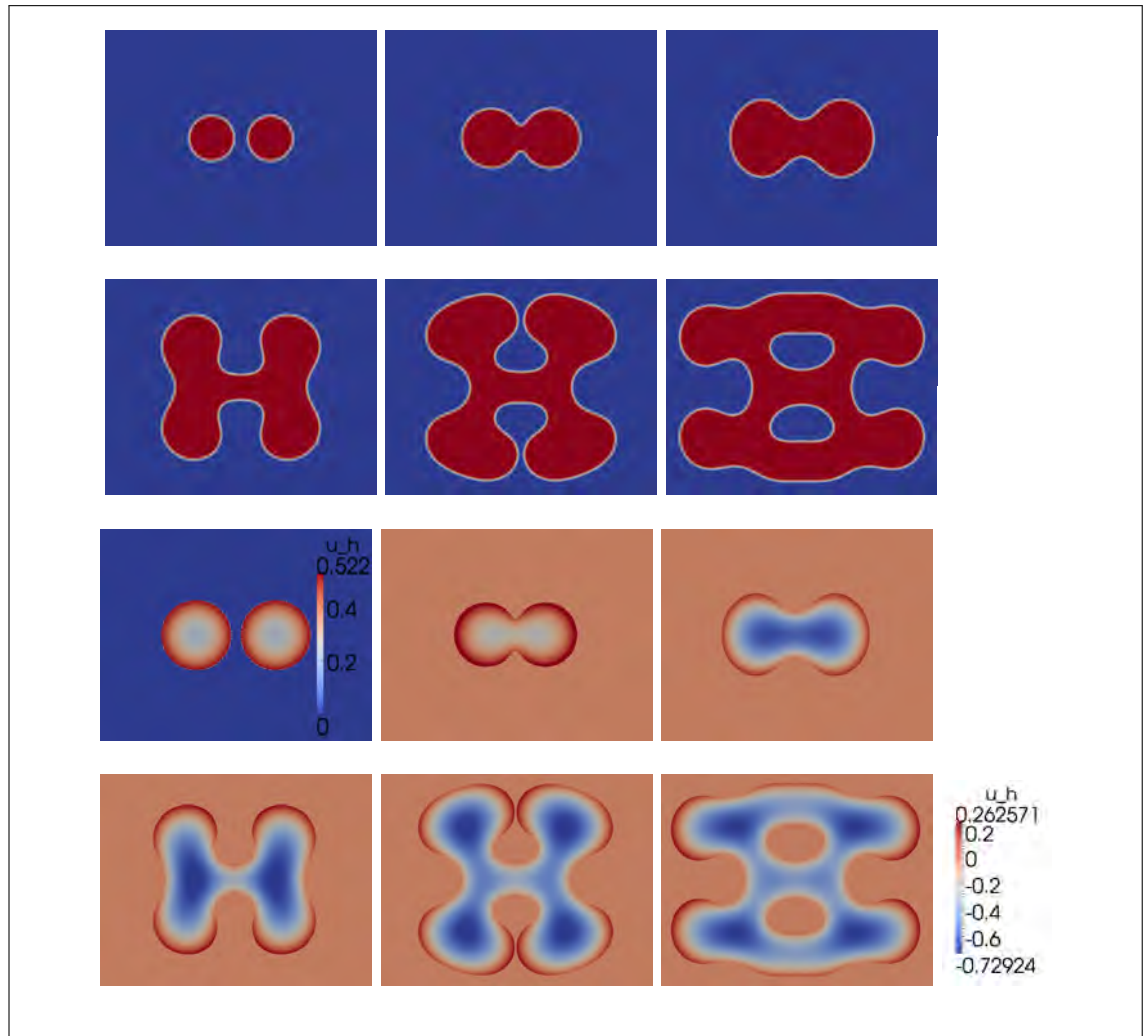


Figure 4.17: Diffuse interface scheme $\tilde{\mathbb{P}}_{DI}^h$, with $\alpha = 1.0$, $\beta = 0.1$, $Q = 1.0$, $\varepsilon = 0.07$, $\Delta t = 5 \times 10^{-4}$, and $h \approx 0.03$, taken at $t = 0, 1, 6, 20, 30$, and 40 . Rows one and two represent φ_h at these times, while rows three and four represent u_h at these times.

4.5.3 The parameter space $\alpha, \beta \ll 1.0$

In Figure 4.18 we display the solutions of the sharp interface schemes \mathbb{P}_{SI}^h and \mathbb{P}_{SIU}^h , and the solution of the diffuse interface scheme $\tilde{\mathbb{P}}_{DI}^h$. These are taken at $t = 0, 3$, and 7 . We take $\alpha = 0.1$, $\beta = 0.1$, and $Q = 1.0$; this is the smallest that we can feasibly take α for the diffuse interface scheme, since reducing α forces us to reduce ε , which greatly increases the computation time. For the sharp interface scheme we choose $\Delta t = 10^{-3}$ and $h \approx 0.03$. For the unfitted sharp interface scheme we choose $\Delta t = 10^{-3}$ and $h \approx 0.02$. For the diffuse interface scheme we take $\varepsilon = 0.01$, $\Delta t = 10^{-4}$, and $h \approx 0.02$. We see a good agreement between the schemes.

Figure 4.19 extends Figure 4.18 in time. We see topological changes occur after $t = 7$. Recall that the model is not biologically valid once “holes” have formed.

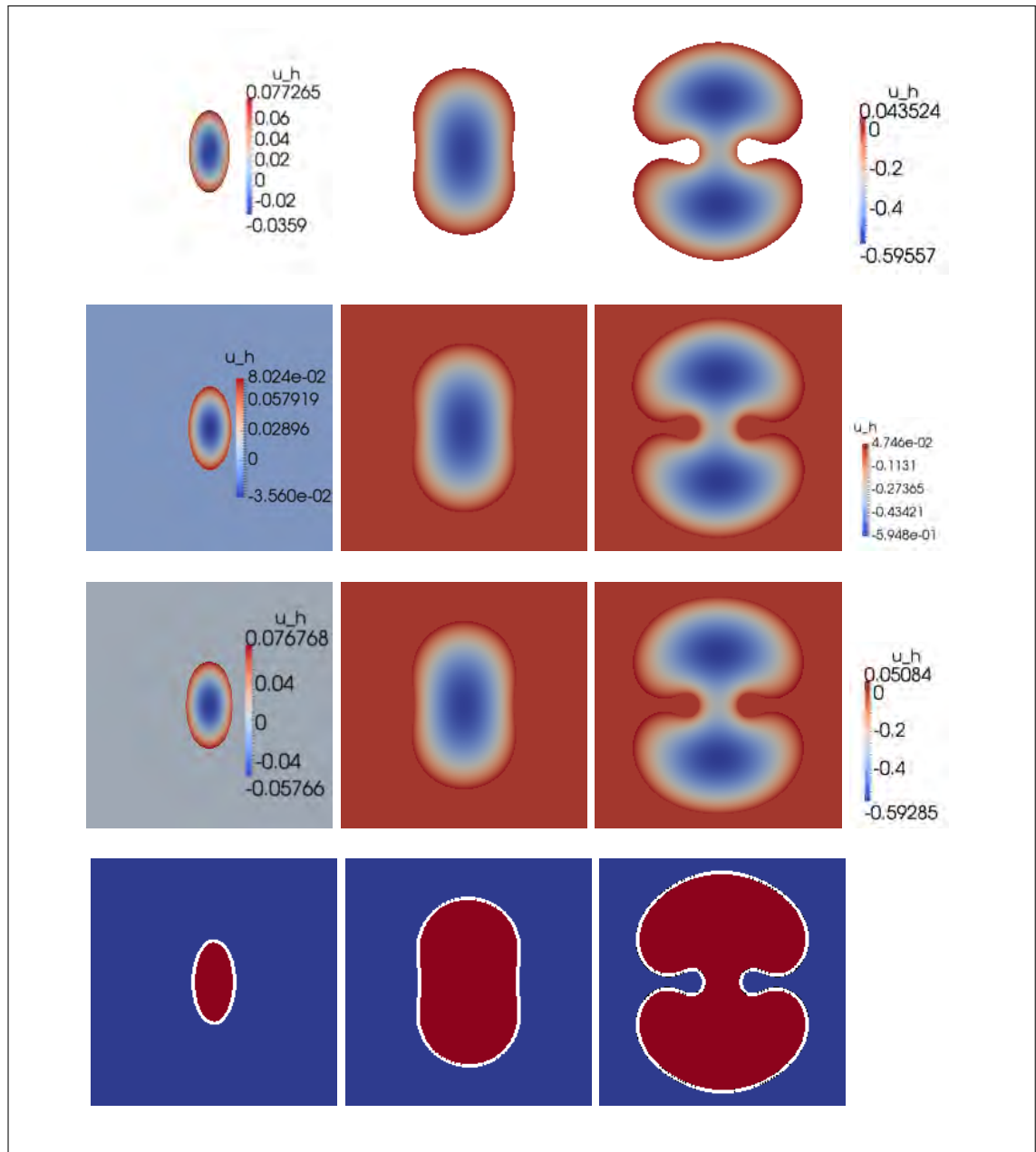


Figure 4.18: Solution u_h from the sharp interface scheme \mathbb{P}_{SI}^h with $h \approx 0.03, \Delta t = 10^{-3}$, (top row), from the unfitted sharp interface scheme \mathbb{P}_{SIU}^h with $h \approx 0.02, \Delta t = 10^{-3}$ (second row), and from the diffuse interface scheme $\tilde{\mathbb{P}}_{DI}^h$ with $\varepsilon = 0.01, h \approx 0.02, \Delta t = 10^{-4}$ (third row) at $t = 0, 3$, and 7 . On the fourth row: a comparison between \mathbf{X}_h from the sharp interface scheme (in white), \mathbf{X}_h from the unfitted sharp interface scheme (in black), and φ_h from the diffuse interface scheme (in red and blue, fourth row). The black line is covered by the white line. With $\alpha = 0.1, \beta = 0.1$, and $Q = 1.0$.

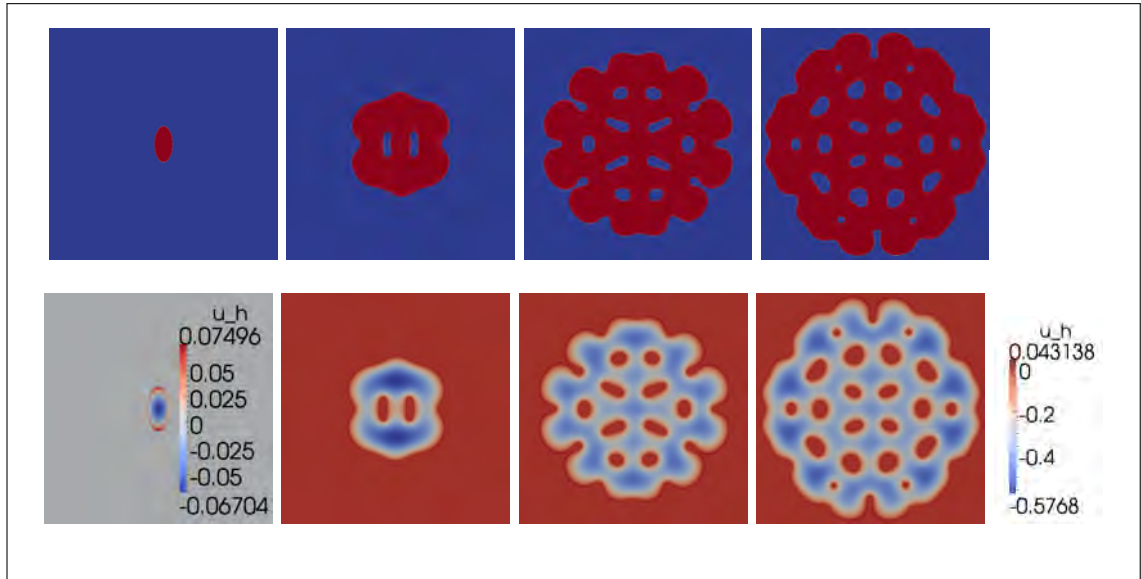


Figure 4.19: φ_h from the diffuse interface scheme $\tilde{\mathbb{P}}_{DI}^h$ (in red and blue) (top row). Diffuse interface solution u_h (bottom row). All taken at $t = 0, 10, 20$, and 24 , with $\alpha = 0.1$, $\beta = 0.1$, $Q = 1.0$, $\varepsilon = 0.01$, $\Delta t = 10^{-4}$, and $h \approx 0.02$. This extends Figure 4.18 in time.

More complex initial geometry

In Figure 4.20 we display two results using the sharp interface scheme \mathbb{P}_{SI}^h , in which the initial geometries match exactly those in Figure 4.16. We choose $\alpha = 0.1$, $\beta = 0.1$, $Q = 1.0$, $\Delta t = 10^{-3}$, and $h \approx 0.017$. We present the simulations at $t = 0, 1, 5$, and 7 . Beyond $t = 7$ we see a change in topology. We can see that the initial geometry has much more of an effect on the final geometry than in Figure 4.16, possibly due to a small α leading to less stability.

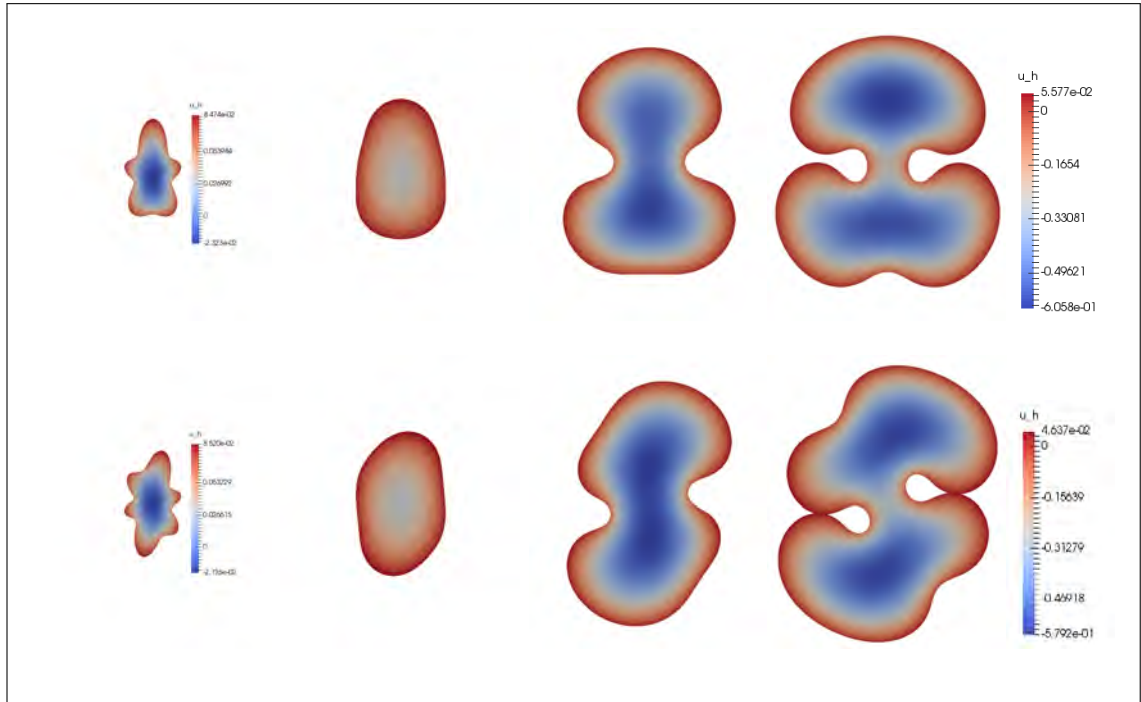


Figure 4.20: Two simulations (top row and bottom row) using the sharp interface scheme \mathbb{P}_{SI}^h , with different initial geometries. The initial geometries are created as described in Section 4.5.2, with the top row generated by $0.2\sin(5\theta)$ and the bottom row generated by $0.2\sin(6\theta)$. We choose $\alpha = 0.1$, $\beta = 0.1$, $Q = 1.0$, $\Delta t = 10^{-3}$, and $h \approx 0.017$. The snapshots are taken at $t = 0, 1, 5$, and 7 .

Sharp interface comparison with the alternate model

In this section we present a comparison between the sharp interface finite element schemes for the original model, \mathbb{P}_{SI}^h , and for the alternate model, $\tilde{\mathbb{P}}_{SI}^h$. Experimentally we see that the sharp interface scheme $\tilde{\mathbb{P}}_{SI}^h$ is unstable for $\alpha \gtrsim 0.01$. For this reason we choose $\alpha = 0.01$, along with $\beta = 0.1$, $Q = 1.0$, $h \approx 0.026$, and $\Delta t = 10^{-3}$. The comparison is presented in Figure 4.21. Note that our comparison is only concerned with the geometry, not the value of u_h , since $(\tilde{\mathbb{M}})$ has different equations for u than (\mathbb{M}) . We see a good agreement.

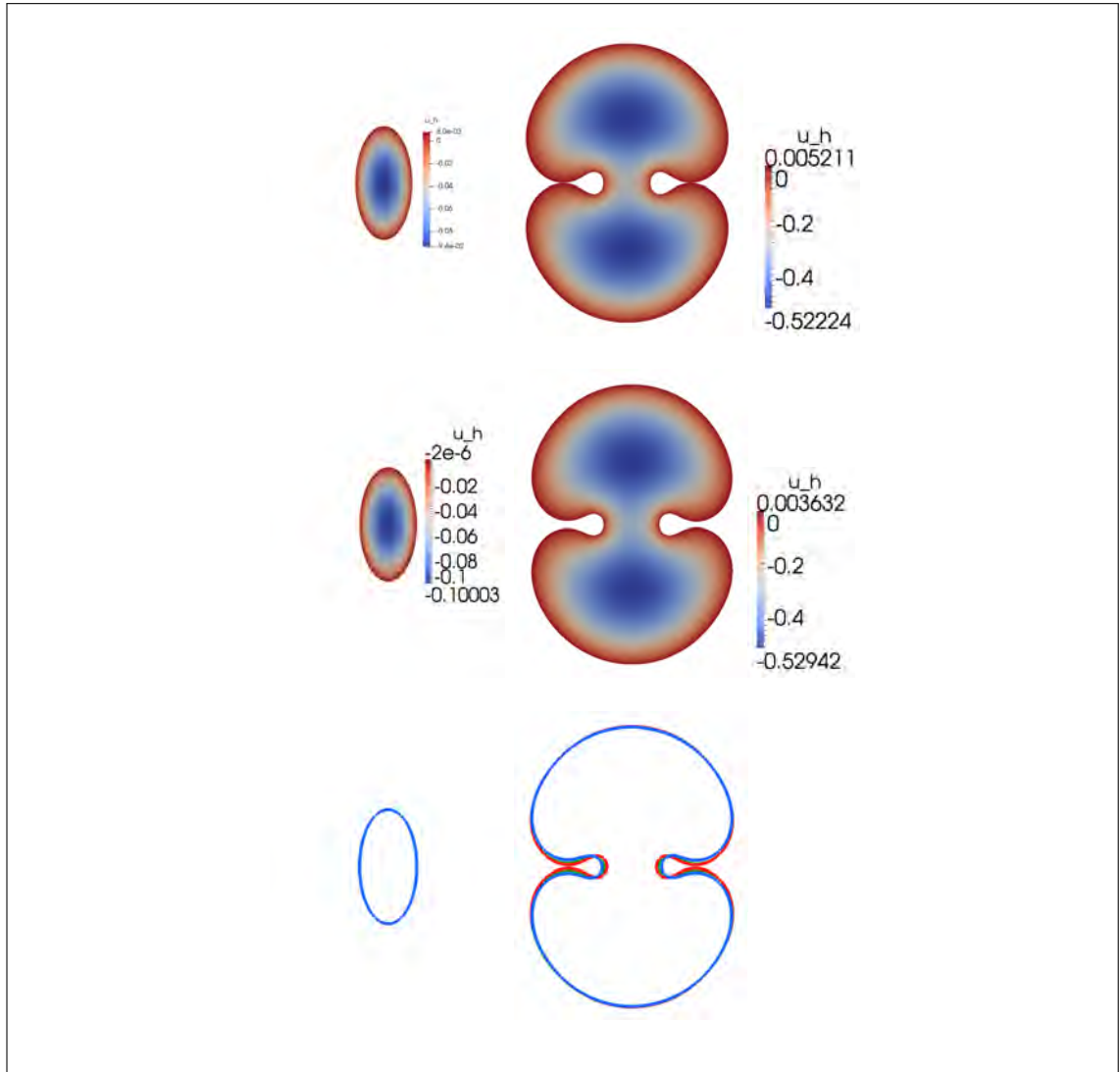


Figure 4.21: u_h from the sharp interface schemes \mathbb{P}_{SI}^h (first row) and $\tilde{\mathbb{P}}_{SI}^h$ (second row). Comparison of \mathbf{X}_h from each scheme (third row). Here \mathbb{P}_{SI}^h is in red and $\tilde{\mathbb{P}}_{SI}^h$ is in blue. The red line is almost entirely behind the blue line. We choose $\alpha = 0.01$, $\beta = 0.1$, $Q = 1.0$, $h \approx 0.026$, and $\Delta t = 10^{-3}$. The initial geometry is an ellipse of width 0.5 and height 1.0. The snapshots are taken at $t = 0$ and 5.

Setting $\alpha = 0$

In this section we investigate the effect of formally setting $\alpha = 0$. We see in [47] that α has a regularising effect on the model.

It is only appropriate to take $\alpha = 0$ in $(\tilde{\mathbb{M}})$. We numerically approximate this with the sharp interface scheme $\tilde{\mathbb{P}}_{SI}^h$, choosing $\beta = 0.1$, $Q = 1.0$, $\Delta t = 10^{-3}$, and $h \approx 0.03$, with an ellipse of width 0.5 and height 1.0 for the initial geometry. The simulation can be seen in Figure 4.22.

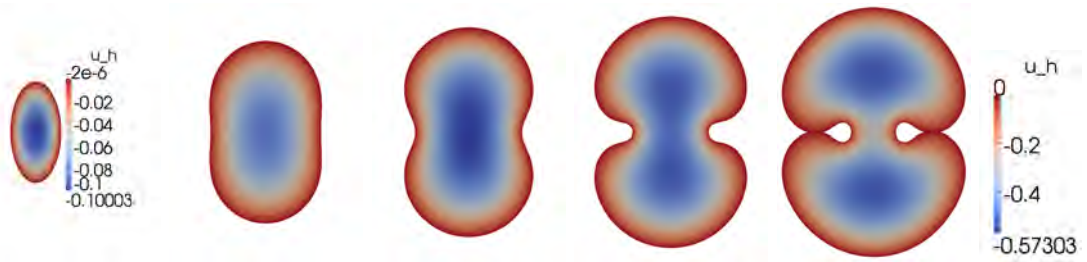


Figure 4.22: We solve the sharp interface scheme $\tilde{\mathbb{P}}_{SI}^h$ with $\alpha = 0$, $\beta = 0.1$, $Q = 1.0$, $\Delta t = 10^{-3}$, and $h \approx 0.03$, with an ellipse of width 0.5 and height 1.0 for the initial geometry. The snapshots are taken at $t = 0, 2, 3, 4$, and 5.

4.5.4 Example of tumours *in vivo*

This section includes a number of examples of tumours *in vivo*. These are included as a counterpoint to the simulations given in the rest of Section 4.5. We include two sets of tumour images: one set (in Figure 4.23) is visually similar to the parameter space $\alpha \geq \beta$, investigated in Section 4.5.2, and one set (in Figure 4.24) is visually similar to the parameter space $\alpha, \beta \ll 1.0$, investigated in Section 4.5.3.

The database used was the same as in [22, 29], and contains 3064 slices of brain tumours, taken from from 233 patients. This includes 708 meningiomas, 1426 gliomas, and 930 pituitary tumours. The slices are T1-weighted contrast-enhanced MRI images, which the authors of [22, 29] acquired from Nanfang Hospital, Guangzhou, China, and General Hospital Tianjing Medical University, China, between 2005 and 2010. The slice thickness is 6mm and the slice gap is 1mm. The tumour border was manually delineated by three experienced radiologists. In Figures 4.23 and 4.24 the slice is displayed in grey scale, while the tumour outline is shown in red. The type of each tumour, file number, and patient ID is written above each image.

In Figure 4.23 there are four images that are similar in morphology to the simulations in the parameter space $\alpha \geq \beta$, investigated in Section 4.5.2. In particular, the simulations in Figure 4.14 appear to show a similar “budding” structure, with two larger regions connected by a relatively long, thinner, strip.

Figure 4.24 displays four images that have a similar morphology to the the simulations in the parameter space $\alpha, \beta \ll 1.0$, investigated in Section 4.5.3. In particular, the simulations in Figure 4.18 have a similar structure, in which two sides have “pinched in”.

It is interesting to note that the tumours in Figure 4.23 and the tumours in Figure 4.24 are of different types. Figure 4.23 consists of gliomas, whilst Figure 4.24 consists of pituitary tumours. This suggests that the different parameters spaces investigated in Sections 4.5.2 and 4.5.1 might relate to different types of tumours.

This comparison has a caveat: the slices of the *in vivo* tumours are in \mathbb{R}^2 , however the tumours themselves are in \mathbb{R}^3 . This is in contrast to the simulations, in which the tumours are in \mathbb{R}^2 (and not slices from \mathbb{R}^3).

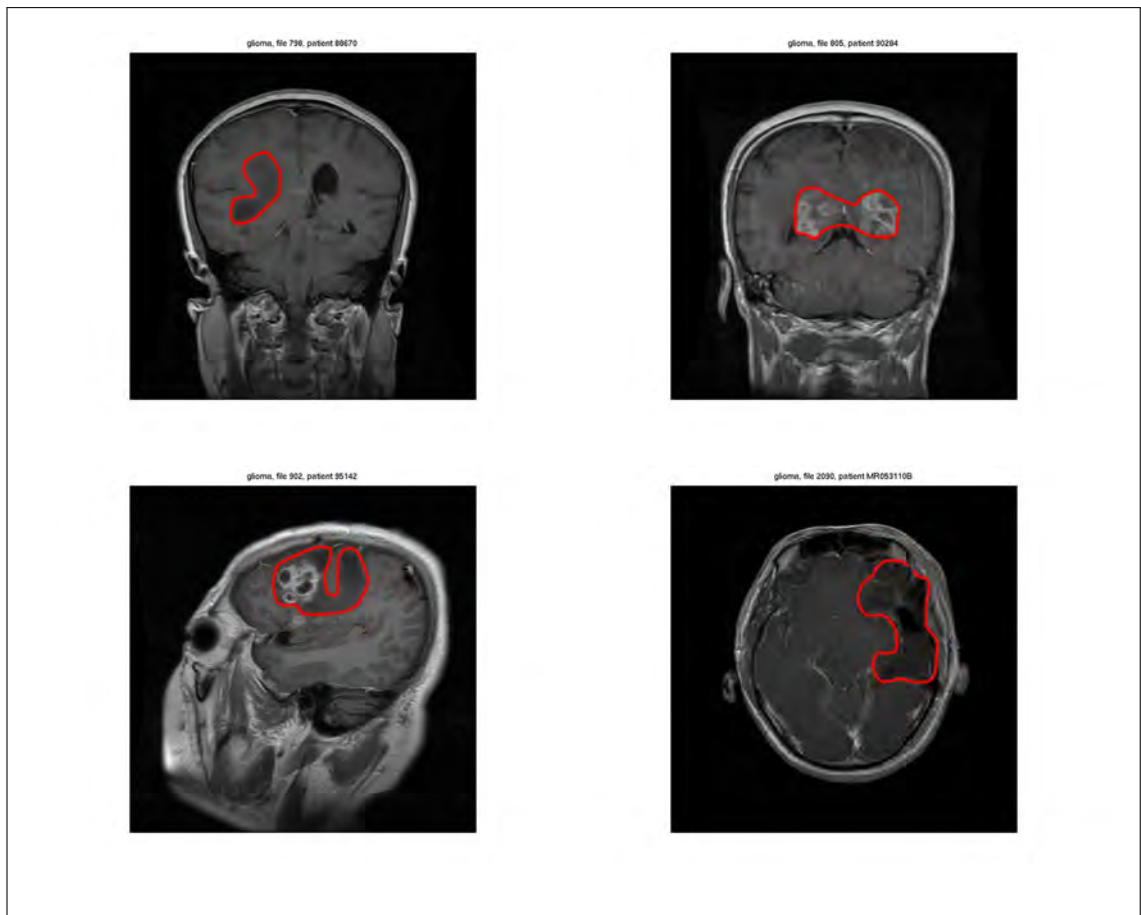


Figure 4.23: Slices of *in vivo* tumours from [22, 29]. The slice is shown in grey scale, while the tumour is outlined in red. Above each image is the tumour type (in this case they are all gliomas), the file number, and the patient ID. Each image is taken from a different patient.

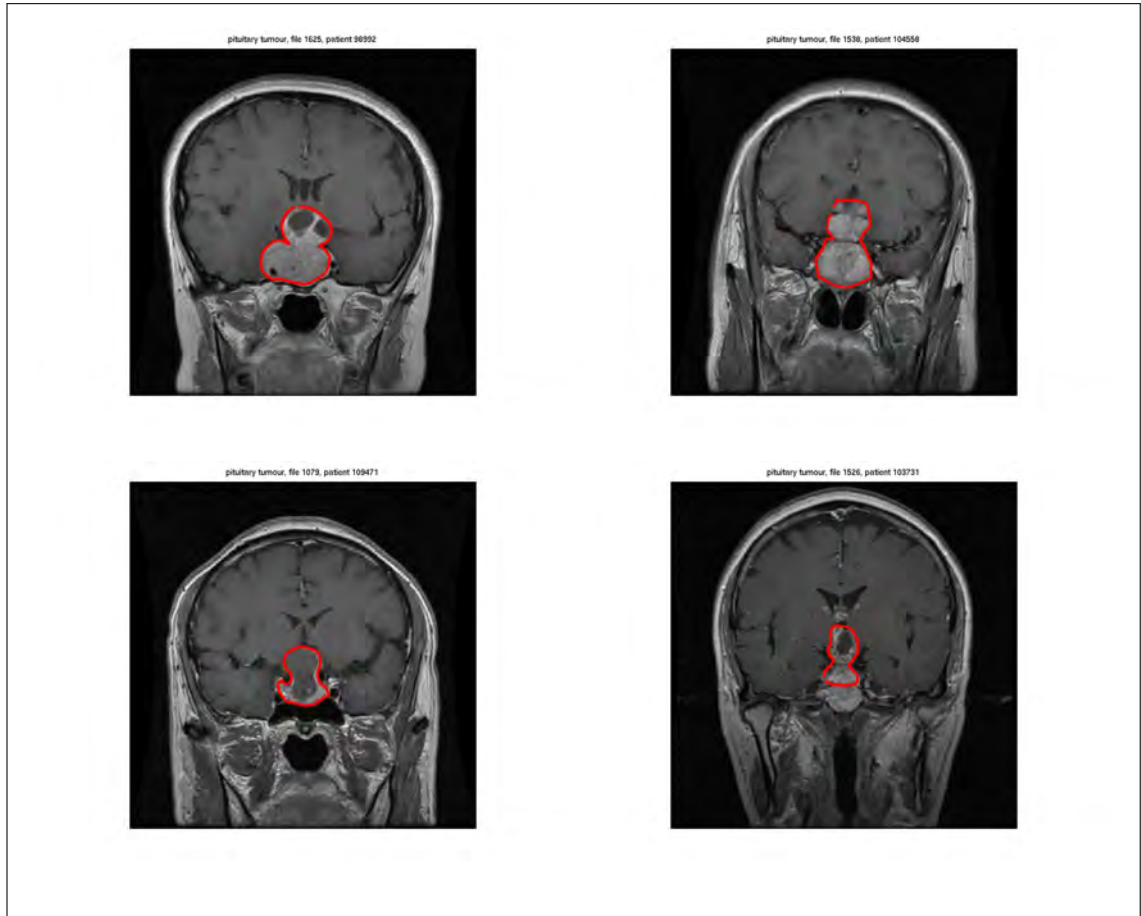


Figure 4.24: Slices of *in vivo* tumours from [22, 29]. The slice is shown in grey scale, while the tumour is outlined in red. Above each image is the tumour type (in this case they are all pituitary tumours), the file number, and the patient ID. Each image is taken from a different patient.

4.6 Simulations in \mathbb{R}^3

In this section we solve the three dimensional (in space) sharp interface scheme $\mathbb{P}_{SI\mathbb{R}^3}^h$ and the diffuse interface scheme $\tilde{\mathbb{P}}_{DI}^h$ (with $D \subset \mathbb{R}^3$). As in \mathbb{R}^2 , we fix $Q = 1.25$ in order to investigate the relationship between α and β . We take $Q > 1$ (in contrast to the simulations in Section 4.5) as we computationally found that in three space dimensions smaller Q leads to trivial solutions, where the tumour shrinks beyond resolution. When taking $\alpha, \beta \ll 1.0$, we do not use the diffuse interface scheme $\tilde{\mathbb{P}}_{DI}^h$, since the smaller value of α requires a smaller ε (and thus smaller h and Δt). This in turn significantly increases the execution time. This investigation of parameter spaces is followed by two examples of *in vivo* tumours.

4.6.1 The parameter space $\alpha > \beta$

We choose $\alpha = 1.0$, $\beta = 0.1$, $Q = 1.25$, and the initial geometry Γ_h^0 is given by the oblate spheroid with equation $\frac{x^2}{1.0^2} + \frac{y^2}{0.5^2} + \frac{z^2}{1.0^2} = 1$. In the sharp interface case $h \approx 0.014$ and $\Delta t = 5 \times 10^{-3}$.

Figure 4.25 shows \mathbf{X}_h , the solution to the sharp interface scheme $\mathbb{P}_{SI\mathbb{R}^3}^h$, from three different angles: looking down the x -axis, down the y -axis, and a cross section in the plane $z = 0$. Figure 4.25 also shows the solution u_h via a cross section in the plane $z = 0$. Note that the morphology has many similarities with the two dimensional simulations. This is particularly noticeable in the cross sections.

In Figure 4.26 we display the solution to the diffuse interface scheme $\tilde{\mathbb{P}}_{DI}^h$ (with identical parameters to the ones used in the sharp interface results shown in Figure 4.25, apart from $\varepsilon = 0.1$, $h \approx 0.04$, and $\Delta t = 10^{-3}$). In Figure 4.26 we see the zero level set of φ_h looking down the x -axis, down the y -axis, and a cross section in the plane $z = 0$. We also see a cross section in the plane $z = 0$ displaying u_h . The relatively large value of h (chosen to reduce the simulation's run time) is the most likely reason for the difference between the sharp interface and phase field solutions for the pressure u_h .

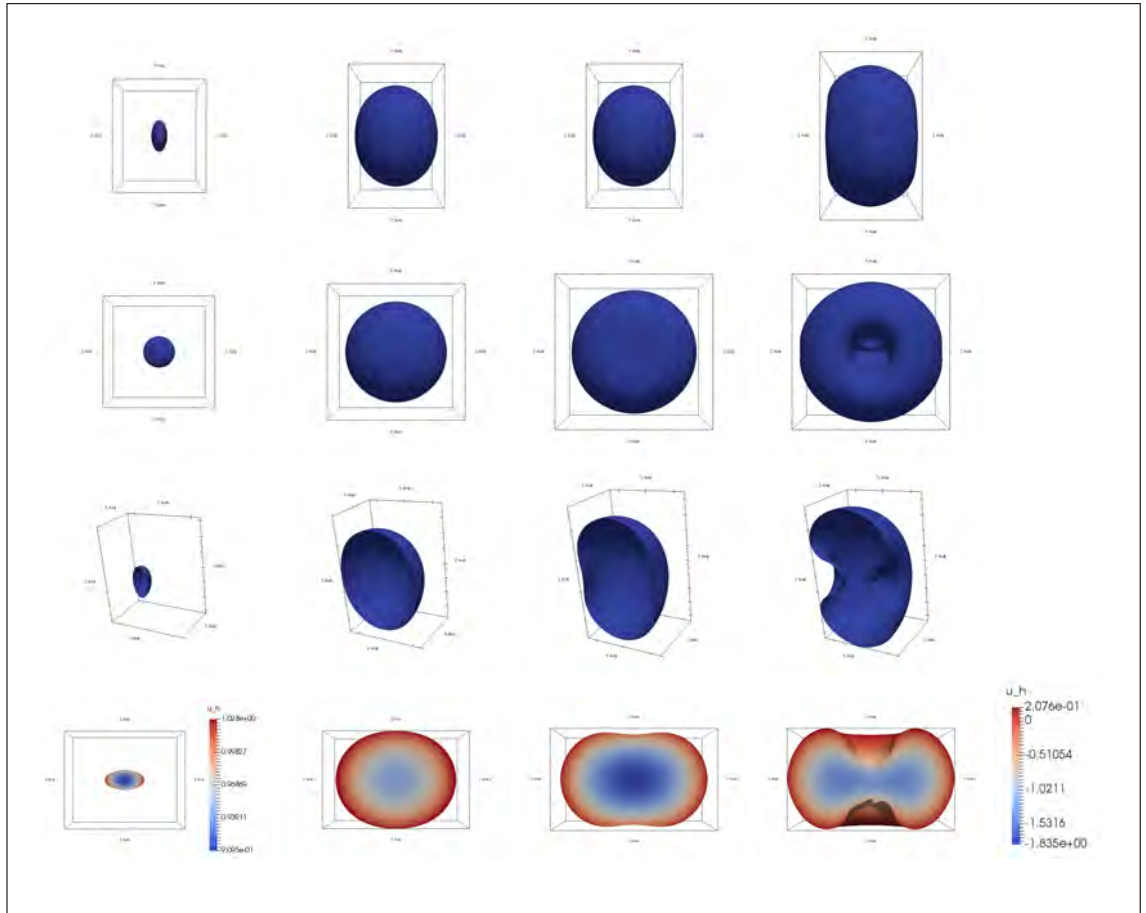


Figure 4.25: \mathbf{X}_h for the sharp interface scheme $\mathbb{P}_{SIR^3}^h$, looking down the x -axis (first line), looking down the y -axis (second line), cross section in the plane $z = 0$ (third line), and u_h in the plane $z = 0$ (fourth line). Taken at $t = 0, 5, 10$, and 15 . The initial geometry is an oblate spheroid with the equation $\frac{x^2}{1.0^2} + \frac{y^2}{0.5^2} + \frac{z^2}{1.0^2} = 1$. We take $\alpha = 1.0$, $\beta = 0.1$, $Q = 1.25$, $h \approx 0.014$, and $\Delta t = 5 \times 10^{-3}$.

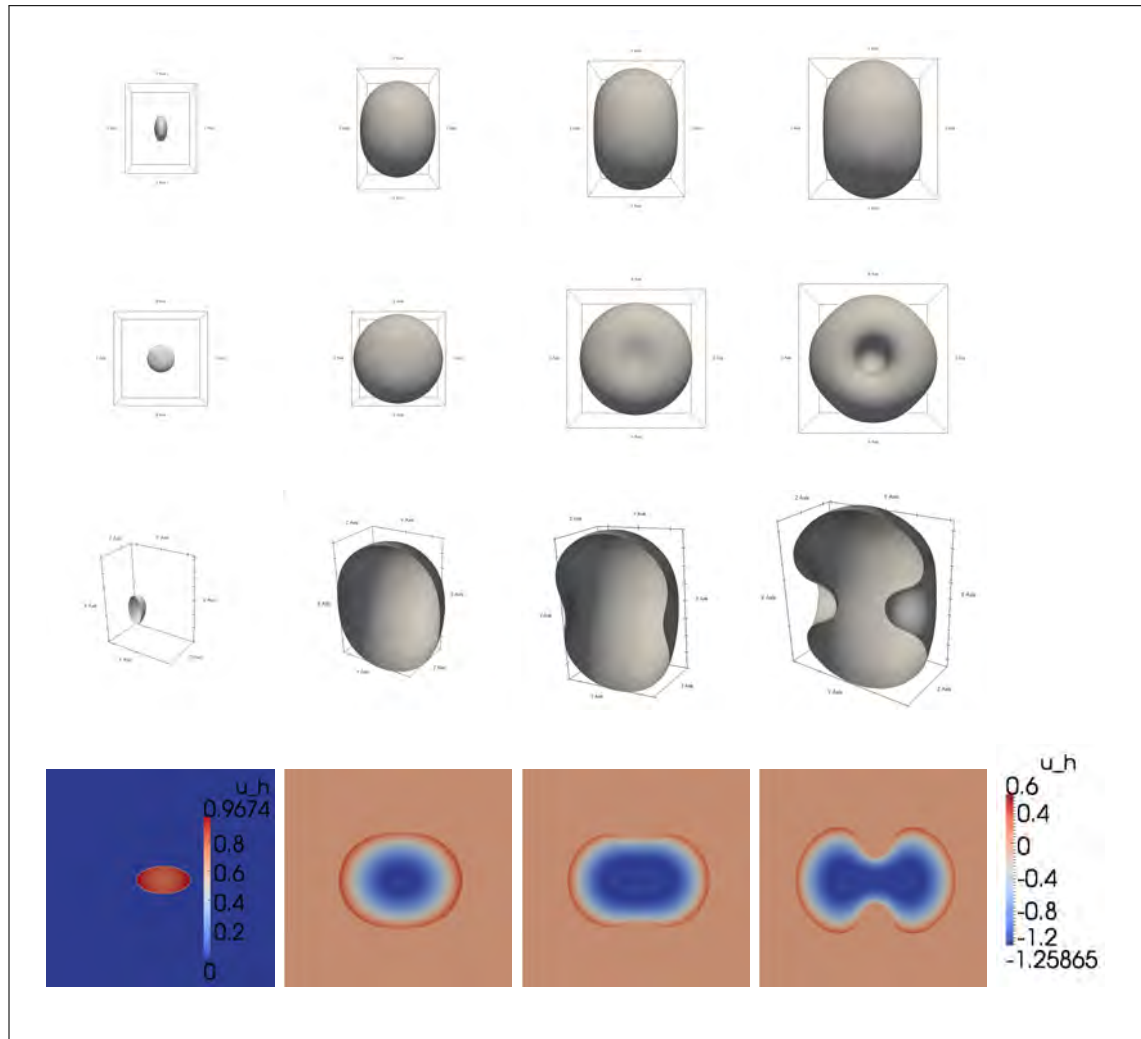


Figure 4.26: The level set $\varphi_h = 0$ for the diffuse interface scheme $\tilde{\mathbb{P}}_{DI}^h$, looking down the x -axis (first line), looking down the y -axis (second line), cross section in the plane $z = 0$ (third line), and u_h in the plane $z = 0$ (fourth line). Taken at $t = 0, 5, 10$, and 15 . The initial geometry is an oblate spheroid with the equation $\frac{x^2}{1.0^2} + \frac{y^2}{0.5^2} + \frac{z^2}{1.0^2} = 1$. We take $\alpha = 1.0$, $\beta = 0.1$, $Q = 1.25$, $\varepsilon = 0.1$, $h \approx 0.04$, and $\Delta t = 10^{-3}$.

We also repeat the simulation shown in Figure 4.25 (solving the sharp interface scheme $\mathbb{P}_{SI\mathbb{R}^3}^h$ with $\alpha = 1.0$, $\beta = 0.1$, and $Q = 1.25$) with a different initial geometry, given by an oblate and prolate spheroid with the equation $\frac{x^2}{1.0^2} + \frac{y^2}{0.5^2} + \frac{z^2}{1.5^2} = 1$. The result of the simulation can be seen in Figure 4.27.

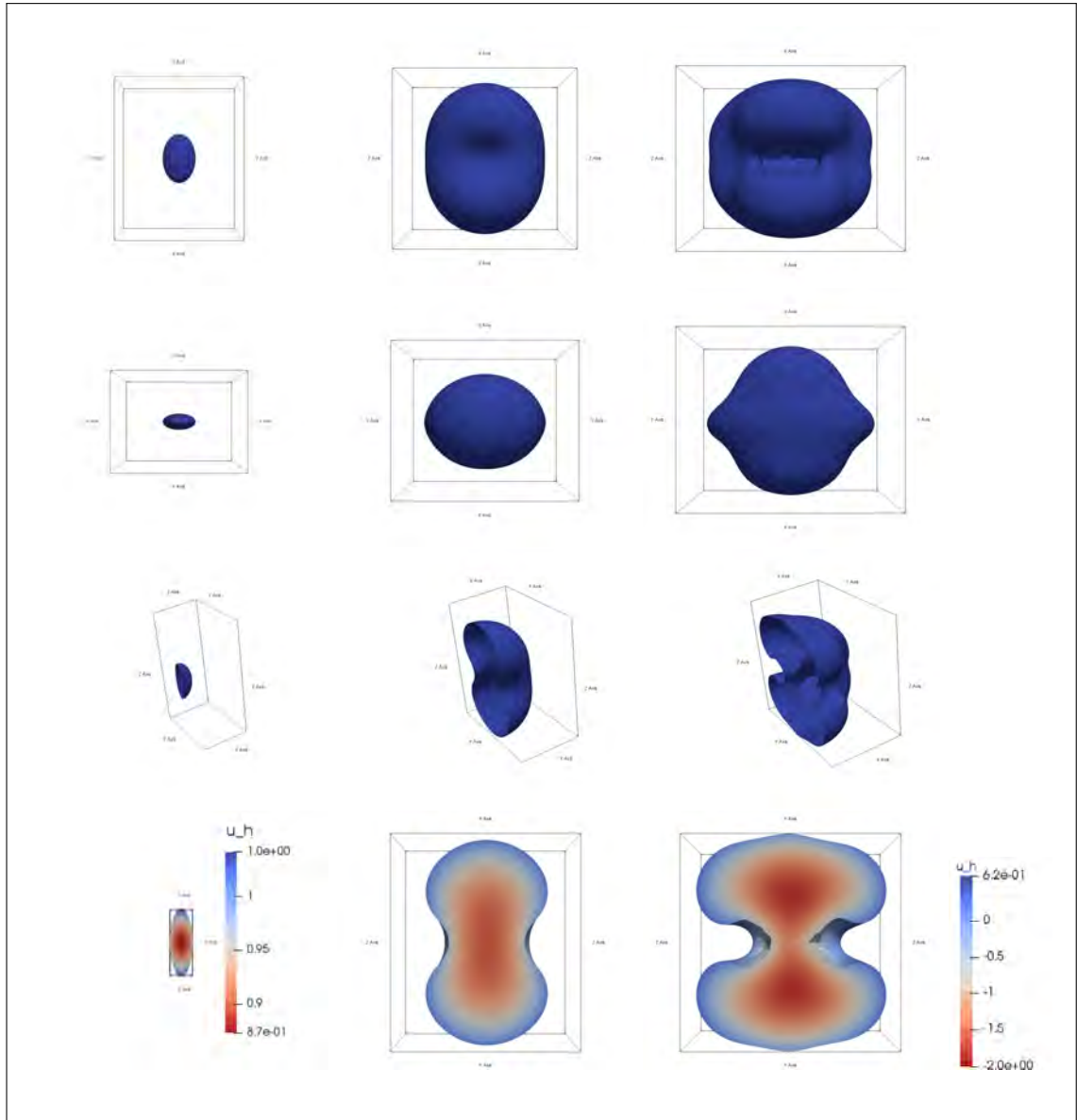


Figure 4.27: \mathbf{X}_h for the sharp interface scheme $\mathbb{P}_{SI\mathbb{R}^3}^h$ looking down the y -axis (first line), looking down the z -axis (second line), cross section in the plane $x = 0$ (third line), and u_h in the plane $x = 0$ (fourth line). Taken at $t = 0, 10$, and 18 . The initial geometry is an oblate and prolate spheroid with the equation $\frac{x^2}{1.0^2} + \frac{y^2}{0.5^2} + \frac{z^2}{1.5^2} = 1$. We take $\alpha = 1.0$, $\beta = 0.1$, $Q = 1.25$, $h \approx 0.014$, and $\Delta t = 5 \times 10^{-3}$.

Topological change

In Figure 4.28 we extend the simulations shown in Figure 4.26 in time. In order to run these simulations in a reasonable time, we had to increase the mesh size to $h \approx 0.09$. We can see that topological change creates “holes” within the tumour. Recall that the model is not biologically valid once these “holes” have formed.

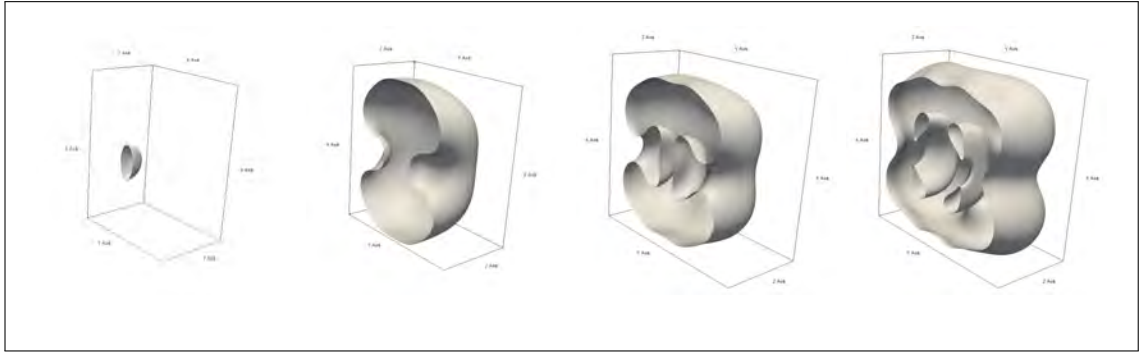


Figure 4.28: The level set $\varphi_h = 0$ for the diffuse interface scheme $\tilde{\mathbb{P}}_{DI}^h$, displayed as a cross section in the plane $z = 0$. Taken at $t = 0, 15, 19$, and 24 . The parameters match Figure 4.26 (but with h increased to $h \approx 0.09$).

4.6.2 The parameter space $\alpha, \beta \ll 1.0$

In this section we investigate the parameter space $\alpha, \beta \ll 1.0$. We take $\alpha = 0.1$ and $\beta = 0.1$. Due to the small α , we are only able to feasibly run the sharp interface scheme $\mathbb{P}_{SIR^3}^h$; the execution time for the diffuse interface scheme $\tilde{\mathbb{P}}_{DI}^h$ is too great. This is because a smaller α requires a smaller ε , which in turn requires greater h and smaller Δt . We take $Q = 1.25$, $h \approx 0.019$, and $\Delta t = 5 \times 10^{-3}$. In Figure 4.29 the initial geometry Γ_h^n is given by the oblate spheroid with equation $\frac{x^2}{1.0^2} + \frac{y^2}{0.5^2} + \frac{z^2}{1.0^2} = 1.0$, while in Figure 4.30 the initial geometry Γ_h^n is given by the oblate and prolate spheroid with equation $\frac{x^2}{1.0^2} + \frac{y^2}{0.5^2} + \frac{z^2}{1.5^2} = 1.0$.

Figure 4.29 shows \mathbf{X}_h , the solution to the sharp interface scheme $\mathbb{P}_{SIR^3}^h$, from three different angles: looking down the x -axis, down the y -axis, and a cross section in the plane $y = 0$. It also shows the solution u_h via a cross section in the plane $x = 0$. Similarly, Figure 4.30 shows \mathbf{X}_h , the solution to sharp interface scheme $\mathbb{P}_{SIR^3}^h$, from three different angles: looking down the y -axis, down the z -axis, and a cross section in the plane $x = 0$. It also shows the solution u_h via a cross section in the plane $y = 0$.

In Figure 4.29 we see that the symmetry in the y direction is lost in the image taken at $t = 4.1$ (this is particularly visible on the second line, looking down the y -axis). It appears to reach a similar geometry to that in Figure 4.30 at $t = 4.3$. This may be related to the effect discussed in Section 4.4.4, although it might be due to instability caused by the relatively large values of h and Δt .

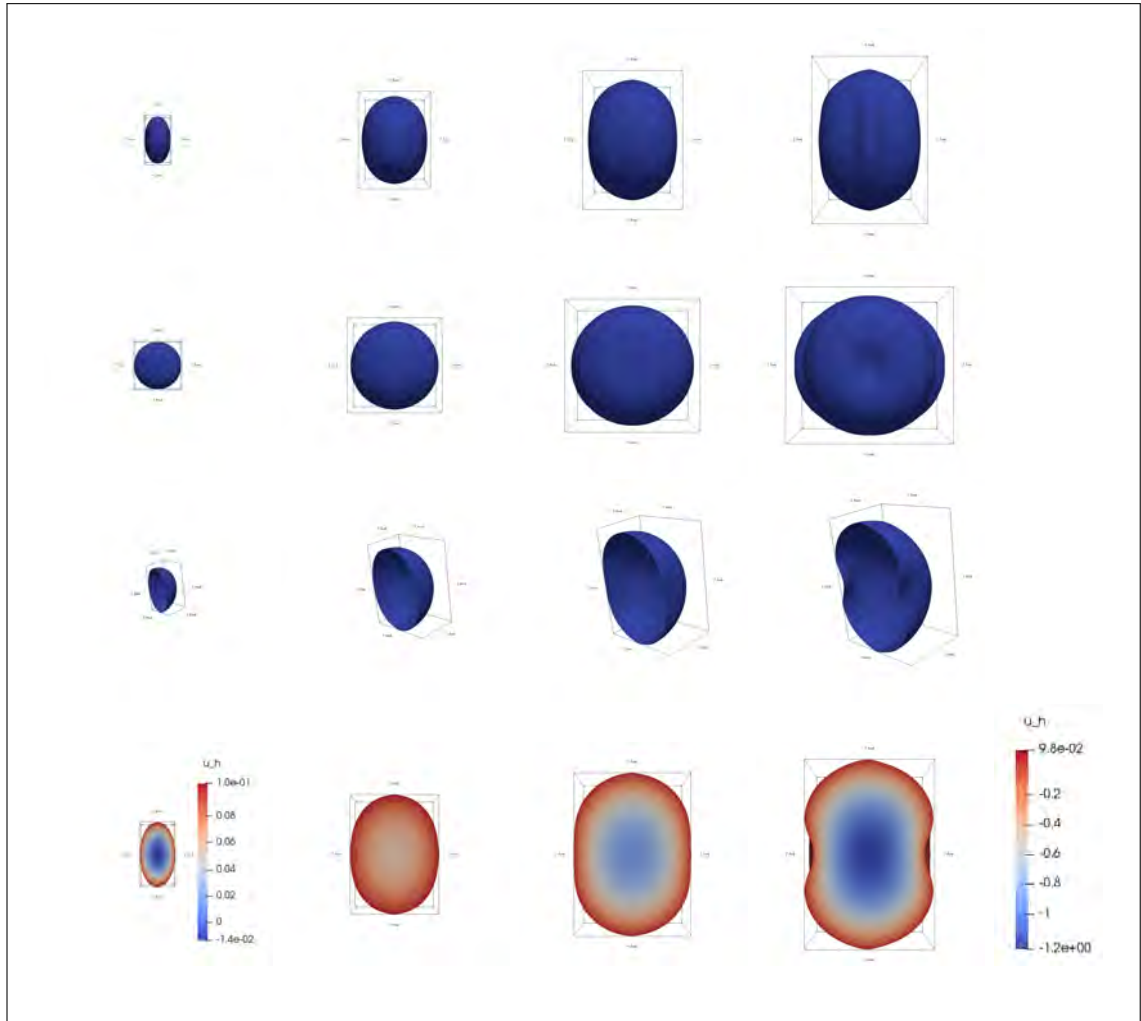


Figure 4.29: \mathbf{X}_h for the sharp interface scheme $\mathbb{P}_{SIR^3}^h$, looking down the x -axis (first line), looking down the y -axis (second line), cross section in the plane $y = 0$ (third line), and u_h in the plane $x = 0$ (fourth line). Taken at $t = 0, 1.4, 2.9$, and 4.1 . The initial geometry is an oblate spheroid with the equation $\frac{x^2}{1.0^2} + \frac{y^2}{0.5^2} + \frac{z^2}{1.0^2} = 1$. With $\alpha = 0.1$, $\beta = 0.1$, $Q = 1.25$, $h \approx 0.019$, and $\Delta t = 5 \times 10^{-3}$.

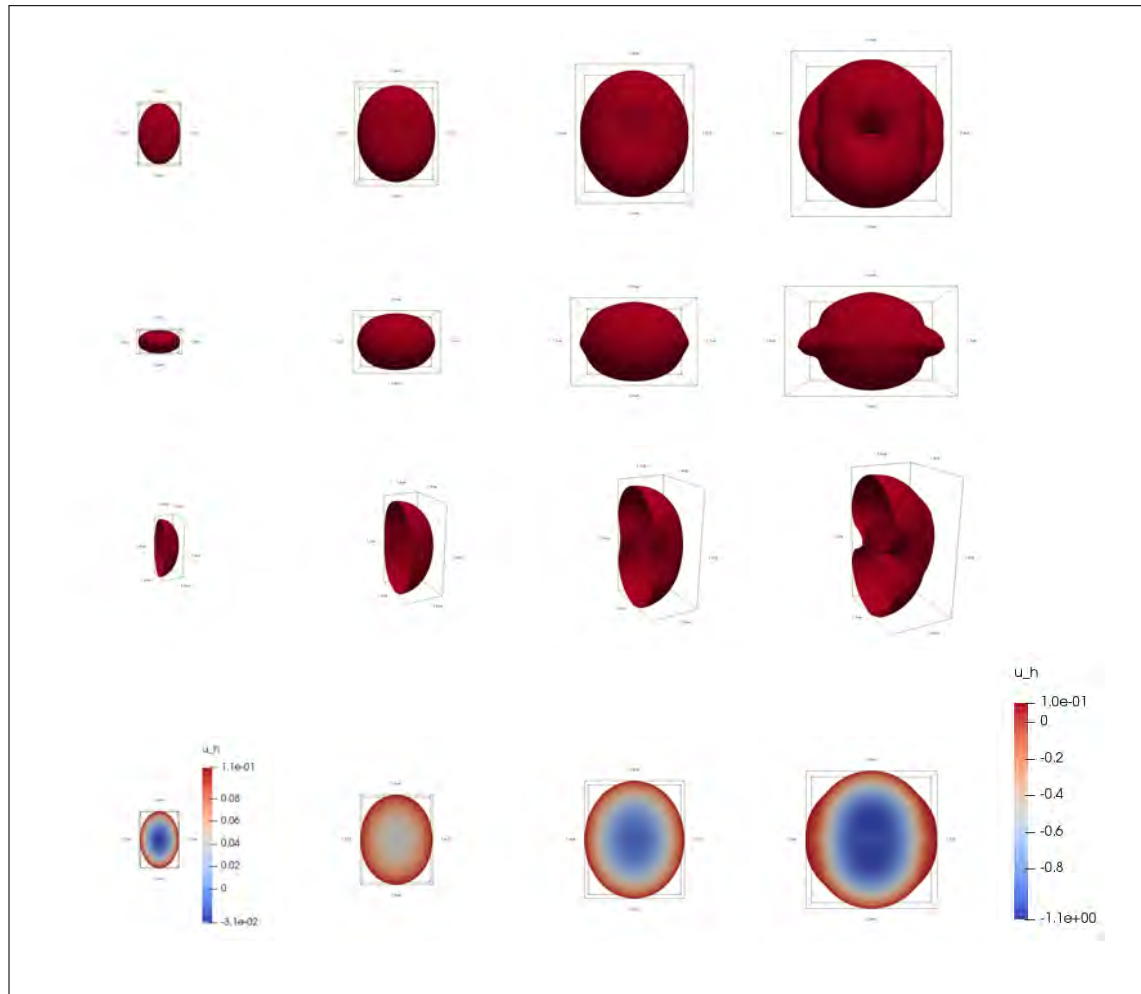


Figure 4.30: \mathbf{X}_h for the sharp interface scheme $\mathbb{P}_{SI\mathbb{R}^3}^h$, looking down the y -axis (first line), looking down the z -axis (second line), cross section in the plane $x = 0$ (third line), and u_h in the plane $y = 0$ (fourth line). Taken at $t = 0, 1.4, 2.9$, and 4.3 . The initial geometry is an oblate and prolate spheroid with the equation $\frac{x^2}{1.0^2} + \frac{y^2}{0.5^2} + \frac{z^2}{1.5^2} = 1$. With $\alpha = 0.1$, $\beta = 0.1$, $Q = 1.25$, $h \approx 0.019$, and $\Delta t = 5 \times 10^{-3}$.

4.6.3 Example of tumours *in vivo*

In this section we present two *in vivo* tumours in \mathbb{R}^3 . These are taken from the IRCAD database, which contains the 3D CT-scans of 10 men and 10 women, 75% of which have hepatic tumours (liver tumours). In Figure 4.31 we see two different tumours (one in row one, and one in row two) from three different angles. The tumours are orientated so that we see them looking down the x -axis, down the y -axis, and down the z -axis. They have been scaled so that they are the same size.

We see “ridges” forming in both tumours, which bear some resemblance to the simulations in Figures 4.29 and 4.30.

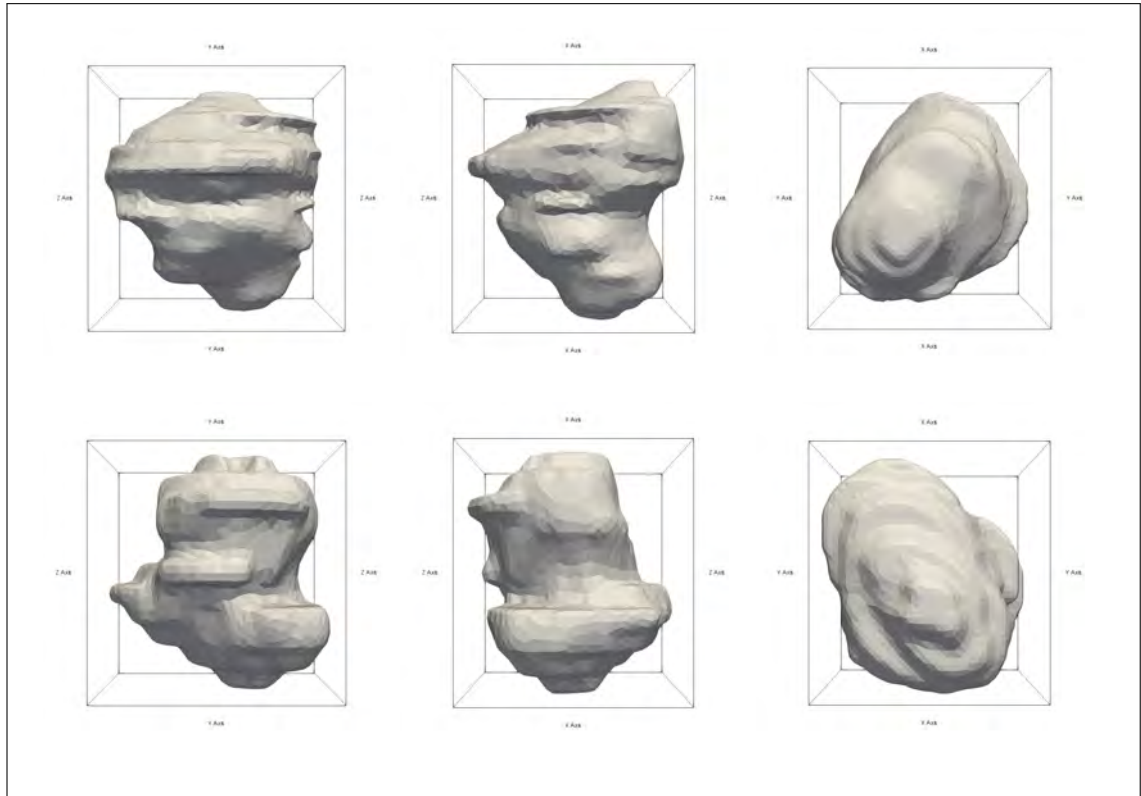


Figure 4.31: Two hepatic tumours taken from the IRCAD database. The first tumour is on the top row, and the second tumour is on the bottom row. We see each tumour looking down the x -axis, down the y -axis, and down the z -axis.

Chapter 5

Conclusion

In this thesis we derive, numerically analyse, and simulate a mathematical model for tumour growth. This model is tractable, which means that we are able to prove a number of applied and numerical analysis results, as well as accurately and effectively compute numerical solutions.

The model involves an evolving domain, the velocity law of which is coupled with an equation in the bulk. This type of model can be adapted to a wide range of phenomena, a few examples of which follow. Phase transitions often couple a parabolic equation with mean curvature flow, see the Stefan problem [28]. There is ongoing research into the modelling of cells, for example their internal chemistry [45], and motility [65]. The modelling of cells often involves reaction diffusion equations coupled with a free boundary. These types of equations are also employed when modelling diffusion induced grain boundary motion [39], in which a mean curvature equation is coupled with a parabolic equation. So, although this thesis is focussed on modelling tumour growth, the techniques can be adapted to apply to a wide range of phenomena; however, there is the notable difference that the examples presented here couple parabolic equations, whilst our model considers an elliptic equation (although in the case of the diffuse interface applied and numerical analysis, the elliptic equation is regularised by transforming it into a parabolic equation).

In order to numerically compute a solution to the model, a number of techniques are employed. The programming complexity of these techniques is high, and the code itself can be used and extended by future researchers.

A major hurdle that we overcame when implementing the sharp interface scheme was

that of the mesh. As the domain evolves, both the boundary and bulk meshes have to be maintained. In this thesis we combine a number of techniques to construct a practical approach to this problem in \mathbb{R}^2 (which can be extended to \mathbb{R}^3), thus allowing us to continue the simulations until a topology change occurs (and thus the model loses biological realism). Our solution was first to implement the technique introduced in [43]. Although effective, this technique only smooths the boundary mesh \mathcal{T}_Γ^h . We thus sought to smooth the bulk mesh \mathcal{T}_Ω^h , and so implemented the technique described in Algorithm 1 of [42]. This powerful algorithm allowed us to maintain high quality meshes for both \mathcal{T}_Γ^h and \mathcal{T}_Ω^h . In the rare instance where the mesh became degraded beyond repair, we employed the re-meshing software GMSH [52] to construct a new mesh for \mathcal{T}_Ω^h . This combination of techniques may be of particular interest when implementing simulations in future research as it is effective, allowing the sharp interface simulations to run until a topology change would occur.

The existence and uniqueness of the solution to the diffuse interface formulation of the model is proved. This proof follows many of the techniques used in [38], in which they prove the existence and uniqueness of a solution to a diffuse interface formulation of a mean curvature equation, coupled with a parabolic equation restricted to the curve. Since our model is a mean curvature equation coupled with a parabolic equation (in the regularised diffuse interface case) on the bulk, we have had to make numerous changes to the proof in order to adapt it to our model.

The proof of convergence of the diffuse interface finite element method follows many of the techniques used in [39]. Similar to the existence and uniqueness proof, the paper that we follow shows convergence of a diffuse interface formulation of a mean curvature equation coupled with a parabolic equation restricted to the curve. We have made significant changes to this in order to adapt it to our diffuse interface model.

5.1 Summary

We start by deriving a model (M) for tumour growth in Chapter 1. Although there are significantly more complex models in the literature, see for example [34], the model that we derive has the advantage of being highly tractable. It uses Darcy flow as its constitutive assumption, and models forces such as the internal pressure and surface tension. The

model is unique in that we pass to the thin rim limit. We conclude the derivation by regularising the model.

The sharp interface approach is discussed in Chapter 2. We first consider the case where $\Gamma(t)$ is an evolving closed curve in \mathbb{R}^2 ; we introduce a weak formulation of the problem which we then use to derive a finite element approximation. Next, mesh smoothing techniques are discussed, and then an unfitted finite element approximation is considered. Lastly, we introduce a finite element approximation for the case where $\Gamma(t)$ is an evolving closed hypersurface in \mathbb{R}^3 .

The following chapter, Chapter 3, introduces the diffuse interface approach. We first write the model (M) in the diffuse interface paradigm; here we regularise the elliptic equation in time with an $\varepsilon^2 u_t$ term, thus transforming it into a parabolic equation. This is followed by the weak form for the diffuse interface version of the model. We then prove the existence and uniqueness of a solution to this model. A finite element scheme is presented, along with a proof of existence and uniqueness of a solution to it. We finally prove a convergence result for the finite element scheme.

Finally, Chapter 4 presents numerical simulations for the finite element schemes given in Chapters 2 and 4. The chapter starts with the introduction of an alternative formulation of the model. We then introduce a diffuse interface approximation that does not include the $\varepsilon^2 u_t$ regularisation term. We follow this with a summary of the techniques used in the implementations of the finite element schemes. The simulations begin in the radially symmetric paradigm. Since we can derive an analytic solution when restricted to radial symmetry, we begin our numerical simulations by using this analytic solution to argue for the accuracy of our finite element schemes. We then include a biologically focussed investigation. Geometries without radial symmetry are then presented (in \mathbb{R}^2 and \mathbb{R}^3), and we investigate the relationship between the parameters α and β (by fixing Q). We conclude the sections on \mathbb{R}^2 and \mathbb{R}^3 with a small number of examples of tumours *in vivo*.

5.2 Future directions

We conclude this thesis with a number of possible future directions for research. This list is not exhaustive, but it represents many ideas that naturally follow from the work presented in this thesis.

- Although we compare our simulations to a small selection of tumours *in vivo*, it would be beneficial to deepen this comparison, as it would help to ground the model in a biological setting. In particular, it would be beneficial to match the evolution of tumours *in vivo* or *in vitro* to simulations in particular parameter spaces.
- The tumour model is intentionally tractable in order to allow a relatively large amount of mathematical analysis to be carried out. A possible future direction would be to extend the model. This extension could, for example, include physical effects, chemical effects, or genetic effects. Ideally, this addition to the model would allow for an extension of the applied and numerical analysis results given in this thesis.
- The external medium is modelled very simply. This medium could be more closely modelled, perhaps so as to induce an external physical pressure on the tumour.
- Implementing topological changes in the sharp interface case, perhaps using [18], would be useful in verifying the topological changes in the diffuse interface case.

Bibliography

- [1] H. Abels, K. F. Lam, and B. Stinner. Analysis of the diffuse domain approach for a bulk-surface coupled PDE system. *SIAM Journal on Numerical Analysis*, 47(5):3687–3725, 2015.
- [2] D. B. Agus, W. Bearer, Y. L. Chuang, V. Cristini, M. Ferrari, H. B. Frieboes, F. Jin, J. S. Lowengrub, and S. M. Wise. Multiparameter computational modeling of tumor invasion. *Cancer Research*, 69(10):4493–501, 2009.
- [3] J. Ahrens, B. Geveci, and C. Law. *ParaView: an end-user tool for large data visualization*. Visualization Handbook, Elsevier, 2005.
- [4] J. W. Barrett, J. F. Blowey, and H. Garcke. Finite element approximation of the Cahn-Hilliard equation with degenerate mobility. *SIAM Journal on Numerical Analysis*, 37(1):286–318, 1999.
- [5] J. W. Barrett, K. Deckelnick, and V. Styles. Numerical analysis for a system coupling curve evolution to reaction-diffusion on the curve. *SIAM Journal on Numerical Analysis*, 55(2):1080–1100, 2017.
- [6] J. W. Barrett and C. M. Elliott. A practical finite element approximation of a semi-definite Neumann problem on a curved domain. *Numerische Mathematik*, 51(1):23–36, 1987.
- [7] J. W. Barrett and C. M. Elliott. Finite-element approximation of elliptic equations with a Neumann or Robin condition on a curved boundary. *IMA Journal of Numerical Analysis*, 8(3):321–342, 1988.

-
- [8] J. W. Barrett, H. Garcke, and R. Nürnberg. On stable parametric finite element methods for the Stefan problem and the Mullins–Sekerka problem with applications to dendritic growth. *Journal of Computational Physics*, 229(18):6270–6299, 2010.
- [9] J. W. Barrett, H. Garcke, and R. Nürnberg. The approximation of planar curve evolutions by stable fully implicit finite element schemes that equidistribute. *Numerical Methods for Partial Differential Equations*, 27(1):1–30, 2011.
- [10] J. W. Barrett, R. Nürnberg, and V. Styles. Finite element approximation of a phase field model for void electromigration. *SIAM Journal on Numerical Analysis*, 42(2):738–772, 2004.
- [11] E. Bearer, V. Cristini, H. B. Frieboes, J. S. Lowengrub, P. Macklin, S. M. Wise, and X. Zheng. Computer simulation of glioma growth and morphology. *Neuroimage*, 37(Suppl 1):S59–S70, 2007.
- [12] D. Bellet, V. Dangles-Marie, and L-B. Weiswald. Spherical cancer models in tumor biology. *Neoplasia*, 17(1):1–15, 2015.
- [13] N. Bellomo, N. K. Li, and P. K. Maini. On the foundations of cancer modelling: selected topics, speculations, and perspectives. *Mathematical Models and Methods in Applied Sciences*, 18(4):593–646, 2008.
- [14] K. Bloch, D. R. Grimes, C. Kelly, and M. Partridge. A method for estimating the oxygen consumption rate in multicellular tumour spheroids. *Journal of the Royal Society Interface*, 11(92):20131124, 2014.
- [15] J. F. Blowey and C. M. Elliott. A phase field model with a double obstacle potential. *Motion by mean curvature*, ed. G. Buttazzo and A. Visintin, de Gruyter, pages 1–22, 1994.
- [16] S. C. Brenner and R. Scott. *The mathematical theory of finite element methods*. Springer, 2008.
- [17] C. J. W. Beward, H. M. Byrne, and C. E. Lewis. A multiphase model describing vascular tumour growth. *Bulletin of Mathematical Biology*, 65(4):609–640, 2003.

-
- [18] R. Bridson and T. Brochu. Robust topological operations for dynamic explicit surfaces. *SIAM Journal on Scientific Computing*, 31(4):2472–2493, 2009.
- [19] H. M. Byrne and M. A. J. Chaplain. Free boundary value problems associated with the growth and development of multicellular spheroids. *European Journal of Applied Mathematics*, 8(6):639–658, 1997.
- [20] H. M. Byrne, J. A. Clements, J. A. Flegg, D. W. Hutmacher, and D. Loessner. Growth of confined cancer spheroids: a combined experimental and mathematical modelling approach. *Integrative Biology*, 5(3):597–605, 2013.
- [21] H. M. Byrne, J. Dold, J. Gibson, and A. F. Jones. A mathematical model of the stress induced during avascular tumour growth. *Journal of Mathematical Biology*, 40(6):473–499, 2000.
- [22] S. Cao, J. Cheng, Q. Feng, W. Huang, Z. Wang, R. Yang, W. Yang, and Z. Yun. Enhanced performance of brain tumor classification via tumor region augmentation and partition. *PLoS ONE*, 10(10):e0140381, 2015.
- [23] P. Carmeliet and R. K. Jain. Angiogenesis in cancer and other diseases. *Nature*, 407:249–257, 2000.
- [24] S. Caserta, V. Cristini, M. Ferrari, H. B. Frieboes, R. Gatenby, and J. Sinek. Morphologic instability and cancer invasion. *Clinical Cancer Research*, 11(19):6772–6779, 2005.
- [25] M. A. J. Chaplain and M. E. Orme. A mathematical model of vascular tumour growth and invasion. *Mathematical and Computer Modelling*, 23(10):43–60, 1996.
- [26] M. A. J. Chaplain and J. Sherratt. A new mathematical model for avascular tumour growth. *Journal of Mathematical Biology*, 43(4):291–312, 2001.
- [27] X. Chen and C. M. Elliott. Asymptotics for a parabolic double obstacle problem. *Proceedings: Mathematical and Physical Sciences*, 444(1922):429–445, 1994.
- [28] X. Chen and F. Reitich. Local existence and uniqueness of solutions of the Stefan problem with surface tension and kinetic undercooling. *Journal of Mathematical Analysis and Applications*, 164(2):350–362, 1992.

-
- [29] J. Cheng, W. Chen, Y. Feng, Q. Feng, M. Huang, W. Huang, J. Jiang, R. Yang, W. Yang, J. Zhao, and Y. Zhou. Retrieval of brain tumors by adaptive spatial pooling and Fisher vector representation. *PLoS ONE*, 11(6):e0157112, 2016.
- [30] P. G. Ciarlet. *The finite element method for elliptic problems*. Elsevier, 1978.
- [31] P. G. Ciarlet and P. A. Raviart. Maximum principle and uniform convergence for the finite element method. *Computer Methods in Applied Mechanics and Engineering*, 2(1):17–31, 1973.
- [32] P. Colli, G. Gilardi, and D. Hilhorst. On a Cahn-Hilliard type phase field system related to tumor growth. *Discrete and Continuous Dynamical Systems*, 35(6):2423–2442, 2015.
- [33] V. Cristini, X. Li, J. S. Lowengrub, and S. M. Wise. Nonlinear simulations of solid tumor growth using a mixture model: invasion and branching. *Journal of Mathematical Biology*, 58(4-5):723–763, 2009.
- [34] V. Cristini and J. S. Lowengrub. *Multiscale modeling of cancer: an integrated experimental and mathematical modeling approach*. Cambridge University Press, 2010.
- [35] V. Cristini, S. J. Madsen, C-H. Sun, and B. J. Tromberg. Multicell tumor spheroids in photodynamic therapy. *Lasers in Surgery and Medicine*, 38(5):555–564, 2006.
- [36] S. Cui and A. Friedman. A free boundary problem for a singular system of differential equations: an application to a model of tumor growth. *Transactions of the American Mathematical Society*, 355(9):3537–3590, 2003.
- [37] K. Deckelnick, G. Dziuk, and C. M. Elliott. Computation of geometric partial differential equations and mean curvature flow. *Acta Numerica*, 14:139–232, 2005.
- [38] K. Deckelnick and C. M. Elliott. An existence and uniqueness result for a phase-field model of diffusion-induced grain-boundary motion. *Proceedings of the Royal Society of Edinburgh*, 131(6):1323–1344, 2001.
- [39] K. Deckelnick, C. M. Elliott, and V. Styles. Numerical diffusion induced grain boundary motion. *European Mathematical Society*, 3(4):393–414, 2001.

-
- [40] G. Dziuk. Convergence of a semi discrete scheme for the curve shortening flow. *Mathematical Models and Methods in Applied Sciences*, 4(4):589–606, 1994.
- [41] G. Dziuk and C. M. Elliott. Finite element methods for surface PDEs. *Acta Numerica*, 22:289–396, 2013.
- [42] C. M. Elliott and H. Fritz. On algorithms with good mesh properties for problems with moving boundaries based on the harmonic map heat flow and the DeTurck trick. *SMAI Journal of Computational Mathematics*, 2:141–176, 2016.
- [43] C. M. Elliott and H. Fritz. On approximations of the curve shortening flow and of the mean curvature flow based on the DeTurck trick. *IMA Journal of Numerical Analysis*, 37(2):543–603, 2017.
- [44] C. M. Elliott and J. R. Ockendon. *Weak and variational methods for free and moving boundary problems*. Pitman Publishing, 1982.
- [45] C. M. Elliott, T. Ranner, and C. Venkataraman. Coupled bulk-surface free boundary problems arising from a mathematical model of receptor-ligand dynamics. *SIAM Journal on Mathematical Analysis*, 49(1):360–397, 2017.
- [46] L. C. Evans. *Partial differential equations*. American Mathematical Society, 1998.
- [47] J. Eyles, J. R. King, and V. Styles. A tractable mathematical model for tissue growth. *In preparation*.
- [48] S. J. Franks and J. R. King. Mathematical modelling of nutrient-limited tissue growth. *Free Boundary Problems. International Series of Numerical Mathematics*, 154:273–282, 2006.
- [49] A. Friedman. *Variational principles and free-boundary problems*. New York: Wiley, 1982.
- [50] S. Frigeri, M. Grasselli, and E. Rocca. On a diffuse interface model of tumor growth. *European Journal of Applied Mathematics*, 26(2):215–243, 2015.
- [51] H. Garcke, K. F. Lam, E. Sitka, and V. Styles. A Cahn–Hilliard–Darcy model for tumour growth with chemotaxis and active transport. *Mathematical Models and Methods in Applied Sciences*, 26(6):1095–1148, 2016.

-
- [52] C. Geuzaine and J-F. Remacle. Gmsh: a three-dimensional finite element mesh generator with built-in pre- and post-processing facilities. *International Journal for Numerical Methods in Engineering*, 79(11):1309–1331, 2009.
- [53] D. Gilbarg and N. S. Trudinger. *Elliptic partial differential equations of second order*. Springer, 3rd edition, 1998.
- [54] H. P. Greenspan. Models for the growth of a solid tumour by diffusion. *Studies in Applied Mathematics*, 51(4):317–340, 1972.
- [55] H. P. Greenspan. On the growth and stability of cell cultures and solid tumours. *Journal of Theoretical Biology*, 56(1):229–242, 1976.
- [56] H. Hagel, G. Harling, M. Jeppesen, L. N. Jorgensen, J. Thastrup, O. Thastrup, and B. Vainer. Abstract 2020: Spheroid culture of primary colorectal cancer cells from liver metastases as an *in vitro* model of patient tumors. *Proceedings: AACR Annual Meeting 2014*, 74(19 Supplement):2020–2020, 2014.
- [57] A. Hawkins-Daarud, J. T. Oden, S. Prudhomme, and K. G. van der Zee. Bayesian calibration, validation, and uncertainty quantification of diffuse interface models of tumor growth. *Journal of Mathematical Biology*, 67(6–7):1457–1485, 2013.
- [58] S. D. Howison. Complex variable methods in Hele-Shaw moving boundary problems. *European Journal of Applied Mathematics*, 3(3):209–224, 1992.
- [59] S. D. Howison, A. A. Lacey, and J. R. Ockendon. Mushy regions in negative squeeze films. *The Quarterly Journal of Mechanics and Applied Mathematics*, 56(3):361–379, 2003.
- [60] A. Y. Hsiao, M. Ingram, G. D. Luker, G. Mehta, and S. Takayama. Opportunities and challenges for use of tumor spheroids as models to test drug delivery and efficacy. *Journal of Control Release*, 164(2):192–204, 2012.
- [61] J. R. King and J. Ward. Mathematical modelling of avascular-tumour growth. *IMA Journal of Applied Medical Biology*, 14(1):39–69, 1997.
- [62] J. R. King and J. Ward. Mathematical modelling of drug transport in tumour multicell spheroids and monolayer cultures. *Mathematical Biosciences*, 181(2):177–207, 2003.

-
- [63] O. A. Ladyzhenskaya and N. N. Uraltseva. *Linear and quasilinear elliptic equations*. Academic Press, 1968.
- [64] K. F. Lam. *Diffuse interface models of soluble surfactants in two-phase fluid flows*. PhD thesis, University of Warwick, 2014.
- [65] H. Levine, W-J. Rappel, and D. Shao. Coupling actin flow, adhesion, and morphology in a computational cell motility model. *Proceedings of the National Academy of Sciences of the United States of America*, 109(18):6851–6856, 2012.
- [66] D. L. McElwain, G. J. Pettet, C. P. Please, and M. J. Tindall. The migration of cells in multicell tumor spheroids. *Bulletin of Mathematical Biology*, 63(2):231–257, 2001.
- [67] R. H. Nochetto, M. Paolini, and C. Verdi. Sharp error analysis for curvature dependent evolving fronts. *Mathematical Models and Methods in Applied Sciences*, 3(6):711–723, 1993.
- [68] A. Sacconi. *Front-tracking finite element methods for a void electro-stress migration problem*. PhD thesis, Imperial College London, 2015.
- [69] A. Schmidt and K. G. Siebert. *Design of adaptive finite element software: the finite element toolbox ALBERTA*. Springer Berlin Heidelberg, 2004.
- [70] J. Simon. Compact sets in the space $L^p(0, T; B)$. *Annali di Matematica Pura ed Applicata*, 146(1):65–96, 1986.
- [71] I. P. M. Tomlinson. Game-theory models of interactions between tumour cells. *European Journal of Cancer*, 33(9):1495–1500, 1997.